FINAL TECHNICAL REPORT

PRECISION ATTITUDE DETERMINATION SYSTEM

13900-6014-RU-00

1 JULY 1973

PADS SYSTEM DESIGN AND ANALYSIS

(TWO-AXIS GIMBAL STAR TRACKER)

Contract No. NAS5-21111

Prepared for

NATIONAL AERONAUTICS AND SPACE ADMINISTRATION
GODDARD SPACE FLIGHT CENTER
Greenbelt, Maryland 20771

TRW
SYSTEMS GROUP

ONE SPACE PARK • REDONDO BEACH, CALIFORNIA 90278

FINAL TECHNICAL REPORT

PRECISION ATTITUDE DETERMINATION SYSTEM

13900-6014-RU-00 1 JULY 1973

PADS SYSTEM DESIGN AND ANALYSIS

(TWO-AXIS GIMBAL STAR TRACKER)

Contract No. NAS5-21111

Prepared for

NATIONAL AERONAUTICS AND SPACE ADMINISTRATION
GODDARD SPACE FLIGHT CENTER
Greenbelt, Maryland 20771

TRW
SYSTEMS GROUP

ONE SPACE PARK • REDONDO BEACH, CALIFORNIA 90278

TABLE OF CONTENTS

1.0 INTRODUCTION

In response to projected requirements for arc-second level attitude determination and pointing control, TRW Systems and NASA/GSFC have pursued the requisite technology through the Precision Pointing Control System (PPCS) study (Contract NAS 5-21111) since early 1970. Noting that the pointing function is often quite mission dependent, particular emphasis was placed on development of an attitude determination approach having near-universal applicability. As a result of the design and development effort expended during the initial studies [1,2], important design simplications were identified which could be realized in the attitude determination hardware implementation with minimal impact on the achievable system performance. These improvements have led to the development of the Precision Attitude Determination System (PADS) having an accuracy goal of 0.001 degree (1σ, per axis).

The PADS design activity documented in this report focuses chiefly on the two-axis gimballed star tracker and electronics design improved from that of PPCS, and application of the improved tracker for PADS at geosynchronous altitude. The report documents system design, system analysis, software design, and hardware design activities. The system design encompasses the PADS configuration, system performance characteristics, component design summarizes, and interface considerations. PADS design and performance analysis includes error analysis, performance analysis via attitude determination simulation, and star tracker servo design analysis. This is followed by discussion of the detailed hardware design of the star tracker and electronics. Sensor electronics schematics are included as an Appendix. Software design provides a detailed characterization of the application software algorithms and computer requirements.

2.0 PADS SYSTEM DESIGN

The Precision Attitude Determination System (PADS) is an advanced spacecraft attitude determination system capable of accuracies exceeding 0.001 degree (1σ, per axis). The PADS concept employs precision strapdown gyros to derive high bandwidth short-term attitude, and a two-axis gimballed star tracker providing low bandwidth attitude data which is periodically filtered to update attitude and gyro drift. The PADS design is similar to that developed for the Precision Pointing Control System [1], both functionally and operationally. The key design differences are associated with the hardware implementation; in particular, the gimballed star tracker and associated electronics.

2.1 Functional/Operational Description

PADS comprises a precision gimballed star tracker and associated electronics, a three-axis gyro package, and an on-board computer and associated software (Figure 2-1). The gimballed Star Tracker Assembly (STA) is used to acquire and track stars and provide a measure of the star line-of-sight (LOS) angle. The Sensor Electronics Assembly (SEA) provides the gimbal servo/drive electronics and gimbal readout processing. The Gyro Reference Assembly (GRA) incorporates a configuration of strapdown pulse rebalanced rate integrating gyros plus electronics. A Reference Block Assembly (RBA) provides a stable thermo-mechanical interface with the spacecraft to which the sensors are mounted and aligned relative to each other. The Digital Processor Assembly (DPA) comprises the computer-I/O to implement system software. Processing of the gyro data provides the basic means used to compute attitude. Due to gyro drift uncertainties, the processed gyro data leads to errors which would, in time, become unacceptably inaccurate. Therefore, attitude and gyro drift corrections are periodically estimated via star measurements processed in a Kalman filter.

Gyro data is in the form of accumulated pulse counts representing the sensed incremental rotation about the gyro input axis over the sample period. The gyro is processed to derive rate and transformed to the PADS reference frame. The transformation is through a "geometry matrix" which is defined from knowledge of gyro input axis alignment and scale factor. The gyro bias compensation is summed with the derived rate to provide the rate estimate for use in the attitude algorithm. The attitude algorithm consists of a closed form solution for Euler Symmetric Parameters.

The gimballed tracker provides exceptional flexibility for the updating procedure, minimizing constraints both on star selection and frequency between star sightings (updates). Star selection is made from a small stored catalog of target stars. A typical algorithm selects that star in the catalog and within the tracker gimbal freedom which has the greatest angular separation from the prior star. For

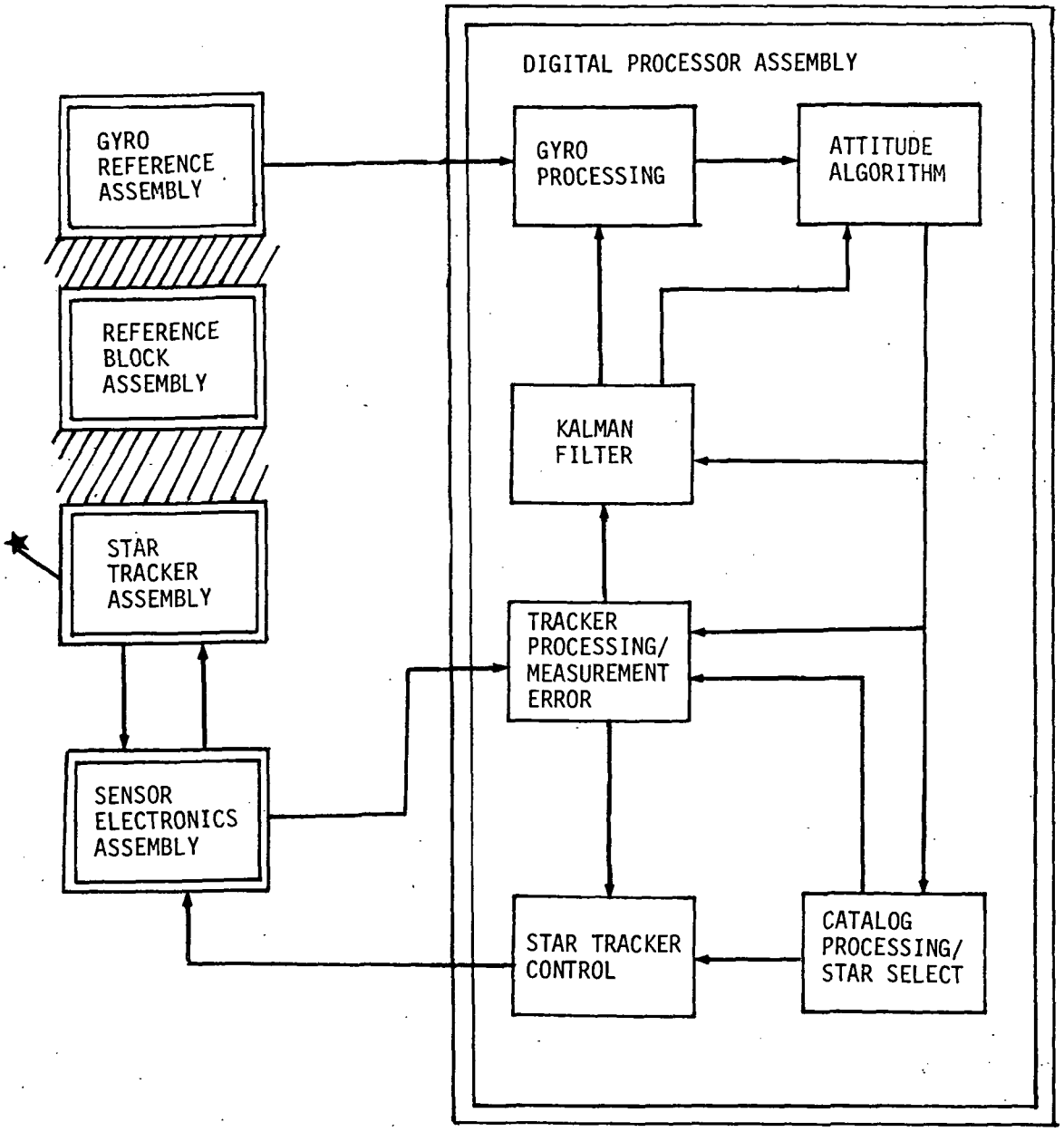

Figure 2-1. PADS Functional Block Diagram

initial star acquisition, a star search algorithm may be used to control the gimbal pointing to locate initial target stars. For spacecraft attitude uncertainty less than the 0.5° x 0.5° tracker optical FOV (e.g., <0.1 degree) star acquisition will occur without a search procedure. With sensor "lock-on" the desired target star established, the star tracker closed-loop null tracking mode (independent of the computer) is initiated.

An estimate of the star line of sight (LOS) gimbal angles is made by first correcting the star coordinates for aberration of the apparent star position and then relating the coordinates to the tracker gimbal angles, detector outputs, and tracker alignment to form the estimated measurement vector. The observed measurement vector is established from the gimbal and detector readout and differenced with the estimated value to attain a measurement residual (i.e., error) which is used in the Kalman filter. The Kalman filter is used to estimate a six-element state vector consisting of three attitude and three gyro bias variables. The Kalman filter develops an "optimal" gain matrix which multiplies the measurement residual to establish the desired correction to the state vector.

Based upon a series of several star sightings, the attitude estimate will converge to an accuracy consistent with system misalignments and biases; typically, steady-state is reached within 30 to 60 minutes. During this period, the system will reach thermal equilibrium. In-flight calibration may be utilized to determine compensation for systematic errors. Observables include gyro input axis misalignments, scale factor uncertainties, and tracker misalignments.

2.2 PADS Performance and Design Characteristics

The PADS performance characteristics are summarized briefly below, and the physical characteristics of the PADS hardware elements are presented in Table 2-1.

- Vehicle Orbital Envelope

  All orbit capability, with appropriate prior definition and satisfaction of minimum FOV constraints.

  Specific design for: 200-2500 nautical miles, sun synchronous synchronous, equatorial

- Vehicle Attitude Envelope

  Three-axis stabilized to earth or celestial reference with attitude error/attitude rate error with respect to reference limited by:

  Attitude: ±3 degrees (3σ)
  Attitude Rate: ±0.03 degree/second (3σ)

Table 2-1. Summary of PADS Physical Characteristics

	Wt (lb)	Power (w.)	Envelope (in.)
Star Tracker Assembly (STA)*	38	9	9.6 x 20.0 x 12.6
Sensor Electronics Assembly (SEA)	8	21	6 x 8 x 8
Gyro Reference Assembly (GRA)(1)	9	10	6 x 6 x 5
Reference Block Assembly (RBA)	10	-	-
Digital Processor Assembly (DPA)(2)	17	27	11.5 x 10.5 x 6.5
Integration Hardware	4	-	-
Total System	86 lb	67 w	21" x 26" x 20" (3)

*Aluminum construction, beryllium is approximately 9 lbs less

(1) Triad, Unheated

(2) Typical

(3) Approximate total envelope occupied

- Update Characteristics/Constraints

  Update capability every 30 seconds, nominally selected update interval of 5 minutes. Gimbal freedom/tracker sensitivity selected to provide three or more stars in FOV mutally separated by >15 degrees.

  Gimbal Tracker FOV: ±45 x ±15
  Tracker Slew Rate: >4 degrees/second
  Star Sensitivity: +3.5 Mv AO and brighter

- Initial Acquisition and Convergence

  30 to 60 minutes

- Accuracy/Stability

  State Vector Estimates: Attitude, better than 0.001 degree (1σ), each axis
  Gyro Bias, better than 0.002 degree/hour (1σ), each axis
  Measurement Accuracy: Better than 1.9 arc-second (1σ)

2.3 PADS Components

A brief functional description and performance summary is provided for each of the PADS hardware/software components. Detailed design of the Star Tracker Assembly, Sensor Electronics Assembly, and software is presented in later sections.

2.3.1 Star Tracker Assembly

2.3.1.1 Functional Description

The Star Tracker Assembly is a precision, two-axis gimballed, null-tracking sensor conceived as an evolution of the TRW PPCS star tracker [2]. Relative to the PPCS unit, the PADS star tracker is smaller and lighter, consumes less power and, although slightly less accurate, provides the required performance characteristics.

The gimballed STA consists of two units - the Sensor Gimbal Unit (SGU) and the Star Sensor Unit (SSU). The function of the SSU is to provide star detection, tracking within the FOV, and error signal generation. The functional elements of the SSU include the optical system, the detector, and the SSU electronics arranged in a single housing in a configuration which is mechanically and thermally symmetric.

- Optical System - An all reflective Cassegrain telescope collects and focuses radiant energy on the detector. The focal length is 33 inches, with an optical field of view of 0.5° x 0.5°. A sun shade permits

tracking to within 45° of the sun and 15° of the spacecraft structure. A sun sensor provides detector protection from direct solar illumination via a shutter and high voltage disable.

- Detector - The photo-detector used is a image dissector, type F 4004. The image dissector converts the stellar optical image into an electron image stream which is modulated by magnetic deflection to obtain star position information in each of two axes.

- Electronics - The electronics provide the voltages and waveforms to operate the image dissector and to process the video signal from the image dissector to develop the error signals.

The star sensor has two modes of operation, search and track. In the search mode, initiated by command or loss of track, the total optical FOV (0.5° x 0.5°) is scanned in a 32 x 32 step raster by a smaller instantaneous field of view (IFOV). Video pulses are processed by mode control circuits to terminate the search scan on the brightest star present in the search field-of-view. With the termination of the search mode, the brightest star image has been deflected into the image dissector aperture. In the tracking mode, a small cruciform tracking pattern provides spatial modulation of the star signal. Video processing circuits and a demodulator then develop correction signals which are fed back to the deflection generator to center the star electron image in the dissector aperture. The tracking loop feedback continues to keep the star image centered regardless of spacecraft motion. The sensor-pointing error is developed by sampling the dc deflection bias required to center the star image.

The function of the Sensor Gimbal Unit (SGU) is to provide two-axis mechanical suspension and drive of the SSU and a precision readout of the angular motion. The SGU consists of the inner gimbal housing assemblies, the gimbal ring, and the outer gimbal assemblies. The gimbal ring is an I-beam casting of aged 356 Aluminum. Each housing assembly (two for each axis) contains Inductosyn gimbal angle encoder, gimbal suspension, gimbal caging mechanism, data link assembly, and drive motor.

- Encoder - The selected feedback elements for measuring displacement are two resolver units (Inductosyn) per axis. One unit is single speed and the other has 256 speed capability.

- The Gimbal Suspension - The gimbal design features a one-ball bearing configuration. The geometry of this scheme provides self alignment feature and facilitates the fabrication of the gimbal system by providing inherent

reference for the establishment of two mutually perpendicular planes which contain the rotational axes of the gimbals. Rotating and stationary elements are purposely inclined with respect to the center line of rotation to provide adjustment capability and to facilitate lubrication.

- Caging System - The gimbal suspension is provided with caging stops which protect the bearing and the SSU by introducing mechanical components in parallel with the normal rotational stops during phases of abnormal excitation.

- Data Link Assembly - The assembly provides transmission of electrical signals without excessive restraint torques by utilizing Rolamite principles for the multiconductor strips.

- Motor Drives - Each gimbal drive assembly has a two phase permanent magnet motor. The commutation to the motors is provided by the Inductosyn resolver signal conditioned to supply the required voltage in terms of sine and cosine functions to the fields of the motor.

Basic design characteristics include high accuracy and stability and capability of earth-bound performance demonstration. These goals are met with careful design of suspension elements (bearings and gimbals) and gimbal encoders. The selected design achieves a compromise between rigidity and weight, with a gimballing system in which structural moments are nominally zero and which has thermal symmetry. Zero structural moments are attained by the particular gimbal configuration and its suspension system and thermal symmetry is achieved by assuring identical power dissipation on each side of the inner and outer gimbal assemblage.

2.3.1.2 STA Performance and Design Summary

Star Sensor Unit

Performance Characteristics

- Field of View

  Acquisition 0.5° x 0.5°
  Instantaneous 84 arc-seconds

- Sensitivity

  +3.5 M AO Stars

- Temperature Range

  +20°C ±15°C

- Tracking Accuracy

  Noise Equivalent: 1.2 arc-second (1σ)

  Electronic Bias Errors: 0.14 arc-second (1σ)

  Thermo Mechanical Stability: 0.46 arc-second (1σ)

Design Characteristics

Optical System

- Type: Cassegrain
- Focal Length: 83 cm
- Effective Clear Aperture: 54 cm^2

Electronics

- Tracking Bandwidth: 25 Hz
- Scale Factor: 6.66 mv/second
- Linear Region: ±0.25°
- Linearity: 5%
- Output Z into 10 KΩ Load: $\leq$100Ω

Sensor Gimbal Unit

Performance Characteristics

- Gimbal Freedom: ±45° (outer); ±15° (inner)
- Maximum Slew Rate: 4 degrees/second
- Alignment Stability: 1.2 arc-second
- Readout Stability (Mechanical): 0.9 arc-second

Design Characteristics

- Unique two-ball suspension design (each axis)
- Aged 356 Aluminum casting for gimbals
- Dual resolver readout: 256 speed plus 1 speed
- Symmetric mechanical design
- Two-phase PM motors with electronic commutation

2.3.2 Sensor Electronics Assembly

2.3.2.1 Functional Description

The Sensor Electronics Assembly provides the support electronics for star tracker gimbal control and readout processing. The STA gimbal-mounted Inductosyn, used to give one-speed and 256-speed analog information of gimbal angle in resolver format, is excited (from the SEA) with a high-purity 10.5 kHz sinusoidal voltage. The inductosyn signals, being very low-level, are first pre-amplified on the gimbal prior to returning the signals to the SEA. Encoding within the SEA uses double-angle phase encoding to convert the suppressed-carrier angle modulation of the Inductosyn signals into an equivalent digital phase angle, which is appropriately sampled for readout of angular data in digital form to the computer.

The gimbal motor, a 12-speed, quadrature-phase device, is electronically commutated, based on angular position data from the coarse Inductosyn encoder.

The motor control signal is compensated in one of three different ways, depending on the computer-commanded mode. In Slew Mode, the computer drives directly without local compensation. This serves to slew the SSU boresight to the vicinity of a desired new star. In Acquisition Mode, drive is still from the computer, but with local rate-damping and the frequency-compensation (integral-plus-proportional) of the pre-amplifier added. In this configuration, the SSU electronically searches its deflection field-of-view for the star. In Track Mode, after the SSU indicates that it has acquired the star, the SEA operates from the SSU analog error signals (measures of the deviation of the star from boresight).

In order to provide wide-range, high resolution SSU error information to the computer, a 12 bit analog-to-digital conversion is performed thereon. The converter, time-shared between the two axes, is of the successive approximation type, and gives resolution equivalent to a fraction of an arc second.

2.3.2.2 SEA Performance and Design Summary

Performance Characteristics

- STA Inductosyn encoding accuracy of 0.6 second
- Gimbal motor drive and control
- System conditioned power: +5v, ±15v, ±24v
- Provide system telemetry and command interface
- A/D conversion of SSU error signals

Design Characteristics

- Unique Inductosyn encoding
  - Sinusoidal excitation (10.5 KHz)
  - Direct rate signal from Phaselock loop
- Analog servo loop, integral-plus-proportional
- Electronic commutation for 12-speed gimbal motors
- Power conditioning for SGU, SSU, and SEA
  - +5v; 5 percent regulation
  - ±15v; 1 percent regulation
  - ±24v; 5 percent regulation
- Successive-approximation A/D conversion of SSU signals

2.3.3 Gyro Reference Assembly (GRA)

PADS has been designed to utilize state-of-the-art gyros available from a number of manufacturers. The GRA design and performance description below is generic and representative of available capability.

2.3.3.1 Functional Description

The Gyro Reference Assembly (GRA) consists of three single-degree-of-freedom gas-bearing rate-integrating gyros orthogonally mounted in a precision mounting block. A block diagram of one of the three GRA channels is shown in Figure 2-2. Pulses are accumulated over a computation cycle (e.g., 200 ms) and read out by the Digital Processor Assembly.

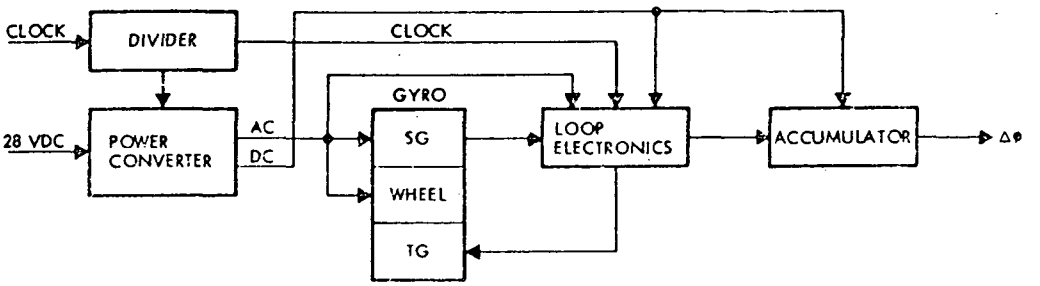

Figure 2-2. Gyro Channel Functional Block Diagram

2.3.3.2 GRA Performance and Design Summary

Performance Characteristics

- Random Drift: less than 1 arc-sec (1σ) in 5 minutes
- Input Axis Stability: 10 arc-seconds
- Scale Factor Stability: 100 ppm
- Maximum Rate: 1.5 degree/second
- Quantization: 0.1 arc-second/pulse

Design Characteristics

- Triad of orthogonal gas bearing gyros
- Pulse rebalance loop
- Integral gyro readout electronics

- Integral power converter
- Provides three-axis attitude increment data

2.3.4 Reference Block Assembly (RBA)

2.3.4.1 Functional Description

The Reference Block Assembly (RBA) for PADS is, of necessity, specialized to the particular spacecraft application and interface and as such becomes a unique development. However, the principles to be employed in its design and fabrication may be established. Criteria governing the RBA design include:

- Lend itself to relatively simple manufacturing methods such as Aluminum casting with subsequent machining operations and appropriate heat treatments to induce dimensional stability.
- Provide alignment pads.
- Capability to sustain vibrational environment.
- Provide required thermo-mechanical stability.

One approach is shown in Figure 2-3, where the block is structurally a thin parallelepiped reinforced by gussets. The wall thickness of the parallelepiped and the gussets is nominally 0.07 inch with the mounting surface 0.1 inch thick. The back surface is enclosed by a shear plate. The block is made of 356 Aluminum casting, appropriately heat treated and machined to provide dimensional stability and flatness. A thickness of 1.75 inch was selected to attain small load deflection to thickness ratio. Two (possibly three) edges of the block will be suspended from the structure of the spacecraft such that they can freely displace in the plane of the block to assure small stresses. The gussets, perpendicular to the plane of the block, distribute the load during launch phase to the structure of the vehicle. They can be also used for suspension of thermal shielding in order to isolate the necessary field-of-view cutout from the remainder of the vehicle.

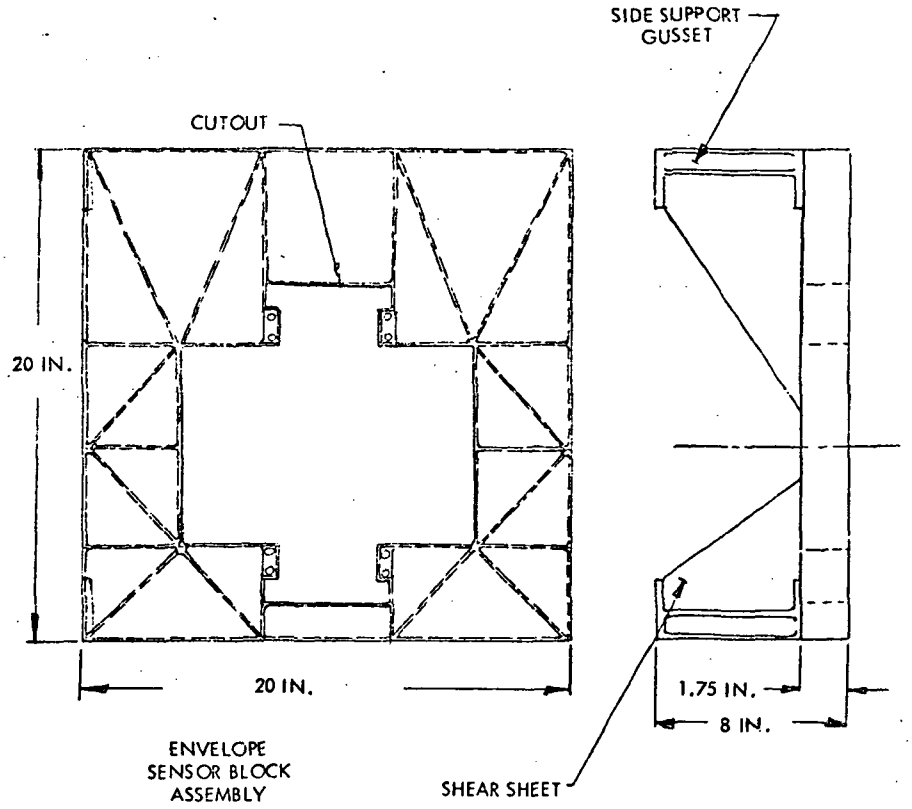

Figure 2-3. Reference Block Assembly Configuration

2.3.4.2 RBA Performance and Design Summary

Performance Characteristics

- Natural frequency: ≥100 Hz
- Vibration level: 20 g's
- Stability: 0.5 arc-second (following equipment warm-up)
- Provide mounting for sensors
- Provide spacecraft mechanical interface

Design Characteristics

- Reference block from 356 Aluminum casting
- Cutout provided for STA mounting
- Alternate design provides thermo-mechanical isolation from spacecraft

2.3.5 Digital Processor Assembly (DPA)

PADS has been designed to utilize state-of-the-art digital processors available from a variety of manufacturers. The DPA design and performance description below is generic and representative of available capability.

2.3.5.1 Functional Description

The Digital Processor Assembly comprises a CPU, memory, I/O section, and power supply. The unit, designed for space application, employs a 16-bit word length, with memory expendable to 16K or more words. The I/O electronics have both analog and digital capabilities, and provide the command and telemetry interface.

2.3.5.2 DPA Performance and Design Summary

Performance Characteristics (Typical)

- Word Length: 16 bits
- Speed: Add (single-precision), 2-10 μsecond
  Add (double-precision), 4-15 μsecond
  Multiply, 10-50 μsecond
  Divide, 30-200 μsecond

Design Characteristics (Typical)

- Fixed point, two's complement, fractional words
- 35 or more basic instructions, including double precision add/subtract
- Byte-organized (or parallel) arithmetic
- Hardware multiply/divide
- Memory addressing to 32K
- Special-purpose (or general) registers
- Low power, weight
- Serial/parallel digital interface, analog input, bilevel/discrete I/O, buffered command interface, buffered telemetry interface

2.3.6 PADS Software

2.3.6.1 Functional Description

The software functions utilize the PADS sensor measurements from the star tracker/electronics and gyros and, through appropriate algorithms, provide a precision computation of attitude. The PADS software is organized into three functional modules, namely: Gyro Reference, Star Reference and Filter/Update.

The Gyro Reference Module incorporates the algorithms for deriving "short term" attitude from the gyros. The gyro outputs are processed to derive rate. Gyro input axis alignment and scale factor are accounted for, and gyro bias compensation is introduced. A closed form solution is employed to compute attitude from the derived rate.

The Star Reference Module provides processing of the star catalog, pointing control of the star tracker, and computation of the estimated and measured star tracker output. The star catalog is processed such that each successive star sighting satisfies FOV constraints and an appropriate selection algorithm. A catalog of less than 50 stars is anticipated. Control of the star tracker includes determining gimbal angle and rate commands and mode control logic for star acquisition and tracking. To establish the measurement residual for the Kalman filter, the estimated tracker outputs are computed (accounting for aberration effects and calibrated mechanical and electronic error sources) and differenced with the measured outputs.

The Filter/Update Module incorporates a Kalman filter with a six-element state vector comprising three attitude elements and three gyro bias parameters. The state transition matrix is computed and used to propagate the error covariance matrix. The Kalman filter optimal gain matrix is computed and used to update the state vector and error covariance.

The software is executed under program control of the DPA executive according to a programmed interactive cycle. A Level 1 computation cycle, executed with a period of 200 ms, incorporates the processing of gyro data, the integration algorithm for maintaining short-term attitude, and computation of the state transition matrix. A Level 2 computation cycle, which may be executed with a longer period, incorporates the star selection and star tracker control algorithms. A Level 3 computation cycle, having a period of 30 seconds or more, depending on desired update frequency, incorporates the functions required for attitude determination update using the star tracker measurements and Kalman filter, i.e., measurement processing, Kalman filter and state vector update.

2.3.6.2 Software Performance and Design Summary

Performance Characteristics

- Accuracy to better than 0.5 arc-second

Design Characteristics

- Modular software elements
- Moderate DPA memory and speed requirements
  - Executive/subroutines/utility < 1K memory
  - Application modules < 3K program, 1K scratchpad
  - Average execution rate of 50-60K ops

2.4 PADS Interface Design

The PADS system configuration utilized with an earth-oriented three-axis stabilized spacecraft implies a variety of demands on the spacecraft interface. These include configuration and mounting constraints requiring adequate volume and field of view allocation; power; thermal; orbital constraints; attitude control constraints; and command and telemetry. The model system shown in Figure 2-4 indicates a representative accommodation of the PADS equipment; thermal shielding associated with the star tracker has been deleted for clarity. The star tracker is provided a clear field-of-view of ±15° x ±45°. The total envelope occupied by the system is approximately 21" x 26" x 20". The PADS design assumes that the thermal environment will remain within the range of +10 to +40°C throughout the mission and steady-state maintained within 5 degrees.

The carrier spacecraft is assumed placed in orbit well suited to PADS utilization, e.g., low altitude sun synchronous or geosynchronous equatorial. Other types of orbits may be treated on a mission peculiar basis. The spacecraft attitude is preferably controlled such that attitude error is within one degree and attitude error rates are less than 0.01 degree/second. One may expect that larger attitude excursions and higher rates can be readily accepted within a particular mission context. Mission peculiar acquisition, slew and/or tracking requirements need be specifically evaluated.

Telemetry and command requirements for PADS are summarized:

- Telemetry
  - Gyro Date - three 16-bit words @ 5/second - 240 bps
  - Star Tracker Data - 80 bps
  - Computed Attitude/Housekeeping Data - 256 bps
- Command (Not time critical)
  - Discrete Commands - 8
  - Parameters - Digital channel to DPA, low data rate OK

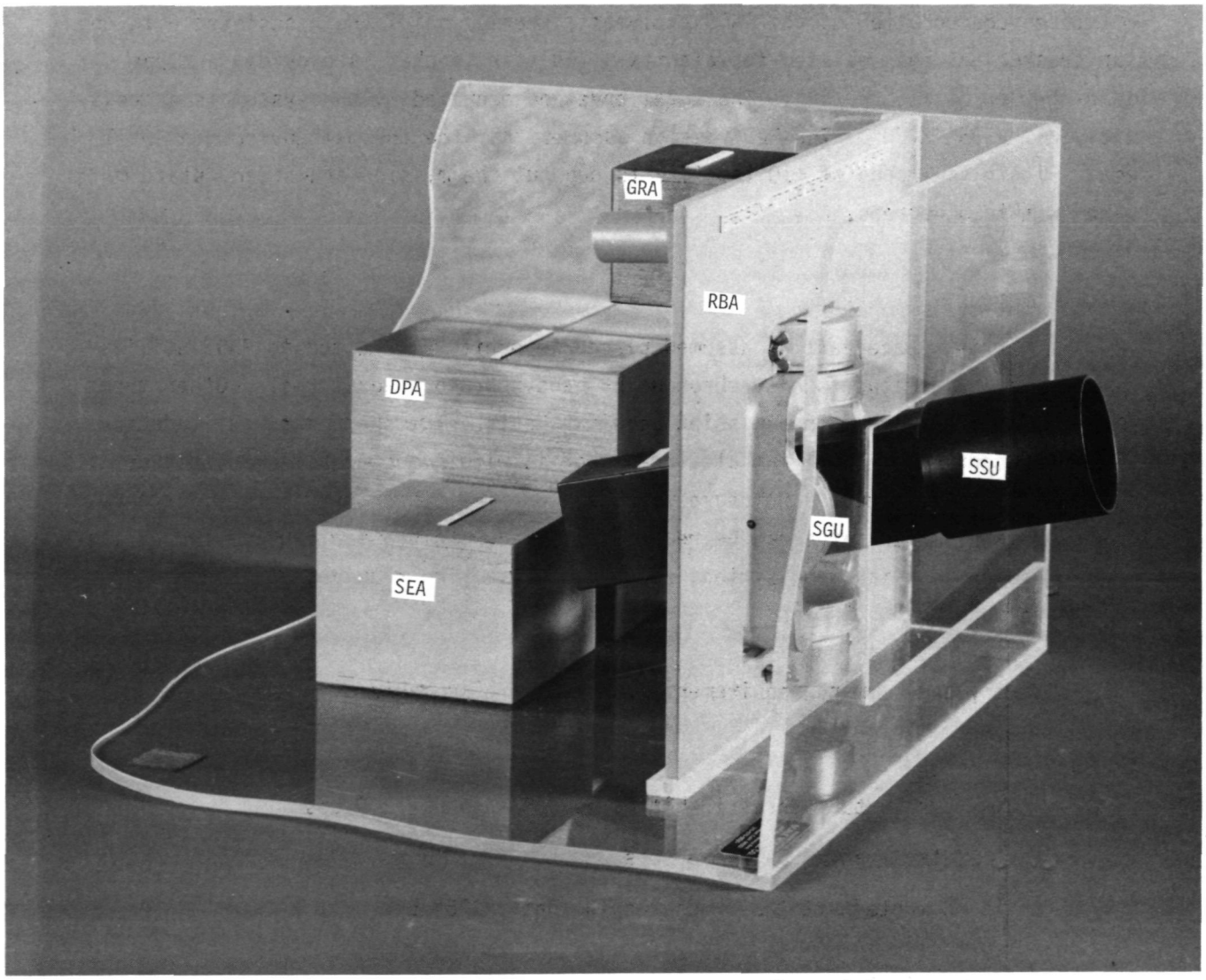

Figure 2-4. Precision Attitude Determination System Configuration (Half-Scale Model)

3.0 SYSTEM ANALYSIS

To a great extent, system analysis performed during the PPCS studies supports the PADS design. Characteristics peculiar to PADS result from the modifications to the star tracker and sensor electronics designs. Thus system error analysis, performance analysis, and star tracker servo design are specifically treated in this section as they support the improved designs.

3.1 PADS Error Analysis

The total system errors for inertial attitude determination are presented in Table 3-1, which shows both the allocated budget and the achievable performance. Assembly level errors are further expanded in Tables 3-2 through 3-4.

Table 3-1. PADS Error Summary

Element	Budget		Capability	
	$\sigma(\widehat{sec})$	$\sigma^2(\widehat{sec}^2)$	$\sigma(\widehat{sec})$	$\sigma^2(\widehat{sec}^2)$
Star Tracker	2.4	5.8	1.73	2.99
Sensor Electronics	1.0	1.0	0.6	0.36
Gyro Reference	2.0	4.0	1.25	1.56
Reference Block	1.0	1.0	0.5	0.25
Computation	1.0	1.0	0.5	0.25
Total RSS	3.6		2.33	

NOTE: 3.6 arc-seconds = 0.001 degree

The most significant error contribution is due to the star tracker and associated gimbal readout electronics. The PADS star tracker has been designed with SSU bias/stability errors approximately a factor of 2 greater and the noise a factor of 3 greater than the PPCS star tracker design to yield a simpler, smaller, and lighter weight star tracker design. The contribution of gimbal errors are essentially identical, as would be expected, as the same gimbal design approach was utilized as for PPCS. The Inductosyn gimbal readout (including both mechanical and electrical) is approximately 50% less accurate in the PADS design due to use of a smaller 256 speed Inductosyn instead of the 360 speed Inductosyn employed in PPCS. The contribution of gyro error sources are essentially the same, the contribution in PADS being somewhat lower than PPCS due to the vehicle motion behavior assumed in each case. The computational error in PADS is consistent with 32-bit computer accuracy using double-precision as appropriate.

Table 3-2. STA Error Analysis

Source (1σ)	Contribution $\sigma(\widehat{sec})$	$\sigma^2(\widehat{sec})^2$
SSU Bias Stability		
Electronic Bias, 0.14 $\widehat{sec}$	0.14	0.02
Thermo-mechanical stability, 0.46 $\widehat{sec}$	0.46	0.21
SSU Noise Equivalent Angle, 1.2 $\widehat{sec}$	1.2	1.44
SGU Alignment Uncertainty		
Runout, 0.5 $\widehat{sec}$	0.5	0.25
Perpendicularity, 0.5 $\widehat{sec}$	0.5	0.25
SGU Thermo-mechanical Stability		
Stress Relaxation, 0.2 $\widehat{sec}$	0.2	0.04
Thermal Shifts, 0.2 $\widehat{sec}$	0.2	0.04
Inductosyn (Mechanical)		
θ, 0.7 $\widehat{sec}$	0.7	0.49
256θ, 0.5 $\widehat{sec}$	0.5	0.25
Total (RSS)	1.73	

Table 3-3. SEA Error Analysis

Source (1σ)	Contribution $\sigma(\widehat{sec})$	$\sigma^2(\widehat{sec}^2)$
Bias Drift		
Zero-crossing offset, 0.13 $\widehat{sec}$	0.13	0.017
Logic Phase Stability, 0.4 $\widehat{sec}$	0.4	0.16
Harmonic (256θ)		
Excitation Harmonics, 0.27 $\widehat{sec}$	0.27	0.073
Second Harmonic (512θ)		
Cross-coupling, 0.27 $\widehat{sec}$	0.27	0.073
Gain Unbalance, 0.13 $\widehat{sec}$	0.13	0.017
A-ϕ Converter, 0.13 $\widehat{sec}$	0.13	0.017
Resolution, 0.3 $\widehat{sec}$	0.08	0.006
Total (RSS)	0.6	

Table 3-4. GRA Error Analysis

Source (1σ)	Contribution(1) $\sigma(\widehat{sec})$	$\sigma^2(\widehat{sec}^2)$
Drift Bias Compensation, 0.002 deg/hr(2)	0.6	0.36
Random Drift, 0.003 deg/hr	0.9	0.81
Scale Factor Stability, 100 ppm	0.54	0.29
IA Alignment Stability, 10 $\widehat{sec}$	0.27	0.07
Gyro Pulse Weight, 0.1 $\widehat{sec}$	0.1	0.01
Total (RSS)	1.24	

(1) Five minute update, limit cycle rate of 0.005 deg/sec

(2) Error in Kalman filter estimate

3.2 Performance Analysis/Simulation

PADS performance was evaluated via digital simulation of the attitude determination process using the PPCS developed program [3-5]. Because of the extensive parameter variation studies conducted for PPCS attitude determination, the extent of the PADS performance analysis effort was limited.

All PADS simulation work was performed assuming the spacecraft in a geosynchronous equatorial orbit with the star tracker directed north for zero gimbal angles. The tracker gimbal FOV was limited to ±15 degrees in the local horizontal plane, and ±45 degrees about the orthogonal axis. Star availability is as shown in Figure 3-1, with the catalog of selected available stars given in Table 3-5.

Parameters used to simulate the nominal PADS performance are given in Table 3-6. The values used for simulation are seen to be consistent (although generally conservative) with the established hardware associated error sources (presented in the error analysis). Consistent with design guidelines developed in the related PPCS analyses, the attitude elements of the state noise covariance matrix have been selected in a slightly conservative fashion, while the elements of the measurement noise covariance matrix have been selected to be slightly optimistic. The initial error covariance has been selected to be consistent with the simulated initial conditions on attitude and drift bias uncertainty. The initial conditions were selected at representative values such that acquisition without search would be readily achieved. The resulting nominal performance is summarized in the graphs of

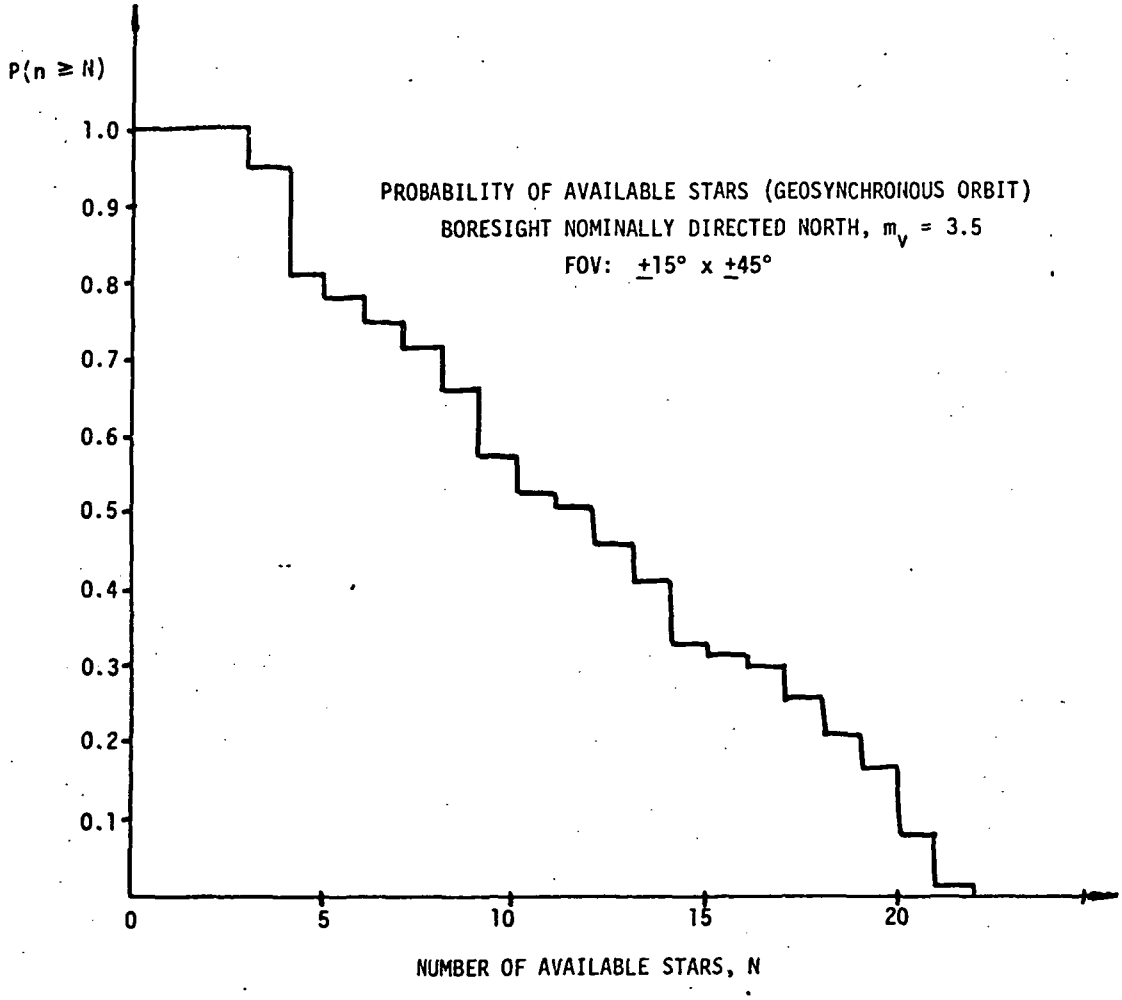

Figure 3-1. Star Availability in Geosynchronous Orbit

Table 3-5. Star Catalog for Geosynchronous Orbit

Yale Catalog No.	Right Ascension	Declination	Magnitude
1708	78.54330	45.96600	.658
7924	310.06800	45.14770	1.349
2088	89.26005	44.94430	1.931
1017	50.47560	49.73100	2.192
264	13.66217	60.53530	2.404
4301	165.40950	61.93130	2.432
424	31.96755	89.08570	2.508
21	1.83834	58.96300	2.561
8162	319.44300	62.44170	2.626
5563	222.79650	74.29170	2.72
403	20.89740	60.05770	2.807
1122	55.12425	47.67570	2.838
7528	295.97700	45.04830	2.849
6705	268.95300	51.48900	2.861
8238	322.05300	70.40270	2.897
168	9.64608	56.34630	2.898
6396	257.17500	65.75630	3.052
5735	230.24550	71.95230	3.1
542	27.98805	63.51330	3.216
3569	134.22195	48.16930	3.312
6132	245.88150	61.57930	3.346
153	8.76851	53.71300	3.388
6536	262.41600	52.33930	3.41
915	45.58380	53.36970	3.439

Table 3-6. PADS Simulation Parameters

Star Tracker Parameters		
Star Sensor Bias		1.4 $\widehat{\text{sec}}$, each axis
Star Sensor Noise		1.3 $\widehat{\text{sec}}$, each axis
Gimbal Axis Perpendicularity		0.5 $\widehat{\text{sec}}$
Gimbal Runout		0.35 $\widehat{\text{sec}}$, each axis
Inductosyn Readout:	θ	0.7 $\widehat{\text{sec}}$
	250θ	0.64 $\widehat{\text{sec}}$
	512θ	0.48 $\widehat{\text{sec}}$
	Noise	0.15 $\widehat{\text{sec}}$
Gyro Reference Parameters		
Gyro Noise (1 second smoothing)		0.02 deg/hr
Input Axis Misalignment		0
Scale Factor Uncertainty		0
Filter Parameters		
State Noise Covariance		1.5×10^{-12} (corresponds to gyro noise of 0.03 deg/hr)
		10^{-16} (drift rate ramp of 0.00003 deg/hr/hr)
Measurement Noise Covariance		1 $\widehat{\text{sec}}$
Initial Conditions		
Attitude Uncertainty (deg)		0.057 (roll)
		0.059 (pitch)
		0.062 (yaw)
Drift Bias Uncertainty		0.05 deg/hr
Initial Error Covariance		0.114 deg
		0.05 deg/hr

Figure 3-2 showing three-axis RSS attitude determination error, the square-root of the trace of the attitude covariance matrix, and a weighted cumulative performance measure. The attitude determination error is seen to be reduced to the 10 arc-second region with the first two star sightings (at 5 minutes and 10 minutes) and the convergence of the attitude covariance being consistent with the true performance, i.e., the filter statistics representing the real world well. The rapid growth in attitude determination error over the 10-20 minute period is due to the somewhat slower convergence of the gyro bias estimate, e.g., an uncertainty of 0.05 degree/hour leads to a 15 arc-second error in 5 minutes.

Parameter variations simulated for exploring performance are summarized in Table 3-7. Star tracker error sources are addressed initially. Figure 3-3 shows the effect on performance resulting from an increase in the SSU noise. An increase to 5 arc-second noise from (nominal) 1.3 arc-second results in a proportionately much smaller increase in the overall cumulative system error. If the filter measurement covariance reflects a 5 arc-second noise, the error increase is only 25%; if covariance for 1 arc-second noise is assumed, the error increases by 62%. The behavior of the elements of the covariance matrix, however, differ markedly and in proportion to the modelled variation. Even though the run time history is over a short period, it can be observed that the heavier weighting given to the star measurements when the covariance is assumed small will lead to filter overconfidence and generally poorer performance than the case where covariance is more accurately specified.

Figure 3-4 is a time history which incorporates a doubling of the SSU bias in each axis. Comparison of this behavior with that shown for the nominal demonstrates that the bias propogates through the system directly (as is expected). Parameter variations of gimbal orthogonality up to a value of 5 arc-second produced no apparent effect; this element was therefore established as a relatively non-critical parameter.

The effect of gyro random drift, modelled as white noise in rate, is shown in Figure 3-5 as related to normalized cumulative error performance. Over an order of magnitude range, the increased random drift contributes a 50% increase in system error relative to the baseline. The character of the resulting performance is seen in the time history of Figure 3-6, where the relatively large growth of attitude error between update periods is noted.

The effect on performance of increasing the period between updates to 10 minutes is not severe. The cumulative error measure for this case increases

Table 3-7. Simulated Parameter Variation Cases

Parameter(s) Varied	Value(s)	Rationale/comments
Star Tracker		
Star Sensor Noise (with and w/o corresponding change in covariance matrix)	5 $\widehat{sec}$	≈4X nominal
Star Sensor Bias	3 $\widehat{sec}$	≈2X nominal
Gimbal Orthogonality	2 $\widehat{sec}$, 5 $\widehat{sec}$	max≈10X nominal
Gyro Reference		
Gyro Noise (state noise covariance unchanged)	0.05, 0.1. 0.2 deg/hr (1 sec smoothing)	max≈10X nominal
Gyro Misalignment (constant)	10 $\widehat{sec}$, 100 $\widehat{sec}$	max≈10X expected
Gyro Scale Factor (constant)	100 ppm, 1000 ppm	max≈10X expected
Other		
Filter Update Period	2 min, 10 min	$\approx\frac{1}{2}$, 2X nominal

approximately 25%. The time behavior of this parameter change is seen in Figure 3-7. Reducing the period between updates to 2 minutes improved the cumulative error performance by only 10%.

3.3 Star Tracker Servo Analysis

The PADS star tracker servo controller is required to accurately null track a star (inertially fixed) while mounted on the spacecraft rotating at orbital rate. The problem is complicated by a very high gimbal coulomb friction, low gimbal inertia, and a moderately low bandpass sensor. The control system is disturbed by the coulomb friction each time the spacecraft (limit cycle) rate reverses. The tracking error resulting from this transient disturbance must be small enough to avoid losing track, and to allow using the sensor readout to accurately determine spacecraft attitude.

Several design approaches were examined. To minimize control errors from torque offsets and circuit biases a controller with proportional plus integral error signal amplification was selected. Controllers with and without gimbal rate feedback were examined, with the controller with gimbal rate feedback resulting in a superior design. Without the gimbal rate feedback, derived error signal rate is required for damping. (In addition, some form of friction compensation is required if operating in a limit cycle mode is not allowed.) With gimbal rate feedback, derived error signal rate is not required but is used to provide lead that will cancel the lag from the gimbal rate loop, thereby improving stability margin (particularly where the gimbal rate loop has a low bandwidth).

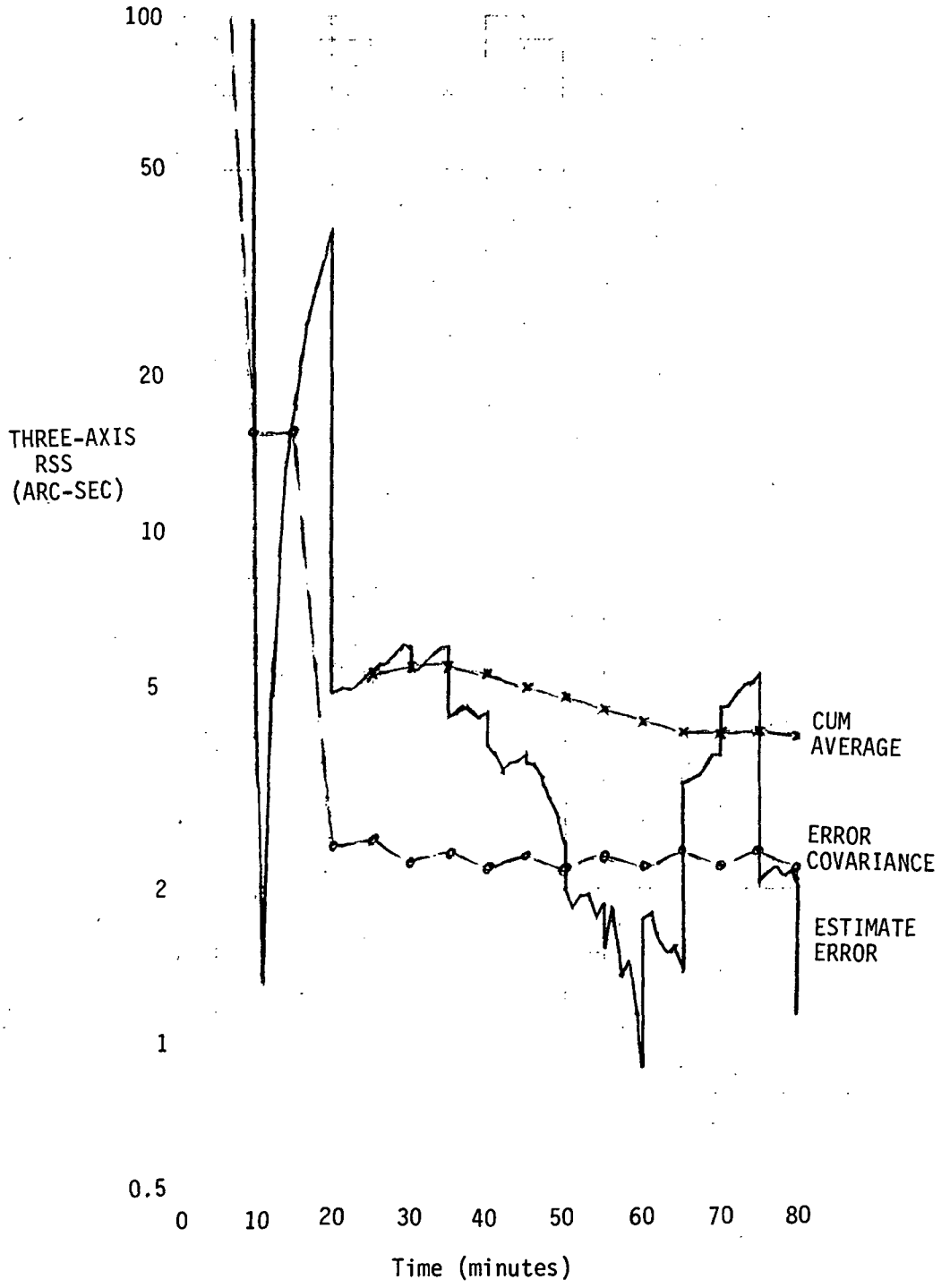

Figure 3-2. PADS Baseline Performance

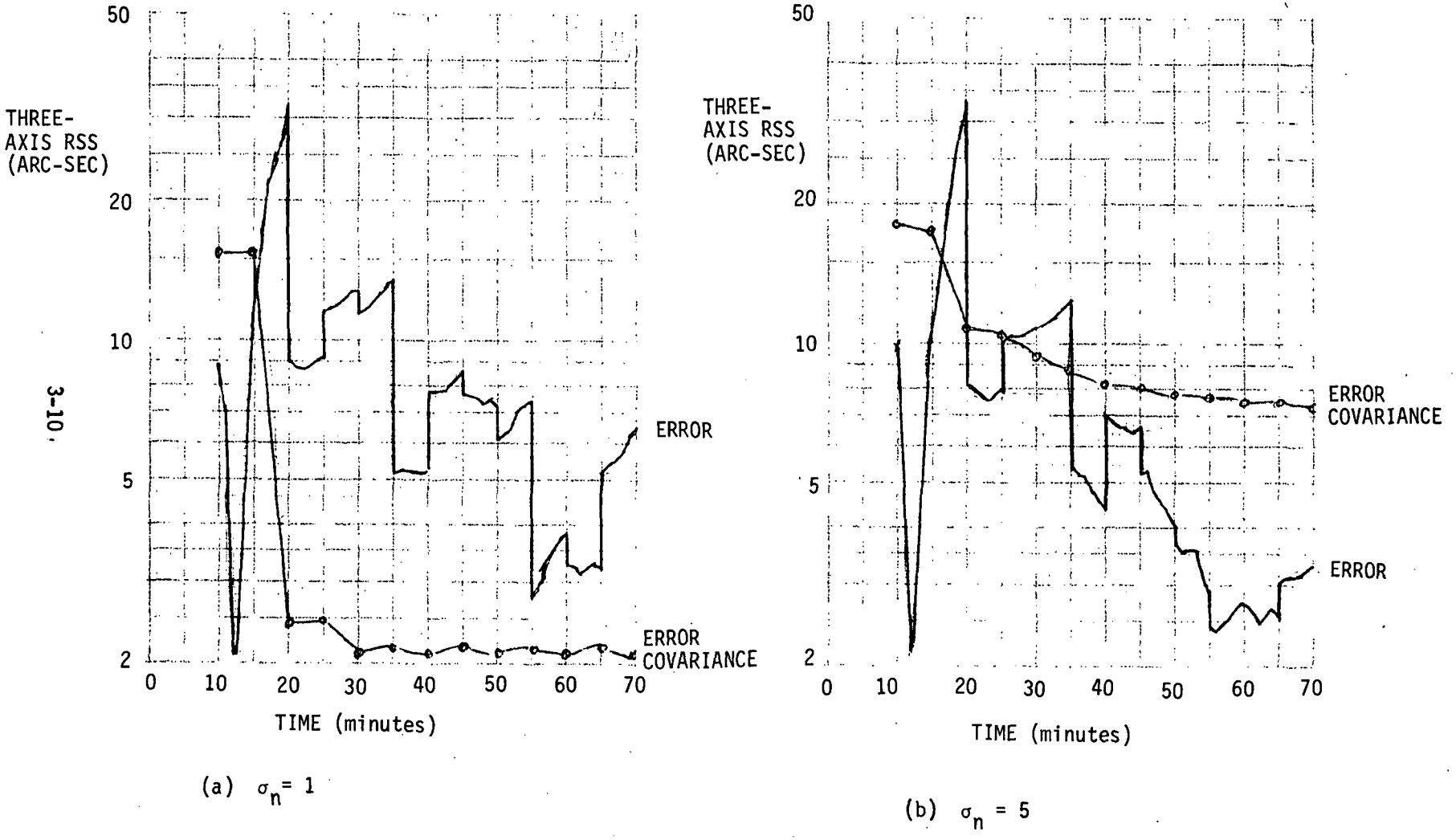

Figure 3-3. PADS Performance with Increased SSU Noise
(SSU Noise = 5 arc-sec)

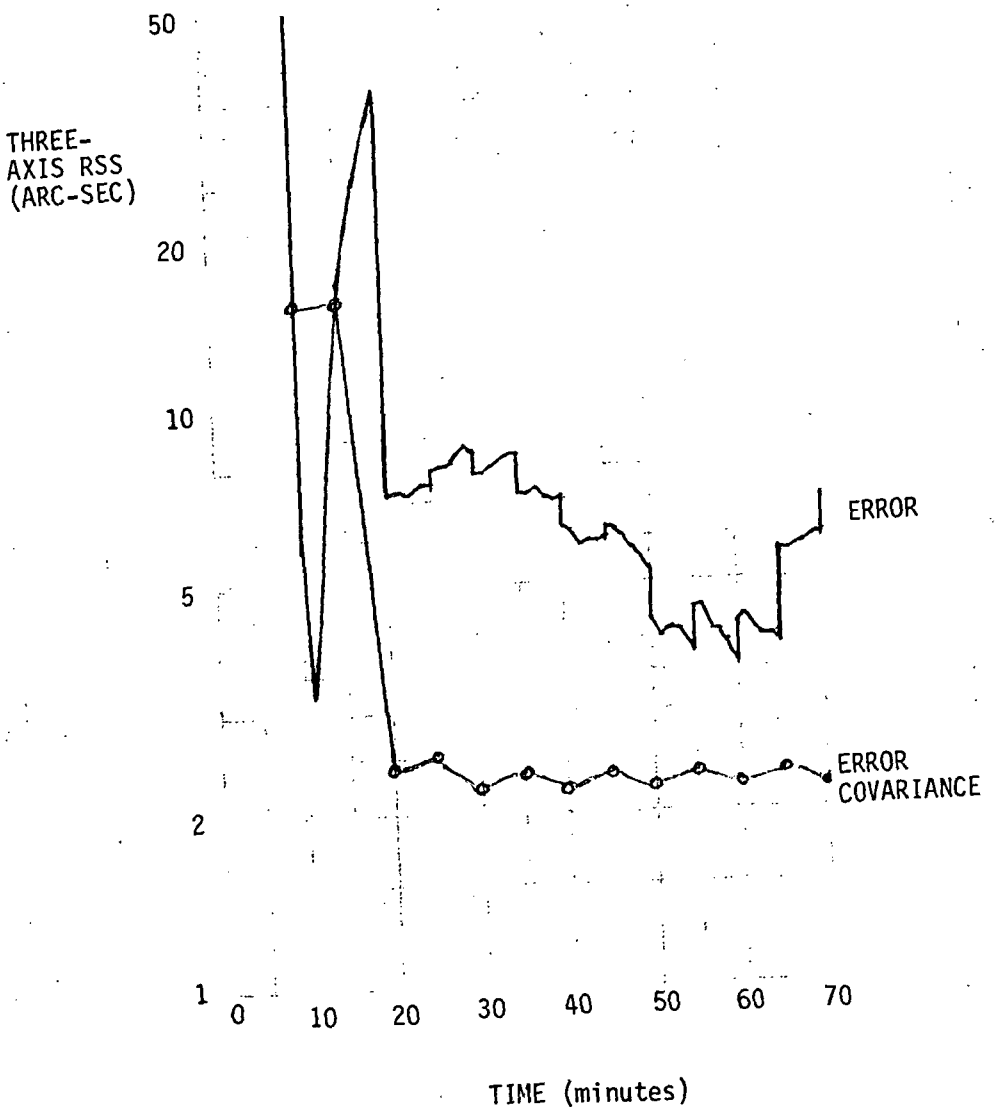

Figure 3-4. PADS Performance with Increased SSU Bias (SSU Bias = 3 arc-sec)

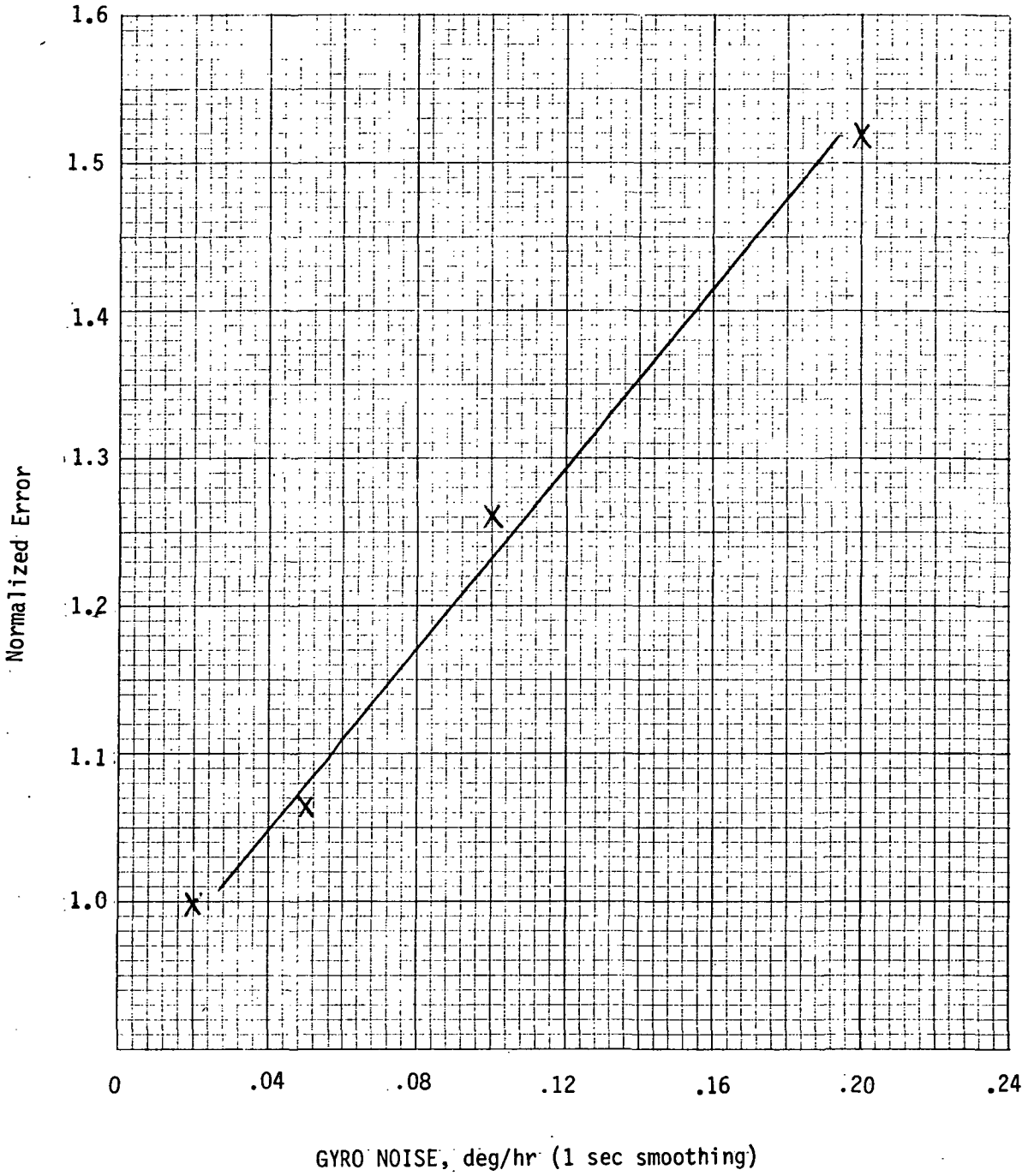

Figure 3-5. Influence of Gyro Random Noise on PADS Performance

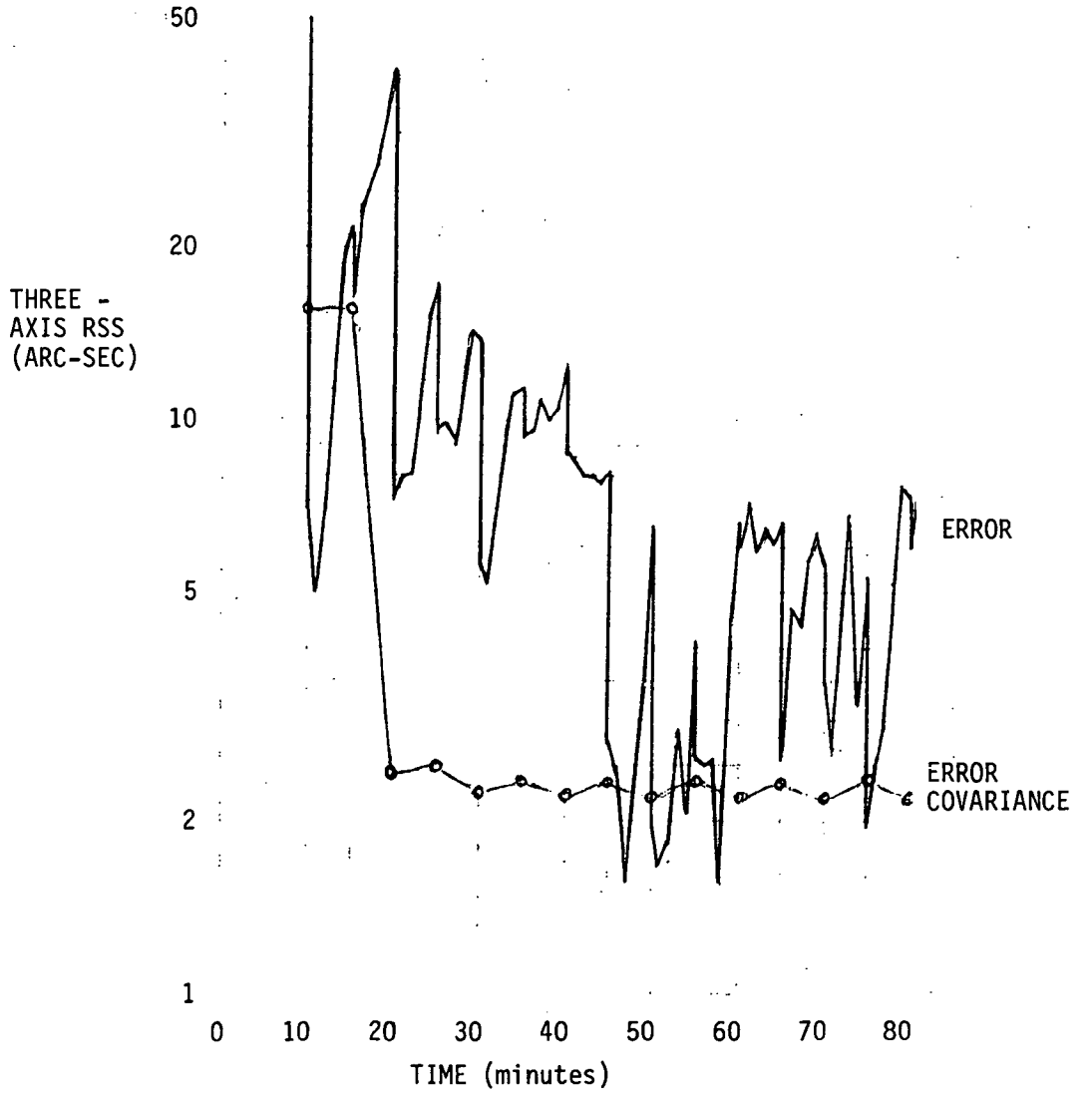

Figure 3-6. PADS Performance with Increased Gyro Noise
(Gyro Noise = 0.2, 1 sec smoothing)

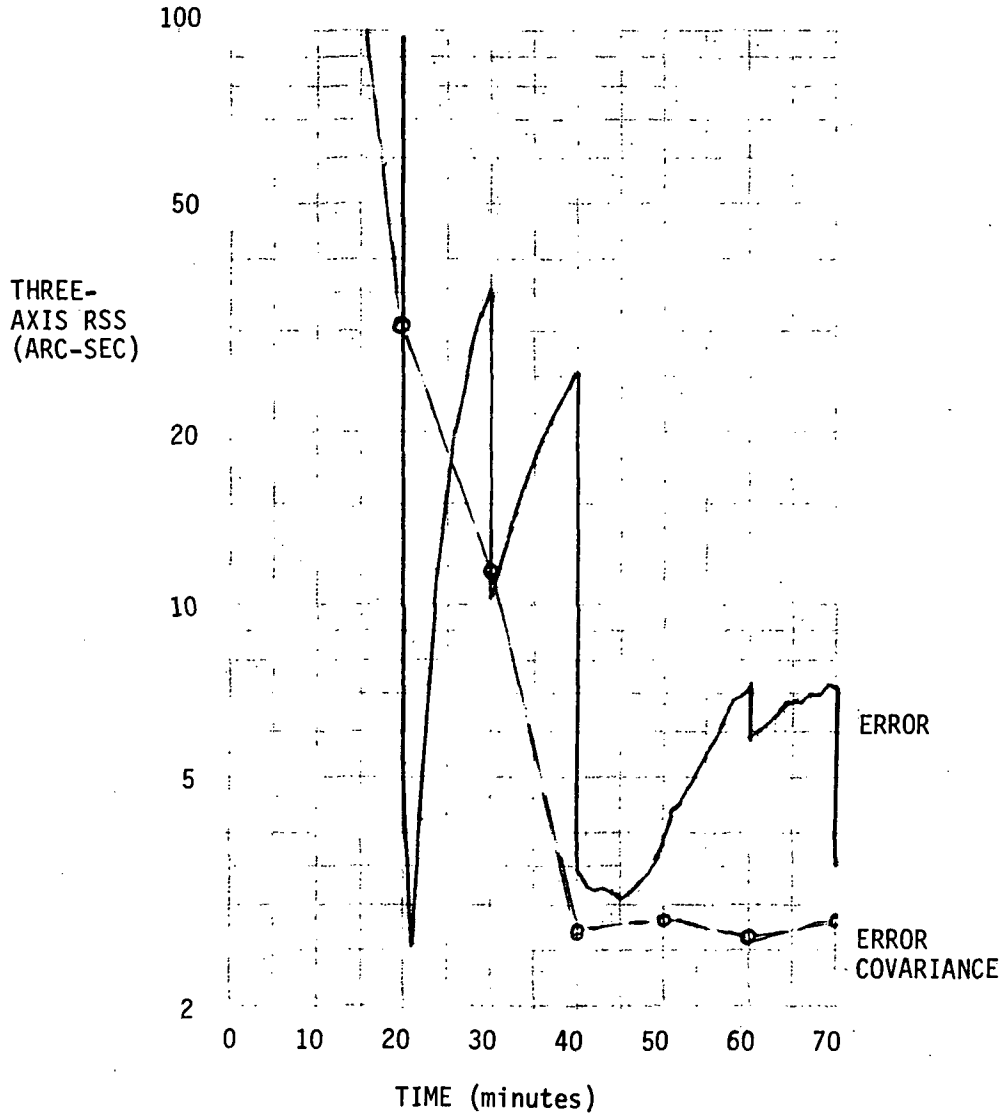

Figure 3-7. PADS Performance with Increased Update Interval (10 minutes between star updates)

The detail design of the controller is presented in the following sections, including consideration of the anomalies present in the use of the Inductosyn for deriving gimbal rate and the effect of bending on the gimbal rate loop. No significant performance degradation as a result of the anomalies was discovered.

3.3.1 Nominal Design/Approach

The controller design, shown in Figure 3-8, is initially treated without consideration of gimbal rate feedback. To avoid instability or limit cycling, the control loop bandwidth should be about a decade below the lowest sensor cut-off frequency. The assumption is that sensor lags are necessary for filtering sensor noise, and cannot be compensated for. For purpose of design, then neglect the sensor lags. The open loop transfer function becomes:

$$\frac{K_I K (K_R s+1)(s/K_I + 1)}{I s^3}$$

and the closed loop transfer function is:

$$\frac{(K_R s+1)(s/K_I + 1)}{\frac{I}{K_I K} s^3 + \frac{K_R}{K_I} s^2 + \left(K_R + \frac{1}{K_I}\right)s + 1}$$

For K_I << Loop Bandwidth (BW) the closed loop transfer function approaches:

$$\frac{(K_R s + 1)}{\frac{I}{K} s^2 + K_R s + 1}$$

The control natural frequency becomes

$$\omega_n = \sqrt{\frac{K}{I}}$$

and

$$\frac{2\zeta}{\omega_n} = K_R$$

or for $\zeta = 0.5$, $K_R = 1/\omega_n$. To satisfy the requirement that K_I << Loop BW and still maximize the torque gain, select $K_I = \omega_n/10$. Therefore, for a selected natural frequency the control parameters should be

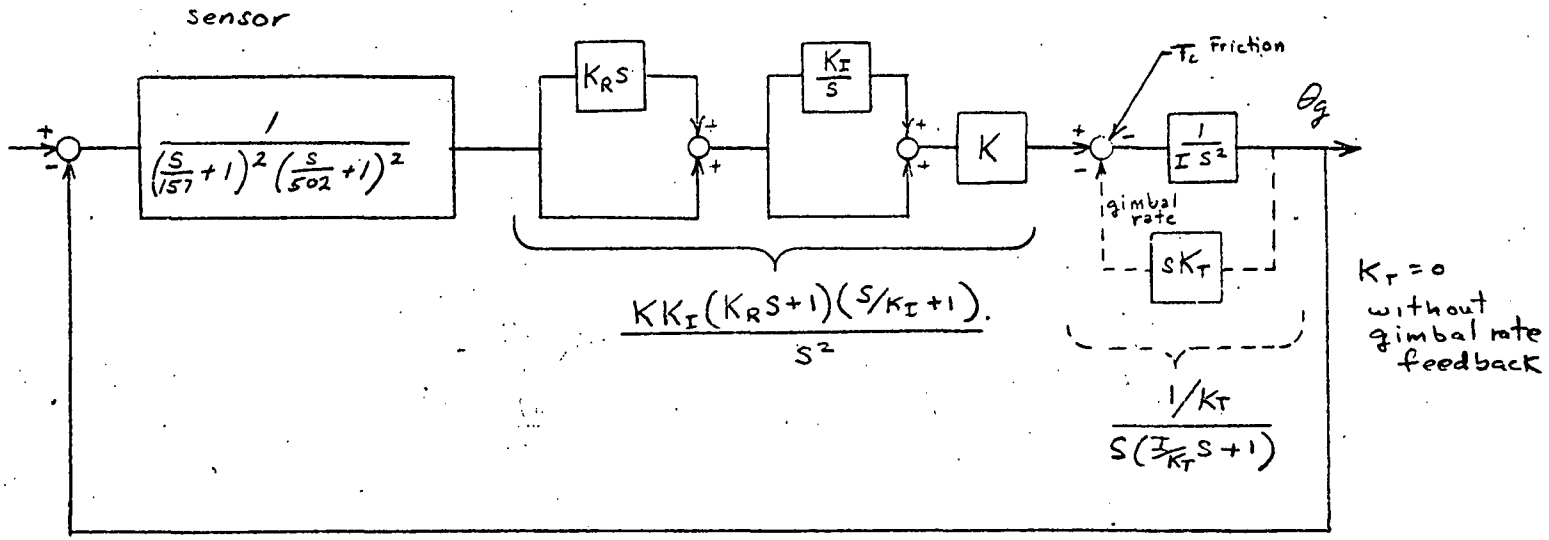

Figure 3-8. Servo Controller Block Diagram

$$K = \omega_n^2 I$$

$$K_I = \omega_n/10$$

$$K_R = 1/\omega_n$$

and for stability ω_n << 157 radians/second.

When the friction torque reverses because of reversal of body rate, the gimbal will become friction locked to the spacecraft and will drift off until the controller can reverse the output torque. The time to reverse the control torque and the maximum error can be calculated from:

$$2T_c = K\left(K_I \int_0^{t_{max}} \varepsilon\, dt + \varepsilon_{max} + |\omega_B|\, K_R\right) = K\left(K_I \frac{T_{max}^2}{2} |\omega_B| + \varepsilon_{max} + |\omega_B|\, K_R\right)$$

$$= \left(K\, K_I \frac{\varepsilon_{max}^2}{2|\omega_B|} + \varepsilon_{max} + |\omega_B|\, K_R\right)$$

$$\varepsilon = |\omega_B|\, t \qquad \varepsilon_{max} = |\omega_B|\, t_{max}$$

where

T = time

ω_B = new spacecraft rate

T_c = coulomb friction

Solving for ε_{max}

$$\varepsilon_{max} = \sqrt{\frac{\omega_B^2}{K_I^2} + \frac{4\, T_c\, \omega_B}{K\, K_I} - \frac{2\omega_B^2\, K_R}{K_I}} - \frac{\omega_B}{K_I}$$

$$\cong 2\sqrt{\frac{T_c\, \omega_B}{K\, K_I}}$$

As can be seen, ε_{max} is minimized by maximizing $K\, K_I$. However, $K\, K_I$ is fixed by ω_n. Thus, the design torque gain is constrained by loop bandwidth.

By the addition of derived gimbal rate feedback, the open loop transfer function (neglecting sensor lags) becomes

$$\frac{K_I\ K\ (K_R\ s+1)\ (s/K_I\ +\ 1)}{K_T\ s^2\ (\frac{I}{K_T}\ s+1)}$$

A large rate feedback moves the pole at the origin to a high frequency (K_T/I) and attenuates the loop gain to lower the loop bandwidth. Select $K_R = I/K_T$ to allow the zero (K_R s+1) to cancel the pole ((I/K_T) s+1). (Note: where K_T/I is much greater than the control bandwidth, it can be neglected and derived rate eliminated, i.e., $K_R = 0$). The open and closed loop transfer functions reduce to:

Open Loop: $\frac{K_I K}{K_T}\ \frac{(s/K_I\ +\ 1)}{s^2}$ Closed Loop: $\frac{(s/K_I\ +\ 1)}{\frac{K_T}{K_I K}\ s^2 + \frac{s}{K_I} + 1}$

In this case

$$\omega_n = \sqrt{\frac{K\ K_I}{K_T}}, \quad \frac{2\zeta}{\omega_n} = \frac{1}{K_I}$$

For

$$\zeta = .5 \quad , \qquad K_I = \omega_n,$$

then

$$K/K_T = \omega_n \qquad \text{or} \qquad K = \omega_n\ K_T$$

To avoid limit cycling or instability let ω_n << sensor cut-off frequency (157 radians/second).

To minimize the transient resulting from the friction disturbance, maximize $K\ K_I$. K_I is fixed by ω_n but K can be made arbitrarily large by making K_T arbitrarily large. Therefore, the limiting value of K depends on the maximum allowable value of K_T. K_T should be selected such that the rate loop natural frequency of K_T/I is significantly less than rate loop filter lags and bending frequencies. A sharp filter cut-off at about 3000 radians/second is expected. Bending frequencies are to be as low as 600 radians/second. Therefore, a rate loop bandwidth of from about 61 to 314 radians/second was chosen. Therefore,

$$K_T = \omega_n \cdot I = 10 \text{ to } 50 \text{ ft-lb/rad/sec}$$

Tables 3-8 and 3-9 show the control characteristics as a function of ω_n for K_T = 10 and 50. The time response of the system as a function of the natural frequency is shown in Figure 3-9.

Table 3-8. With Gimbal Rate Feedback, K_T = 10

ω_n rad/sec	K_I 1/sec	K $\frac{\text{ft-lb}}{\text{rad}}$	K K_I $\frac{\text{ft-lb}}{\text{rad/sec}}$	Maximum Transient Error* arc-sec	Limit Cycle arc-sec
1	1	10	10	1540	None
10	10	100	1000	154	None
20	20	200	4000	78	None
40	40	400	16000	40	29
80	80	800	64000	20	Unstable

*T_c = 0.2 ft-lb

K_R = 1/61

ω_B = 0.04 deg/sec

Table 3-9. With Gimbal Rate Feedback, K_T = 50

ω_n rad/sec	K_I 1/sec	K $\frac{\text{ft-lb}}{\text{rad}}$	K K_I $\frac{\text{ft-lb}}{\text{rad/sec}}$	Maximum Transient Error* arc-sec	Limit Cycle arc-sec
1	1	50	50	690	None
10	10	500	5000	69	None
20	20	1000	20000	35	None
40	40	2000	80000	18	None
80	80	4000	320000	9	Unstable

*T_c = 0.2 ft-lb

ω_B = 0.04 deg/sec

K_R = 1/312 sec

3.3.2 Loop Anomalies and Bending

In the previous section, the gimbal rate feedback device was assumed to be a perfect differentiator with a series filter. However, the gimbal rate is derived from differentiating the signal from a multi-speed Inductosyn and demodulating it. Anomalies exist both in the differentiator and the demodulator circuits that could cause performance degradation. The major anomalies identified were (see Figure 3-10):

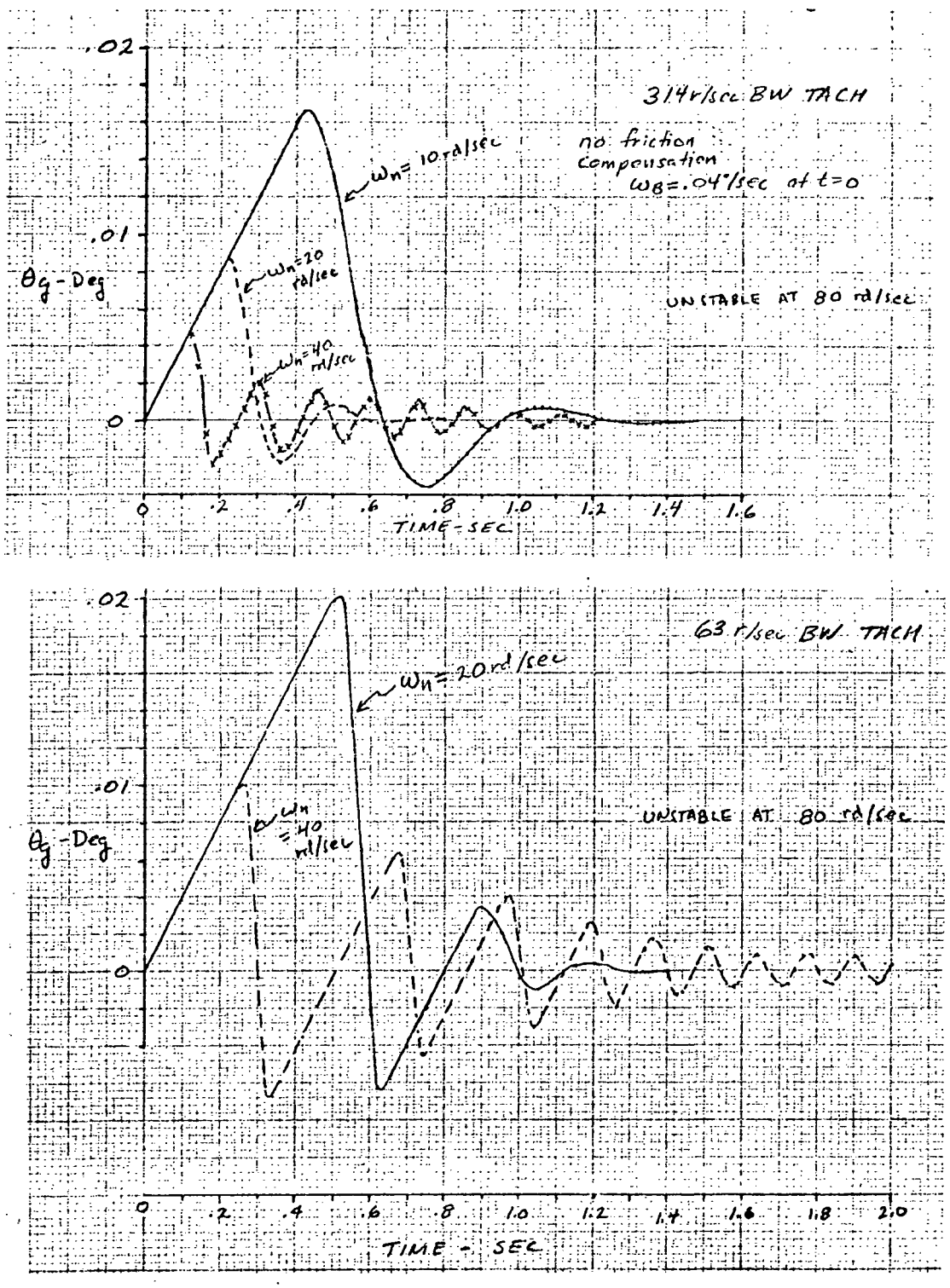

Figure 3-9. Gimbal Rate Feedback Design Transient Performance as a Function of Tach Bandwidth

- differentiator leakage
- carrier modulation ripple
- voltage spikes during demodulation

It will be shown below that none of these anomalies are of significant magnitude to cause noticeable performance degradation. Also, bending effect on rate loop stability was examined.

Differentiator Leakage

The differentiator transfer function has been represented as

$$\frac{K_T\, s}{\frac{s^2}{\omega_T^2} + \frac{2\zeta_I}{\omega_T} s + 1}$$

but because of a leakage factor it is actually (see Figure 3-10):

$$\frac{K_T\, s + K_L}{\frac{s^2}{\omega_T^2} + \frac{2\zeta}{\omega_T} s + 1} = \frac{K_L\left(\frac{K_T}{K_L} s + 1\right)}{\frac{s^2}{\omega_T^2} + \frac{2\zeta}{\omega_T} s + 1}$$

Neglecting the filter lags, the open loop transfer function of the gimbal rate loop becomes

$$\frac{K_L\left(\frac{K_T}{K_L} s + 1\right)}{I\, s^2}$$

As long as the frequency K_L/K_T is much lower than the natural frequency of the outer position loop, the performance should be unaffected. The estimated value of K_L/K_T is 0.0002 radians/second. For K_T = 50 feet/pound/radian/second, this corresponds to K_L = 0.01 foot-pound/radian. This leakage gain was incorporated into the digital simulation and increased by factors of 10 and 100. The result is shown in Figure 3-11. The effect is unnoticeable at leakages equal to or less than 0.1 foot-pound/radian. At 1 foot-pound/radian leakage gain, the performance difference can be noticed but degradation is insignificant.

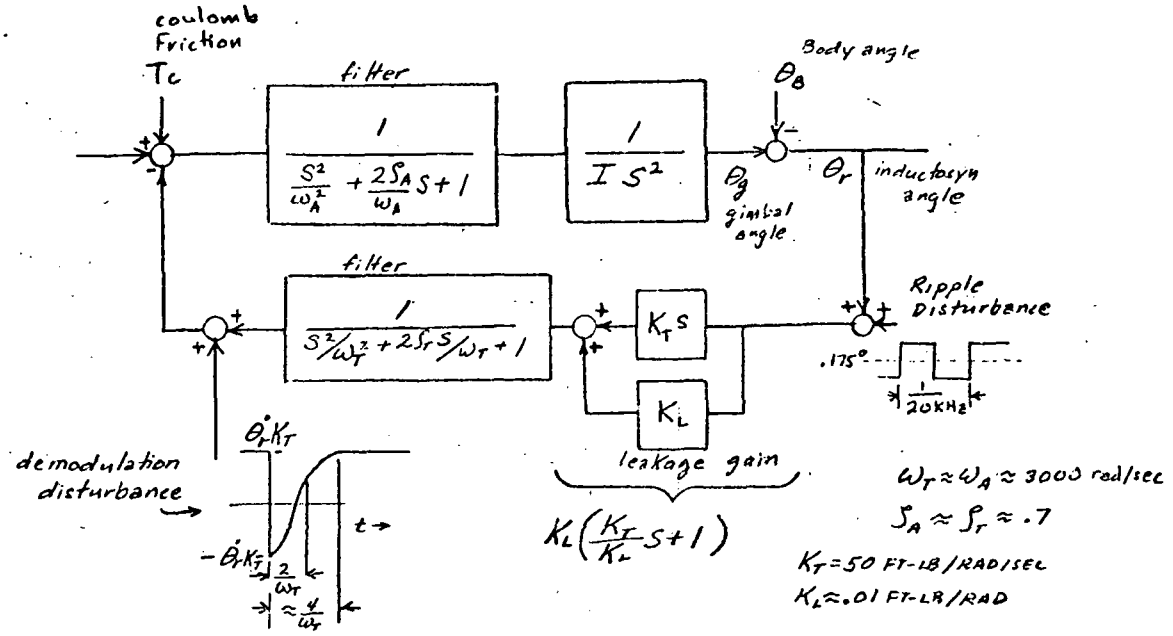

Figure 3-10. Block Diagram of Gimbal Rate Feedback Loop Showing Anomalies and Filters

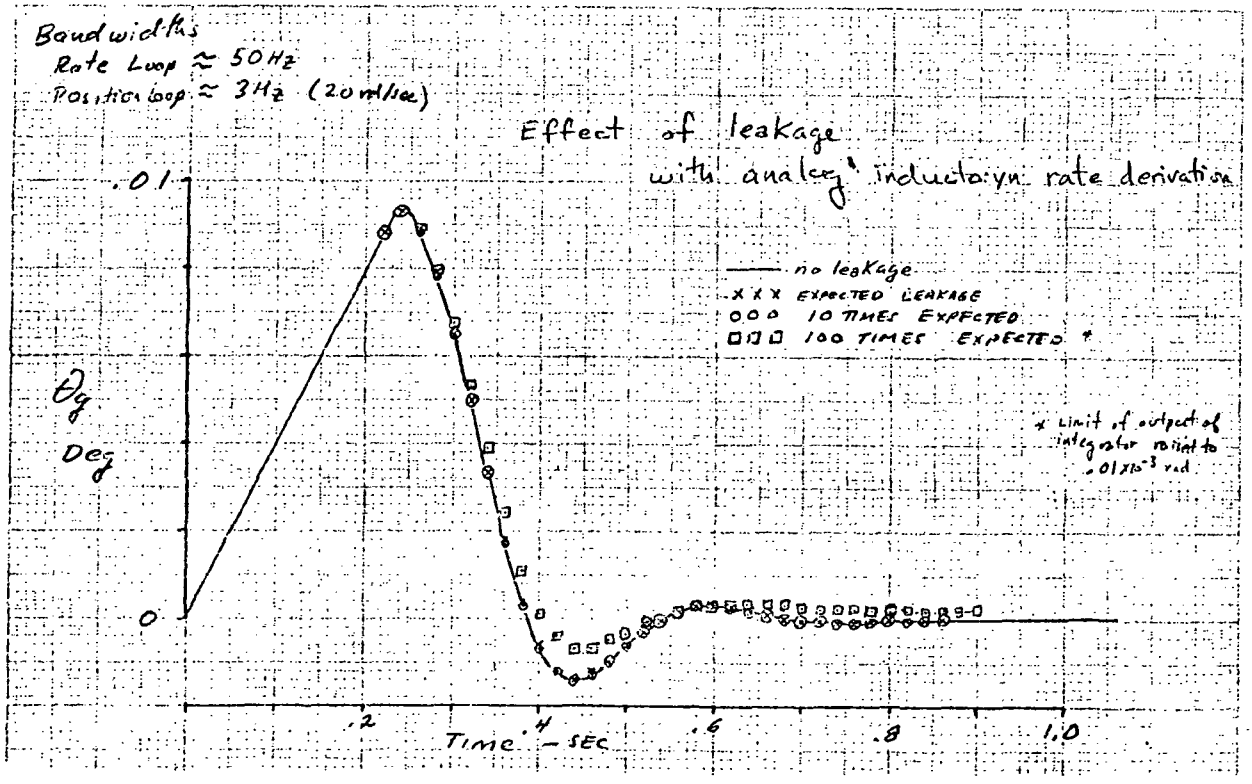

Figure 3-11. Response with Gimbal Position Leakage in Gimbal Rate Loop

Carrier Modulation Ripple

One revolution of the multispeed resolver represents an angle of 1.38 degrees, which is further divided into quadrants representing 0.35 degree each. Logic is used to identify the quadrant, and the differential angle within the quadrant is determined from the duty cycle of a 20 KHz pulsewidth modulated signal. The worst case ripple occurs at the 50% duty cycle representing a differential angle of 0.175 degree. Therefore, the ripple is equivalent to a 0.350 degree peak-to-peak 20 KHz square wave. The attenuation of the 20 KHz (approximately 120,000 radians/second) fundamental is calculated from the transfer function

$$\frac{50}{.16\ s\left(\frac{s^2}{3000^2} + \frac{1.4}{3000}\ s + 1\right)^2}$$

to be -160 db which results in insignificant sensor jitter (<0.00001 arc-second).

Voltage Spikes During Demodulation

The voltage spike shown in Figure 3-10 occurs at each resolver quadrant transition point. Neglecting torque saturation, its effect is to cause the velocity to increase by an amount approximately equal to the integral of the decaying exponential or

$$\Delta\dot{\theta}_r \approx \int_0^\infty \frac{2\dot{\theta}_r K_T}{I} e^{-\omega_T t/2}\, dt = \frac{4\,\dot{\theta}_r K_T}{\omega_T I}$$

or in terms of percentage

$$\frac{\Delta\theta_r}{\dot{\theta}_r} = \frac{4K_T}{\omega_T I} = \frac{4(50)}{3000(.16)} = 42\%$$

The rate loop will then exponentially reduce $\Delta\dot{\theta}_r$ to zero, with the time constant of I/K_T, the gimbal angle changing by

$$\Delta\theta_r = \Delta\dot{\theta}_r\left(\frac{I}{K_T}\right) = 4\dot{\theta}_r/\omega_T$$

$$\Delta\theta_r/\dot{\theta}_r = 4/\omega_T \quad \text{for} \quad \dot{\theta}_r = 1 \text{ deg/sec}, \ \Delta\theta_r = 4.8 \text{ arc sec}$$

However, because of friction and torque saturation, the change in velocity is limited to

$$\Delta\dot{\theta}_{r_{max}} \approx \left(\frac{T_{max} - T_c}{I}\right)\left(\frac{4}{\omega_T}\right) = 1.67 \times 10^{-3} \text{ rad/sec}$$

$$\Delta\theta_{r_{max}} = \Delta\dot{\theta}_{max}\left(\frac{I}{K_T}\right) = 1.1 \text{ sec}$$

During steady-state $\dot{\theta}_{r_{max}} = \omega_{B_{max}} = 0.04$ degree/second and the voltage spikes will result in a peak error of

$$\Delta\theta_r = .04 \text{ deg/sec } (3600 \text{ arc sec/deg}) \; 4/3000 = .19 \text{ arc sec}$$

which is negligible.

Preliminary Estimate of Bending Effects on the Gimbal Rate Loop Stability

The bending model without damping is shown in Figure 3-12, where very high compliances have been neglected and inertias between them were lumped. Neglecting very high frequencies these expressions reduce to:

Inner gimbal:

$$\theta_T - \theta_B \approx \frac{T_m}{I_T s^2} \cdot \frac{\left(\frac{(I_H + 2I_T)}{K} s^2 + 1\right)}{\left(\frac{I_H}{K} s^2 + 1\right)}$$

Outer gimbal:

$$\theta_H - \theta_B \approx \frac{T_m}{(I_H + I_T)s^2} \cdot \frac{\left(\frac{I_H + 2I_T}{K} s^2 + 1\right)}{\left(\frac{I_H I_T}{(I_H + I_T) K} s^2 + 1\right)}$$

$I_H = 0.065$ ft-lb-sec^2

$I_T = 0.1$ ft-lb-sec^2

$K = 45{,}000$ ft-lb/rad

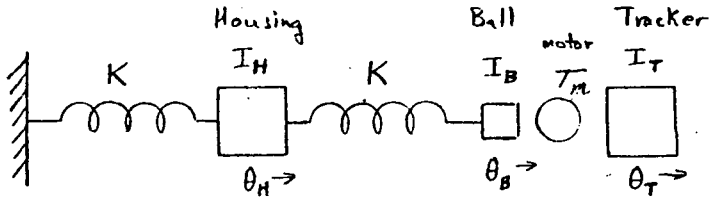

$$I_H \ddot{\theta}_H = -K\theta_H - K(\theta_H - \theta_B)$$
$$I_B \ddot{\theta}_B = -K(\theta_B - \theta_H) - T_m$$
$$I_T \ddot{\theta}_T = T_m$$

$$\theta_T - \theta_B = \frac{T_m}{I_T S^2} \cdot \frac{I_H(I_B+I_T)S^4 + K(I_H+2I_B+2I_T)S^2 + K^2}{I_H I_B S^4 + (I_H+2I_B)KS^2 + K^2}$$

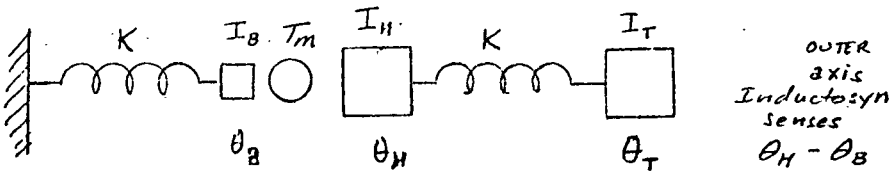

$$I_B \ddot{\theta}_B = -K\theta_B - T_m$$
$$I_H \ddot{\theta}_H = T_m - K(\theta_H - \theta_T)$$
$$I_T \ddot{\theta}_T = -K(\theta_T - \theta_H)$$

$$\theta_H - \theta_B = \frac{T_m}{(I_T+I_H)S^2} \cdot \frac{I_T(I_B+I_H)S^4 + K(I_H+2I_T+I_B)S^2 + K^2}{\left[\left(\frac{I_H I_T}{I_H+I_T}\right)S^2 + K\right]\left[I_B S^2 + K\right]}$$

Bending model without friction locking. When friction locked $\theta_T - \theta_B = 0$ for inner gimbal and $\theta_H - \theta_B = 0$ for outergimbal.

Figure 3-12. Bending Effect on Inductosyn Signal

and the bending frequencies are:

	Poles (rad/sec)	Zeros (rad/sec)
Inner	835	410
Outer	1500	410

The expected bending damping factor (ζ) is 0.003. Figure 3-13 illustrates the frequency response of the inner gimbal with bending for a 50 Hz (314 radians/second) bandwidth both with and without the filter. Note that the bending zero occurs at a lower frequency than the bending pole, and that the control loop without the filters is phase stabilized in a relatively low bending frequency region. But, with the filters in, the loop is only marginally stable. By increasing the filter frequencies by one octave (to 6000 radians/second) stability margins of 6 db and 40 degrees can be obtained. However, the most conservative approach is to lower the gimbal rate loop bandwidth and use a filter to gain stabilize the loop. This is accomplished by lowering the gain at 835 radians/second by 50 db. Reducing the BW to 60 to 120 radians/second will lower the gain by 8 to 14 db. The rest of the gain attenuation can be accomplished by a sharp cut-off filter (36 db/octave) at about 400 radians/second.

3.3.3 Design Implementation Summary

The PADS STA servo design uses gimbal rate feedback with the rate loop bandwidth set at 60 radians/second and filtered to gain stabilize the computed bending modes. The controller block diagram is shown in Figure 3-14, including both the star tracking and Inductosyn positioning modes.

Design of the Inductosyn mode is non-critical and is shown in Figure 3-15. The control parameters can be determined from the following constraining equations.

(1) $K_{IP}/K_P = \omega_n$

(2) $\frac{K_P \, K_{PA1}}{K_T} = \omega_n/K_S$

(3) $K_T \, K_{PA2} = BW_T \, I/K_A \, K_M$

(4) $K_{PA1} \, L2/K_T = RL1$

(5) $L1 \cdot K_{PA1} \cdot K_{PA2} = 1.1 \, T_c/ \, K_A \, K_M$

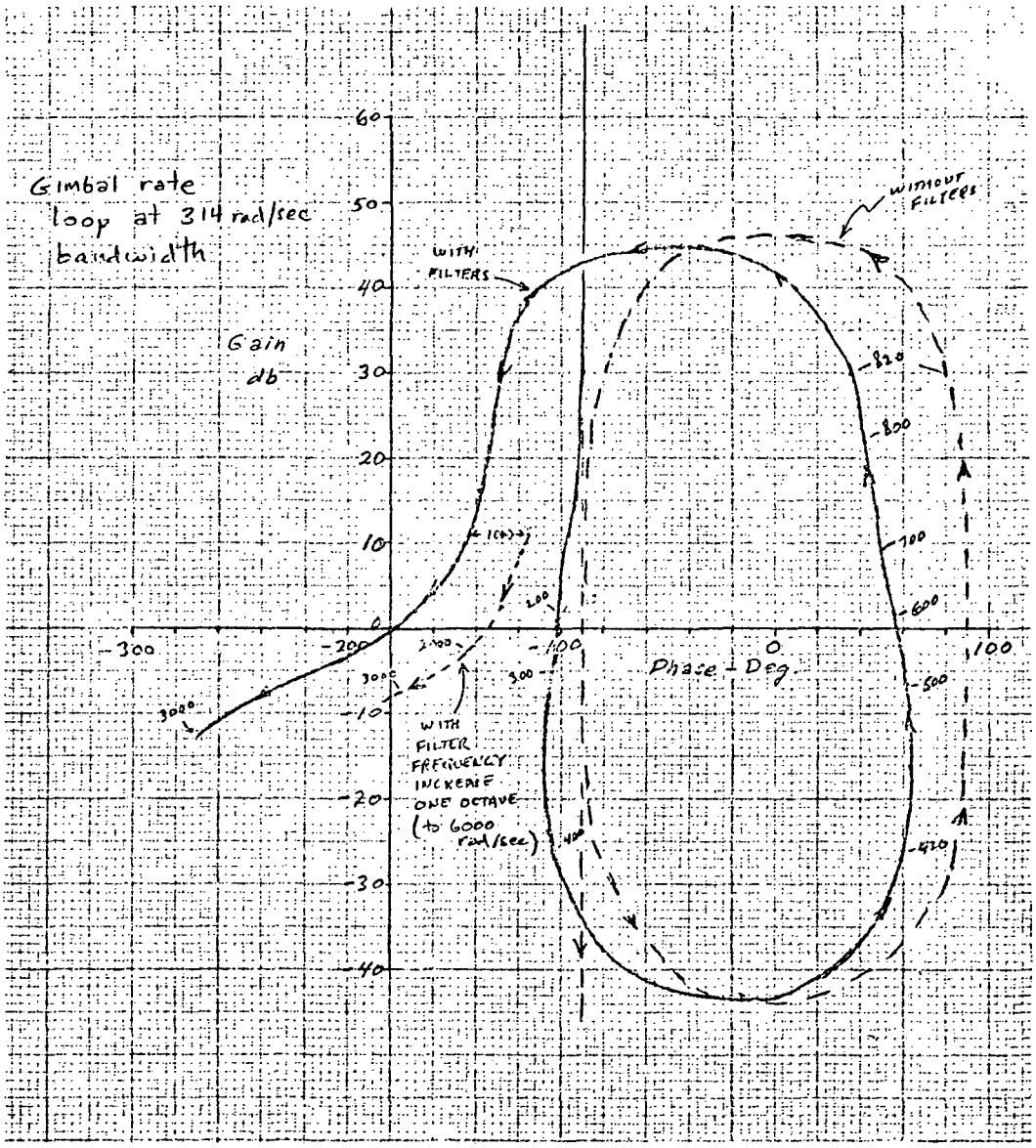

Figure 3-13. Gain-Phase Plot, Gimbal Rate Loop, Inner Gimbal with Bending

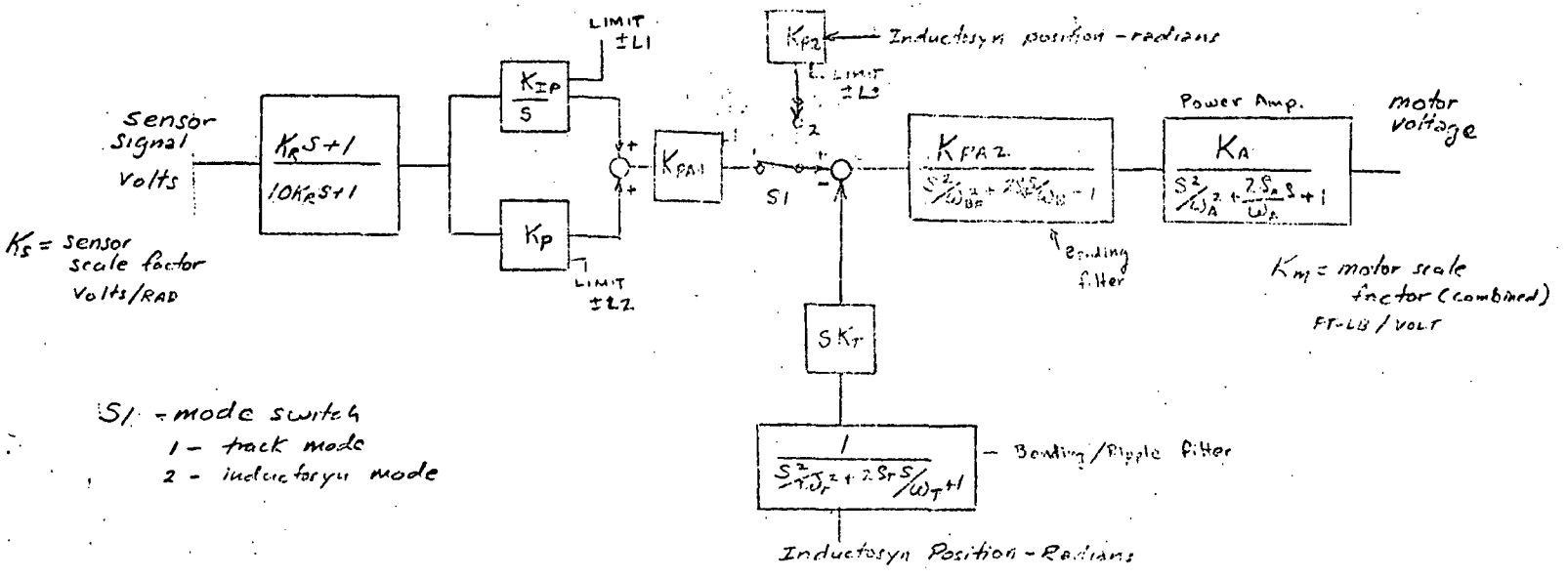

Figure 3-14. Controller Block Diagram - PADS Star Tracker Servo

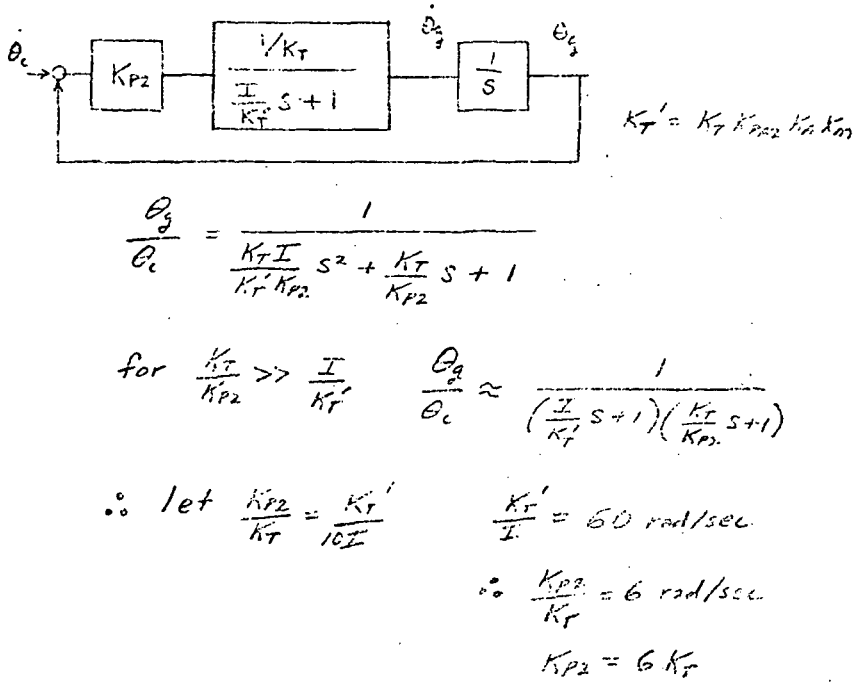

Figure 3-15. PADS Star Tracker Coarse Mode (Inductosyn) Servo Design

(6) $K_R = 1/BW_T$

(7) $K_{P2} = 0.1\ BW_T\ K_T$

(8) $(L3 - RL2 \cdot K_T)\ K_{PA2}\ K_A\ K_M = T_c$

where

K_A = power amplifier gain = 4 v/v

K_M = motor constant = 0.0312 ft-lb/volt

I = gimbal inertia

I_{inner} = 0.039 ft-lb-sec^2

I_{outer} = 0.098 ft-lb-sec^2

BW_T = rate loop bandwidth selected = 60 rad/sec

RL1 = rate limit in track mode (at maximum friction) = 1.0 deg/sec

RL2 = rate limit in slew mode = 4 deg/sec

K_s = sensor scale factor = 1375 v/rad

ω_n = position loop natural frequency = 20 rad/sec

T_c = coulomb friction (max) = 0.2 ft-lb

It should be noted that the above set of equations do not result in a unique solution, unless additional constraints (e.g., circuit constraints such as voltage scaling on limits, etc.) are added. To attenuate damping modes, for BW_T = 60 radians/second, ω_{BF} and ω_T are set at 400 radians/second, and ζ_T and ζ_B at 0.5 ± 0.2. ω_A then should be $\geq$3000 radians/second. Detailed implementation of this design is discussed in Section 4.2.2.

4.0 HARDWARE DESIGN

A major activity during the PADS design effort has been design, development, and test of the PADS star tracker and supporting electronics. The tracker and electronics design is presented in the following sections. Test activity has been documented separately [6].

4.1 Star Tracker Assembly

The PADS Star Tracker Assembly (STA) consists of a Star Sensor Unit (SSU) mounted within a two degree of freedom Sensor Gimbal Unit (SGU). The SSU incorporates the optics, detector, and supporting electronics. The SGU is an exceptionally precise and stable mount providing gimbal drive for null tracking stars and precision angular readout of the gimbals. The STA interfaces with the Sensor Electronics Assembly (SEA) which provides the gimbal angle processing and servo drive signals. The SSU mounted within a single-axis (inner) gimbal assembly is shown in Figure 4-1.

4.1.1 Star Sensor Unit Design

Optical/Mechanical Design

The optical design resulted from a tradeoff between the desire for a short focal length to obtain small size and weight and the requirement to maintain arc-second level accuracy. The selected design is a Cassegrain telescope utilizing aluminum optics. The optics design is shown in Figure 4-2. This two-element design provides an effective focal length of 32.63 inches. The diameter of the primary is 4 inches with a central obscuration of 2 inches. The effective collecting aperture is 54 cm^2. The use of standard optical coatings gives an optical efficiency of better than 70%.

The sensor unit is shown partially disassembled in Figure 4-3. The mechanical layout is shown in Figure 4-4, incorporating the optics, detector and electronics in an assembly with a sun shade. A sun shade is required to track within 45° of the sun. However, because of the optical system utilized, the size of the shade can be effectively minimized. The inner portion of the shade is the barrel of the optics assembly, so that while the effective length of the sun shade is 11 inches, it is only necessary to add 5.5 inches to the sensor.

A bright object sensor and shutter assembly are incorporated in the sensor along with the high voltage power supply. The high voltage power supply will be incapacitated by the bright object sensor when the sun is within the 45° field, and also, a rotary solenoid will be actuated which will close the shutter in front of the photocathode.

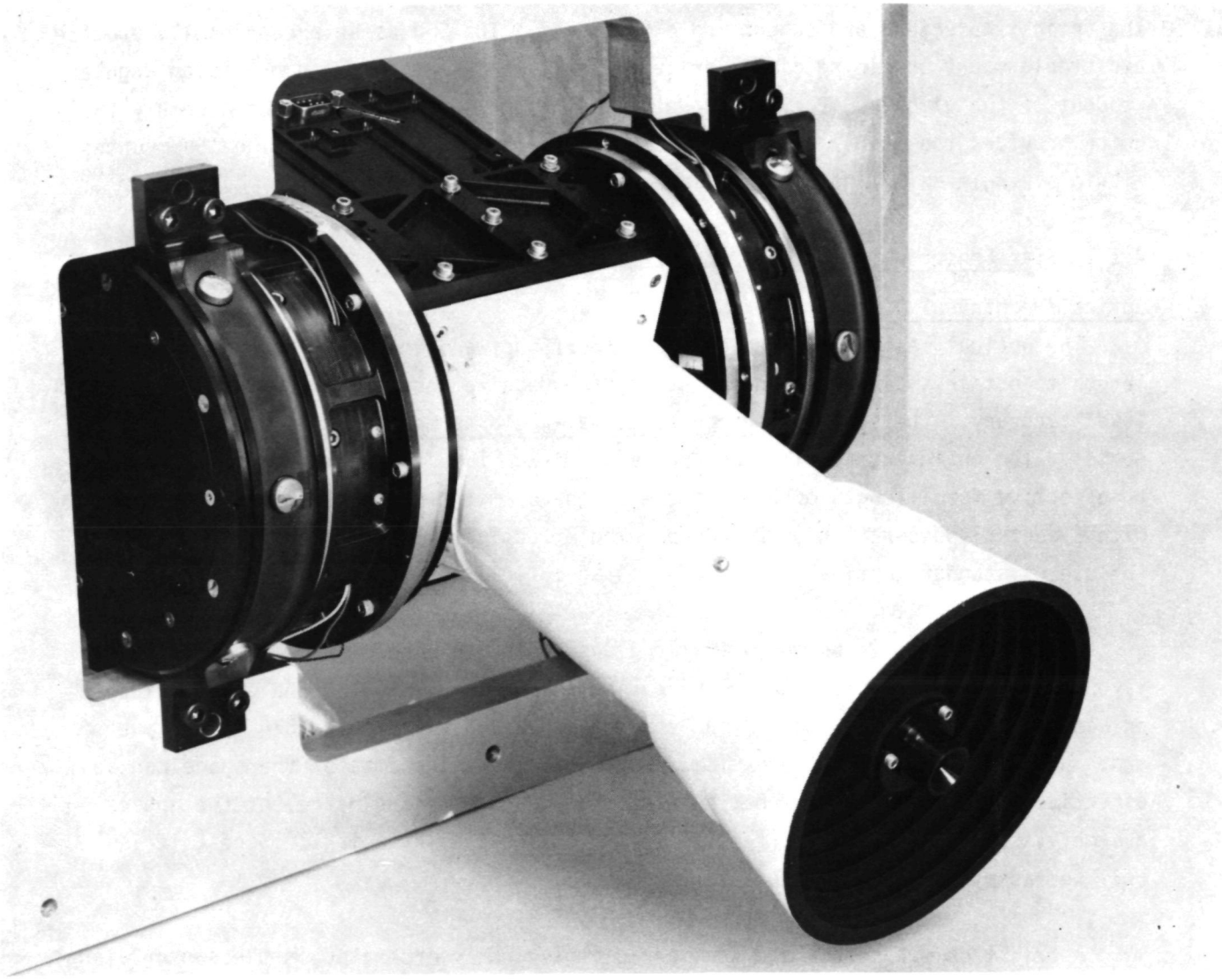

Figure 4-1. Star Tracker Assembly (Inner Gimbal)

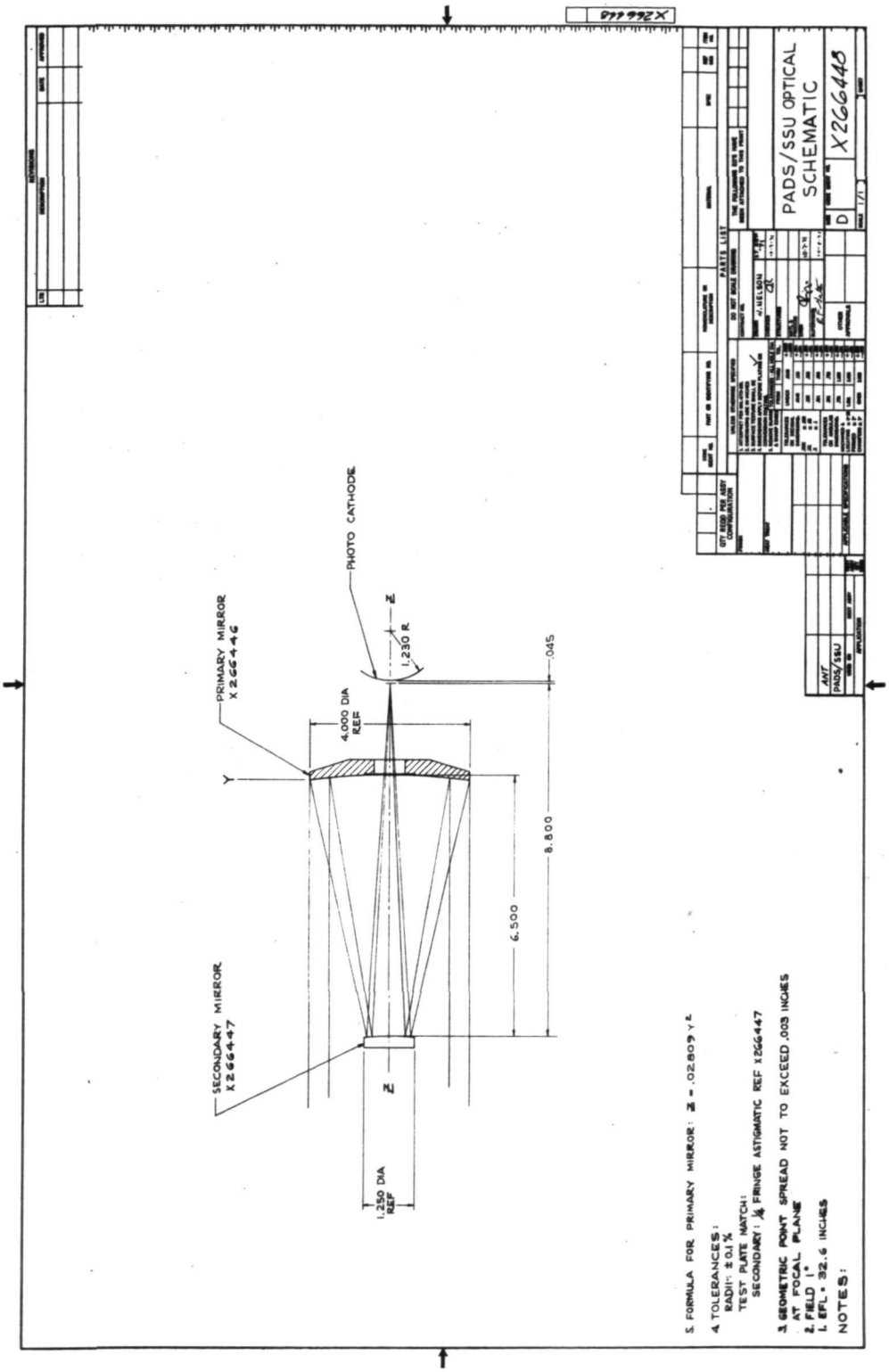

Figure 4-2. Star Sensor Unit Optics Design

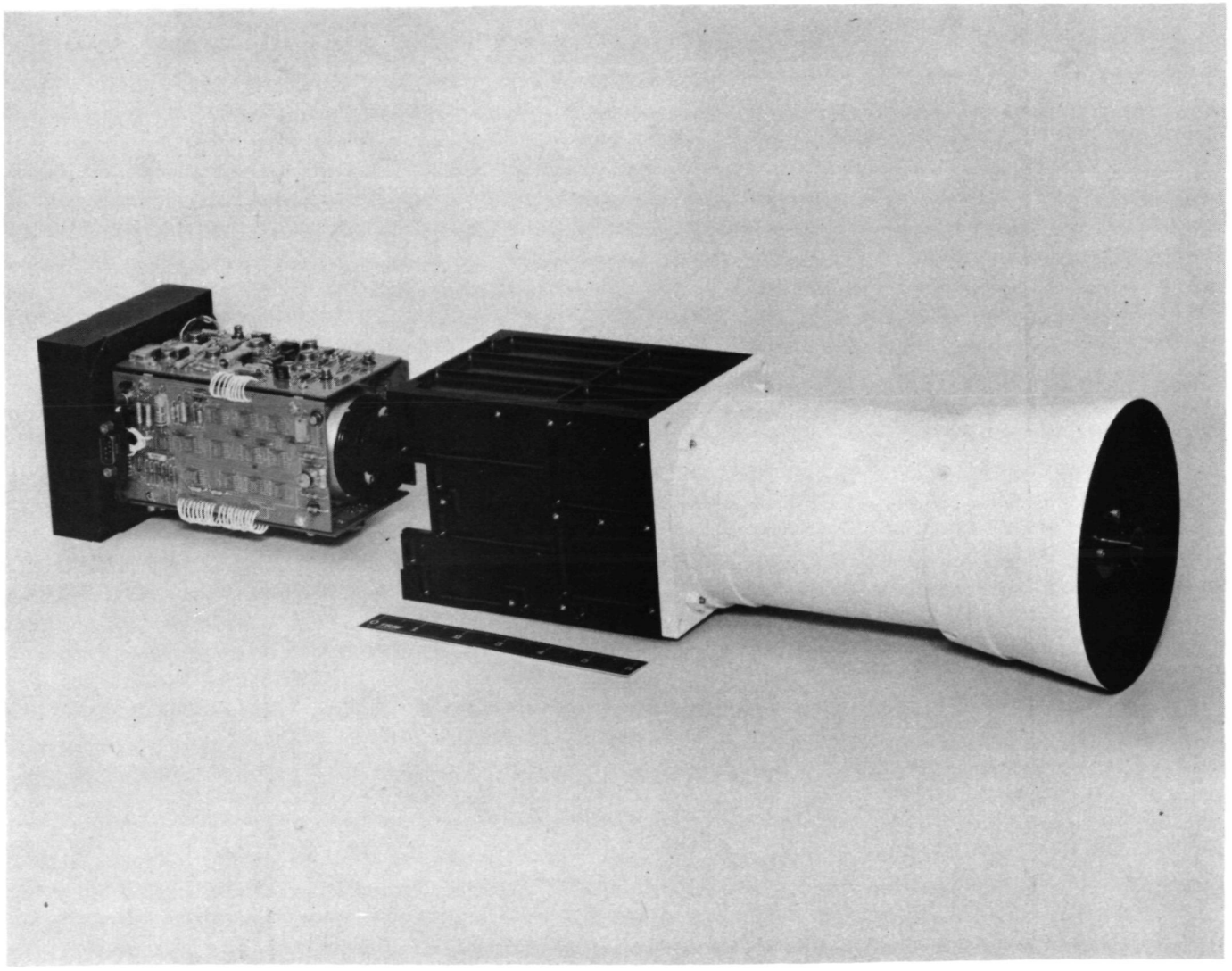

Figure 4-3. Star Sensor Assembly (Partially Disassembled)

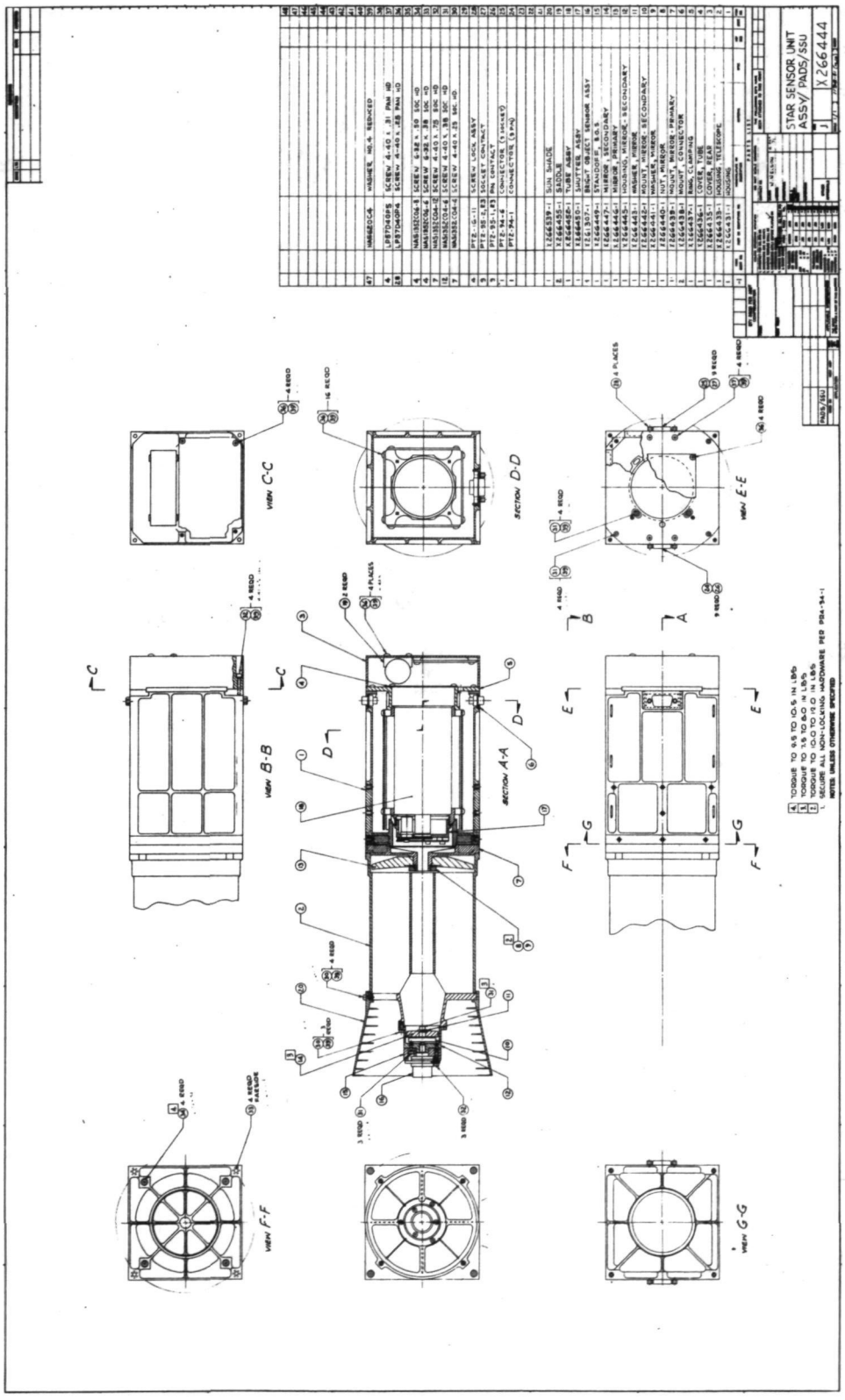

Figure 4-4. Star Sensor Assembly Layout

The sensor assembly has been designed with great care for thermal symmetry to provide maximum thermal-mechanical stability. In particular, the electronics are equally spread around the tube assembly. The high voltage power supply and line voltage converter, behind the tube assembly and the flange mounting, provide symmetrical heat transfer through the structure into the mounting plate. This minimizes thermal gradients across the structure and the effects of thermal time constants which could produce boresight axis tilt.

The image dissector, deflection yoke, focus coil, and high voltage biasing network are all contained in a single, integral, encapsulated assembly. The outer structure of this assembly consists of the necessary magnetic shielding to prevent stray fields, or the earth's field, from affecting the image dissector, and is mechanically indexed directly to the optics. The electronics are contained on four flex-print interconnected printed circuit boards which are installed in the housing as a subassembly around the tube assembly.

Detector

The image dissector used is an ITT F 4004. One of the advantages of the F 4004 is the ability to have the photocathode remotely processed and tested before it is incorporated into the tube. This results in better photocathode uniformity. Also, there is less chance of stray photocathode contamination because the chemical sacs are not left in the tube.

The F 4004 has a resistance divider network potted within the base of the tube, reducing the possibility of network contamination affecting the tube gain.

The photocathode of the image dissector is a red-extended S-20 surface. The peak spectral response is nominally 0.072 amperes/watt. The F 4004 has a 15-stage secondary emission multiplier structure, giving it a nominal gain of 10^6. In most cases, the gain will exceed this by an order of magnitude.

Electronics

The star sensor electronics are summarized (see Figure 4-5):

- Video Processor - The video processor performs the following functions. During the search mode, automatic gain and threshold control circuits select only the largest video pulse present and send it to the mode control logic. When in the track mode of operation, the image dissector video is shaped into a digital pulsewidth-modulated signal and is fed to the demodulator. A digital star-presence signal and an analog star-magnitude signal are also developed.

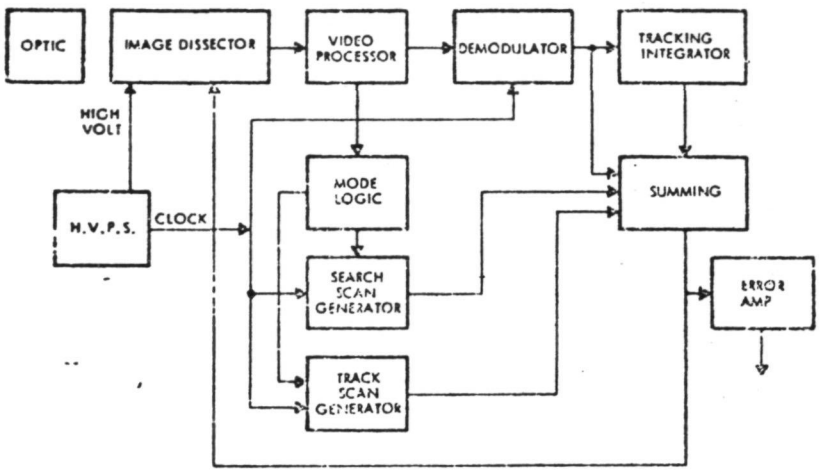

(Only one error channel is shown.)

Figure 4-5. Functional Block Diagram of Star Sensor Unit

- Mode Control Logic - The mode control logic establishes the mode of operation: search or track. The timing of the search cycle, the gating of the tracking loop, and search-scan waves are also controlled by the mode logic.

- Demodulator - The demodulator circuits consist of timing gates to process the pulsewidth-modulated video and precision voltage switches which develop the tracking loop correction error voltage at the input to the tracking integrator.

- Tracking Integrators - This circuit consists of an integration stage (op-amp) which provides correcting dc voltages to the deflection generator to keep the star image centered in the image-dissector aperture by taking the integral of the error demodulator output.

- Scan Generator - The scan generator provides three separate circuit functions. A triangular waveform is generated by a counter-integrator combination and is used as the track mode scan waveform. Two binary counters and D/A converters are used to develop the stairstep-type search mode scan waveforms. The above scan waveforms and the dc-correcting voltage from the tracking integrator are summed in current dividers to provide the deflection coil current required.

- Error Amplifier - The dc component of the deflection coil current is determined by a current sampling resistor and the corresponding voltage is then amplified and filtered to give the required output pointing error gradient.

The circuitry used for this design is identical with that utilized for the PPCS STA electronics design [1,2] with the following exceptions:

- The internal ±12.0 volt regulator were deleted and the ±15 volt input is used directly. This necessitated the change of several bias resistors.

- The PPCS high voltage supply was replaced by a Venus Scientific module and the high voltage regulator was modified to control the total current going to the tube assembly instead of regulating only the last dynode current as was the case in the PPCS unit.

- Replacing the high voltage supply required the addition of a separate timing clock circuit.

- The tuned LC bandpass filter circuit of the video processor was replaced with an equivalent RC bandpass filter circuit.

Design/Performance Analysis

The sensor sensitivity and noise equivalent angle (NEA) are derived on the basis of tracking a +3.5M AOV star. The amount of radiant energy available in the spectral band of the sensor is found by convolving the detector spectral response with the spectral energy distribution of the AO star. Thus,

$$H = C_1 \int_{.3\mu}^{.9\mu} H(\lambda) \quad S(\lambda) \quad d\lambda$$

where

C_1 = the normalizing constant to convert $H(\lambda)$ from a relative spectral energy distribution to an absolute S.E.D.

$H(\lambda)$ = the relative spectral energy distribution of the AO class star

$S(\lambda)$ = is the relative spectral response of the red-extended S-20 photocathode

If the above integration is carried out, the effective power is found to be 6×10^{-14} watts/cm^2.

The photocathode current I_p, is found by:

$$I_p = \text{HAST} = 1.64 \times 10^{-13} \text{ amperes}$$

where

H = effective power on cathode

A = area of collecting aperture = 54 cm^2

S = peak of S-20 response = 0.072 amps/watt

T = transmission efficiency of optics = 0.7

The anode current, I_A, is related to the photocathode by

$$I_A = KI_p$$

where K is the gain of the secondary emission multiplier. For $K = 5 \times 10^6$, the anode current, I_A, equals 8.2×10^{-7} amperes.

With the photocathode current of 1.64×10^{-13} amperes for a limiting star, the RMS number of electrons emitted from the photocathode per second is

$$N(t) = \frac{I_p}{q} = 1.02 \times 10^6 \text{ electrons/second}$$

where q is the charge on an electron, i.e., $q = 1.6 \times 10^{-19}$ coulombs.

In the tracking mode, each axis is sampled in 1/1200 of a second, so that the RMS number of electrons emitted from the photocathode during this sampling period is 850. If the RMS number of effective photo electrons emitted from the photocathode during any sampling period is N, the RMS deviation from this number, for repeated measurements is $\sqrt{N}$. It limits the accuracy with which a measurement can be made in a given time interval irrespective of other sources of error. Thus, finding the location of the star signal with respect to the center of the aperture (Instantaneous Field of View) is directly related to the number of electrons passing through the aperture. For an IFOV, θ, of 88.6 arc-seconds, the center of this can be found to an accuracy ψ given by,

$$\psi = \frac{\theta}{\sqrt{N}} = 3.04 \text{ arc-seconds for each scan}$$

If the bandwidth, B, of the sensor is 25 Hz, then the overall number of samples per measurement, η, is

$$\eta = f_s/2B$$

where f_s is the sweep frequency (300 Hz).

Therefore

$$\eta = 6$$

The NEA is given by

$$NEA = \frac{\psi}{\sqrt{\eta}} = 1.24 \text{ arc seconds}$$

Three different sources of sensor null shift errors are identified as follows:

ΔV_{dl} = equivalent input dc level shifts to the track integrator

This item includes:

(a) Error detector summing point variations

(b) Integrator op-amp input offsets

(c) Video waveshape variations

ΔV_{d2} = equivalent input dc level variations to the deflection coil driver

This item includes:

(a) Coil driver input op-amp offsets

(b) Acquisition sweep input dc level variations

ΔV_{d3} = equivalent input dc offsets of the output error amplifiers

The sensor output voltage in terms of the three error terms and the input angle θ has been derived (Figure 4-6) and is:

$$\Delta V_O = K_{EA}\,\Delta V_{d3} + \frac{K_{EA}\,R_C}{R_D\,K_I\,K_{ED}}\,\Delta V_{d2} + \frac{K_{EA}\,R_C}{K_D\,K_{ED}}\,\Delta V_{d1}$$

where

K_I = 5×10^4 v/v

K_D = 1.32 IFOV/ma

K_{EA} = 3.7 v/v

K_{ED} = 0.84 volts/IFOV

R_C = 0.2 v/ma

Substituting these values gives:

$$\Delta V_O = 3.7\,\Delta V_{d3} + 0.13 \times 10^{-4}\,\Delta V_{d2} + 0.67\,\Delta V_{d1}$$

ΔV_{d1} is due to the integrator LM101A and error detector:

LM101A effect	=	0.076 mv
Error detector	=	0.3 mv
RSS total		0.31 mv

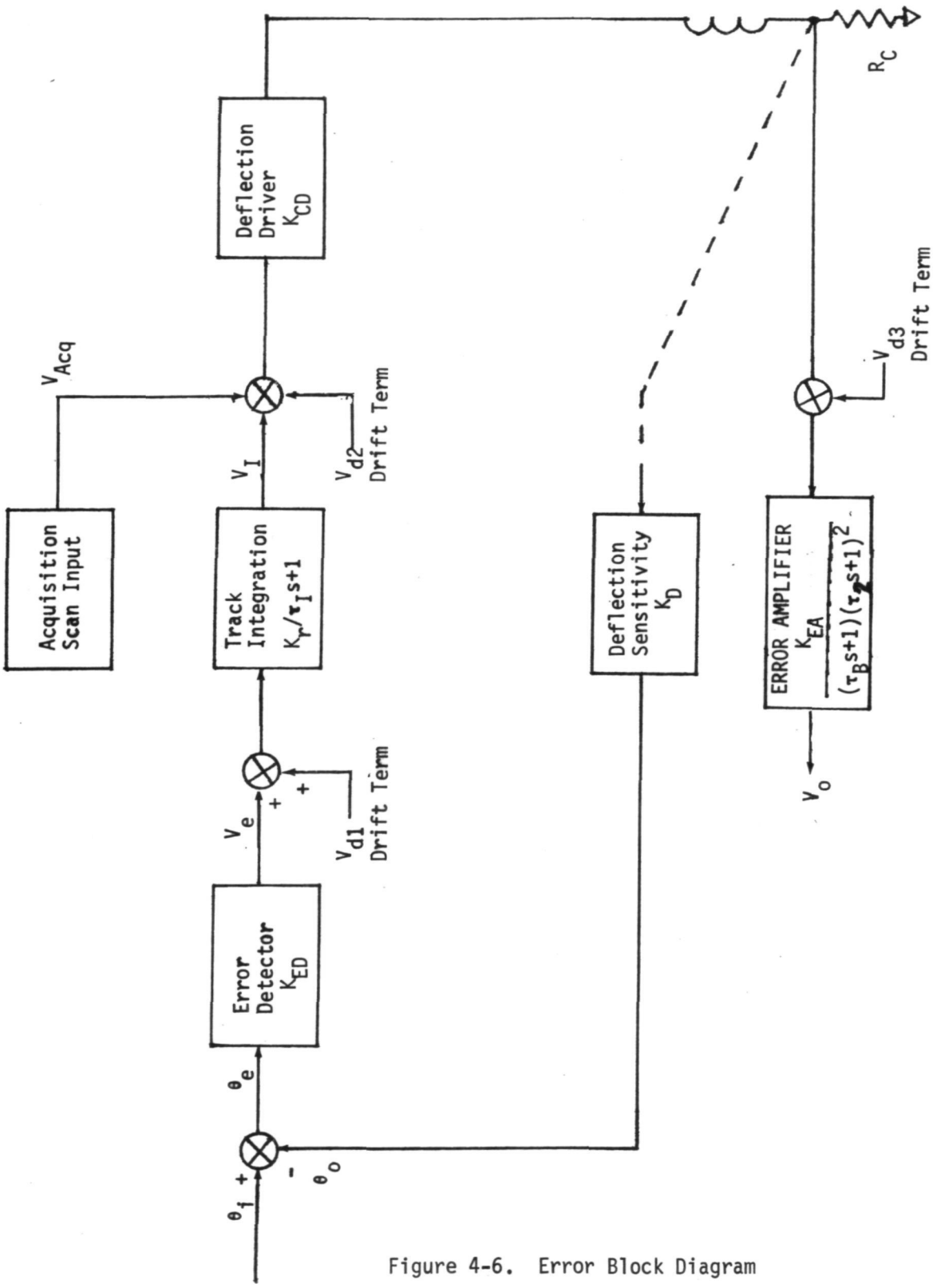

Figure 4-6. Error Block Diagram

The effects of ΔV_{d2} are shown to be neglible.

ΔV_{d3} is all due to LM101A offset:

$$\Delta e_{os} = \pm 15\ \mu v/°C$$

$$\Delta i_{os} = 0.2\ na/°C,\ R = 90K$$

Over $\pm 5°C$,

$$\Delta V_{d3} = \left([(15 \times 10^{-6})(\pm 5)]^2 + [(0.2 \times 10^{-9})(90 \times 10^3)(\pm 5)]^2 \right)^{1/2}$$

$$= \pm 0.117\ mv,\ RSS$$

As a result, the overall error is

$$\Delta V_o = \left([(3.7)(\pm 0.117)]^2 + [(0.67)(0.31)]^2 \right)^{1/2} = \pm 0.48\ mv$$

At a scale factor of 6.67 mv/$\widehat{sec}$, this represents an error of ± 0.072 $\widehat{sec}$.

4.1.2 Sensor Gimbal Unit Design

The two degree of freedom gimbal assembly utilizes the proven PPCS single ball/flexure suspension system and Inductosyn readout. The SGU layout is shown in Figure 4-7. The inner gimbal is formed by identical drive housing assemblies attached on each side of the star sensor unit. A structural I-beam ring connects the inner gimbal to the outer gimbal drive. The outer gimbal is structurally identical to the inner except that its gimbal housing includes the mounting foot for the unit. The drive housings incorporate the suspension/bearing system, drive motors, Inductosyn encoders, and data link. A disassembled view of these elements is shown in Figures 4-8 and 4-9.

The use of identical drives on both ends of each axis is motivated by the desire to obtain mechanical and thermal symmetry. The star sensor mass is centered between the supporting bearings of the inner gimbal, the mass of the rotating components is centered between the outer gimbal bearings and the mass center of the entire system is contained in the plane of the mounting feet. Nearly identical power dissipation in each housing minimizes thermal gradient variations. Further, zero structural slope mounting points are chosen so that one-g distortions result in translation only -- not in angular rotations. With this approach, testing can be accomplished with negligible errors due to gravity induced droop. A similar design on PPCS produces less than 0.25 arc-second droop.

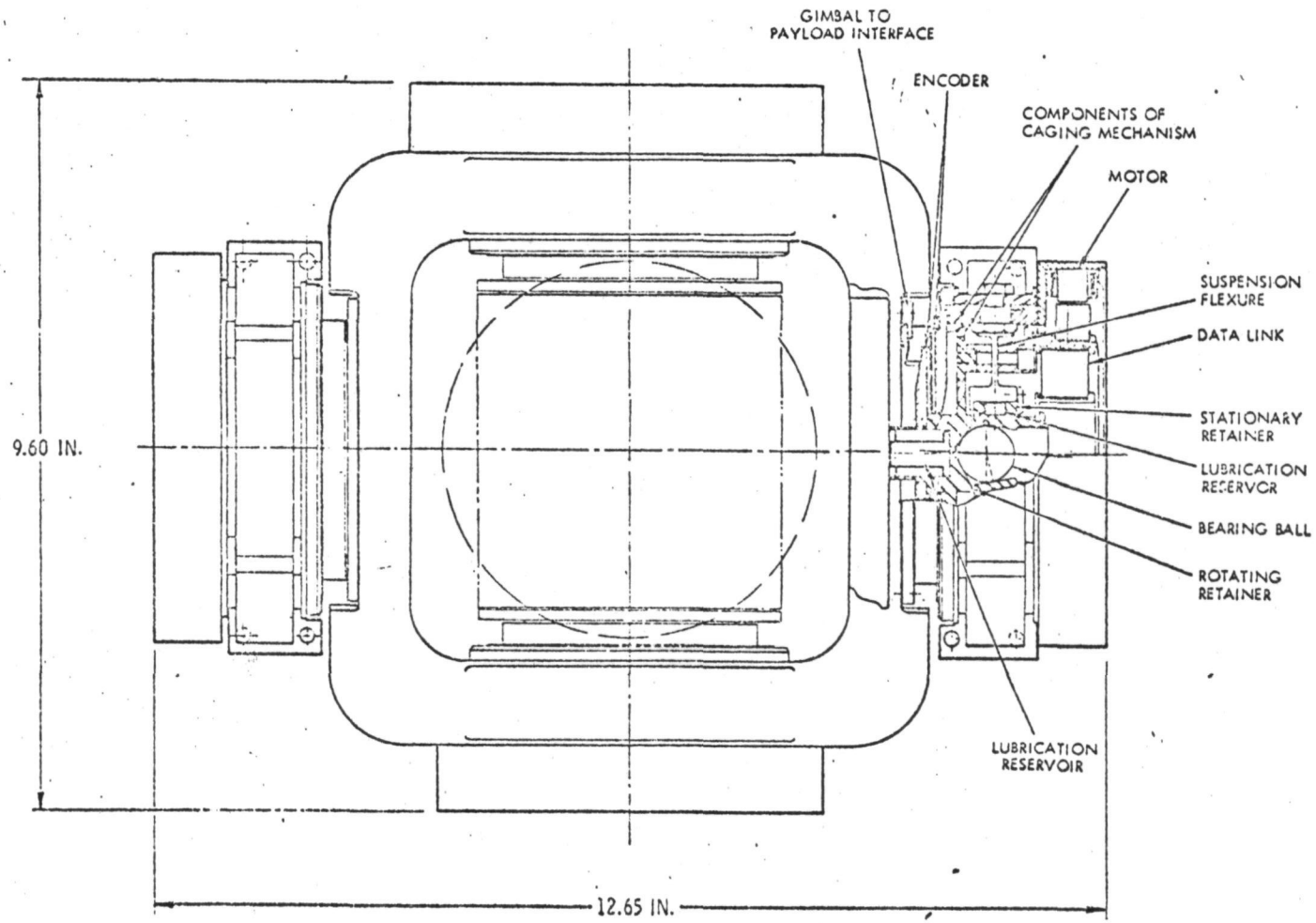

Figure 4-7. Sensor Gimbal Unit Layout

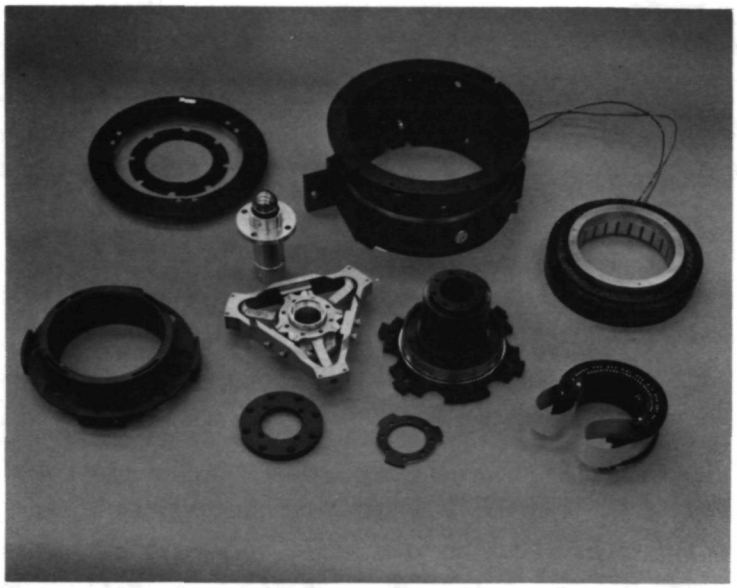

Figure 4-8. Drive Housing (Disassembled)

Figure 4-9. Indutosyn Plates, Drive Housing and Frame

Gimbal Suspension

The gimbal design features a one-ball bearing configration. The geometry of this scheme provides self-alignment features and facilitates the fabrication of the gimbal system by providing inherent reference for the establishment of two mutually perpendicular planes which contain the rotational axes of the gimbals.

The desired axes are established by a line of contact of the balls with the cone surfaces of their retaining cups. The accuracy of the gimbal axes is set by the cups radii of contact and the ball sphericity. Since the ball sphericity can be obtained to two parts in a million and the cups radius of contact is established by lapping, and since all other critical surfaces are indexed to the payloads balls, the achievement of very accurate alignment is possible. As shown on Figure 4-10, the suspension consists of two single spherical balls supporting the payload. Each ball locates itself via two cone type cups. One cup (rotating retainer) is located on each side of the payload and the other cup (stationary retainer) is inclined 40 minutes of arc with respect to the center line passing through the centers of the spherical balls; the stationary cup cone is eccentrically offset with respect to the centerline of the cylindrical shaft containing the cone. The shaft element is housed in the bore of the flexure, which is an intermediate element between the retainer and the gimbal frame.

The purposeful inclination and offsets of the rotating and the stationary retainers provides adjustment capabilities to accommodate manufacturing tolerance and the elimination of runout. By rotation of the stationary retainers perpendicularity of the gimbal axes can be established; also the relative motion of the rotating cups with respect to the body of the payload can essentially eliminate undesirable shaft runout. By virtue of the inclination of the rotating cup, lubrication of all the sliding surfaces is facilitated by continually changing (nutating) the circle of contact. The lubricant is provided to the bearing balls and the rotating retainer contact surfaces by the Nylasint reserviors, one located inside a shaft comprising a portion of the rotating retainer and the other located outside the stationary retainer. The first reservior provides lubricant to the space surrounding the ball below the nominal line of sliding contact, and the second reservior provides molecules of lubricant to the space outside the line of sliding contact. The access holes for the lubricant are also filled with Nylasint material. This affords flow of lubricant directly into the bearing chamber by wicking action, thus eliminating the molecular flow lubrication of the bearing vestibular surfaces.

The materials chosen for the bearing subassembly are stellite and tungsten carbide. The retainers are made from stellite and the balls from tungsten carbide. Carbide was chosen for its hardness, known dimensional stability and relatively good

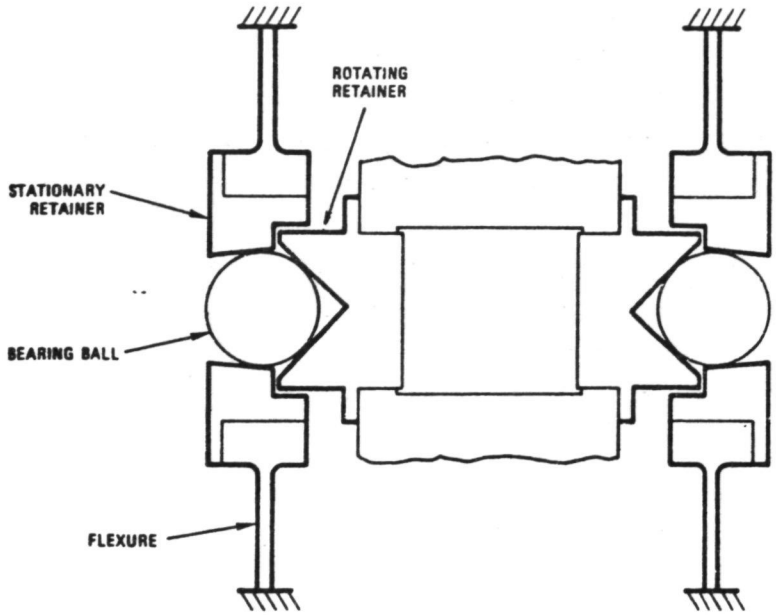

Figure 4-10. Sensor Gimbal Unit Suspension Concept

porosity. Stellite Alloy Number 6B was selected mainly to obtain reasonable hardness and the nonmagnetic properties desired. The combination of these materials, and the particular geometric configuration allows direct application of bearing loads approaching 200 pounds with no visible Brinelling. Larger loads can be accommodated by using different material for fabrication of the retainers.

The friction torques are a function of the preload, the ball diameter and the coefficient of friction. For this design, friction torques of 15 and 30 inches-ounce for the inner and the outer axes, respectively, were determined.

The design success of the single ball bearing suspension concept significantly depends on the performance characteristics of the flexures that support the stationary retainers of the spherical balls. Functionally, the flexures provide clearance support for the stationary retainers, bearing preload characterized by minimal changes due to temperature variation (and hence minimal gap changes between the stators and rotors of the inductosyn encoders), and continual measurement of the location of the ball centers as well as the changes of preload and friction torques in the direction of rotation.

Structurally, the flexure consists of a hub with a bore which accepts the stationary retainers. The outboard end of the stationary retainers, after appropriate alignment schedules, are clamped to the flexure hub. The hub is supported by three flexure elements located 120 degrees apart. Each element has a cross sectional area of 0.10 x 0.75 inch with the larger dimension perpendicular to the rotational axes. The outboard end of the flexural elements have a solid section of which four sides are flat and are guided by mating surfaces of the two-section housing sleeve. The outboard section of the flexure terminates the double threaded boss. The internal thread is used to provide radial tension to the flexure members by preloading them to the housing sleeve and outer thread is used to lock the preload bolt to the sleeve and at the same time preload the bolt to tensions larger than those applied to the flexure elements. The latter aspect is useful in providing additional torsional rigidity when needed.

The gimbal suspension is provided with a caging stops system which protects the bearings and the payload from exposure to excessive stresses by introducing mechanical components in parallel with the element of interest during phases of abnormal excitation. The introduced elements are always of higher structural stiffness than the principal elements of interest. To affect caging condition, the drive motors must rotate their payloads an angle greater than 45° and 15° for the outer and inner gimbals, respectively. The motors are required to maintain the caged condition

(note that other concepts such as detenting are also feasible for the subject design). At the caged region, six sector elements of the rotating members are allowed to approach their mating components on the stationary portion of the gimbal to within 1.5×10^{-3} inches. Such arrangements during abnormal excitation periods provides three directional restraints and snubbing of the payload after nominal deflection of the preload flexure. For the baseline design, the load distribution between the caging mechanism and the bearing balls is in a ratio of 1/10 such that forces not greater than 40 pounds will be absorbed by the bearings. Because the line of contact between the ball and the retainers nutates as a function of displacement, for the chosen caging concept (with excursions greater than the operational angular displacements), brinelling (should it take place) occurs in the circle of contact regions which are never operationally used.

Drive Motors

Each gimbal motor drive assembly is identical in performance and general configuration. It consists of a two phase permanent magnet motor and appropriate support structure. The motor has 24 poles and 4 skewed slots between pole spaces. The commutation to the motor is provided by the Inductosyn resolver signal which is conditioned to provide the required power in terms of sine and cosine functions with periods satisfying the number of poles (12 speed). Interconnecting of the sine and cosine inputs to the respective motor winding results in a brushless motor exhibiting DC torquer characteristics. Each gimbal drive (two drives for each gimbal) was sized to provide redundancy such that one motor can drive the expected loads. The two motor drive concept not only satisfies the thermal symmetry design criteria, but also can provide almost complete elimination of motor slot ripple by appropriate indexing of the motor set.

Inductosyn Encoders

The angular rotation of each gimbal is measured using a precision Inductosyn. The inductosyn is a pair of discs, in this case 5" in diameter, which are mounted such as to rotate coaxially with respect to one another with facing surfaces in close proximity. The facing surfaces have printed conductors, forming winding circuits which may be flux linked, disc-to-disc. One disc, designated the rotor, has a single winding; the other, the stator, has two windings. The winding geometry is arranged so that the transformation coupling from rotor to stator varies trigonometrically with relative disc rotation. The two stator windings are in mechanical quadrature to one another. Thus, the device is electrically identical to a synchro resolver, except for a very low coupling efficiency and for a larger number of poles than are normally found in a conventional resolver.

The Inductosyn rotor is driven with a low-distortion sinusoidal 10 kHz signal. The inductosyn stator produces a pair of signals at the same frequency whose amplitudes are respectively proportional to the sine and cosine of gimbal angle. This signal is processed to derive the gimbal angle. For the high precision required, the Inductosyn used has a single-speed and a 256-speed section on the same axis for coarse and vernier measurement.

The resolver patterns are printed on soft iron discs which are imbedded in the beryllium interface elements. The lamination provides the required dimensional stability by utilizing beryllium as the backup to the soft iron disc. Utilization of iron increases the voltage transformation ratio of the Inductosyn by a factor of 30 (when compared with a resolver pattern placed directly on beryllium material). To minimize noise, the resolver output is preamplified on the gimbal. For proper mechanical alignment and initial indexing, the Inductosyn stationary (stator) element is provided with sufficient mounting freedom to afford minimization of eccentric and non-parallel motions.

Data Link

The data link provides transmission of electrical signals across the gimbals without excessive restraint torques. The design utilizes an "S" folded conductor strip which is attached at the ends of and slides between a cylindrical stationary member attached to the housing sleeve and a smaller diameter cylindrical component (the rotating member) attached to the motor shaft. The inner and the outer members are lined with nylon rings to provide electrical insulation and mechanical guide for the rolamite action of a 6 conductor strip. There are four such strips providing the capability of ±60° motion with restraints not exceeding 1/2 inch-ounce. Both the stationary and the rotating members of this assembly are made from beryllium. Appropriate electrical connectors (miniature) are attached to the periphery of the rotating and stationary component. The data link itself is so designed that it can be removed from the system without disturbing the various electrical interconnections.

4.2 Sensor Electronics

The Sensor Electronics Assembly provides encoding of the Inductosyn gimbal angle signals and implements the controller/drive for the gimbal motors. Figure 4-11 shows the SEA functional block diagram for one of the two gimbal axes. The Inductosyn Electronics has as its function the excitation and processing of both multi-speed and single-speed Inductosyn output signals to derive the precision measure of gimbal angle. The Drive Electronics provides for loop compensation and appropriate commutation and motor power drive functions. The developed breadboard electronics are shown in Figure 4-12, and detailed schematics are provided in the Appendix.

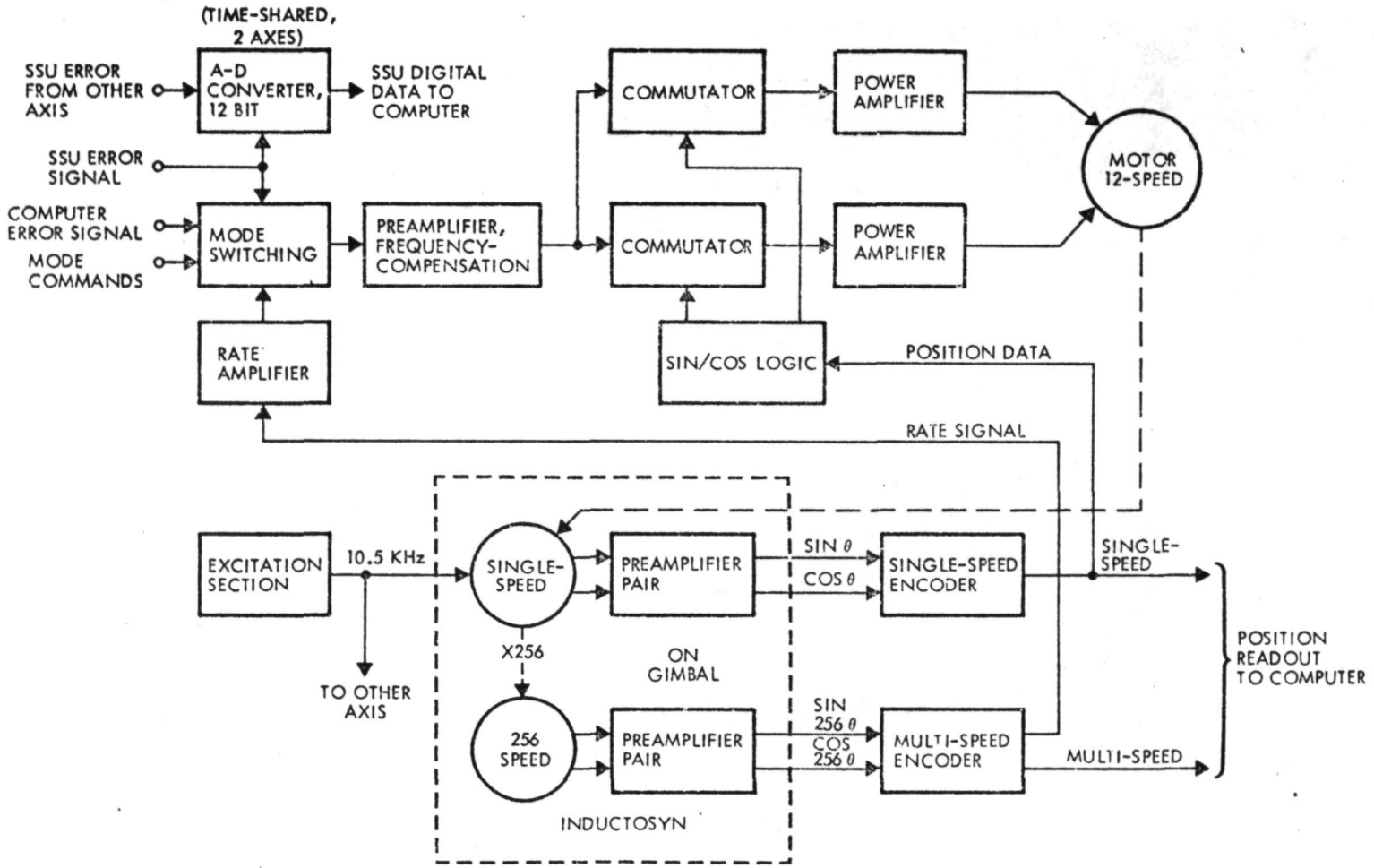

Figure 4-11. Sensor Electronics Assembly Functional Block Diagram

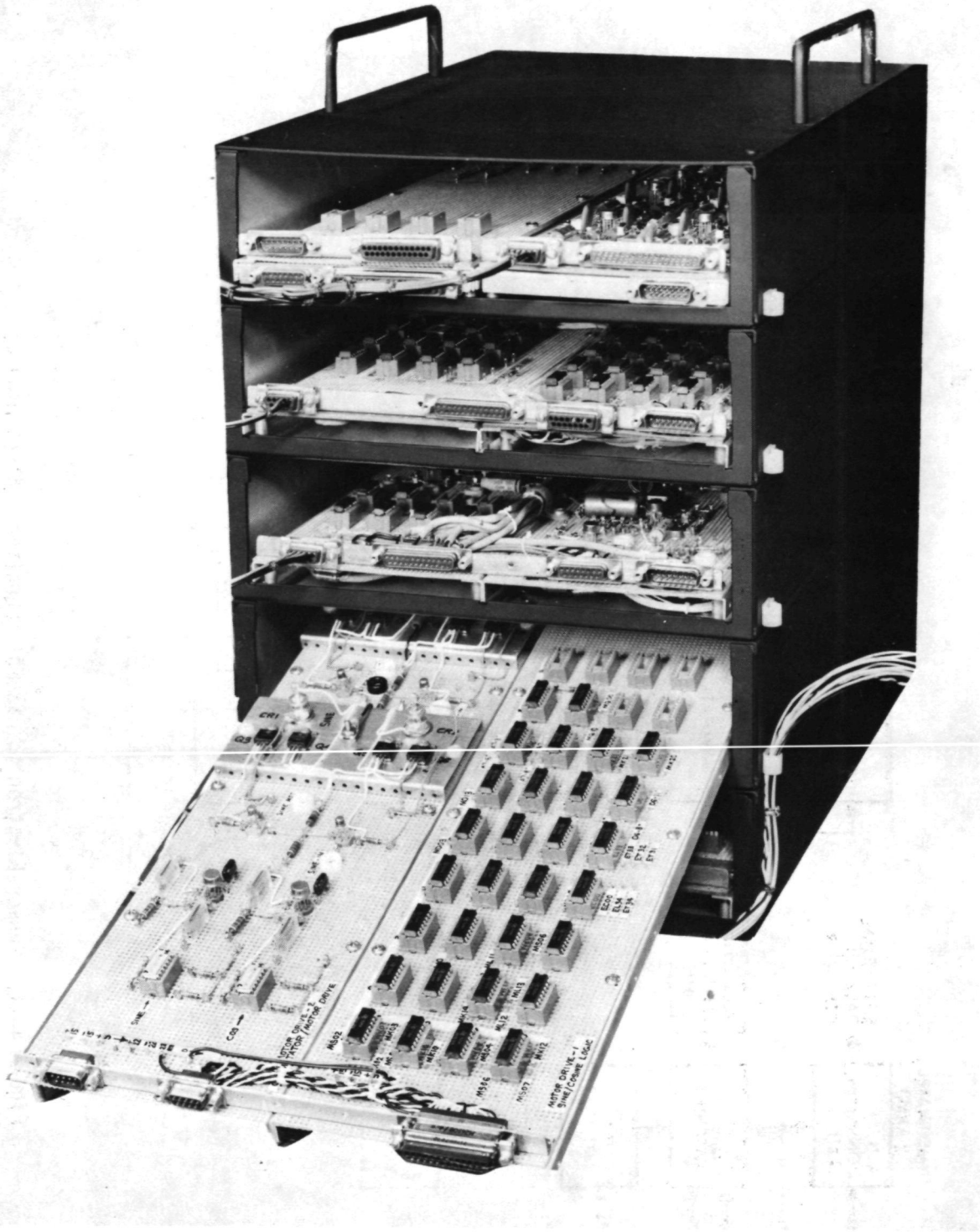

Figure 4-12. Sensor Electronics Assembly Breadboard

4.2.1 Inductosyn Electronics

An Inductosyn is analogous to a resolver. It has a primary, the rotor, which is sinusoidally excited at some frequency, 10.3 kHz in this case. It has two secondary (stator) output signals of the same frequency, whose amplitudes are trigonometrically amplitude-related to the device's mechanical angle:

$$V_s = kV_e \sin n\theta \sin \omega_e t$$

$$V_c = kV_e \cos n\theta \sin \omega_e t$$

where θ is the mechanical angle, V_e is the rotor excitation amplitude, and ω_e is its frequency. The transformation ratio, k, is extremely small for an Inductosyn, such that the output signal is only a few millivolts. Each Inductosyn has a single-speed and a 256 speed set of windings. The speed ratio, n, is unity for the single-speed section and 256 for the multi-speed section. Thus, the single-speed outputs advance one electrical revolution for each mechanical revolution, while the multi-speed signals advance 256 electrical revolutions for the same mechanical rotation. By processing both pairs of signals an extremely high resolution can be achieved.

The functional block diagram of the Inductosyn Electronics is shown in Figure 4-13. The Excitation Section generates a high-frequency digital clock signal from a crystal oscillator at a frequency f_c = 2.820 mKz. It also generates the Inductosyn excitation signal, of frequency f_e, which is precisely locked to f_c in the ratio:

$$f_e = \frac{15}{4096} f_c \approx 10.328 \text{ kHz}$$

The Excitation Section also produces a reference signal, which is a phase shifted logic square-wave image of the excitation signal, for use by the Encoder. Its relative phase and purpose are described below.

Because of the low amplitude, the Inductosyn signals are amplified by special preamplifiers located on the gimbal, and the resultant signals transmitted to the SEA for further processing. Within the SEA, the signals are converted from amplitude to phase format. Each pair, as described above is converted to a phase pair:

$$V_A = V \sin (\omega_e t + n\theta)$$

$$V_B = V \sin (\omega_e t - n\theta)$$

Thus, gimbal angle information now resides in the relative phase of the signals, in "double-angle" form, i.e., the relative phase between V_A and V_B changes twice as fast

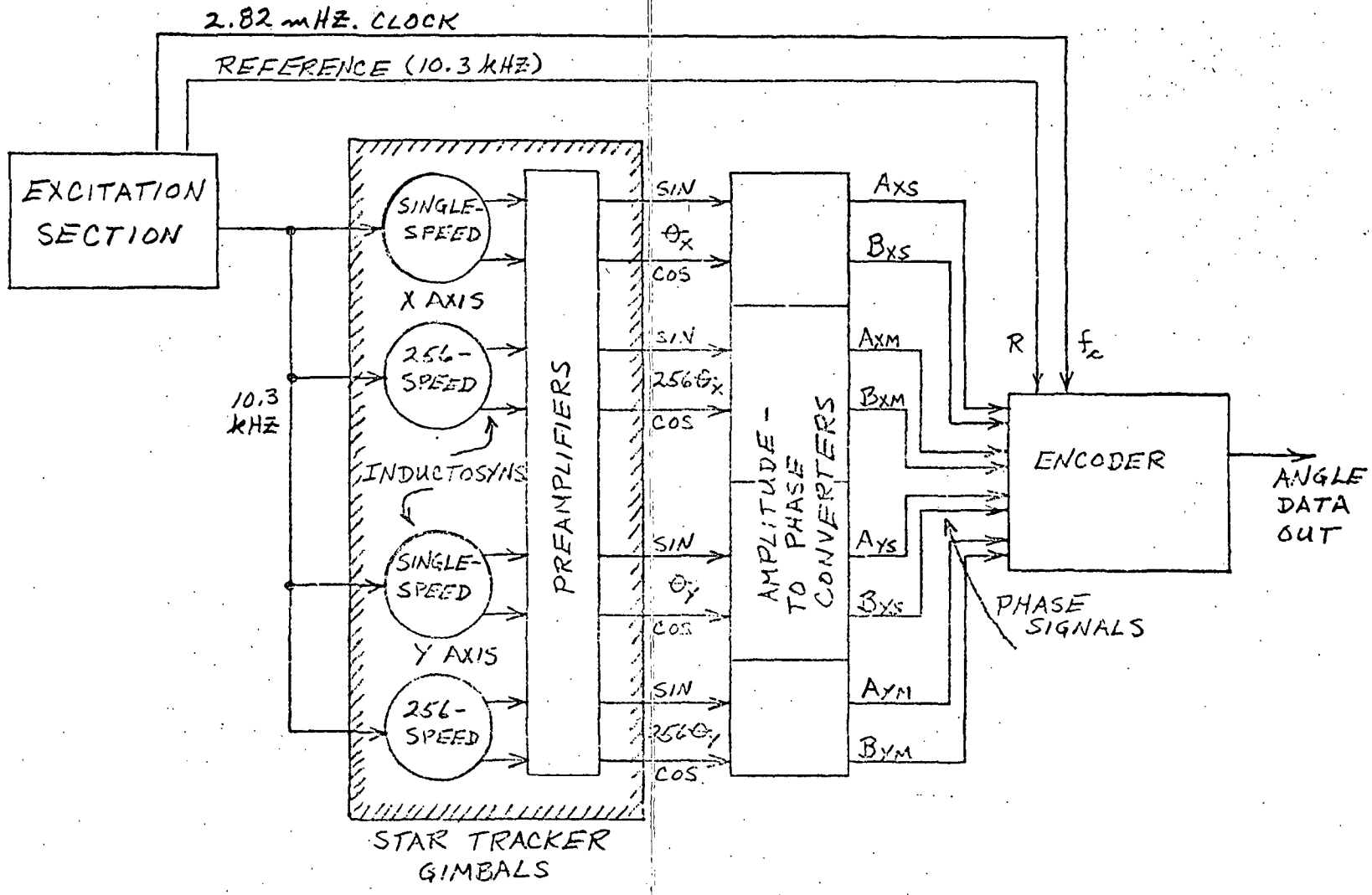

Figure 4-13. Inductosyn Readout Electronics Functional Block Diagram

as $n\theta$. These signals are then converted to standard logic signals, A and B, for use by the Encoder logic. The amplitude-to-phase converters are specially designed to preserve the inherent Inductosyn accuracy. A computer analysis has shown a worst-case error of ± 0.03 degree electrical for the converter itself, excluding preamplifier gain variations and zero-crossing detector propagation delay variations.

The Encoder section is used to digitally measure the relative phases of the A and B signals from the amplitude-to-phase converters, and thus, to develop a digital quantity representing the gimbal angles. The circuitry is moderately complex with a good deal of this complexity being contributed by the following factors:

- A single Encoder is time-shared among 4 channels - two axes, single-speed and 256-speed per axis.

- Phase measurement is made over 15 excitation cycles for high resolution, while preserving moderate logic speeds, and thus, power.

- Phase measurement is made in such a way as to be independent of symmetric phase distortions caused by DC offset drifts in the amplitude-to-phase converters.

- Fine-to-coarse data overlap ambiguities are automatically resolved in the Encoder.

- Data ambiguity, when the phase signals are migrating through zero relative phase, cannot be tolerated. (This is a hazard unique to multiple-cycle encoding.)

- Resolution is required better than one arc-second mechanical.

In a phase-encoding system, a resolution limitation is created if encoding is to occur over a single carrier cycle, since the resolution ratio is the ratio of the carrier to the clock frequencies. To maintain reasonable Inductosyn signal amplitudes with reasonable excitation power, 10 kHz represents a practical lower limit on carrier frequency because of the nature of the Inductosyn. Thus, the single-cycle resolution limit for 3 mHz clock is only about 1:300, or about 8 bits. A 256-speed Inductosyn gives a "magnification" of another 8 bits. One more bit is gained by the double-angle approach, i.e., for each $\Delta\theta$ increment of shaft rotation, the A and B signals undergo a relative phase change of $2n(\Delta\theta)$. The total single-cycle equivalent resolution is then 17 bits, or about 10 arc-seconds.

With a single-cycle scheme the sampling bandwidth is approximately the carrier frequency, 10 kHz in this case. For applications where such high bandwidth is not required, multiple-cycle encoding is a means of trading sampling bandwidth directly for resolution while maintaining a moderate clock rate. For valid resolution, however, the clock cannot be integrally related to the carrier frequency. If such were the case, each clock pulse, say the Nth from the beginning of a carrier cycle, would occur at the same instant within every carrier cycle. Thus, as a "phase mark", which is starting or stopping an encoding counter, is moved in phase within the carrier, it adds or drops discretely as many pulses from the net count as the number of cycles over which counting occurs. Hence, nothing is gained in resolution, unless one wishes to depend on mere system noise to dither the phase mark and/or the clock.

Resolution is validly increased by having a non-integral carrier to clock relationship. In the present case, each carrier cycle contains exactly 273 1/15 clock cycles, and 15 carrier cycles is the smallest number to contain an integral number of clock cycles - 4096. Because of a 1/15 cycle mismatch, there is a general precession of the clock phase within the carrier cycle framework, such that no two clock pulses occur at exactly the same carrier phase over a block of 15 carrier cycles. As the "phase mark" moves within the carrier cycle, it adds or drops but one pulse at a time from the net 15 cycle count. This provides an additional resolution of 2^4, yielding resolution accuracy of better than 1 arc-second.

4.2.1.1 Excitation Section Design

The Excitation Section generates a high-frequency clock signal to be used in the Inductosyn encoding and a relatively low-frequency sinusoidal signal at a suitable power level to excite the Inductosyn rotors. The excitation signal is designed to have a specific frequency relationship to the clock signal, since the encoding scheme uses multiple cycle encoding. The clock and excitation frequencies are related as follows:

$$\frac{f_c}{N_q} = \frac{f_e}{n_c}$$

where f_c is the clock frequency, f_e is the excitation frequency, N_q is the quantization number, and n_c is the number of cycles of excitation over which encoding is to take place. N_q and n_c are relatively prime, hence the least number of f_e cycles to contain an exactly integer number of f_c cycles is N_q, and the number of contained f_c cycles in n_c.

The encoder is 2-θ, or double angle, i.e., every $\Delta\theta$ increment is shaft angle gives $2\Delta\theta$ increment in phase-shift. As a result, the (256-speed Inductosyn) encoder

really provides data that is 512-speed = 2^9. Then if $N_q = 4096 = 2^{12}$, a shaft circle is divided into $2^9 \times 2^{12} = 2^{21}$ parts. The resolution is then 0.000172 degree which is equivalent to 0.618 arc-second.

The excitation frequency f_e is chosen at about 10 kHz for 3 reasons:

- It is the manufacturer's "standard" reference frequency. All Inductosyn parameters which are frequency-dependent are quoted at this frequency.
- The Inductosyn transformation ratio is extremely low - about 10^{-3}, and falls as 1/f. Hence f_e must be kept relatively high in order to have a reasonable output voltage.
- Accuracy is critically dependent on identical amplification of the sine and cosine channels. f_e must be kept reasonably low to have good control of gain precision. 10 kHz is a reasonable compromise between this requirement and that immediately above.

More specifically, f_e is chosen closer to 10.5 kHz because there exists a standard telemetry tone filter with that as its center frequency. This is used to filter the digitally generated f_e before power amplification.

For n_c, a value of 15 is chosen. It is relatively prime to 4096. Then encoding an Inductosyn requires 15 cycles of 10.5 kHz, $\approx$ 1.5 milliseconds, or an encoding bandwidth of about 670 Hz. The design values are:

$$f_c = 2.82 \text{ mHz}$$

$$N_q = 4096$$

$$n_c = 15$$

$$f_e = \frac{n_c}{N_q} f_c = 10.327 \text{ kHz}$$

Note that each cycle of f_e contains exactly $4096 \div 15 = 273\frac{1}{15}$ clock cycles, i.e., one integer cycle being made up over 15 excitation cycles.

Figure 4-14 is a block diagram of the Excitation section. The crystal oscillator operates at 2.82 mHz. A power buffer inverts the signal and provides it to the encoders. A frequency divider counts down to 1.377 kHz - modulo 2048 = 2". A phaselock loop is used to multiply 1.377 kHz by 225, yielding a VCO frequency of 309.81 kHz.

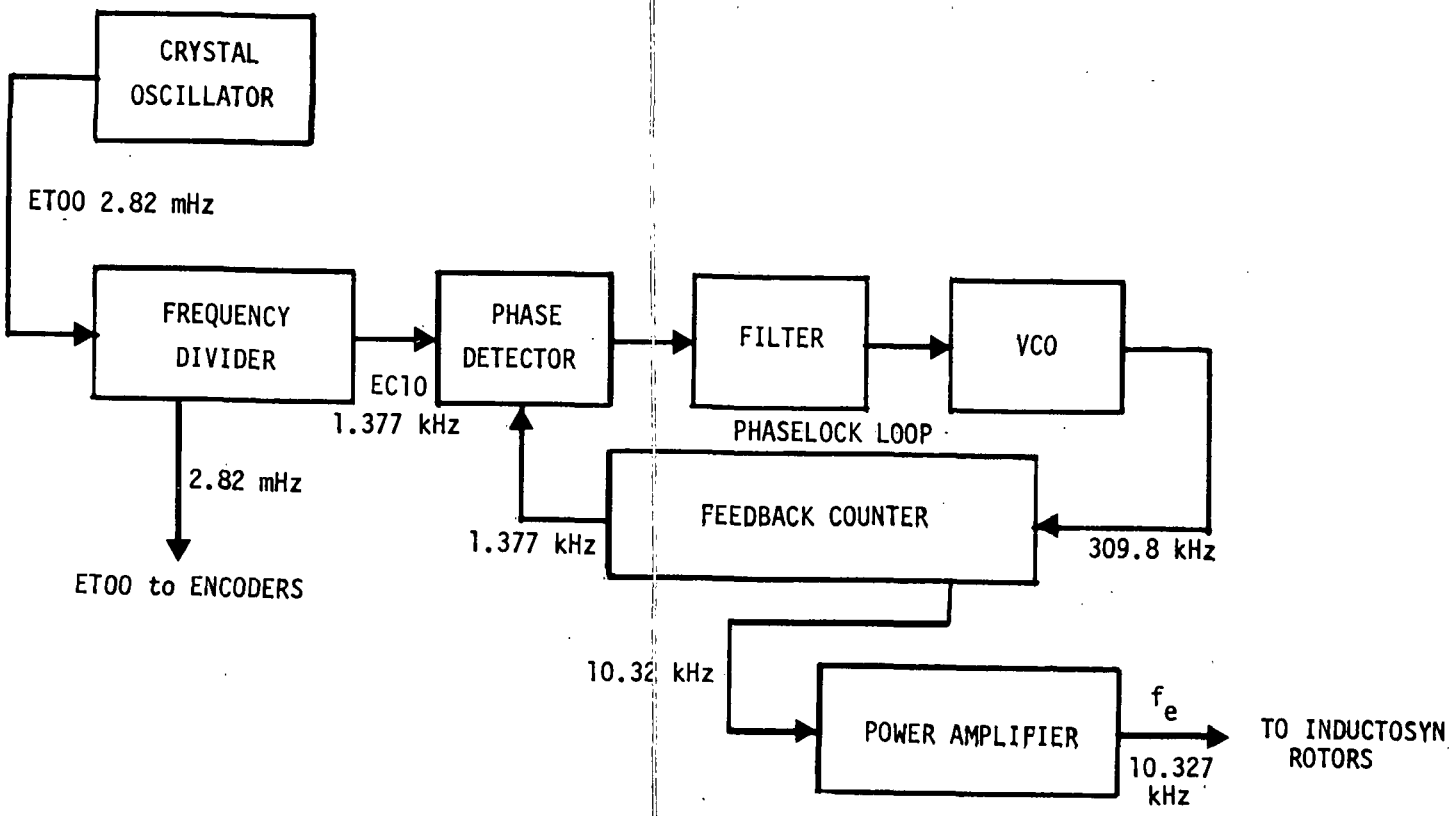

FIGURE 4-14. BLOCK DIAGRAM EXCITATION SECTION

The moduli of the phaselock loop feedback counter is arranged as 15 x 15. At the intermediate level comes 20.65 kHz. Dividing this by two gives f_e = 10.327 kHz. The extra factor of 15 enables f_e to be synthesized as a closer sine approximation to reduce 3rd and 5th harmonics.

4.2.1.2 Preamplifier Design

The preamps are located on-gimbal to amplify the Inductosyn sine and cosine signals with a gain of ∿ 100 for transmission to the SEA. Gain identity for a sine/cosine pair is critical to accuracy. Figure 4-15 shows the general circuit configuration used. It features high input impedance, (∿ 1 meg) hence variations in Inductosyn resistance do not affect gain.

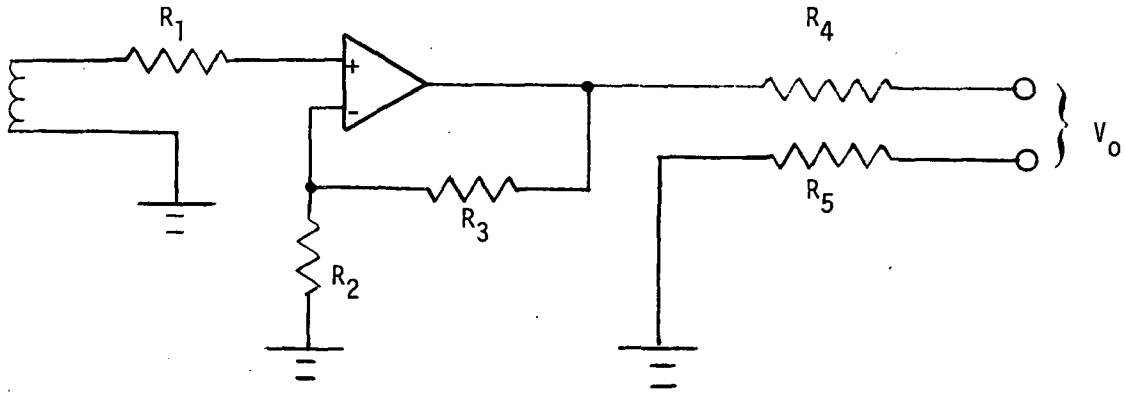

Figure 4-15

Gain match between channels is analyzed as follows:

$$G = \frac{A}{1 + \frac{A}{K}} = \frac{AK}{A + K}$$

$$\Delta G = \frac{\partial G}{\partial A} \Delta A + \frac{\partial G}{\partial K} \Delta K$$

$$\frac{\Delta G}{G} = \frac{1}{G} \left[\frac{\partial G}{\partial A} \Delta A + \frac{\partial G}{\partial K} \Delta K \right]$$

$$\frac{\partial G}{\partial A} = \frac{(A + K)K - AK}{(A + K)^2} = \frac{K^2}{(A + K)^2}$$

$$\frac{\partial G}{\partial K} = \frac{(A + K)A - AK}{(A + K)^2} = \frac{A^2}{(A + K)^2}$$

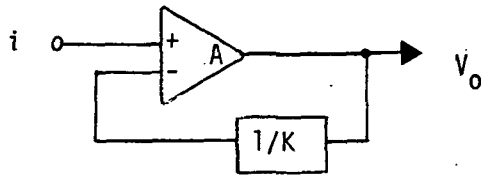

$$\frac{\Delta G}{G} = \frac{A + K}{AK} \frac{K^2}{(A + K)^2} A \frac{\Delta A}{A} + \frac{A + K}{AK} \frac{A^2}{(A + K)^2} K \frac{\Delta K}{K}$$

$$\frac{\Delta G}{G} = \frac{K}{A + K} \frac{\Delta A}{A} + \frac{A}{A + K} \frac{\Delta K}{K}$$

For $K = 100$, $A = 3 \times 10^4$: $A >> K$. Then

$$\frac{\Delta G}{G} = \frac{K}{A} \frac{\Delta A}{A} + \frac{\Delta K}{K} = 3.3 \times 10^{-3} \frac{\Delta A}{A} + \frac{\Delta K}{K}$$

For an amplifier pair-gain match of 5% of one another and if the feedback network resistors are within 0.01%, then

$$\frac{\Delta G}{G} = 3.3 \times 10^{-3} \times 5 \times 10^{-2} \pm 10^{-4}$$

$$= 1.65 \times 10^{-4} + 2 \times 10^{-4} \text{ (abs)} = 3.65 \times 10^{-4}$$

as the absolute gain difference.

4.2.1.3 Amplitude-to-Phase Converter Design

The A-θ converter uses a novel means of combining a single capacitor within a dual operational amplifier configuration, forming a resolver amplitude-to-phase converter for use in Kronacher style resolver encoding. The single capacitor serves a dual phase-shifting role, reducing the capacitance sensitivity by a factor of about one hundred over the conventional passive Kronacher approach.

Figure 4-16 shows the general circuit approach which requires only the uninverted forms of the Inductosyn signals. The transfer functions are:

$$\left.\begin{aligned} V_1 &= -A_1 \frac{s\tau_1 - 1}{s\tau + 1} V_S - K_1 V_c \\ V_2 &= -A_2 \frac{-s\tau_2 + 1}{s\tau + 1} V_S - K_2 V_c \end{aligned}\right\}$$

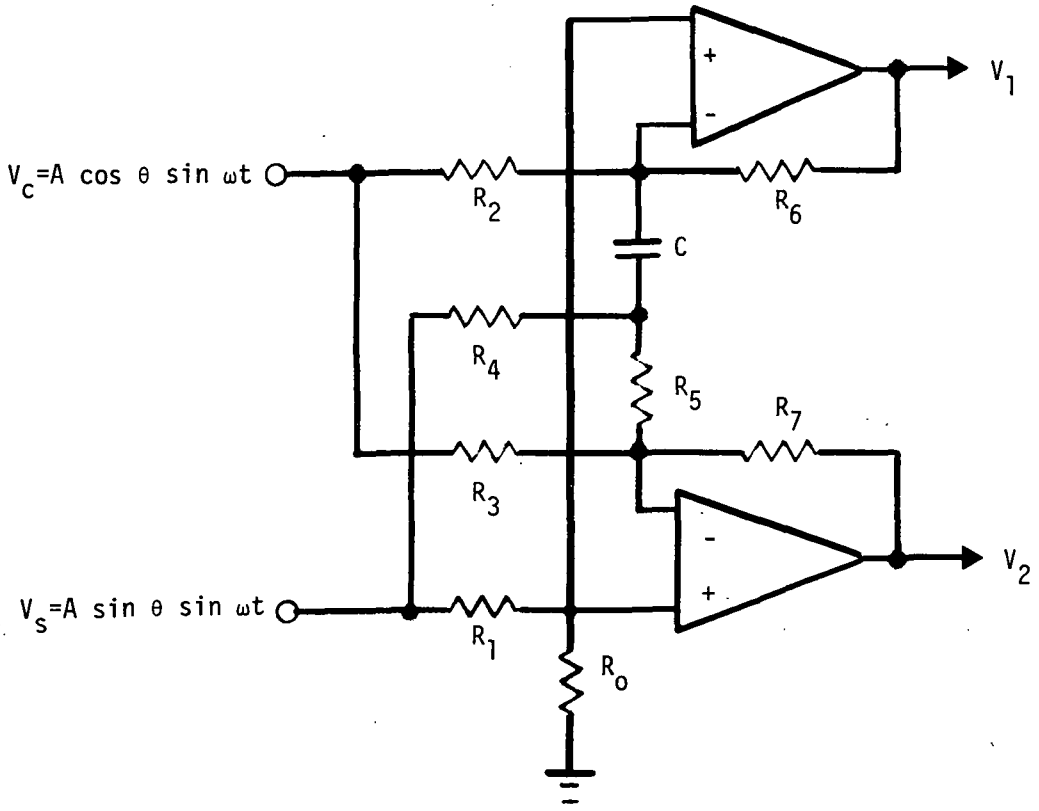

Figure 4-16 Amplitude-to-Phase Converter Configuration

where:

$$A_1 = \frac{R_o}{R_o + R_1} \left(1 + \frac{R_6}{R_2}\right)$$

$$K_1 = \frac{R_6}{R_2}$$

$$\tau_1 = \frac{CR_5}{R_4 + R_5} \left[\frac{R_1}{R_o} \frac{R_2R_6}{R_2 + R_6} - R_4\right]$$

$$A_2 = \frac{R_1}{R_o + R_1} \frac{R_7}{R_4 + R_5} - \frac{R_o}{R_o + R_1} \left(1 + \frac{R_7}{R_3}\right)$$

$$K_2 = \frac{R_7}{R_3}$$

$$\tau_2 = \frac{CR_4R_5}{\frac{R_1}{R_o} \frac{R_3R_7}{R_3 + R_7} - (R_4 + R_5)}$$

$$= \frac{1}{A_2} \frac{R_o}{R_o + R_1} \left(1 + \frac{R_7}{R_3}\right) \tau$$

$$\tau = \frac{CR_4 R_5}{R_4 + R_5}$$

The design criteria are as follows:

For a scalar gain constant K, choose C, R_4, and R_5 such that

$$\tau = \frac{CR_4R_5}{R_4 + R_5} = \frac{1}{\omega_e}$$

where ω_e is the radian frequency of the Inductosyn excitation. Then

$$R_o = K R_1$$

$$R_2 = 2(1 + K)R_4$$

$$R_6 = K R_2$$

$$R_3 = 2(1 + K) (R_4 + R_5)$$

$$R_7 = K R_3$$

Despite the apparent symmetry of the circuit, it is not possible for $R_2 = R_3$, $R_6 = R_7$, since the equations imply:

$$\frac{R_3}{R_2} = 1 + \frac{R_5}{R_4}$$

and also that if R_5 approaches zero, the C must approach infinite values in order to maintain finite time constants.

The circuit is seen to be naturally inverting. The phase angle of $-V_1$ is:

$$\phi_1 = \text{Tan}^{-1} \frac{A_1 \omega_e(\tau + \tau_1) + V_s}{-A_1(1 - \omega_e^2 \tau\tau_1) V_s + K_1(1 + \omega_e^2 \tau^2) V_c}$$

and that of $-V_2$ is:

$$\phi_2 = \text{Tan}^{-1} \frac{-A_2 \omega_e(\tau + \tau_2) V_s}{A_2(1 - \omega_e^2 \tau\tau_2) V_S + K_2(1 + \omega_e^2 \tau^2) V_c}$$

Note that for $A_1 = K_1$, $A_2 = K_2$, $\tau = \tau_1 = \tau_2 = 1/\omega_e$:

$$\phi_1 = \text{Tan}^{-1} \frac{2 \text{ Sin } \theta}{0 \text{ Sin } \theta + 2 \text{ Cos } \theta} = \theta$$

$$\phi_2 = \text{Tan}^{-1} \frac{-2 \text{ Sin } \theta}{0 \text{ Sin } \theta + 2 \text{ Cos} \theta} = \theta$$

For encoding purposes, the net phase angle is interpreted as

$$\phi = \frac{1}{2}(\phi_1 - \phi_2)$$

A computer error analysis shows that maximum phase errors can be held to ±0.025 degree (electrical), at least an order of magnitude better than passive phase shifters. The multi-speed Inductosyn reduces this error by a factor of 256 in encoding mechanical rotation.

4.2.1.4 Encoder Section Design

The Encoder Section block diagram is shown in Figure 4-17. Provision is made for 4 Inductosyn channel inputs, one single-speed and one 256-speed channel comprising a gimbal axis. A channel signal pair is the output from an amplitude-to-phase converter, which converts the raw Inductosyn signals into logic-level phase form. One channel signal pair is selected in turn by the Channel Select and Sync for encoding. This block also synchronizes the selected signals to the 2.83 mHz main clock received from the Excitation Section.

Also received from the Excitation Section is a reference signal R at the same frequency, 10.3 kHz, as the Inductosyn carrier. This is used as a basis to generate the control timing for the Encoder. It triggers the Reference Synchronizer to generate 3 short sequential R pulses once every carrier cycle. A complete channel encoding period takes 16 carrier cycles, 15 for actual phase counting and one as a time buffer for control "housekeeping". This time framework is generated by the Cycle Counter. At housekeeping time, which is at the beginning of an encoding cycle, the Cycle Counter enables the R pulses, which are output as R_m.

The Frame Counter counts modulo 4, advanced by one of the R_m pulses from the Cycle Counter. It generates in sequence the channel addresses.

One of the housekeeping tasks is to sample the synchronized phase signals A, B from the Channel Select, and to store the result in the Quadrant Register. This value indicates the electrical quadrant of the A, B signals and is used to control several functions for the duration of the channel period.

The heart of the Encoder is the Phase Counter. By counting between various logic "mark" points of the A and B signals at the fixed rate of the 2.82 mHz clock, their electrical phase is determined, effectively measuring the Inductosyn angle. Actually, the Phase Counter in effect operates at 3 different rates: 0, 1, and 2 times the clock rate, controlled by the sequence of the relative phases of the A and B signals, as sensed by the Sense Counter. This strategem mechanizes a "full-wave" phase determination, immune from the waveform symmetry disturbances in the A and B signals caused by DC offset drift effects in the A-ϕ Converters. The Phase Counter is 14 bits.

The Preset Gates are used to properly initialize the Phase Counter prior to the Phase Counting.

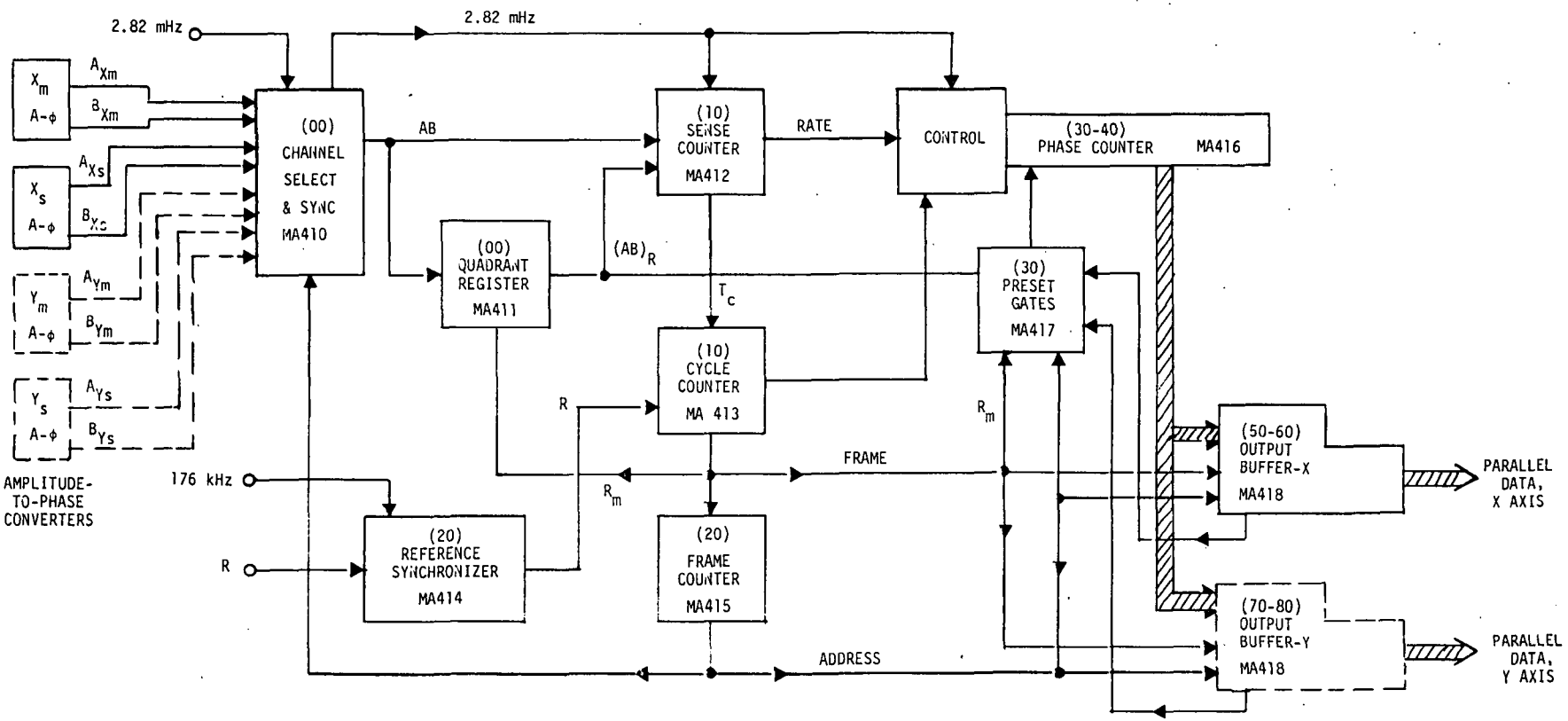

DOTTED LINES INDICATE ELEMENTS FOR SECOND AXIS. THE A-φ CONVERTERS ARE REFERENCE ONLY AND NOT PART OF THE ENCODER SECTION.

FIGURE 4-17. ENCODER SECTION

The Output Buffers are channel-dedicated. They receive and store the phase data from the Phase Counter for external access, and for use by the Motor Electronics section in commutating the gimbal motors. Each Buffer contains data complete to an axis, coarse and fine. The coarse data occupies 8 bits and the fine 14, for a total 22 bit datum.

The "housekeeping" pulses, R_{m0}, R_{m1}, R_{m2}, which are short compared with a carrier cycle, mark the beginning of an encoding cycle (16 carrier cycles). The first, R_{m0} causes the contents of the Phase Counter to be dumped into the proper Output Buffer, and proper segment thereof, according to the address of the channel just encoded. At the same time, this pulse advances the Frame Counter, causing a new channel address, which in turn, selects a new pair of phase signals. The second pulse, R_{m1}, zeros the Phase Counter and samples the newly selected A and B into the Quadrant Register. The third pulse, R_{m2}, is used to set ONE's into specific bits of the Phase Counter, based on the indicated quadrant, and if it is a coarse channel being converted, based on the previously encoded result of the fine channel for that axis. This last feature automatically resolves the natural "range ambiguity" which occurs because of small misalignments between a fine and a coarse channel. R_{m2} also sets the cycle counter into a "ready" state, completing the housekeeping.

The Cycle Counter now waits for a particular phase combination of A and B to occur, indicated by T_c from the Sense Counter. This combination varies with indicated quadrant in such a way as to quarantee that T_c always occurs at least 1/2 of a carrier cycle after R_m. T_c triggers the Cycle Counter to begin the "frame" marking the beginning of actual encoding. Precisely 15 T_c cycles later, the frame ends, stopping any further Phase Counter action. The Cycle Counter then waits out the unused balance of the R-cycle. At the next R time, the R_m pulses are again enabled, initiating a new housekeeping sequence to encode the next channel.

4.2.2 Gimbal Control Electronics

4.2.2.1 Loop Compensation Design

The Motor Preamplifier provides controller frequency-compensation for the Star Tracker Gimbal servo. The frequency compensation is taken from the servo design of Section 3.3. This is shown, as modified, in Figure 4-18 and as translated into the electronic mechanization in Figure 4-19.

The major portions within this section are:

- D/A Converter to convert the digital slew error command from the processor
- the integral plus proportional path, including separate buffering of the Sensor signal for external use

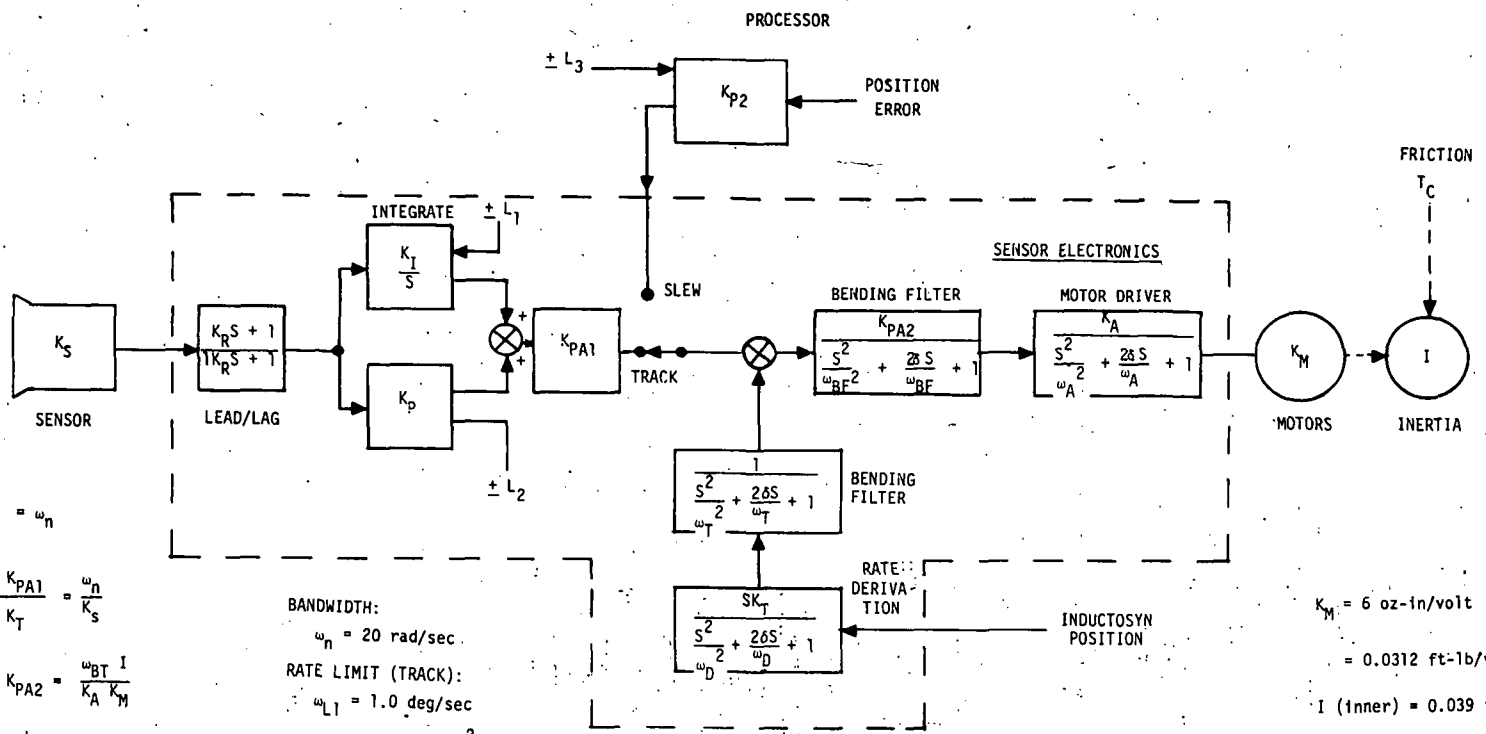

1. $\frac{K_I}{K_P} = \omega_n$

2. $\frac{K_P K_{PA1}}{K_T} = \frac{\omega_n}{K_S}$

3. $K_T K_{PA2} = \frac{\omega_{BT} I}{K_A K_M}$

4. $\frac{K_{PA1} L_2}{K_T} = \omega_{L1}$

5. $L_1 K_{PA1} K_{PA2} = \frac{1.1 T_c}{K_A K_M}$

6. $K_R = \frac{1}{\omega_{BT}}$

7. $K_{P2} = 0.1 \omega_{BT} K_T$

8. $L_3 = \frac{T_c}{K_{PA2} K_A K_M} + \omega_{L2} K_T$

BANDWIDTH:

ω_n = 20 rad/sec

RATE LIMIT (TRACK):

ω_{L1} = 1.0 deg/sec

= 1.74×10^{-2} rad/sec

RATE LIMIT (SLEW):

$\omega_{L2} = 7.0 \times 10^{-2}$ rad/sec

= 4.0 deg/sec

RATE BANDWIDTH

ω_{BT} = 60 rad/sec

ω_T = 400 rad/sec = 63.7 Hz

ω_{BF} = 400 rad/sec = 63.7 Hz

K_M = 6 oz-in/volt

= 0.0312 ft-lb/volt

I (inner) = 0.039 ft-lb-sec^2

= 7.5 oz-in-sec^2

T_c = 0.2 ft-lb

= 38.4 oz-in

$K_S = 1.375 \times 10^3$ volt/rad

= 6.667 mv/arc sec

FIGURE 4-18. SEA SERVO PRESCRIPTION

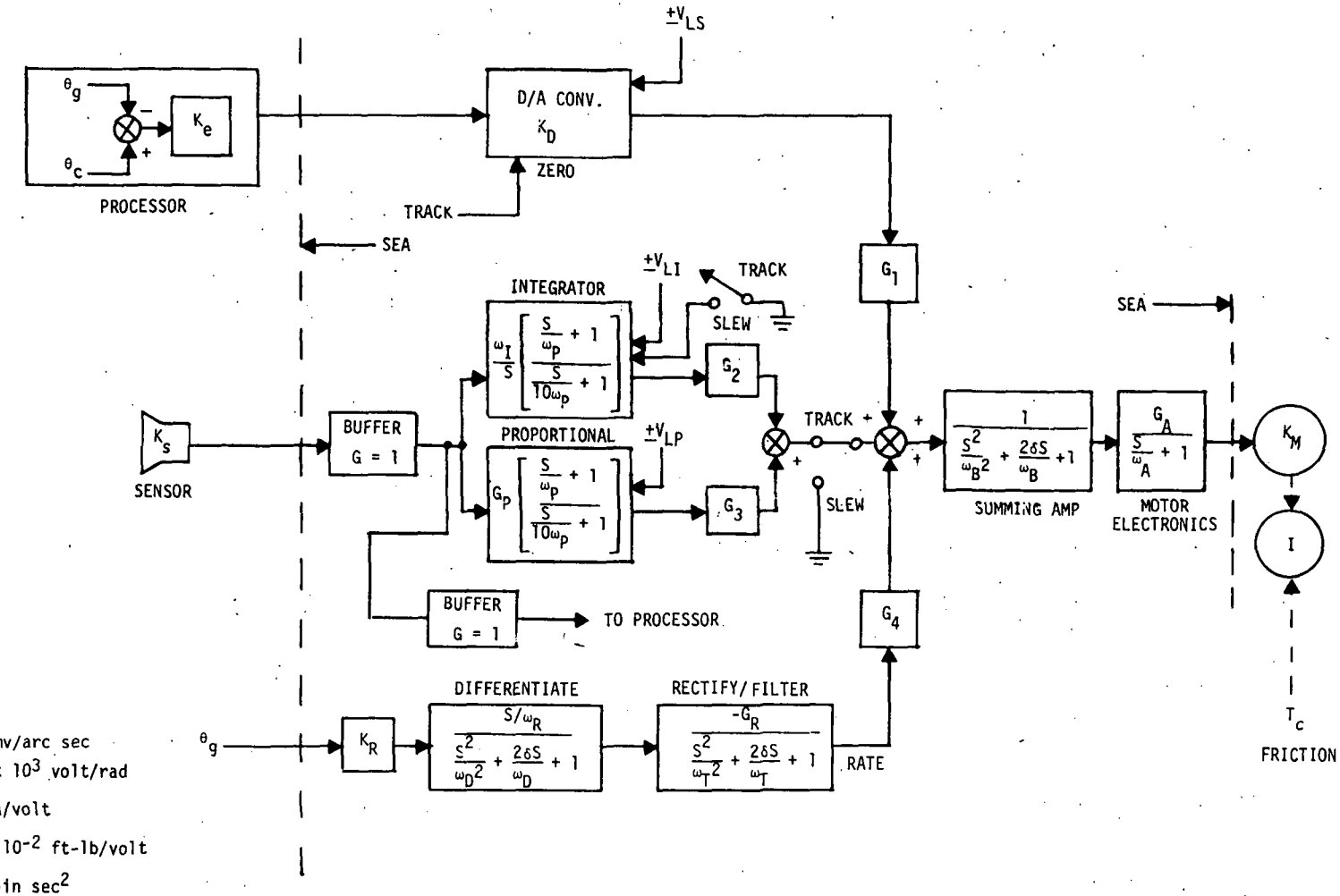

K_S = 6.667 mv/arc sec
= 1.375×10^3 volt/rad

K_M = 6 oz-in/volt
= 3.12×10^{-2} ft-lb/volt

I (inner) = 7.5 oz-in sec^2
= 3.9×10^{-2} ft-lb-sec^2

I (outer) = 18.8 oz-in sec^2
= 9.8×10^{-2} ft-lb-sec^2

T_c (max) = 38.4 oz-in
= 0.2 ft-lb

K_R = 1.63×10^3 volt/rad

ω_R = 2.23×10^2 rad/sec

G_R = 5.0 volt/volt

ω_D = 3.14×10^3 rad/sec

ω_T = 400 rad/sec

FIGURE 4-19. SEA SERVO MECHANIZATION

- the rate derivation
- the summing amp

The motor power amplification/drive section is discussed separately (Section 4.2.2.3).

4.2.2.2 Rate Derivation Section Design

The lead and lag phase signals from the multi-speed Amplitude-to-phase Converter are converted to an analog voltage rate signal for use in damping the gimbal servo. The signals from the A-ϕ Converter are a pair of logic square waves at 10.327 kHz, whose relative phase varies as a function of gimbal angle. For a positive angular rotation, the lead signal, A advances in phase (earlier), while the lag signal, B, retards (later). Because the multi-speed signals are used, the electrical phase ϕ of A varies 256 times faster than the gimbal angle θ. It is noted that an exclusive-OR between A and B can be considered as a duty-cycle modulated signal proportional to phase, and therefore to position. On a normalized basis of zero to unity, the DC component varies from zero at $\phi_A = 0$ to unity at $\phi_A = 90°$. When $\phi_A = 90$, $\phi_B = -90°$, so that the relative phase is 180°, and thus the DC component is 0.

If the gimbal has some constant rate, the DC component will be a triangular waveform whose slopes will be proportional to rate. If this is differentiated, ignoring the high-frequency components, the result will be a square wave of amplitude and period proportional to rate. The transitions of the square wave correspond to the passage of ϕ_A through the discontinuities at the cardinal angles. Since both positive and negative rate indications are desired, without ambiguity, it is necessary to synchronously rectify the differentiated signal. The sign signal can be logically derived from the A and B signals.

A conceptual block diagram is shown in Figure 4-20. The A and B signals are combined by an Exclusive-OR and the result used to drive an analog switch chopper. A constant voltage V_R is used to standardize the amplitude of the resultant rectangular wave, whose duty-cycle is proportional to the relative phase of A and B.

This is applied to a differentiator of the form

$$D(s) = \frac{s\,\tau_1}{s^2\tau_2^2 + s\sqrt{2}\,\tau_2 + 1}$$

where τ_2 is chosen to correspond to a frequency beyond the range of relevance to the servo.

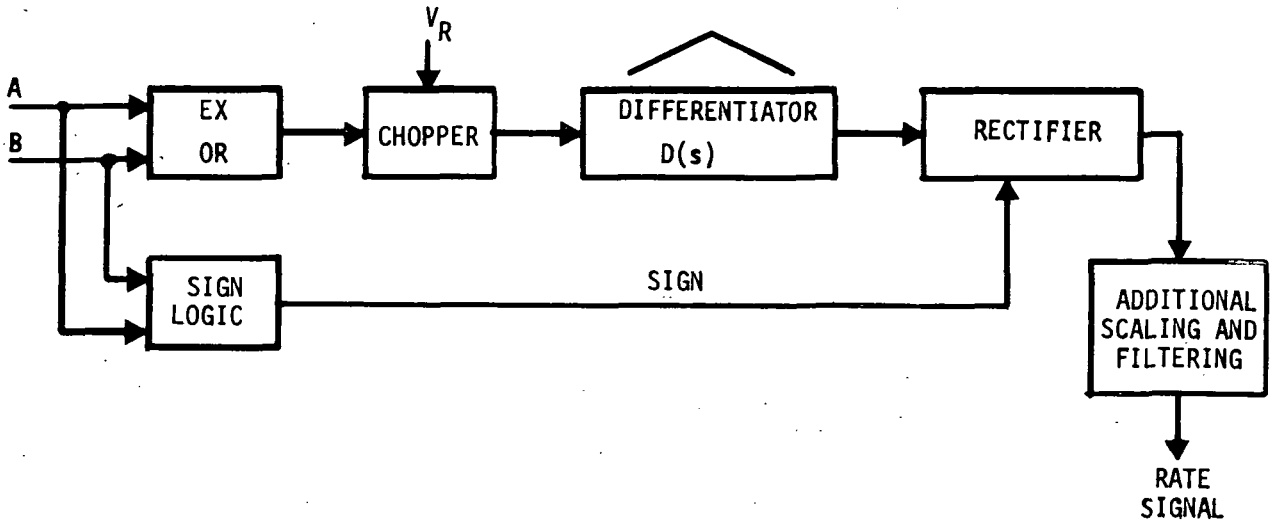

Figure 4-20

The sign signal is logically derived from the phase of the A and B signals and causes the rectifier to apply a positive or negative sense to the differentiator output. An additional gain stage follows the rectifier to act as a buffer, and to apply additional amplification and filtering.

4.2.2.3 Motor Electronics Section Design

The motor electronics includes functions of gimbal motor commutation and power driving. A block diagram is shown in Figure 4-21. The power amplifier is a class B configuration to reduce standby power. Because of local feedback, the crossover deadband, inherent to class B power stages, is insignificant compared with that due to the gimbal friction.

A relatively novel type of D/A conversion technique was applied in the Commutator to effect Sine/Cosine modulation of the respective 12-speed motor channels. This technique utilizes a single-line "difunction" logic waveform, applied to a single analog switch. The waveform is a sort of duty-cycle modulation at a high frequency, proportional to the sine or cosine of the gimbal angle, as derived from the Inductosyn. In effect, this accomplishes a multiplication of the analog servo voltage V_i by the sine/cosine:

$$V_s = V_i \sin 12\theta$$

$$V_c = V_i \cos 12\theta$$

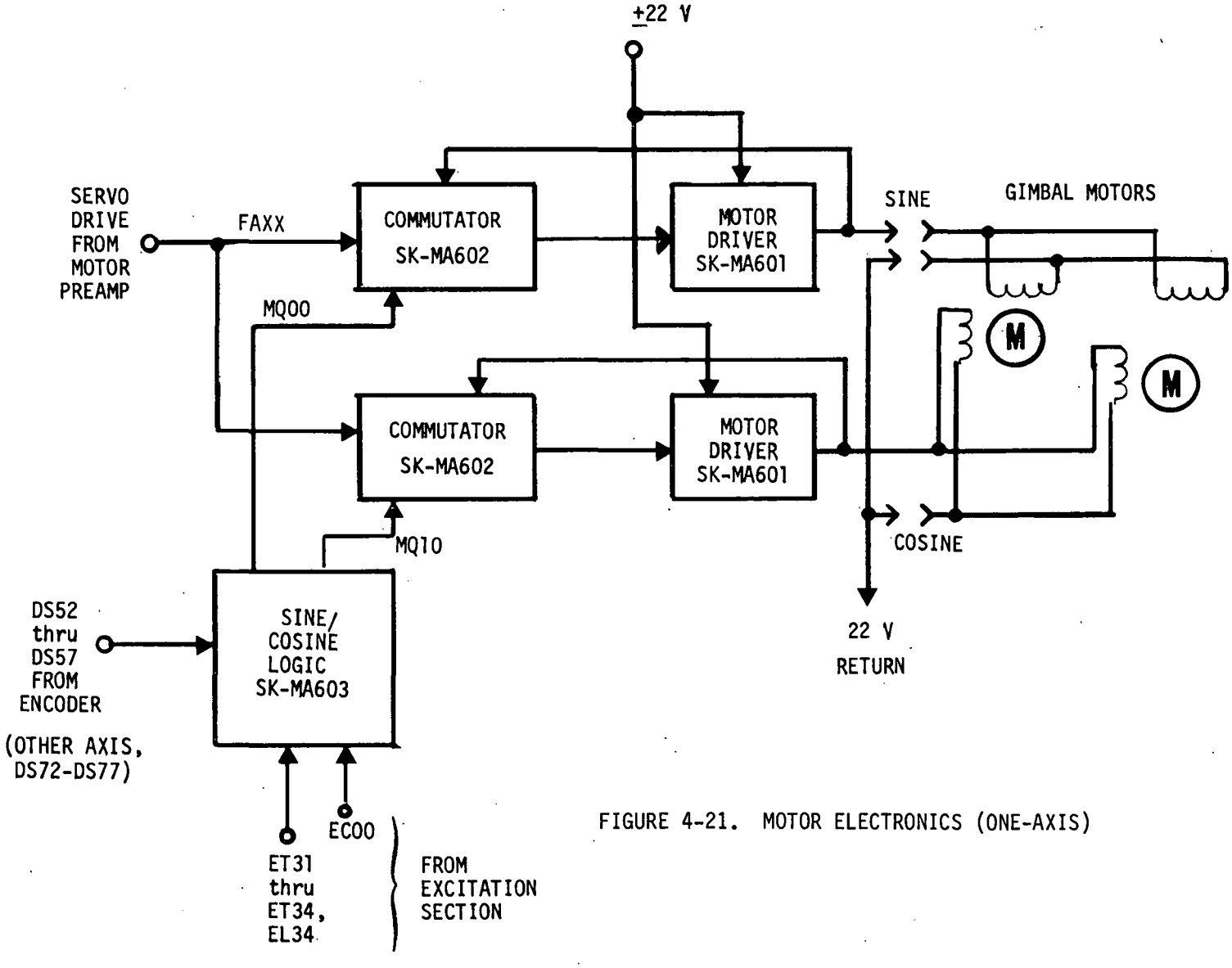

FIGURE 4-21. MOTOR ELECTRONICS (ONE-AXIS)

The Sine/Cosine logic receives angle position data DS52 through DS57 from the Encoder, and derives a "4 $\frac{1}{2}$" bit approximation for the Sine and Cosine of 12θ therefrom. It also digitally modulates this data with a set of binary pulse streams from the Excitations, resulting in a pair of difunction representations.

These switching functions MQ00, MQ10, are used to modulate FAXX, the servo control voltage, resulting in an effective multiplying D/A conversion. This is done in the commutator, which also filters out the modulation frequencies. The result drives the Motor Drivers, a pair of linear class B power amplifiers.

5.0 SOFTWARE DESIGN

The PADS software is used to process gyro data to derive rate and attitude, and to process star tracker measurements in a Kalman filter to develop periodic estimates for updating attitude and gyro drift. The algorithms used for PADS have been utilized directly from those developed for PPCS [1].

The PADS software is organized in terms of individual software modules defined to handle specific functional requirements. The actual linking of these functions is under control of the Executive software. Functional flow of the software execution is shown in Figure 5-1. The succeeding sections summarize the software program design and detail the modules to the level of equation definition and flow. In addition, preliminary generic coding of the software was conducted to determine computational requirements. The overall computer requirements for the PADS software are summarized in Table 5-1. A total computer memory of 8K and average short instruction speed of 10 μsecond provides ample margin for implementation.

5.1 Gyro Reference Module

5.1.1 Functional Requirements

This software module provides the functions associated with maintaining an inertial attitude reference in conjunction with a configuration of strapdown rate integrating gyros. The gyro outputs are processed to compensate for known misalignments, scale factor uncertainties and bias. Rate and attitude of a known reference frame, nominally fixed with respect to the gyro configuration, is derived with respect to a known inertial reference frame, e.g., Earth-Centered-Inertial (ECI). Updates to the attitude and gyro compensation, periodically available from an external source, will be incorporated as available.

Computational Functions

The computational functions are summarized as follows:

- Process gyro output data and provide transformation to defined orthogonal PADS reference frame.
- Compensate for gyro error sources (e.g., drift bias, input axis alignment, and scale factor).
- Maintain precise angular rate reference.
- Maintain precise short-term inertial attitude reference.

Table 5-1. PADS Software Requirements Summary

Storage (Memory, including Data Base)	Program	Scratch
Gyro Reference Module	510	146
Star Tracker Module	661	222
Filter/Update Module	1648	446
Subroutines	650	---
Total	3469	814

Execution	Execution	Iteration Rate	Equivalent Speed (Adds/sec)*
Gyro Reference Module			
Gyro Processing	535+36M	5/sec	4,115
Attitude Algorithm	1334A+117M+11D	5/sec	12,230
Direction Cosine Matrix	232A+30M	5/sec	2,360
Star Tracker Module			
Star Select/Processing	1950A+175M+35D	1/sec	3,910
Tracker Control	462A+64M+7D	5/sec	5,430
Star Measurement	305A+25M+9D	1/30 sec	22
Filter/Update			
State Transition Matrix	3294A+192M+3D	5/sec	24,390
Covariance Propagation	16163A+999M	1/30 sec	805
Measurement Matrix	881A+97M+2D	1/30 sec	56
Gain Matrix	3583A+216M	1/30 sec	177
Covariance Update	7068A+432M	1/30 sec	351
State Vector Update	457A+36M	1/30 sec	25
Total			53,871

*Assume M = 8A, D = 16A

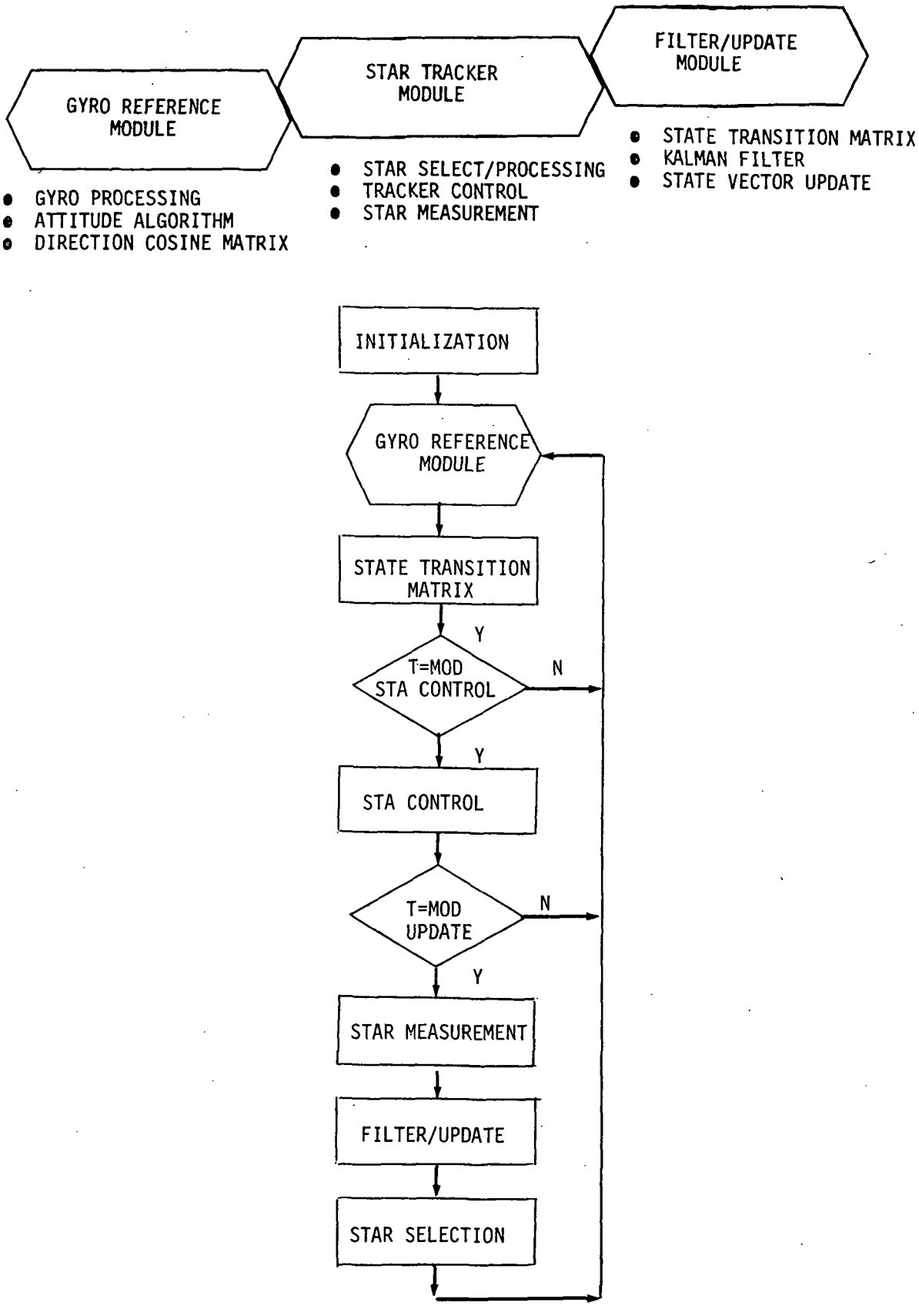

Figure 5-1. PADS Software Functional Flow

- Compute elements of direction cosine matrix relating reference frame attitude to ECI.

Operating Modes

There are two basic operating modes for operation of the gyro reference software. They are:

- Free. The gyro outputs are periodically processed to maintain current attitude and rate reference.

- Align. This mode is used for initializing and/or updating the attitude and/or gyro compensation from an external source.

Input/Output

- Input. The inputs which may be utilized by the gyro reference software are summarized.

  Gyro Data: Each gyro output is a digital word whose scaled value represents the incremental angular rotation measured about the gyro input axis.

  Mode Flag: A mode flag indicating when update information is available.

  Gyro Parameters: Input axis alignment, scale factor, and bias.

  Attitude Update: Attitude variables provided for update.

- Output. The outputs to be provided by the gyro reference software are summarized.

  Kinematic Parameters: The kinematic parameters are available for use in other software functions, e.g., Kalman filter state transition matrix.

  Rate: Angular rate components referenced to PADS axes.

  Direction Cosine Matrix: The direction cosine matrix relating PADS reference axes to ECI reference axes.

5.1.2 Functional Description

The software functional block diagram is shown in Figure 5-2. The output of each of the N_g gyros is scaled to yield the measured rate, and the resultant rate vector is transformed to a known fixed orthogonal reference frame. The "geometry

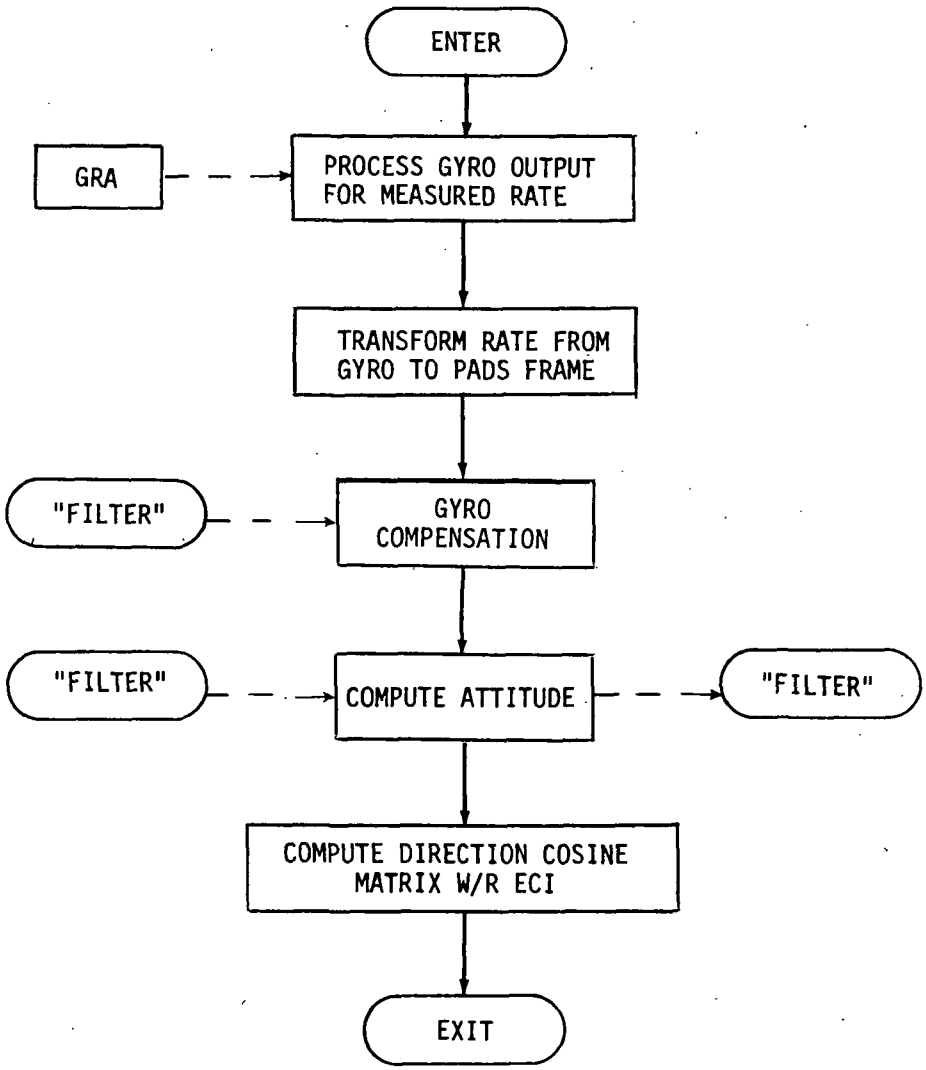

Figure 5-2. Gyro Reference Module Functional Block Diagram

matrix" used for the transformation incorporates terms which accout for "known" individual gyro input axis alignment and scale factor. The gyro bias compensation is added to complete the rate estimate. The equation for estimated rate takes the form

$$\hat{\omega} = \hat{G}\tilde{\omega} - \hat{b}$$

where

$\hat{\omega}$ = estimate of rate in PADS coordinate frame, 3 x 1

$\tilde{\omega}$ = measured rate along each of N_G gyro input axes, N_G x 1

$\hat{b}$ = gyro bias compensation, 3 x 1

$\hat{G}$ = "geometry matrix", 3 x N_G (determined through preflight measurement and/or flight calibration).

Euler Symmetric Parameters are employed as the kinematic variables for computation of vehicle attitude. This choice, as opposed to selection of direction cosines, was based upon the fact that a four, rather than nine, parameter system of equations is involved; and also, the periodic re-normalization that must be performed to combat computer roundoff error is much simpler. As is well known,

$$\dot{\bar{\rho}} = \frac{1}{2}\Omega\bar{\rho}$$

where

$$\rho = \begin{bmatrix} \xi \\ \eta \\ \zeta \\ \chi \end{bmatrix} \qquad \Omega = \begin{bmatrix} 0 & \omega_3 & -\omega_2 & \omega_1 \\ -\omega_3 & 0 & \omega_1 & \omega_2 \\ \omega_2 & -\omega_1 & 0 & \omega_3 \\ -\omega_1 & \omega_2 & -\omega_3 & 0 \end{bmatrix}$$

Selecting the integration period sufficiently small, Ω can be assumed constant over the integration interval, ΔT, and

$$\rho_{k+1} = \exp(\Omega_k \Delta T/2)\, \rho_k$$

where Ω_k represents the constant matrix assumed on the interval $[t_k, t_{k+1}]$. It is possible to obtain a simple closed form expression for exp $(\Omega_k \Delta T/2)$ which tends to inhibit the truncation error that would normally exist in the power series representation of the exponential. This is given by

$$\exp(\Omega\Delta T/2) = (\cos b\Delta T)I + \frac{\sin b\Delta T}{2b}\Omega$$

where

$$b = \frac{1}{2}\left(\sum_{i=1}^{3}\omega_i^2\right)^{1/2}$$

The kinematic variables are used to derive the direction cosine matrix which relates the PADS to ECI. The matrix A has the form

$$A = \begin{bmatrix} \xi^2 - \eta^2 - \zeta^2 + \chi^2 & 2(\xi\eta + \zeta\chi) & 2(\xi\zeta - \eta\chi) \\ 2(\xi\eta - \zeta\chi) & -\xi^2 + \eta^2 - \zeta^2 + \chi^2 & 2(\eta\zeta + \xi\chi) \\ 2(\xi\zeta + \eta\chi) & 2(\eta\zeta - \xi\chi) & -\xi^2 - \eta^2 + \zeta^2 + \chi^2 \end{bmatrix}$$

$$= [a_{ij}];\ i,j = 1,2,3$$

5.1.3 Design Requirements

Method and Flow

The algorithms and flow chart are shown in Figure 5-3.

Computation Requirements (Double Precision)

Storage (Memory, including Data Base)	Program	Scratch
Gyro Processing	47	24
Attitude Algorithm	201	82
Direction Cosine Matrix	262	40
Total	501	146

Execution (Operations, including subroutines)

Gyro Processing	535A + 36M
Attitude Algorithm	1334A + 117M + 11D
Direction Cosine Matrix	232A + 30M

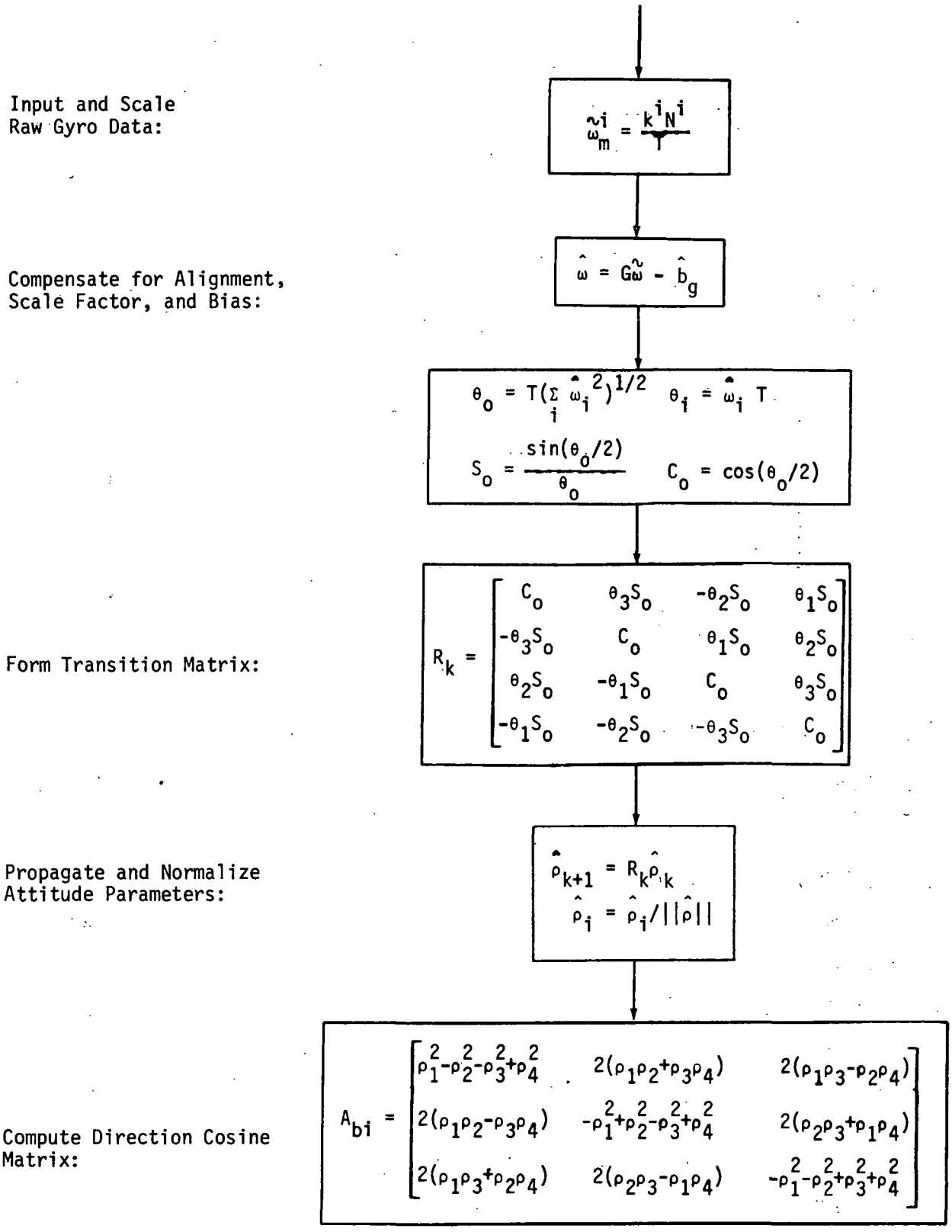

Figure 5-3. Gyro Reference Module Flow Diagram

Subroutine Usage (10 A/Subroutine call included above)

Gyro Processing	1 Matrix-vector mult.	[3 x N_G] [N_G x 1]
Attitude Algorithm	1 sin/cos	
	2 square root	
	1 Matrix-vector mult.	[4 x 4] [4 x 1]
Direction Cosine Matrix	———	
Data Base	Geometry Matrix [3 x N_G]	
Usage	Roundoff and Commutation Error Effects are indicated in Figures 5-4 and 5-5	

5.2 Tracker Reference Module

5.2.1 Functional Requirements

This software module provides the functions associated with acquisition, tracking, and measurement of star data using a two-axis gimballed star tracker. Target stars are selected from an on-board catalog and the gimballed tracker slewed to the region of the star to (search for and) acquire the desired target star. The tracker outputs provide a measure of the star line-of-sight which is compared (differenced) with an estimate (prediction) of that measure to form a measurement residual.

Computational Functions

- Establish star selection/availability
- Compute aberration correction
- Compute nominal STA gimbal angles and provide STA command/control as appropriate
- Compute estimated STA star measurement
- Determine observed STA star measurement
- Compute difference between observed and estimated STA star measurement, i.e., measurement residual

Operating Modes

There are two basic operating modes for operation of the tracker reference software. They are:

o Acquisition. This mode operates during periods when the tracker is between star sightings, i.e., slew, search, etc.

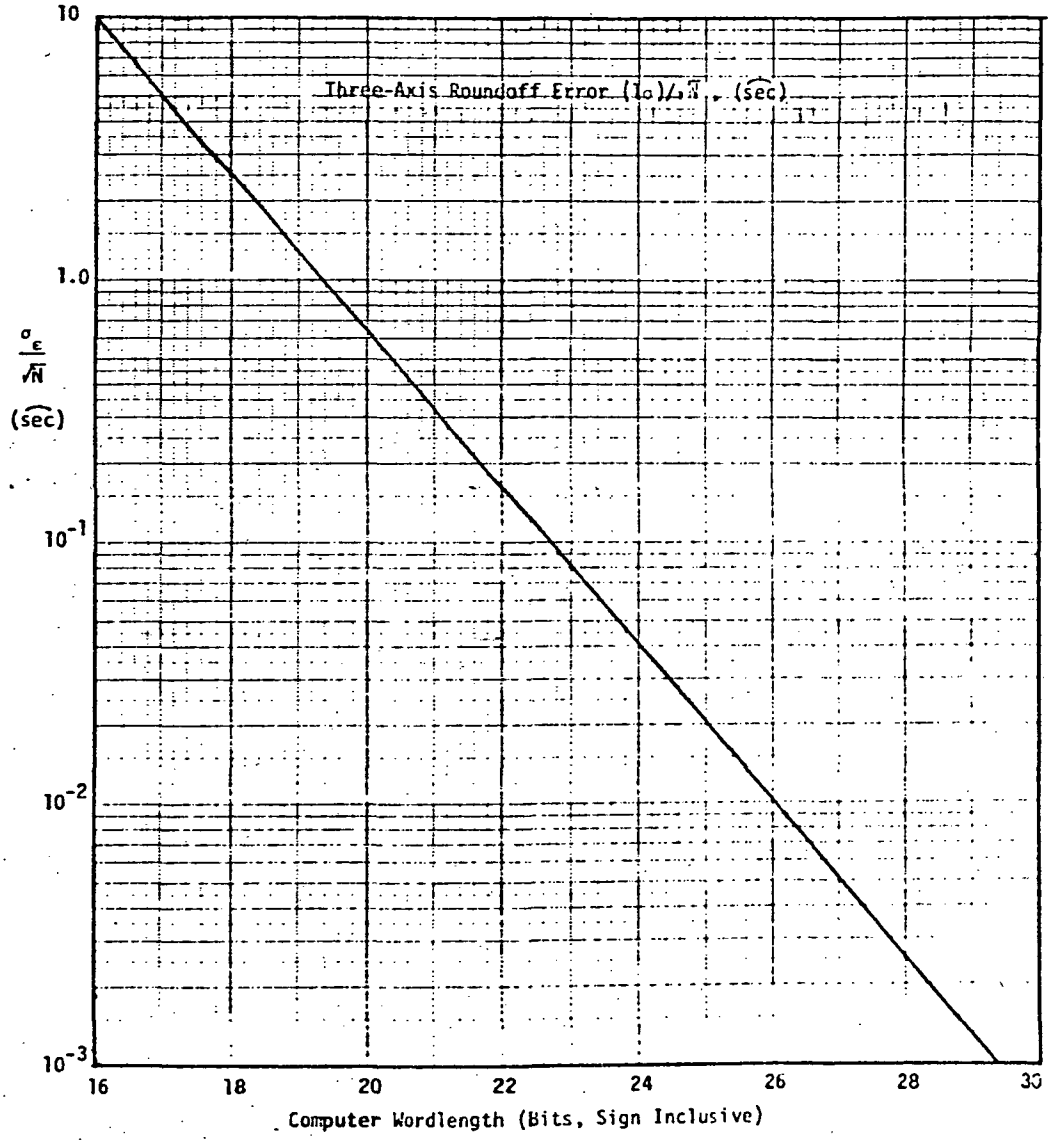

Figure 5-4. Effects of Roundoff Error

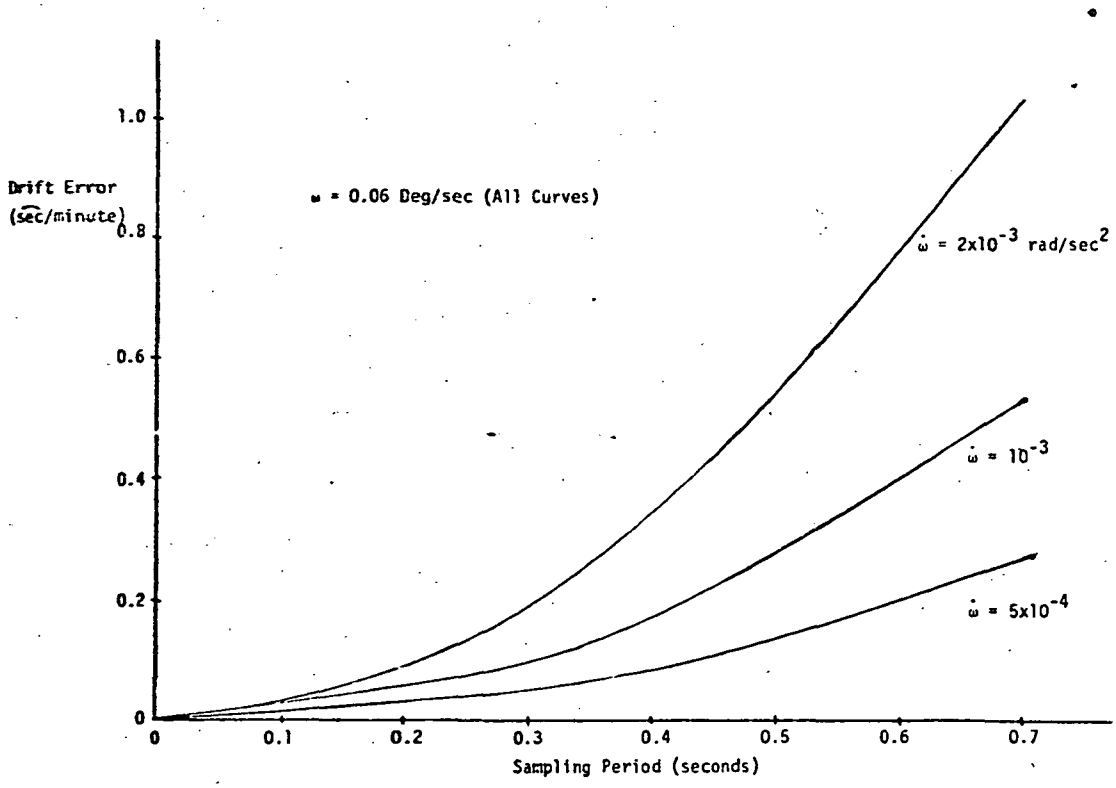

Figure 5-5. Bounds on Effects of Commutation Error

- Track. This mode operates when the tracker is locked onto the desired target star. Star measurements are processed based upon request.

Input/Output

- Input. The inputs which are available to the star reference software are summarized.

Gimbal Angles:	Tracker gimbal angles in each of two orthogonal axes.
Star Sensor Error:	Deflections of the star image from the sensor electromechanical boresight in each of two orthogonal axes.
Star Sensor Mode Logic	
Star Brightness	
Star Tracker Parameters:	STA alignments, biases, scale factors
Catalog of Stars	

- Output. The outputs provided by the star reference software are summarized.

Tracker Gimbal Commands

Star Tracker Mode Switch Command/Override

Measurement Residual

5.2.2 Functional Description

The software functional block diagram is shown in Figure 5-6. The three primary functions of the software are: star selection and computation of aberration corrected target star coordinates, star tracker gimbal control, and star measurement processing.

The gimballed tracker provides inherent flexibility in star selection, both in terms of which stars are selected and frequency between star measurements. Therefore, considerable freedom exists in the choice of stars for the on-board catalog. It is noted that a catalog of less than 50 stars can provide coverage throughout a complete mission (e.g., several stars within gimbal FOV at any point in orbit). The method and frequency of star sightings may depend, to some extent, on performance criteria associated with the update filter sensitivity. A straightforward approach, which has been found to provide good performance results, is selection of a sequence of star sightings such that the current star selected has the greatest angular separation from the star just previously used.

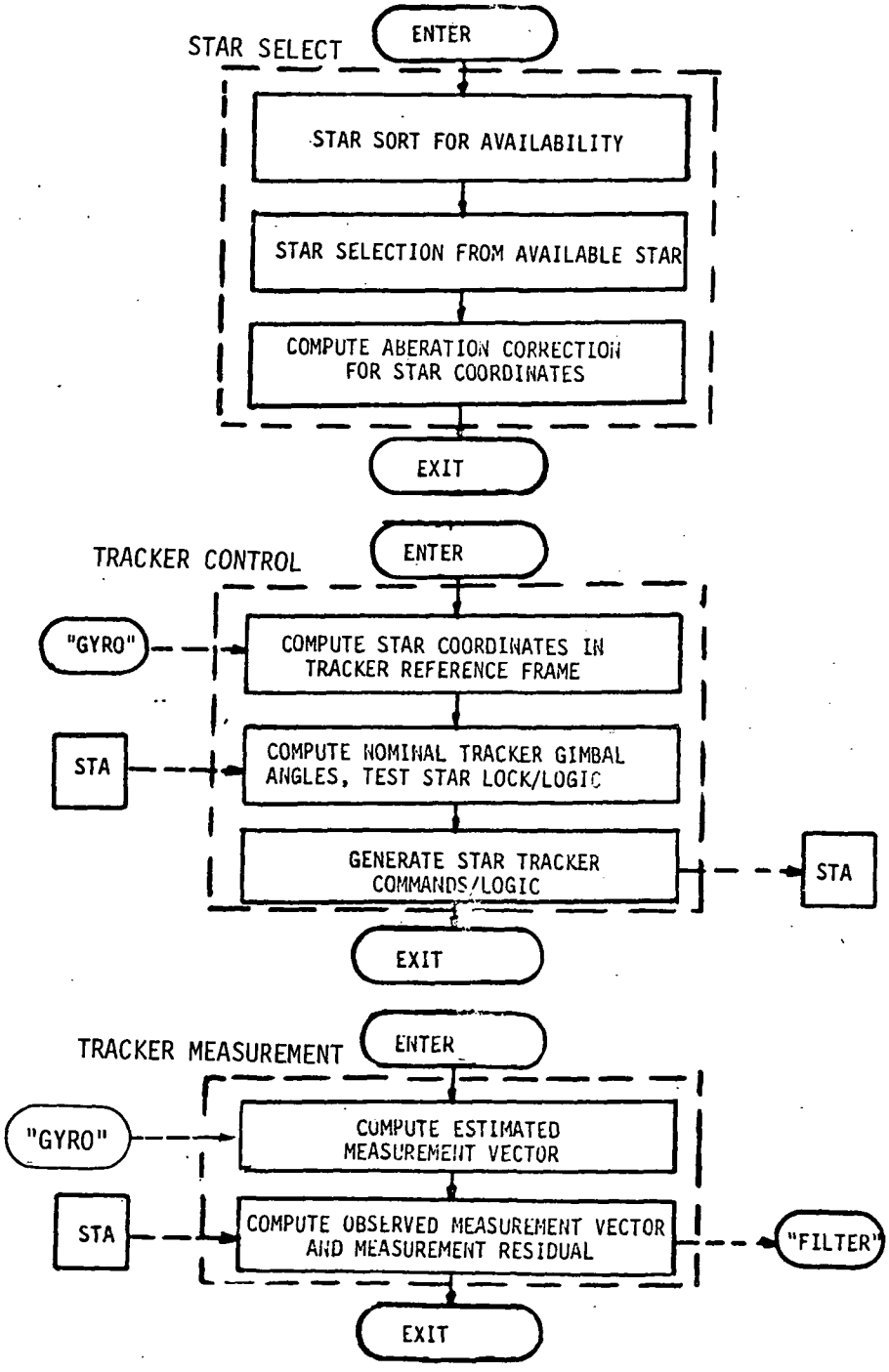

Figure 5-6. Star Tracker Module Functional Block Diagram

In computing the coordinates of the target star, it is necessary to correct for aberration of the apparent star position due to the spacecraft velocity relative to the stars (which cannot be considered negligible relative to the speed of light). If a_i (i = 1, 2, 3) represent the cataloged ECI star coordinates, the apparent star coordinates given by

$$\begin{bmatrix} \hat{a}_1 \\ \hat{a}_2 \\ \hat{a}_3 \end{bmatrix} = \left(1 - \frac{\beta^a}{c}\right) \begin{bmatrix} a_1 \\ a_2 \\ a_3 \end{bmatrix} + \frac{1}{c} \begin{bmatrix} V_1^a \\ V_2^a \\ V_3^a \end{bmatrix}$$

where $\overline{V}^a$ is the spacecraft velocity, c is the velocity of light, and β^a is the inner product of $\overline{V}^a$ and the star unit vector. The velocity, $\overline{V}^a$, is computed from knowledge of the earth velocity about the sun and the spacecraft velocity about the earth. The star coordinates in the PADS reference axes, u_i, i = 1, 2, 3, are found by appropriately transforming the ECI coordinates,

$$\begin{bmatrix} u_1 \\ u_2 \\ u_3 \end{bmatrix} = A(\rho) \begin{bmatrix} \hat{a}_1 \\ \hat{a}_2 \\ \hat{a}_3 \end{bmatrix}$$

The u_i are related to the tracker measurement through the gimbal angles, detector outputs, and tracker alignments. The estimated value of the selected tracker measurement vector, $\hat{y}$, can be implicitly determined as

$$\hat{y} = \begin{bmatrix} \sin\hat{\theta}_I \\ \sin\hat{\theta}_O \end{bmatrix} = \begin{bmatrix} 0 & 0 & -(1-u_1^2)^{1/2} \\ \dfrac{-u_2}{1-u_1^2} & \dfrac{u_1 u_2}{1-u_1^2} & 0 \end{bmatrix} \begin{bmatrix} \hat{\alpha}_1 \\ \hat{\alpha}_2 \\ \hat{\alpha}_3 \end{bmatrix} + \begin{bmatrix} -u_1 \\ \dfrac{u_3}{(1-u_1^2)^{1/2}} \end{bmatrix}$$

where the $\hat{\alpha}_i$ are tracker misalignments and $\hat{\theta}_I$ and $\hat{\theta}_o$ are the inner and outer gimbal angles, respectively. The values of $\hat{\alpha}_i$ are established through preflight alignment and calibration and, in addition, are observable in the tracker measurements so that flight calibration can be implemented if desired. The observed tracker measurement vector, $\tilde{y}$, has the form

$$\tilde{y} = \begin{bmatrix} \sin\tilde{\theta}_I + (1-u_1^2)^{1/2} & \tilde{\delta}_3 \\ \sin\tilde{\theta}_0 + \dfrac{u_2}{1-u_1^2} & \tilde{\delta}_1 \end{bmatrix}$$

where $\tilde{\delta}_1$, $\tilde{\delta}_3$ are the measured star coordinates relative to the tracker boresight and $\tilde{\theta}_I$, $\tilde{\theta}_0$ are the measured Inductosyn angles. The estimated measurement vector, $\tilde{y}$, is differenced with the observed measurement vector, $\tilde{y}$, to form the measurement residual, $\delta\hat{y}$, which is used in the Kalman filter, i.e., $\delta\hat{y} = \tilde{y} - \hat{y}$.

5.2.3 Design Requirements

Method and Flow

The algorithms and flow charts are shown in Figures 5-7, 5-8 and 5-9.

Computation Requirements (Selected Double Precision)

Storage (Memory, including Data Base	Program	Scratch
Star Selection/Processing	291	164
Tracker Control	201	20
Star Measurement Processing	169	38
Total	661	222

Execution (Operations, including Subroutines)

Star Selection/Processing	1950A + 175M + 35D (max)
Tracker Control	462A + 64M + 7D
Star Measurement Processing	305A + 25M + 9D

Subroutine Usage

Star Selection/Processing	2 sin/cos 1 square root 1 $\tan^{-1}$
Tracker Control	1 sin/cos 2 $\tan^{-1}$ 1 Matrix-vector mult. [3 x 3] [3 x 1]
Star Measurement Processing	1 square root 2 sin/cos

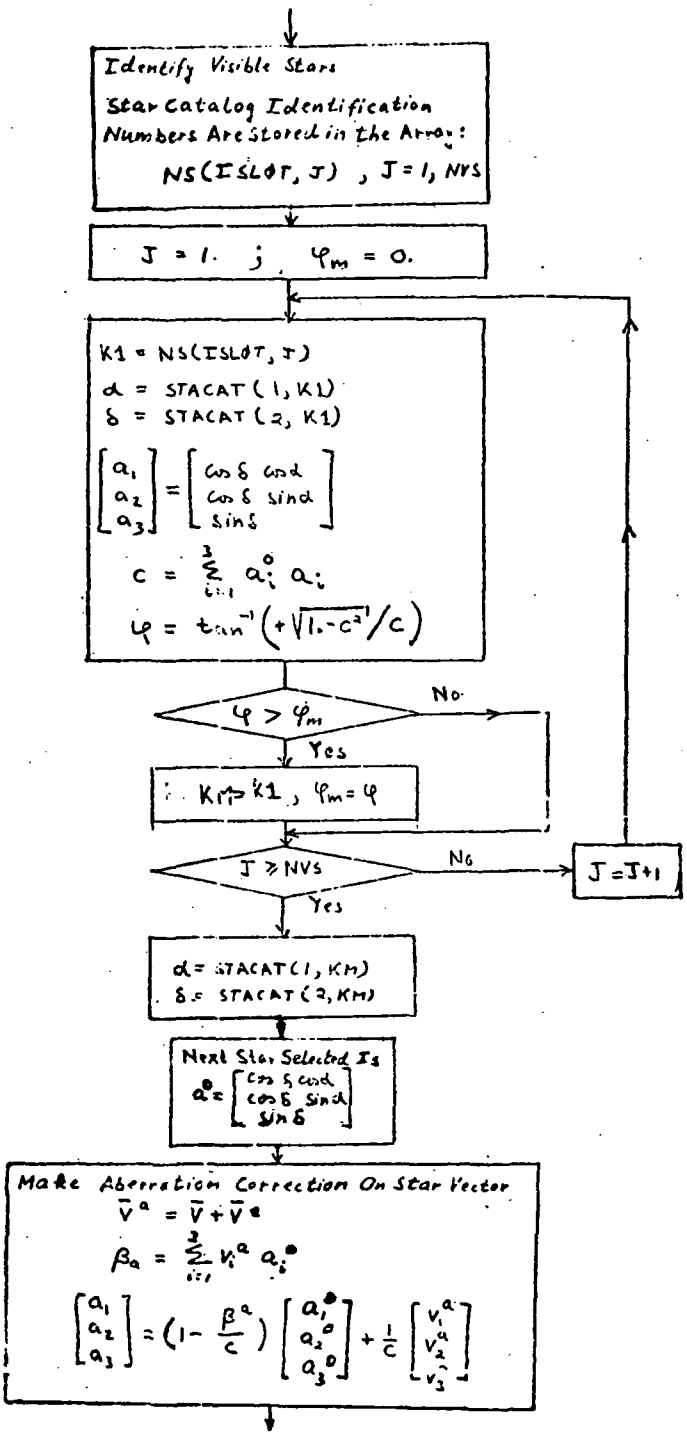

Figure 5-7. Algorithms/Flow for Star Selection

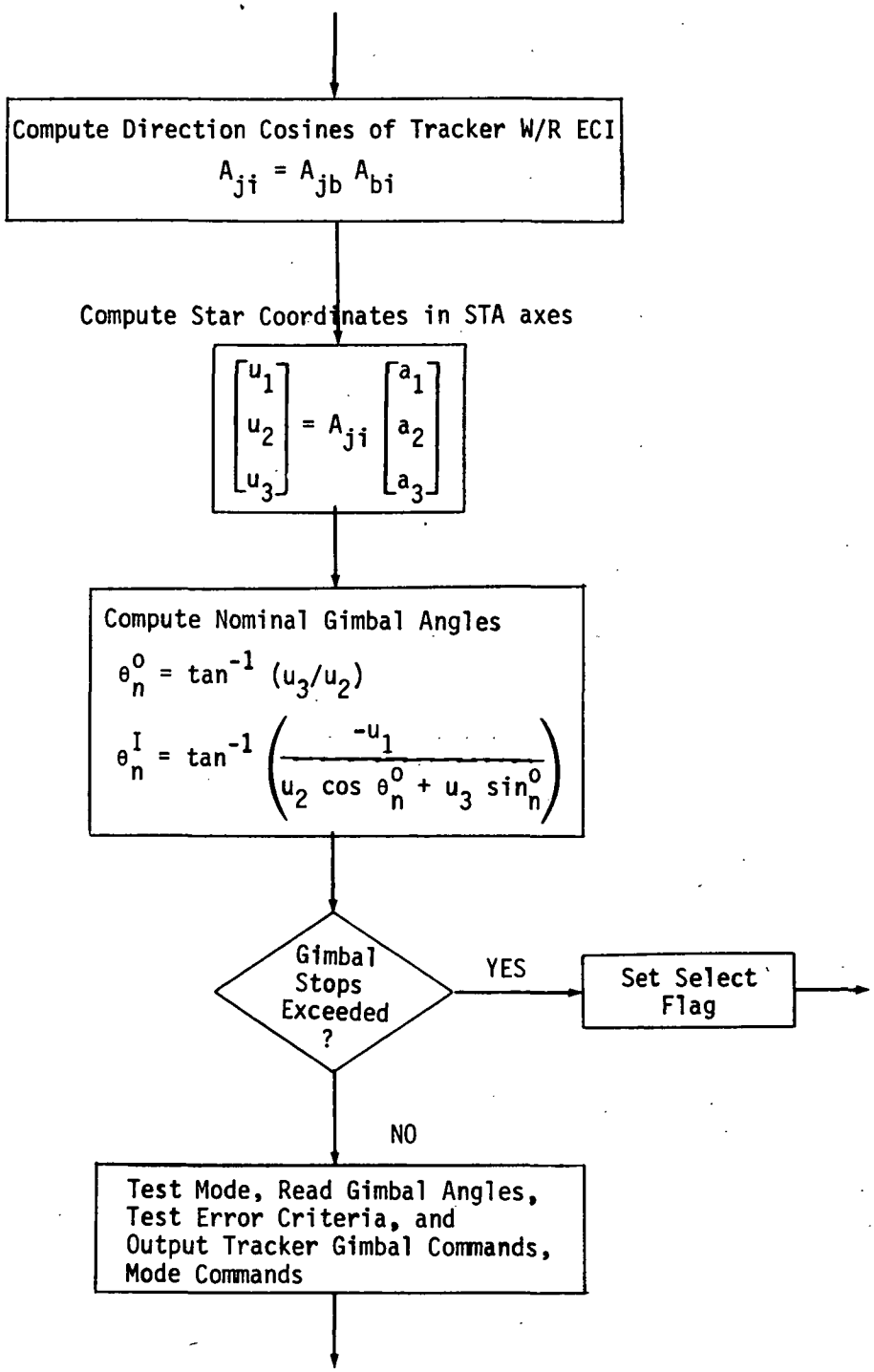

Figure 5-8. Algorithms/Flow for Tracker Control

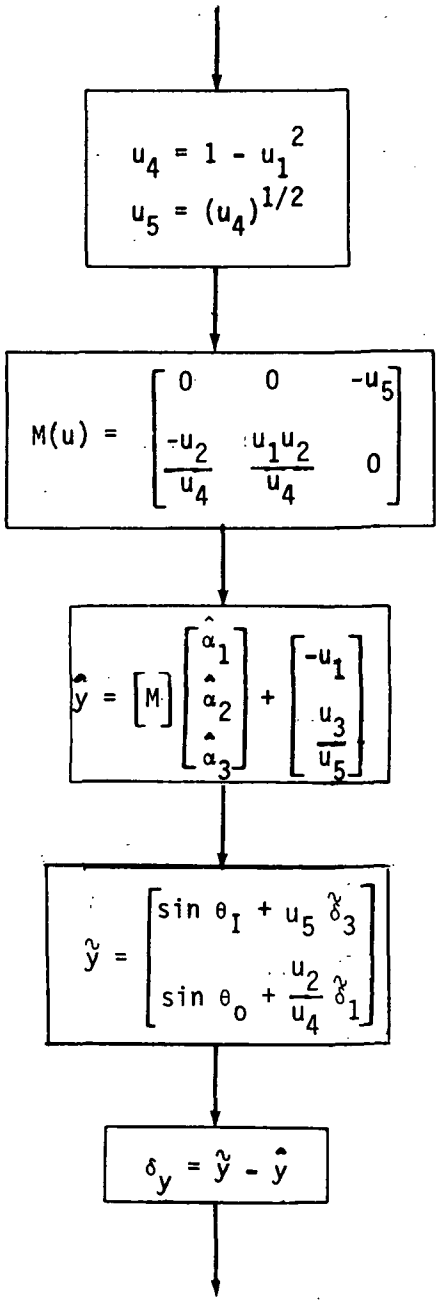

Figure 5-9. Algorithms/Flow for Star Measurement

Data Base	Master Star Catalog (50 stars) Temporary Star Catalog (<5 stars) Tracker Parameters

5.3 Kalman Filter Module

5.3.1 Functional Requirements

This software incorporates the Kalman filter associated with providing an optimal estimate of the attitude determination state vector.

Computational Functions

- Propagation of the state transition matrix is performed each attitude integration cycle using gyro derived data. The matrix is re-initialized at each filter update.

- The covariance matrix is propagated from the previous update time to the current time using the state transition matrix.

- The measurement matrix is computed.

- The filter (optimum gain) weighting matrix is computed.

- The covariance matrix is updated to reflect reduced uncertainty after an observation has been processed.

- Corrections to the Culer parameter and drift bias parameters are computed using the weighting matrix and the measurement residuals.

Input/Output

- Input. The inputs available to the Kalman filter software are summarized.

  Attitude variables

  Transformed star coordinates

  Filter parameters

- Output. The outputs available from the Kalman filter software are summarized.

  State vector correction

  Update ready flag

5.3.2 Functional Description

The software functional block diagram is shown in Figure 5-10. The Kalman filter for attitude determination has a six-element state vector consisting of three attitude variables and three gyro bias variables. In using the Euler parameters to represent attitude, it is noted that one of the parameters is redundant, i.e., constrained by a simple algebraic relation. This makes it possible to unambiguously represent variations in the fourth parameter in terms of variations in the first three. It follows that the Kalman filter need estimate only the three variables, and thus its state vector contains only three attitude terms. The linearization of the equations as required by the filter formulations are taken about the past filter estimate.

The equations for the extended Kalman filter are well known.

$$P = \Phi P \Phi^T + Q$$

$$K = PH^T[HPH^T + R]^{-1}$$

$$P = [I - KH]P$$

$$\hat{\delta x} = K\hat{\delta y}$$

The state error covariance matrix, P, is propagated using the state transition matrix, Φ, and the state noise covariance matrix, Q. The state transition matrix is initialized at the time of each update and computed between updates at each integration step using the gyro derived attitude. The state noise covariance matrix, Q, is 6 x 6, with time varying elements. In this application, with a fixed update interval, the upper left 3 x 3 and lower right 3 x 3 are simplified by including only the diagonal elements as fixed terms which are derived a priori based upon the character of the gyro noise, short-term random drift, and drift rate ramp. The optimal gain matrix, K, is computed from the measurement matrix, H, and the measurement noise covariance matrix, R. The measurement matrix relates variations in the measurement vector to variations in the state vector. The measurement noise covariance matrix, R, is 2 x 2 and the elements are constants whose value is selected based upon the expected (or measured) noise in the star measurement. The gain matrix K, is used to establish a state correction $\hat{\delta x}$, to the state vector using the measurement residual, $\hat{\delta y}$. The state error covariance matrix is also updated using the gain matrix and measurement matrix, and constrained to remain positive definite.

5.3.3 Design Requirements

Method and Flow

The algorithms and flow charts are shown in Figures 5-11 and 5-12.

Computation Requirements (Double Precision)

Storage (Memory, including Data Base)	Program	Scratch
State Transition Matrix	107	118
Covariance Propagation	351	144
Measurement Matrix	788	60
Gain Matrix	99	32
Covariance Update	106	72
State Vector Update	197	20
Total	1648	446

Execution (Operations, including Subroutines)

State Transition Matrix	3294A + 192M + 3D
Covariance Propagation	16163A + 999M
Measurement Matrix	881A + 97M + 2D
Gain Matrix	3583A + 216M
Covariance Update	7068A + 432M
State Vector Update	457A + 36M

Subroutine Usage

State Transition Matrix	1 Matrix mult. [4 x 4] [4 x 4]
Covariance Propagation	12 Matrix mult. [3 x 3] [3 x 3]
Measurement Matrix	1 Matrix mult. [2 x 4] [4 x 3]
Gain Matrix	2 Matrix mult. [3 x 3] [3 x 2]
	1 Matrix mult. [2 x 3] [3 x 3]
	1 Matrix mult. [2 x 3] [3 x 2]
	2 Matrix mult [3 x 2] [2 x 2]
Covariance Update	4 Matrix mult. [3 x 3] [3 x 3]
	2 Matrix mult. [3 x 2] [2 x 3]
State Vector Update	———

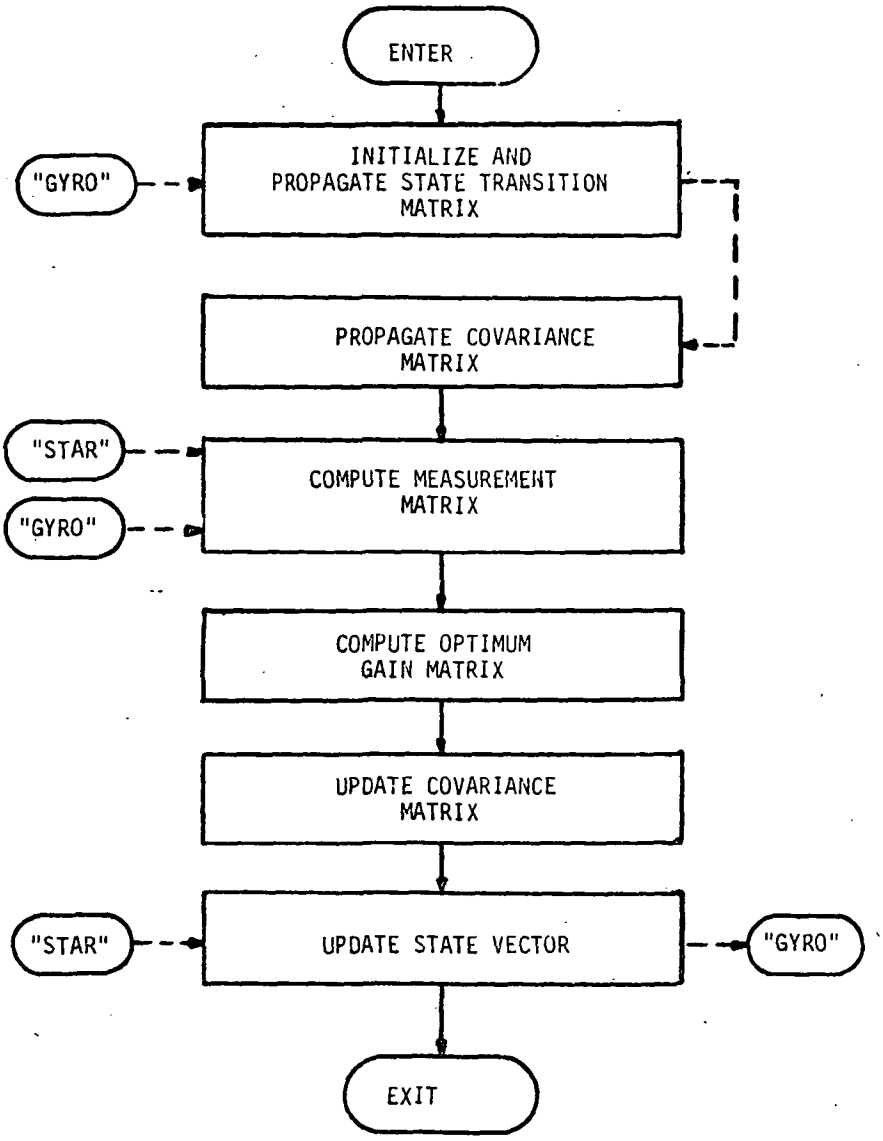

Figure 5-10. Filter/Update Module Functional Block Diagram

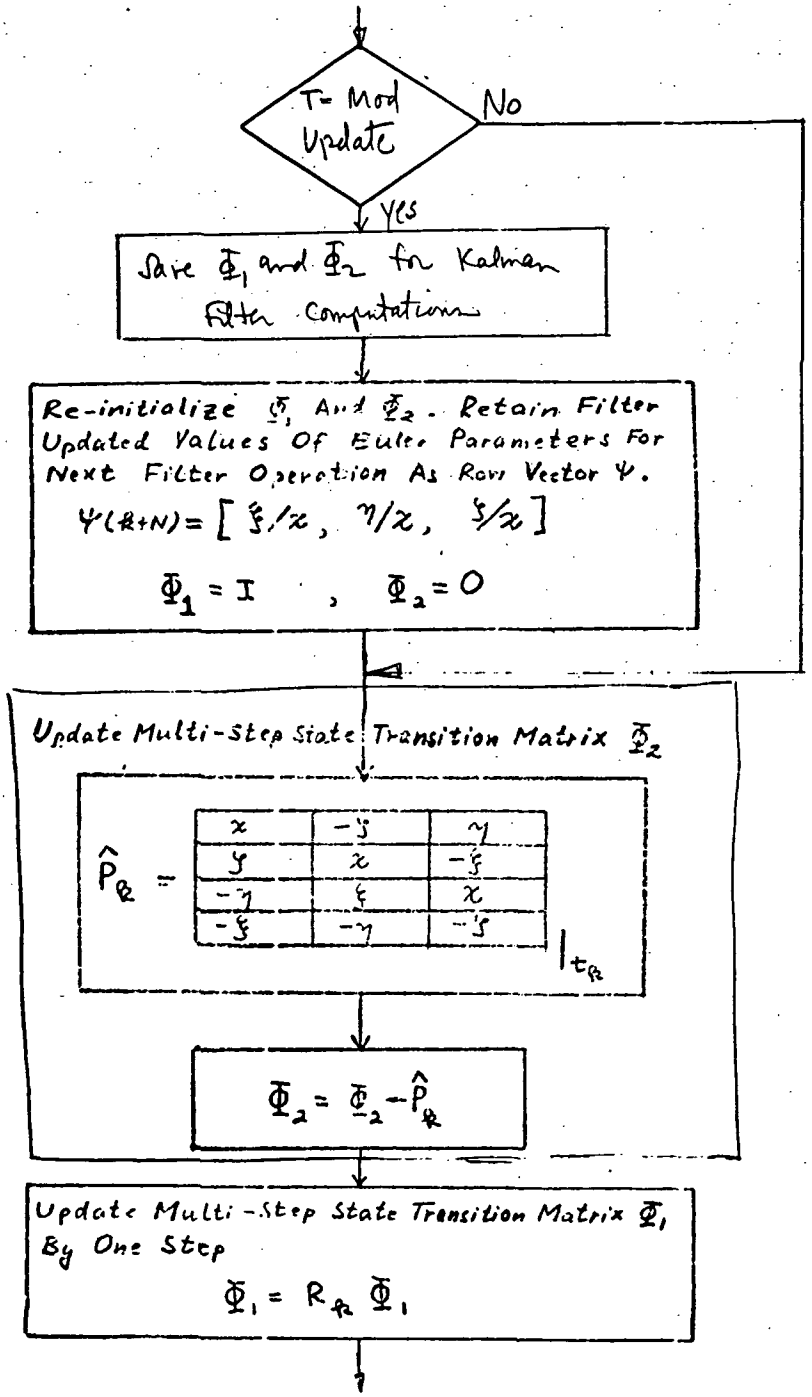

Figure 5-11. Algorithms/Flow for State Transition Matrix

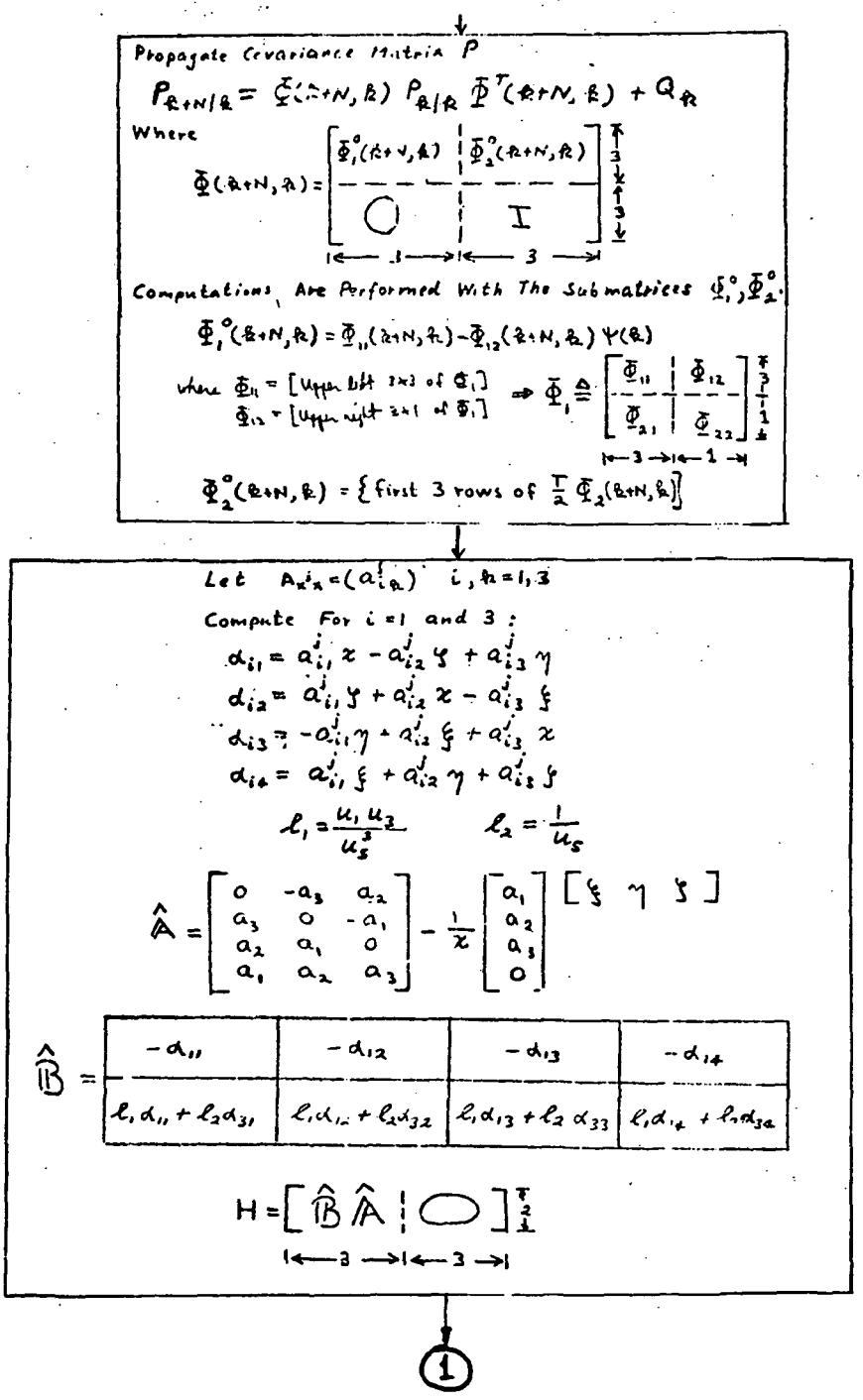

Figure 5-12. Algorithms/Flow for Filter/Update

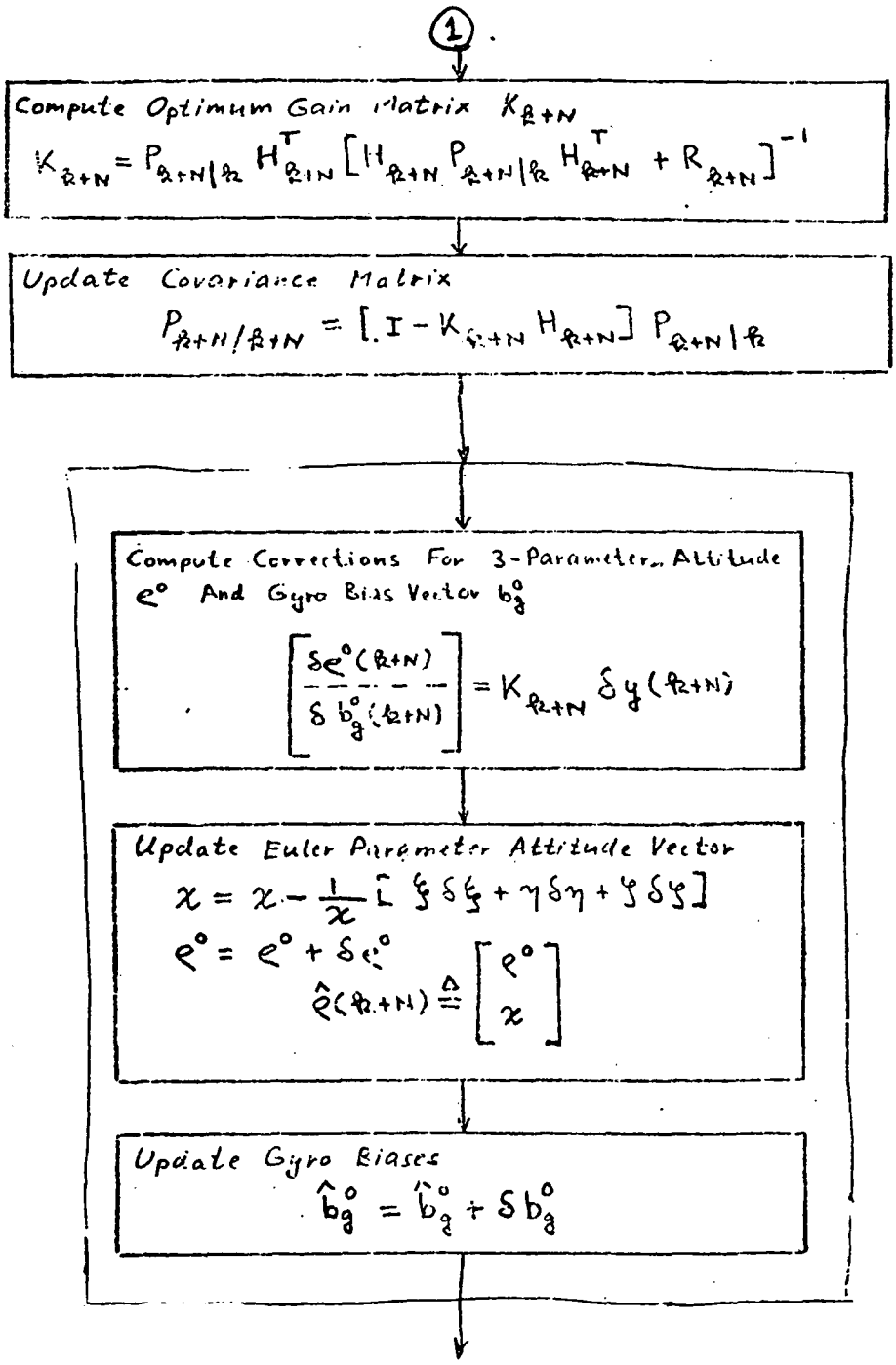

Figure 5-12. Algorithms/Flow for Filter/Update (Continued)

6.0 REFERENCES

(1) Frew, A. M., et al, PPCS System Design and Analysis, July 1972, TRW Report 13900-6012-RO-01.

(2) Gates, R. F. Mann, R. J., Zaremba, J. G., et al, PPCS Engineering Model Design, July 1971, TRW Report 13500-6011-RO-01.

(3) Farrenkopf, R. L., PPCS Attitude Reference Simulation Development, June 1970, TRW Report 13900-6003-RO-00.

(4) Belsky, F. J., PPCS Attitude Reference Simulation User's Manual, June 1970, TRW Report 13900-6005-RO-00.

(5) Frew, A. M. Iwens, R. P., PPCS Simulation, September 1970, TRW Report 13900-6009-RO-00.

(6) 13900-6015-RU-00, PADS Star Tracker Test, 1 July 1973.

APPENDIX

PADS SENSOR ELECTRONICS SCHEMATICS

SK

CHG LTR

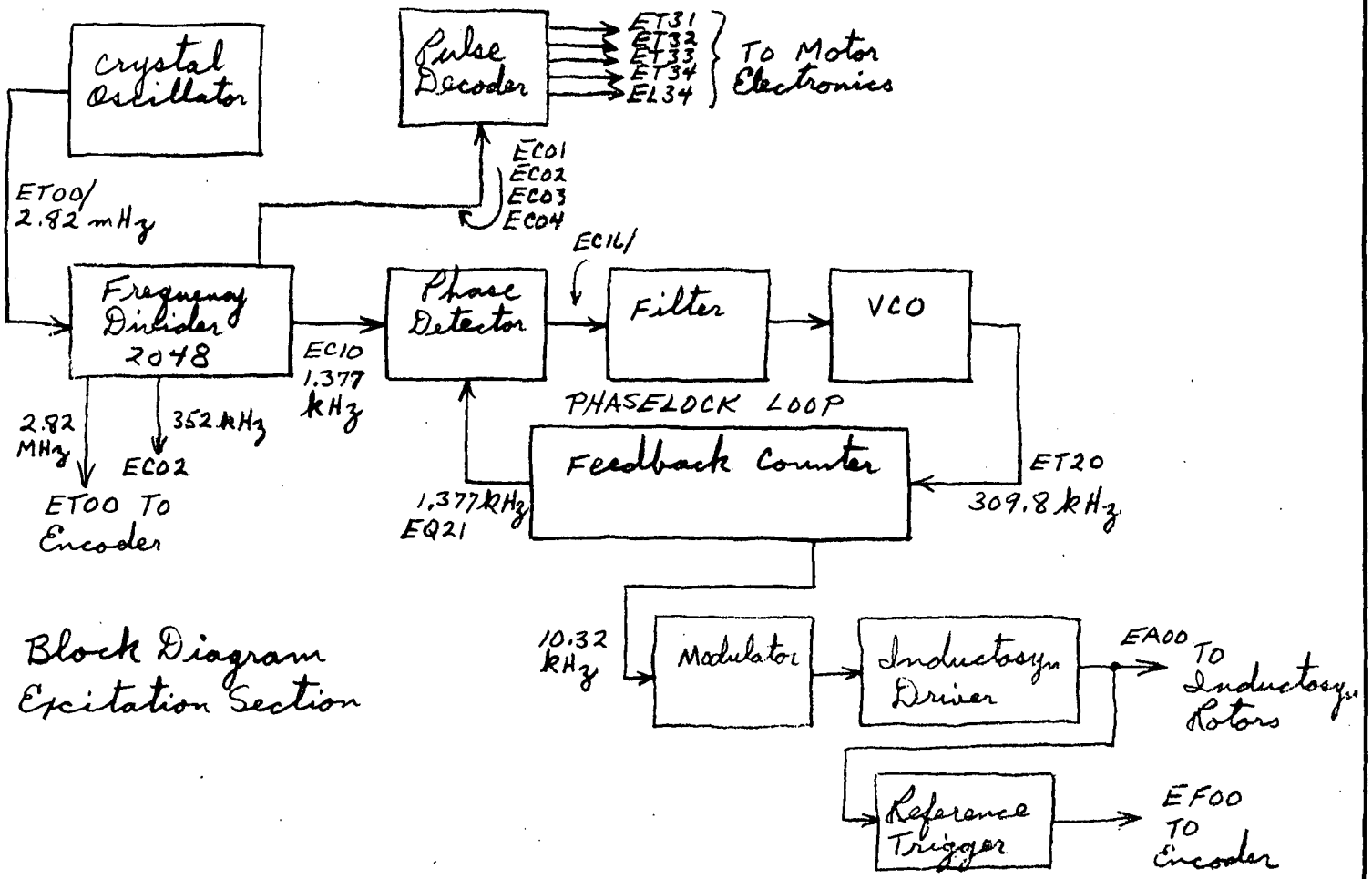

Block Diagram
Excitation Section

ORIGINATOR A. Kim
MJO PADS SEA
B
DATE 7/28/71
3/15/72

TITLE Excitation Section Block Diagram

ENGINEERING SKETCH

TRW
ONE SPACE PARK · REDONDO BEACH, CALIFORNIA

SK-MA100 B

SHEET 5 OF

SYSTEMS 529 REV. 5-67

SK

CHG LTR

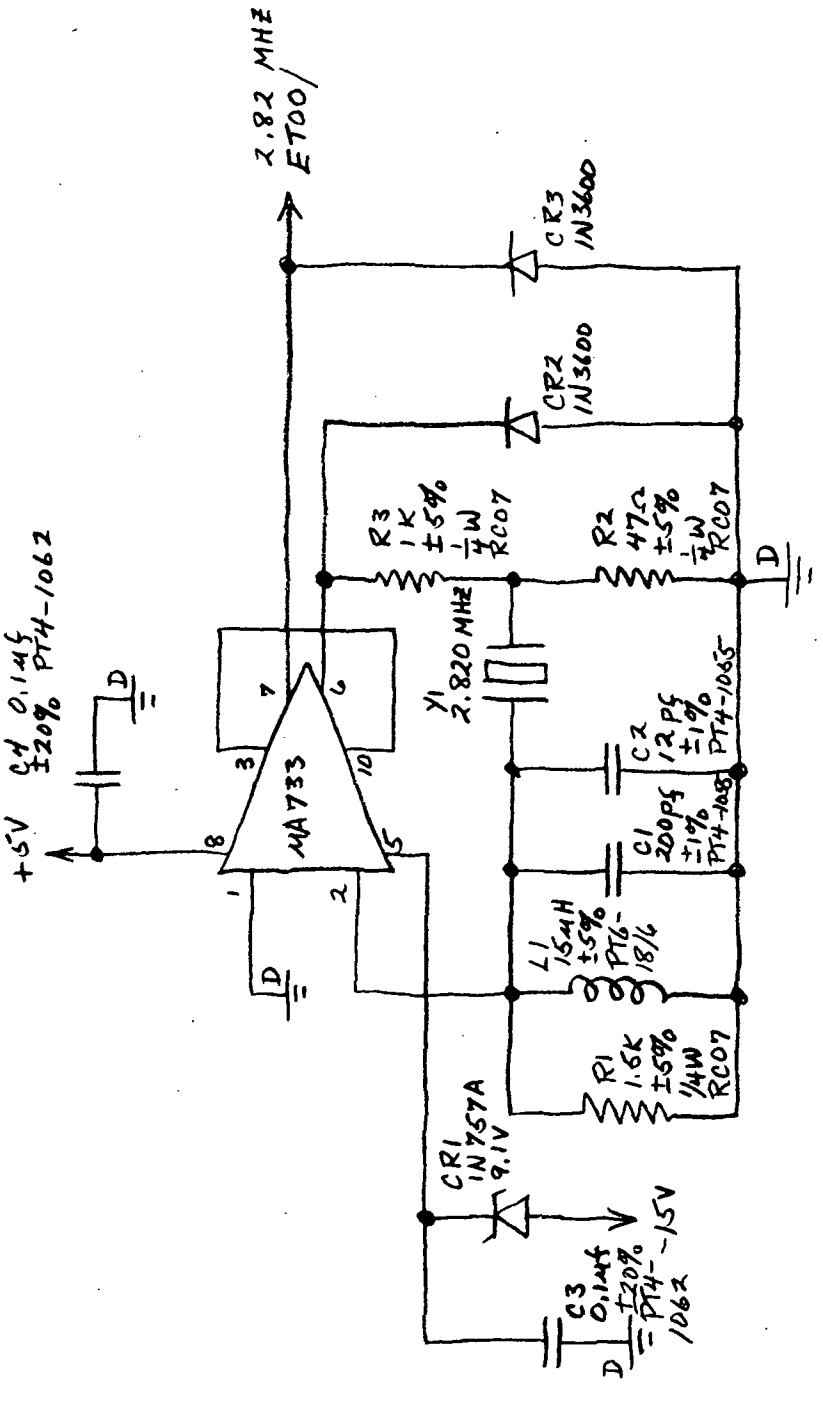

Notes:
1. Digital Ground $\frac{D}{=}$

ORIGINATOR	DATE	TITLE	ENGINEERING SKETCH
KJM FEB	5 1971	Crystal Oscillator	TRW SYSTEMS GROUP, ONE SPACE PARK · REDONDO BEACH, CALIFORNIA
A KJM	7/28/71		SK-MA101B
B KJM	3/15/72		SHEET 2 OF
MJO PADS SEA			

SYSTEMS 523 REV. 5-67

SK

CHG LTR

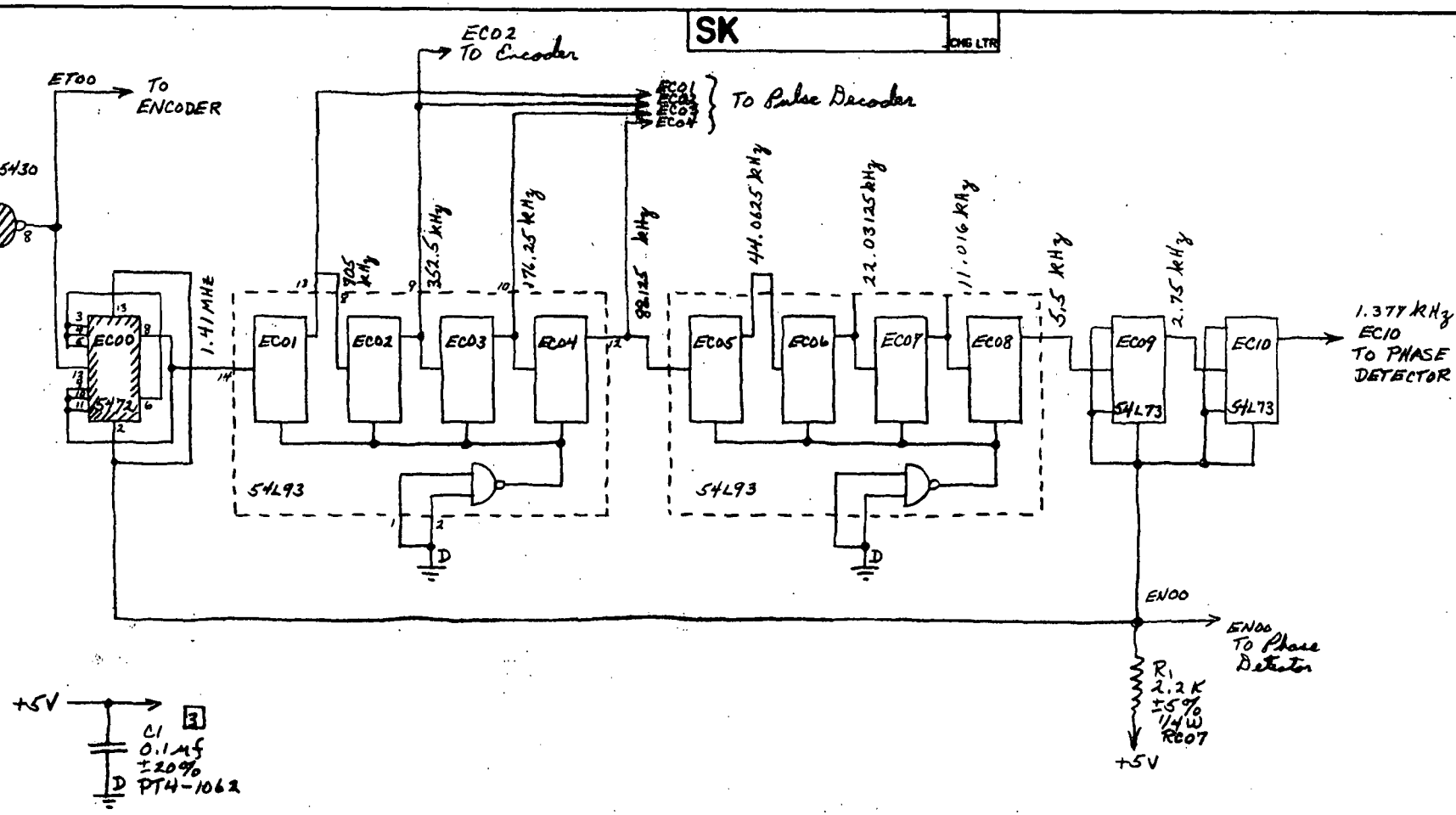

Notes:

1. //// Denotes medium power element
2. Digital ground $\frac{D}{=}$. Includes power return of all logic elements.

[3] Locate C1 near EC00, ET00

ORIGINATOR	DATE
RJM	2/25/71
A RJM	7/28/71
B RJM	3/15/72
MJO PADS SEA	

TITLE: Frequency Divider

ENGINEERING SKETCH

TRW SYSTEMS GROUP

ONE SPACE PARK · REDONDO BEACH · CALIFORNIA

SK-MA102B

SHEET 3 OF

TRW SYSTEMS 8048 REV. 9-67

SK

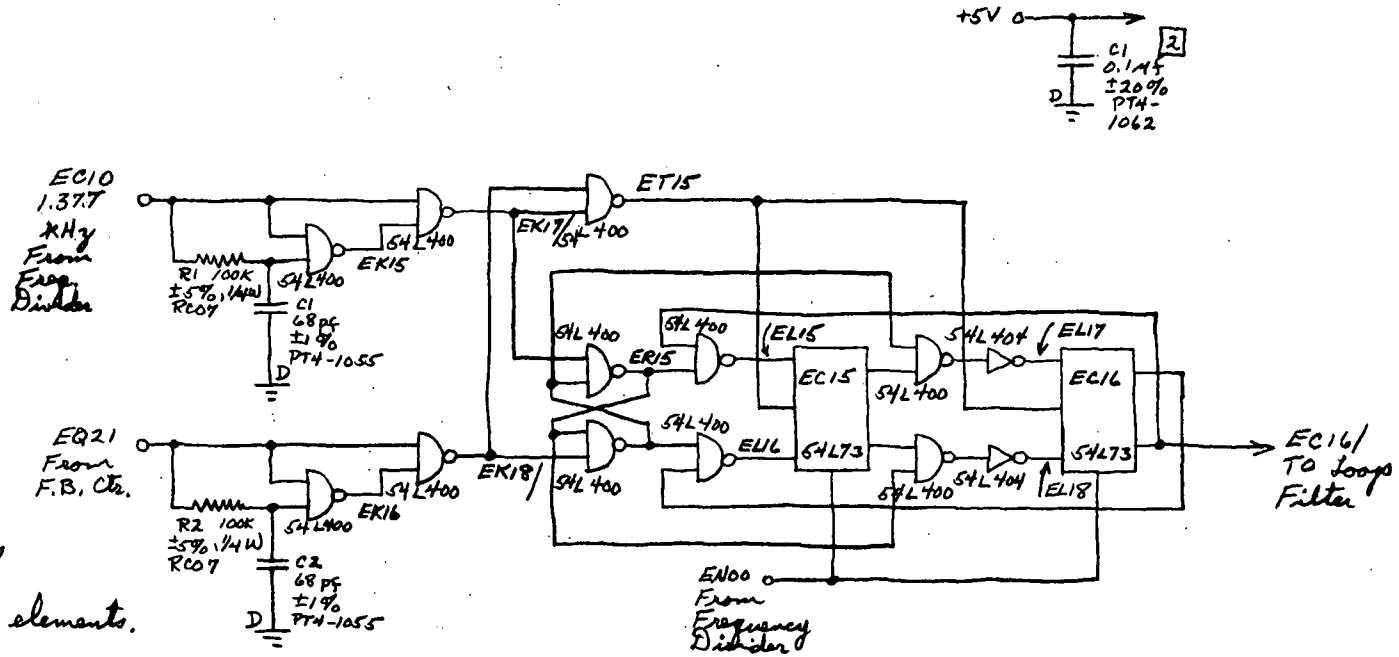

Notes:
1. Digital ground ⏚ includes all logic power returns.
2. Locate C1 near these logic elements.

ORIGINATOR	DATE	TITLE
RJM	2/15/71	Phase Detector
A RJM	7/29/71	
B RJM	3/15/72	
MJO PADS SEA		

ENGINEERING SKETCH
TRW SYSTEMS GROUP
ONE SPACE PARK · REDONDO BEACH · CALIFORNIA
SK-MA1038
SHEET 2 OF

SK

CHG LTR

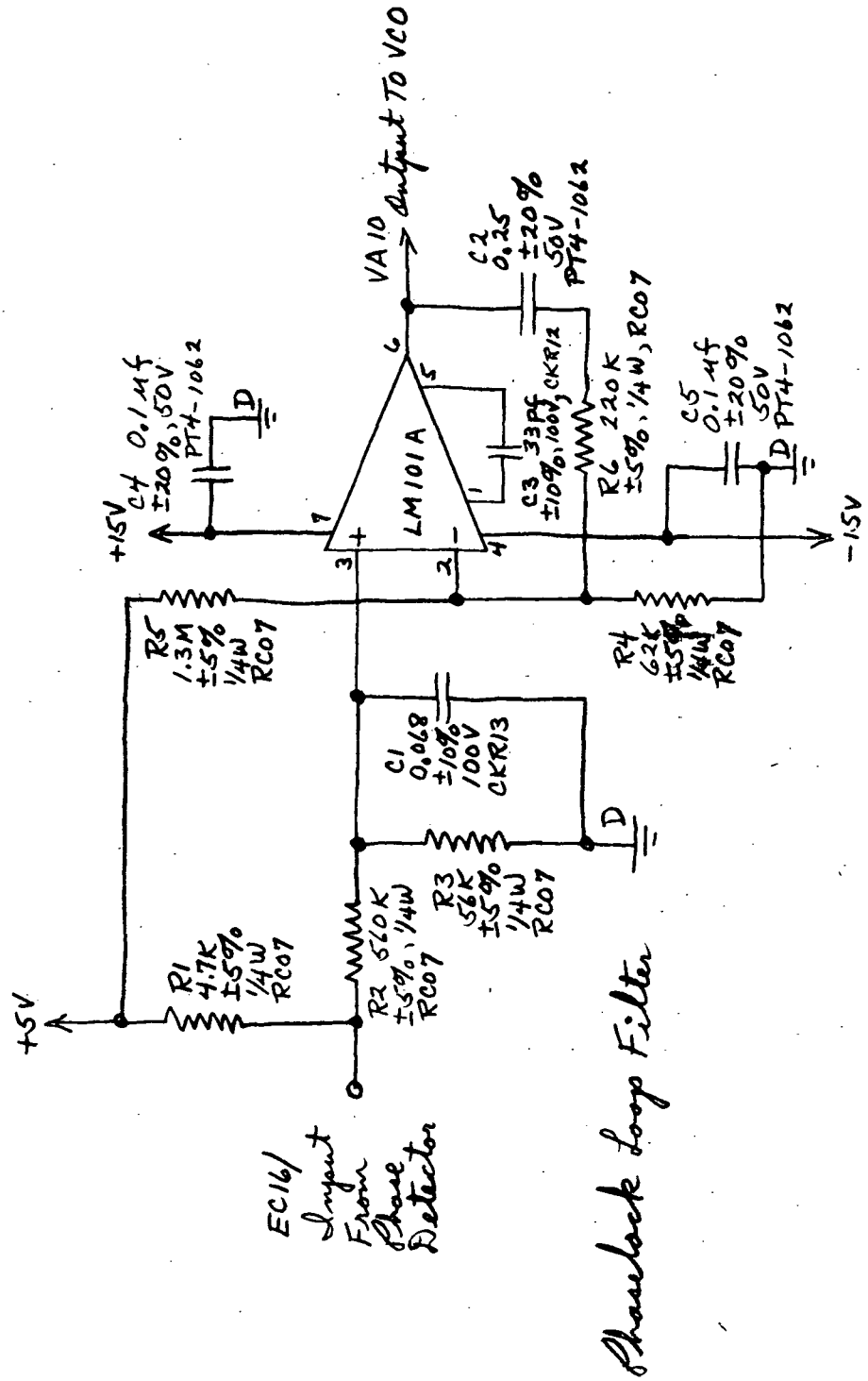

ORIGINATOR	DATE	TITLE	ENGINEERING SKETCH
RJM FEB	23 1971	Phaselock Loop Filter	TRW SYSTEMS GROUP ONE SPACE PARK • REDONDO BEACH, CALIFORNIA
			SK - MA104
MJO PPCS			SHEET 8 OF

SYSTEMS 023 REV. 5-67

Voltage Controlled Oscillator, Design Notes

FEB 17 1971

Topology

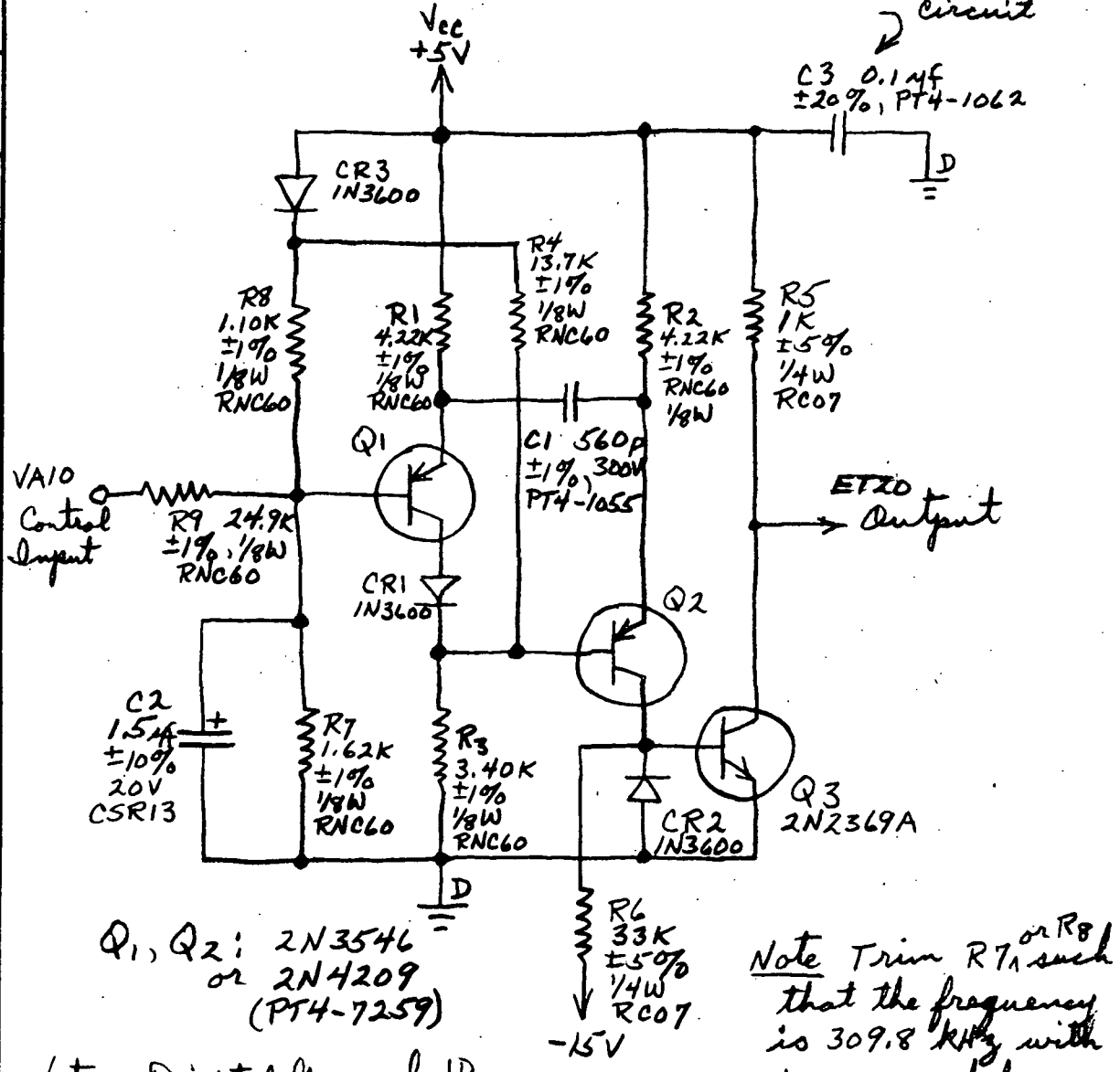

Q_1, Q_2: 2N3546 or 2N4209 (PT4-7259)

Note: Digital Ground ⏚D

Note Trim R7, or R8 such that the frequency is 309.8 kHz with VA10 grounded.

CHG LTR

SK

ORIGINATOR	DATE	TITLE	ENGINEERING SKETCH
RJM	3/16/71	Voltage Controlled Oscillator	TRW, ONE SPACE PARK · REDONDO BEACH, CALIFORNIA
A RJM	7/28/71		SK-MA105B
			SHEET 1 OF
MJO PADS SEA			

SYSTEMS 523 REV. 5-67

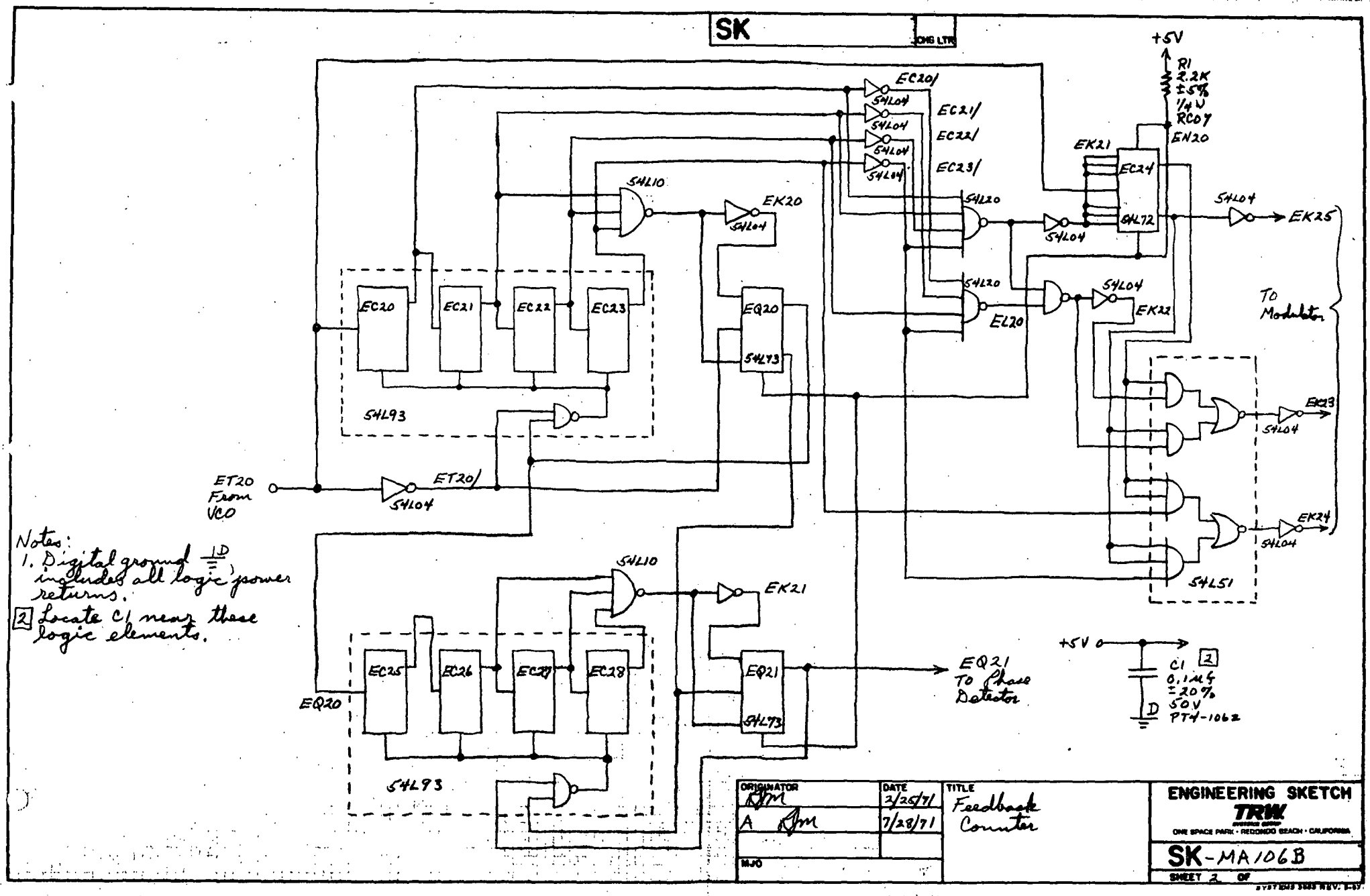
SK
+5V
R1
2.2K
±5%
1/4 W
RC07
EN20
EC20/
EC21/
EC22/
EC23/
54L04
54L10
EK20
54L20
EK21
EC24
54L72
EK25
EL20
EK22
To Modulator
EC20
EC21
EC22
EC23
54L93
EQ20
54L73
ET20
From VCO
ET20/
EK23
EK24
54L51
EC25
EC26
EC27
EC28
EQ21
EQ21 To Phase Detector
C1
0.1μf
±20%
50V
PT4-1062
Notes:
1. Digital ground (D) includes all logic power returns.
2 Locate C1 near these logic elements.
ORIGINATOR
DATE
2/26/71
A
7/28/71
MJO
TITLE
Feedback Counter
ENGINEERING SKETCH
TRW
ONE SPACE PARK · REDONDO BEACH · CALIFORNIA
SK-MA106B
SHEET 2 OF

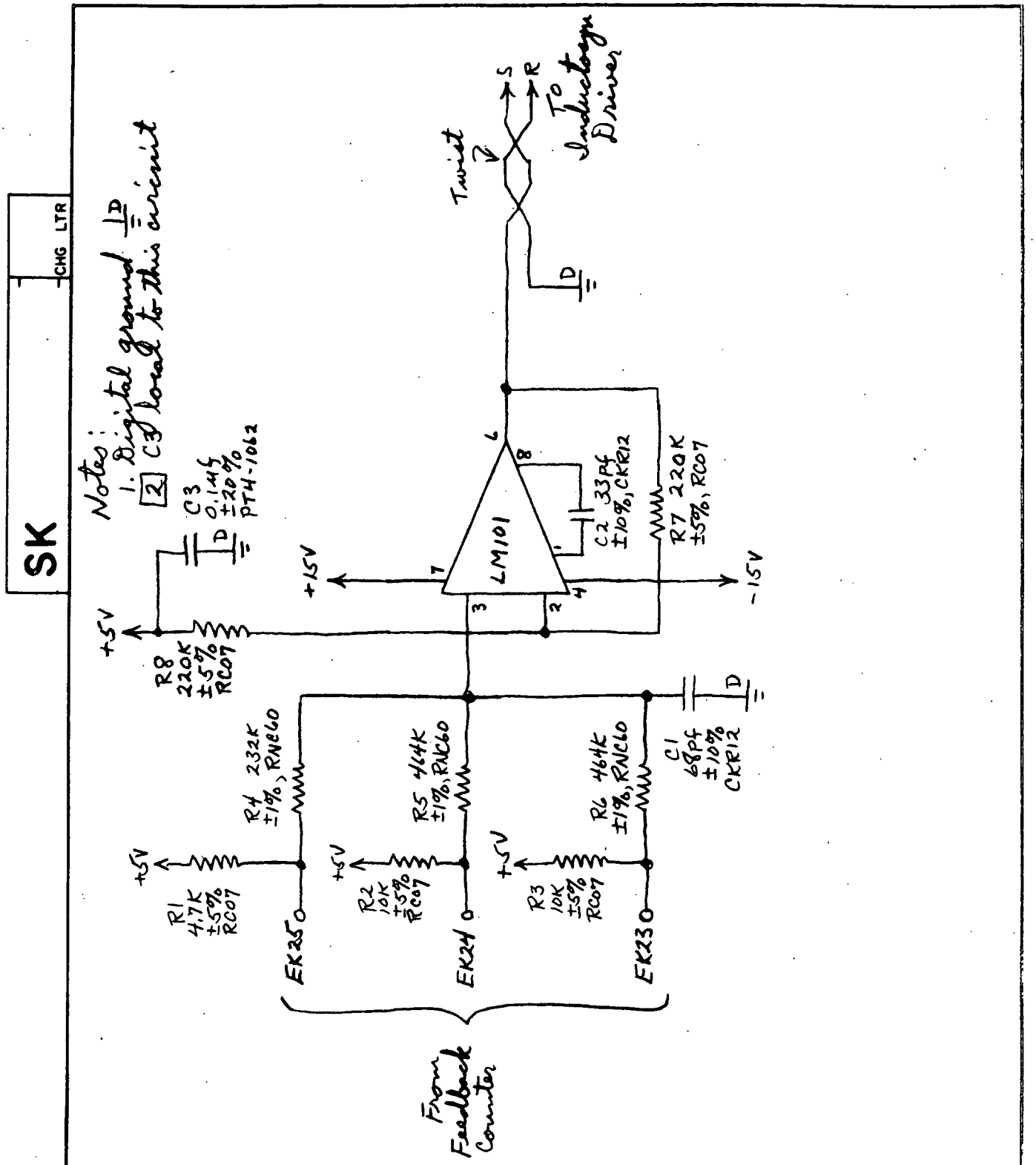

ORIGINATOR	DATE	TITLE	ENGINEERING SKETCH
RJM A	3/15/72	Modulator	TRW SYSTEMS GROUP, ONE SPACE PARK • REDONDO BEACH, CALIFORNIA
			SK-MA107A
MJO PADS/SEA			SHEET 2 OF

SYSTEMS 523A REV. 5-67

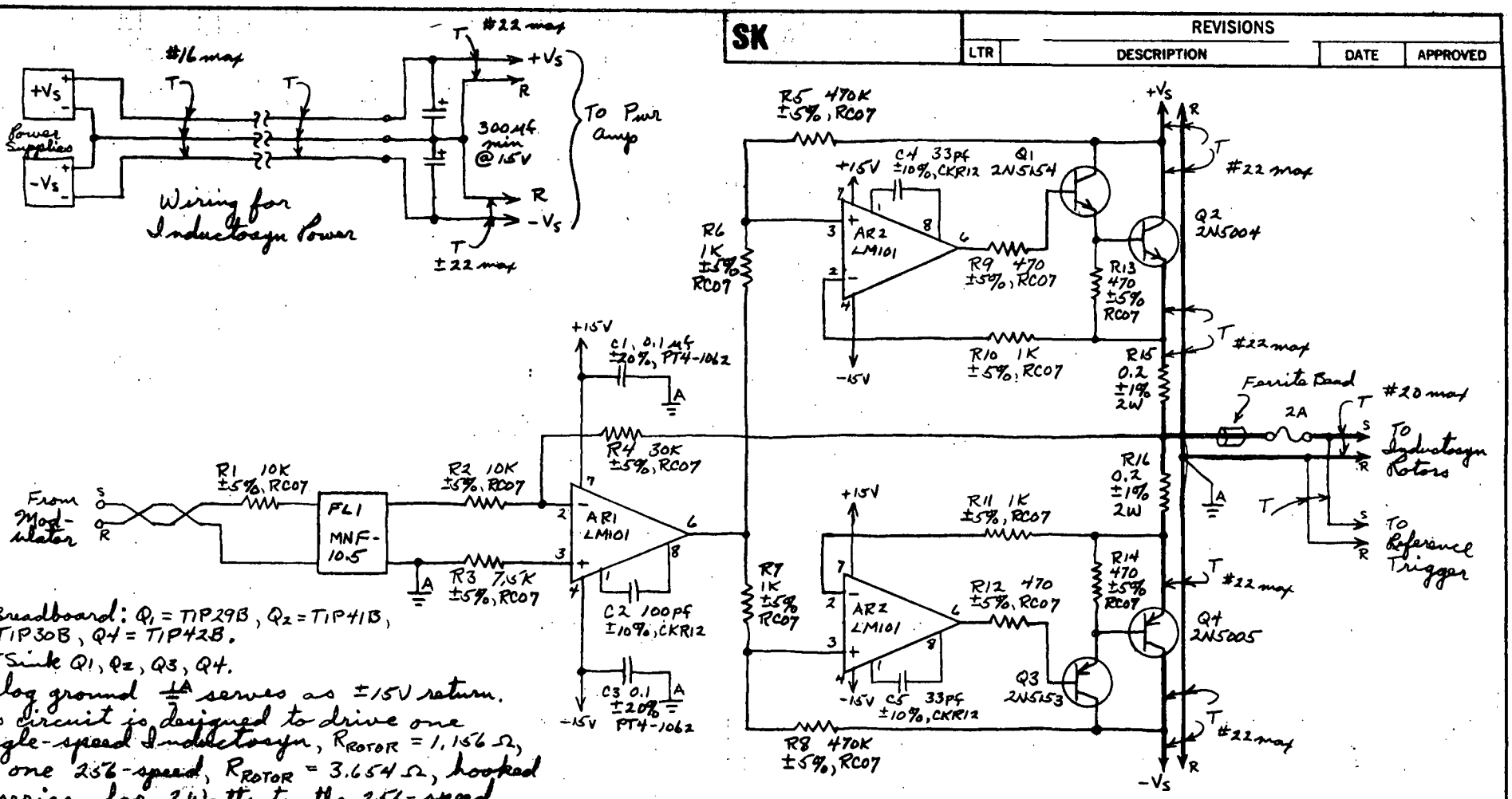

Notes:

1. For Breadboard: Q_1 = TIP29B, Q_2 = TIP41B, Q3 = TIP30B, Q4 = TIP42B.
2. Heat Sink Q1, Q2, Q3, Q4.
3. Analog ground $\pm A$ serves as ±15V return.
4. This circuit is designed to drive one single-speed Inductosyn, R_{ROTOR} = 1,156 Ω, and one 256-speed, R_{ROTOR} = 3.654 Ω, hooked in series, for 2 Watts to the 256-speed. V_S = 7.0 V, V_{OUT} = 5.0 V_{pk}.

ENGINEERING SKETCH		
ORIGINATOR		DATE
RJM	A	3/17/72
MJO PADS/SEA		

TRW SYSTEMS GROUP
ONE SPACE PARK • REDONDO BEACH, CALIFORNIA

Inductosyn Driver

SIZE	CODE IDENT NO.	
B	11982	SK-MA108A
SCALE		SHEET 1 OF

SYSTEMS 3643 REV. 12-71

SK

CHG LTR

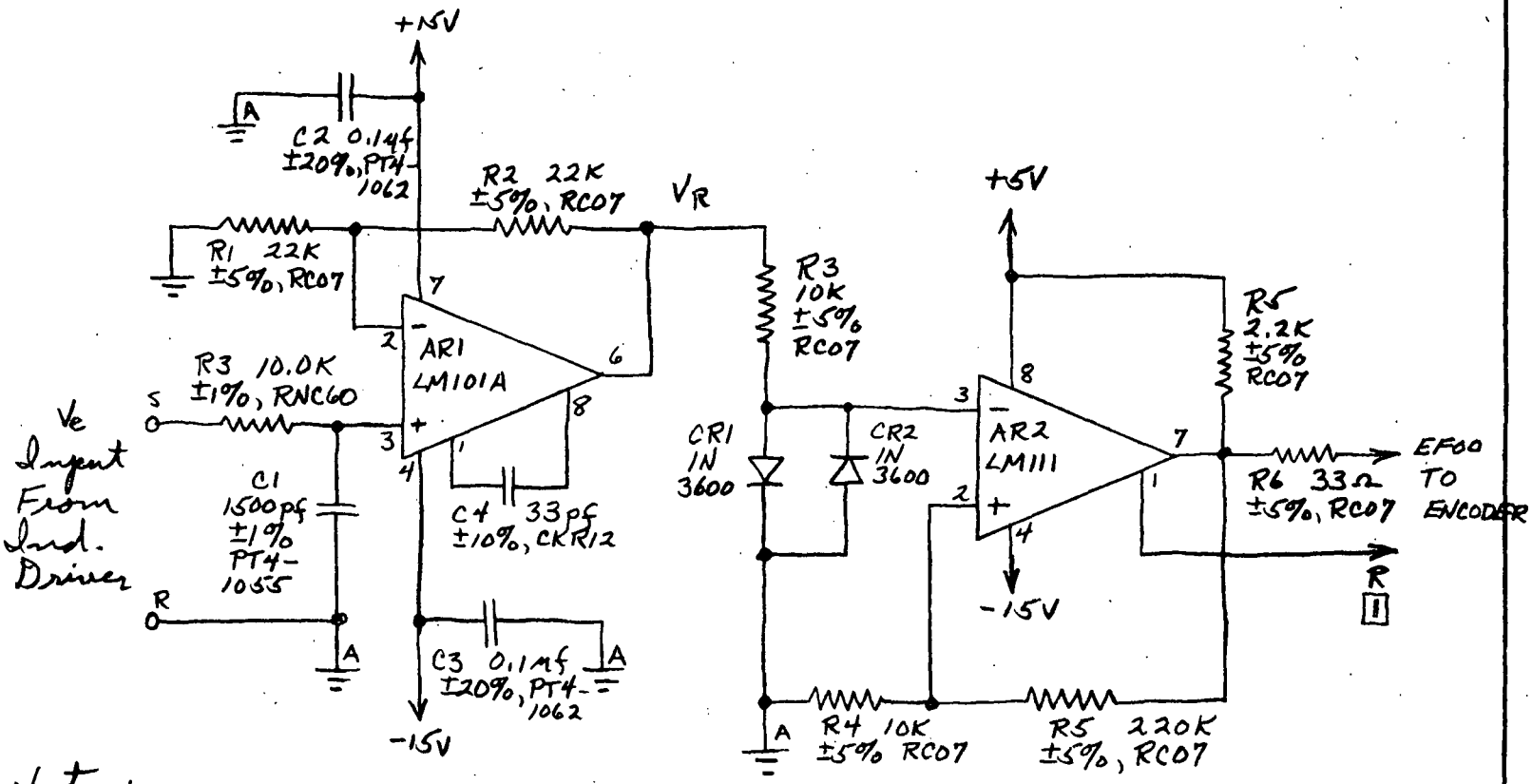

Notes:

[1] Tie EF00 return (R) to Encoder digital ground ($\perp^D$). Route EF00 and return twisted pair.

2. Analog ground $\perp^A$, input return is sufficient.

ORIGINATOR RJM A 4/20/71

MJO 3/16/72

TITLE Reference Trigger

CODE IDENT NO. 11982

ENGINEERING SKETCH

TRW SYSTEMS GROUP ONE SPACE PARK - REDONDO BEACH, CALIFORNIA

SK-MA109A

SHEET 2 OF

SYSTEMS 523 REV. 10-70

CHG LTR

SK

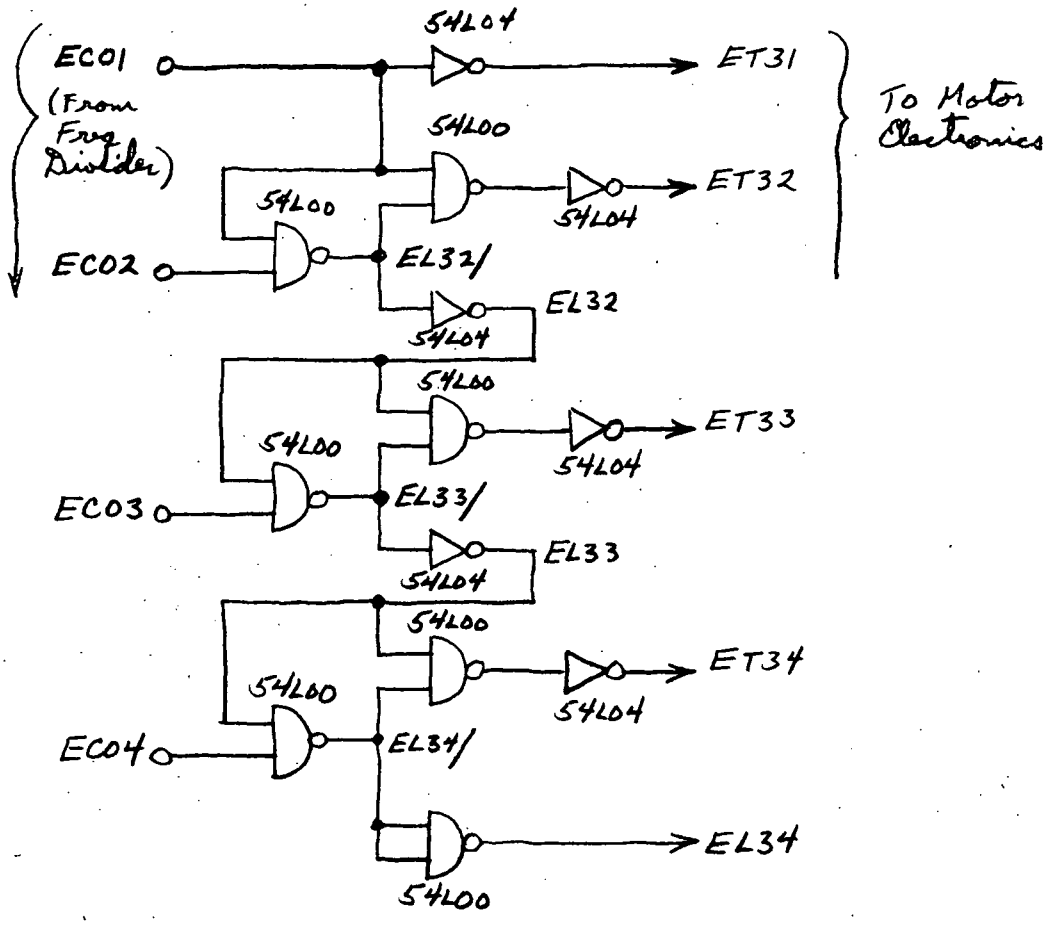

ORIGINATOR	DATE	TITLE	ENGINEERING SKETCH
KJM	8/6/71	Pulse Decoder	TRW SYSTEMS GROUP, ONE SPACE PARK • REDONDO BEACH, CALIFORNIA
			SK - MA110
MJO PPCS/PADS			SHEET 1 OF

SYSTEMS 523 REV. 5-67

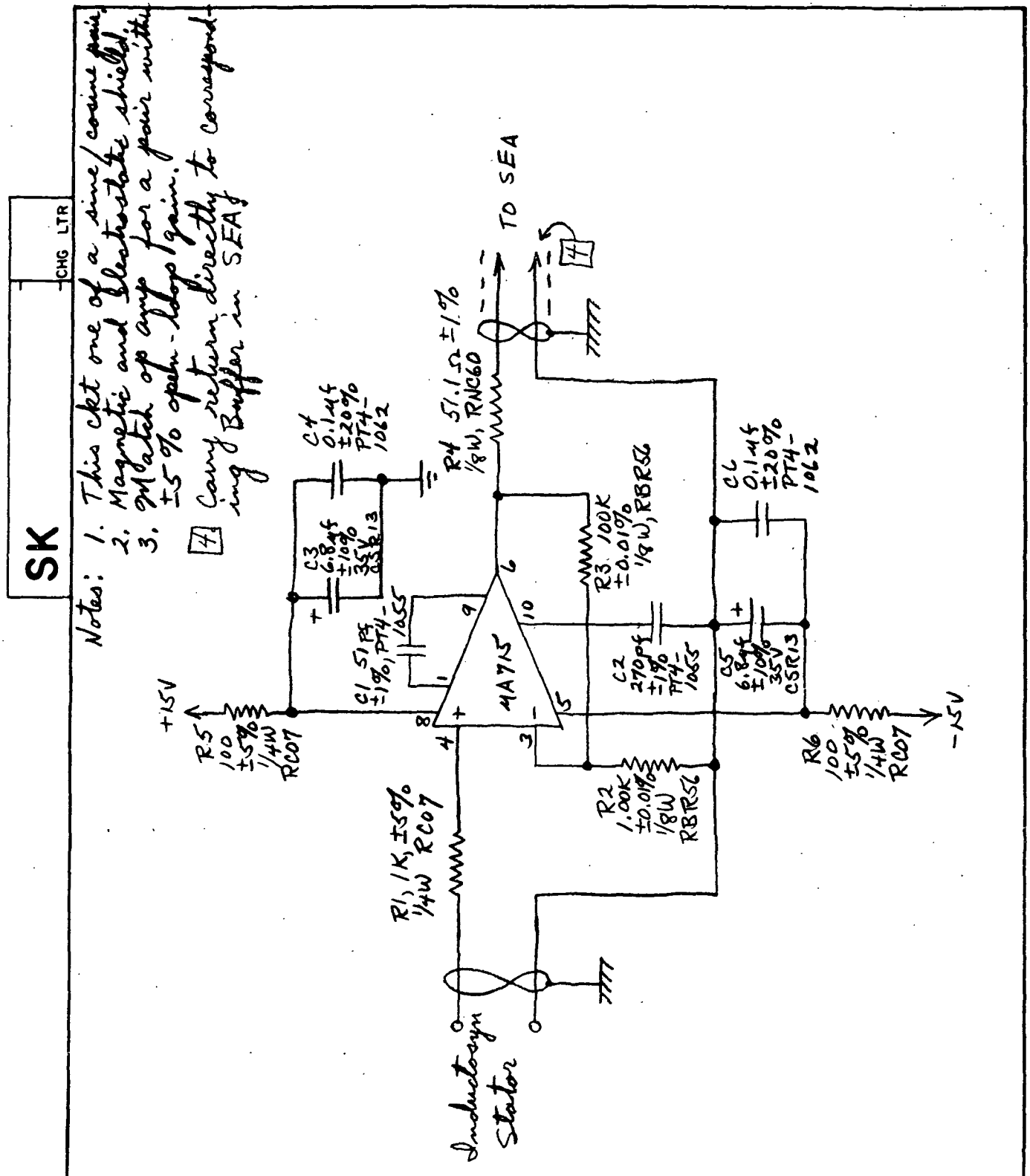

ORIGINATOR RJM	DATE 3/9/71	TITLE Preamplifier	ENGINEERING SKETCH.
A RJM	11/3/71		TRW SYSTEMS GROUP ONE SPACE PARK · REDONDO BEACH, CALIFORNIA
			SK-MA200A
MJO PADS/SEA			SHEET / OF

SYSTEMS 523 REV. 5-67

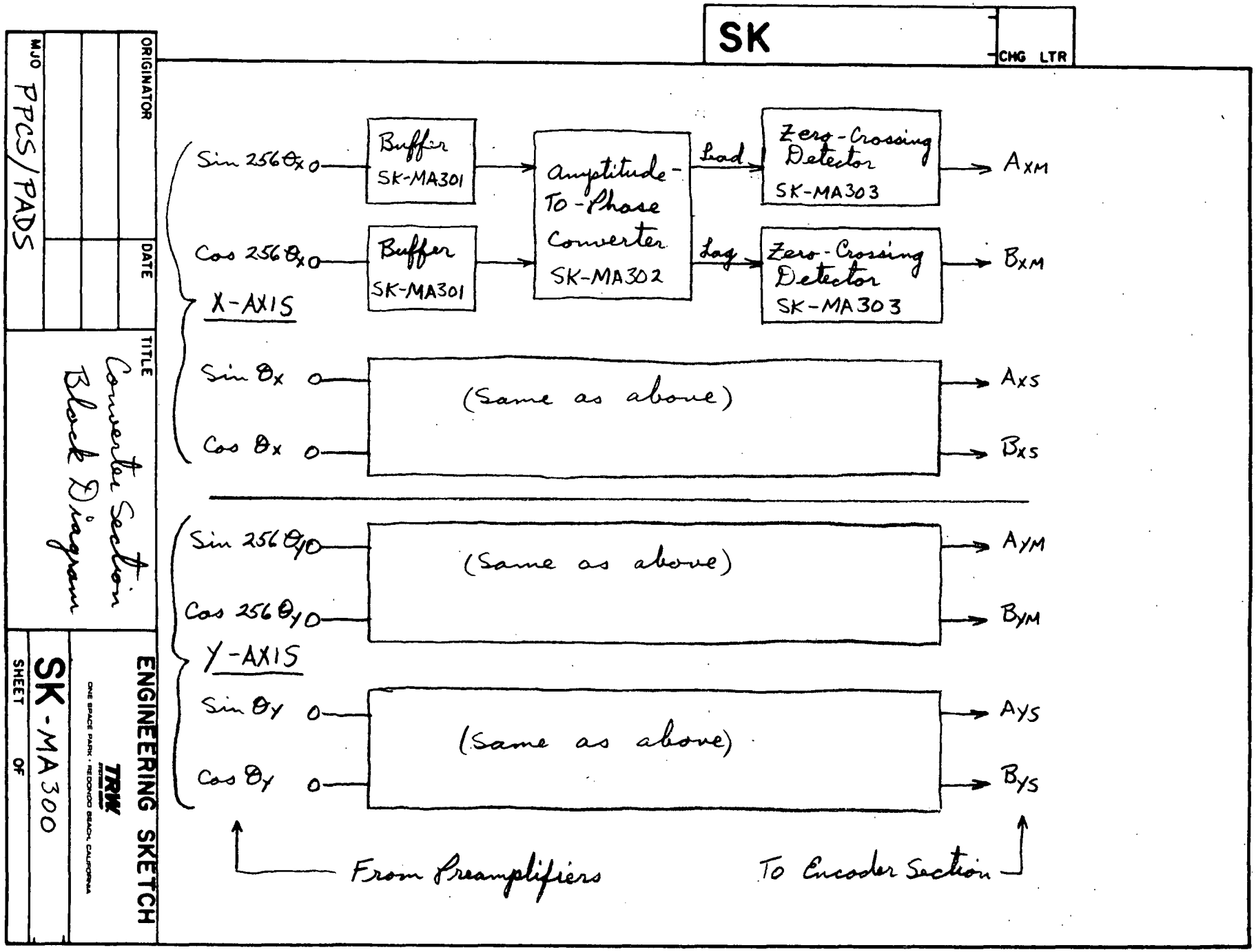
SK
CHG LTR
ORIGINATOR
MJO PPCS/PADS
DATE
TITLE
Converter Section Block Diagram
ENGINEERING SKETCH
SK-MA300
SHEET OF
TRW
ONE SPACE PARK · REDONDO BEACH, CALIFORNIA
SYSTEMS 528 REV. 5-67
Sin 256θx o
Cos 256θx o
Buffer SK-MA301
Buffer SK-MA301
Amplitude-To-Phase Converter SK-MA302
Lead
Lag
Zero-Crossing Detector SK-MA303
Zero-Crossing Detector SK-MA303
AXM
BXM
X-AXIS
Sin θx o
Cos θx o
(Same as above)
AXS
BXS
Sin 256θy o
Cos 256θy o
(Same as above)
AYM
BYM
Y-AXIS
Sin θy o
Cos θy o
(Same as above)
AYS
BYS
From Preamplifiers
To Encoder Section

SYSTEMS 823 REV. 5-67

ORIGINATOR	DATE	TITLE	ENGINEERING SKETCH
MJO	4/8/71	Output Buffer	SK-MA301
			SHEET 2 OF

TRW SYSTEMS — ONE SPACE PARK • REDONDO BEACH, CALIFORNIA

SK

CHG LTR

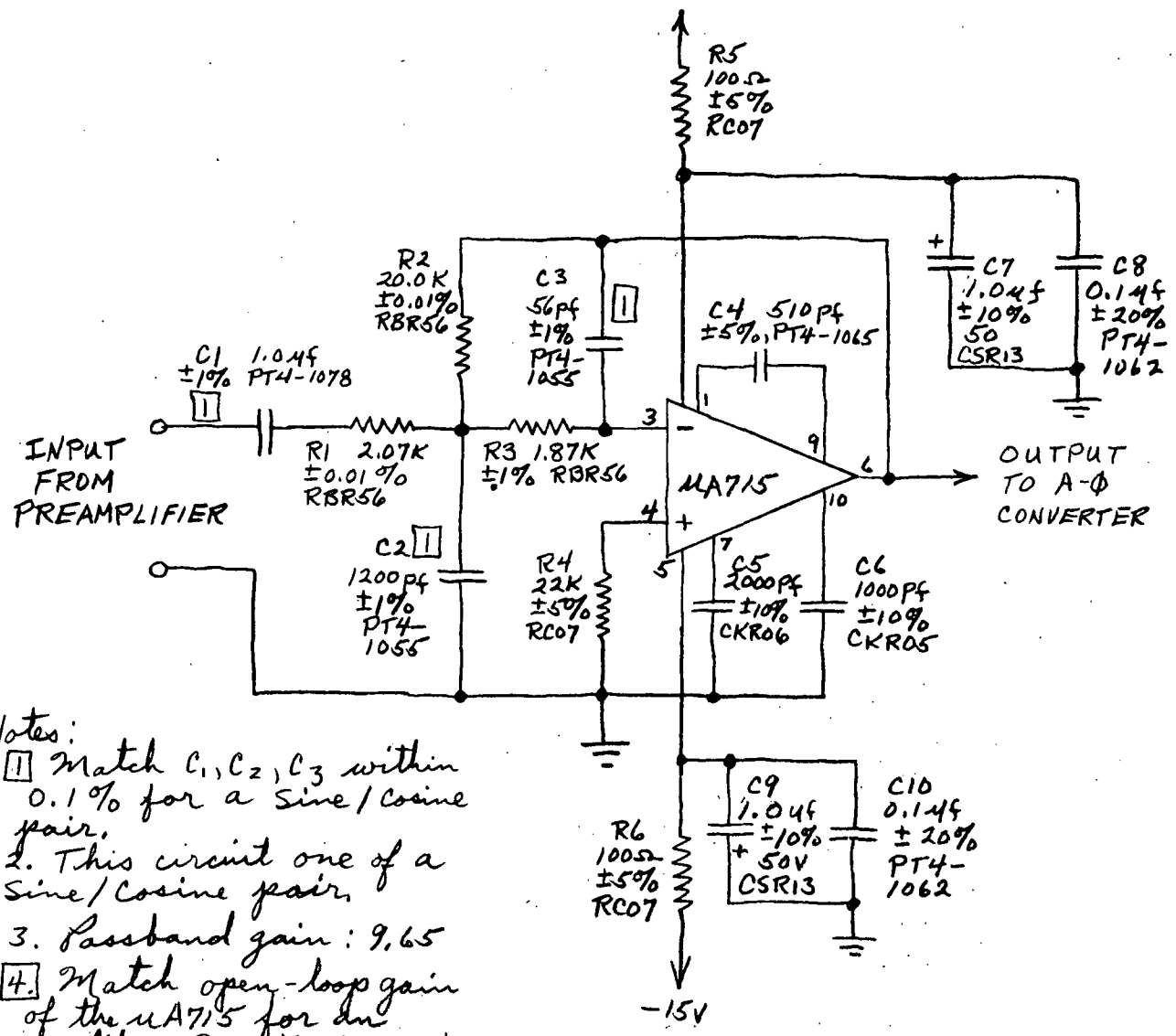

Notes:

1. Match C_1, C_2, C_3 within 0.1% for a Sine/Cosine pair.
2. This circuit one of a Sine/Cosine pair.
3. Passband gain: 9.65
4. Match open-loop gain of the μA715 for the amplifier Sine/Cosine pair to within ±5%.

SK
ENGINEERING SKETCH
TRW
ONE SPACE PARK • REDONDO BEACH • CALIFORNIA
SK-MA302A
SHEET 1 OF
TITLE
Amplitude-To-Phase Converter
DATE 11/12/11
ORIGINATOR "A"
M/O PADS/SEA
SINE
COSINE
FROM BUFFERS
LEAD (A)
LAG (B)
AR1 LM101A
AR2 LM101A
C2 0.1Mf ±20% PTH-1062
C3 0.1Mf ±20% PTH-1062
C4 0.1Mf ±20% PTH-1062
C5 0.1Mf ±20%
C1 0.015Mf ± 1% PTH-1078/2
C6 300PF ±10% CKR
C7 30PF ±10% CKR
C8 300PF ±10% CKR
C9 30PF ±10% CKR
R1 8.06K ±0.01% RBR52
R2 8.06K ±0.01% RBR52
R3 118K ±0.1% RBR52
R4 2.05K ±0.01% RB
R5 2.10K ±0.01% RBR52
R6 10.0Ω ±0.1% RBR52
R7 16.5K ±0.01% RBR52
R8 16.5K ±0.01% RBR52
R9 4.22K ±0.01% RBR52
R10 4.22K ±0.01% RBR52
R10 10K ±5% RC07
R9 10K ±5% RC07
+15V
-15V

SK

CHG LTR

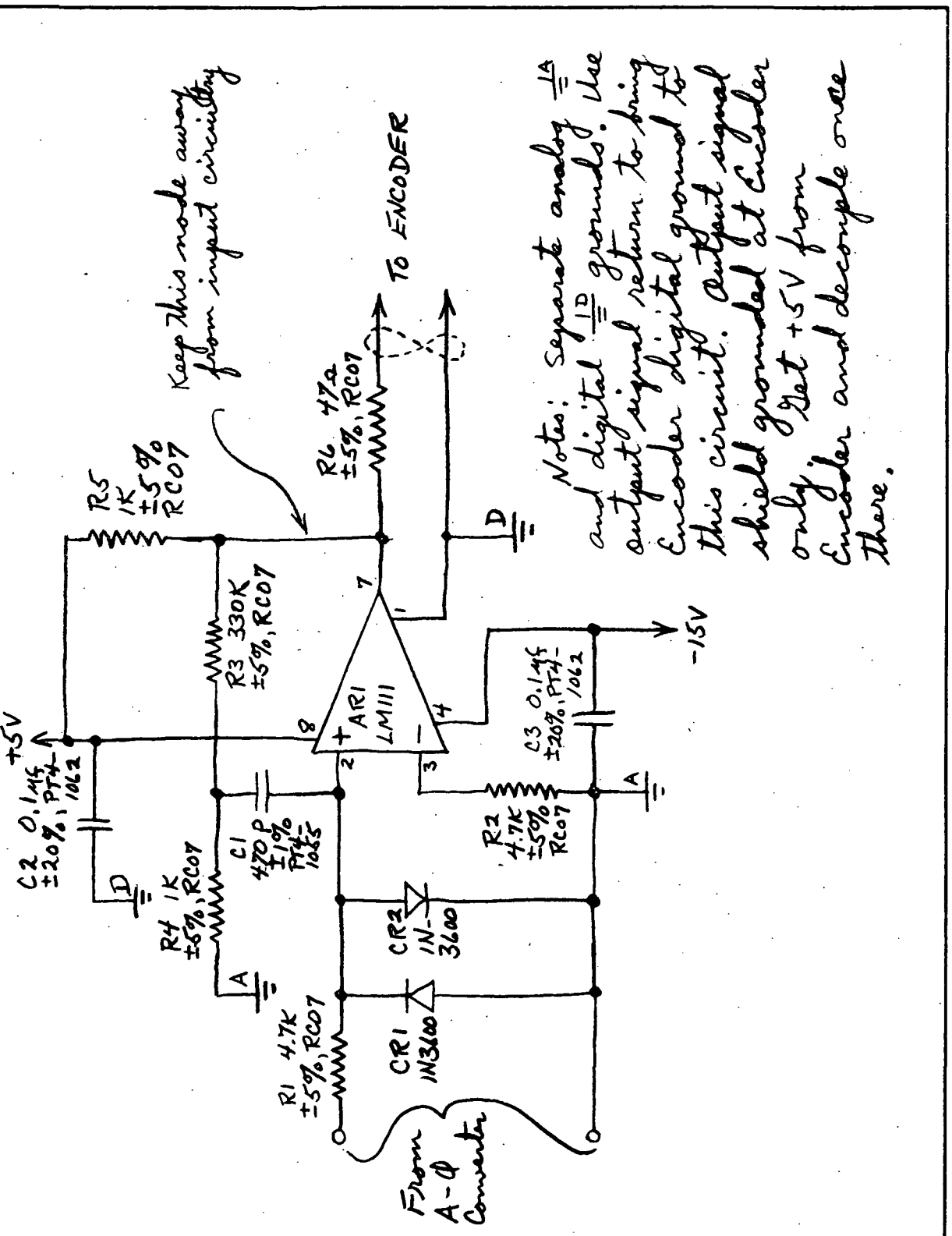

ORIGINATOR	DATE	TITLE	ENGINEERING SKETCH
KJM	11/1/71	Zero-Crossing Detector	TRW SYSTEMS GROUP, ONE SPACE PARK · REDONDO BEACH, CALIFORNIA
			SK-MA303A
MJO PADS/SEA		CODE IDENT NO. 11982	SHEET 1 OF

SYSTEMS 523 REV. 10-70

SK

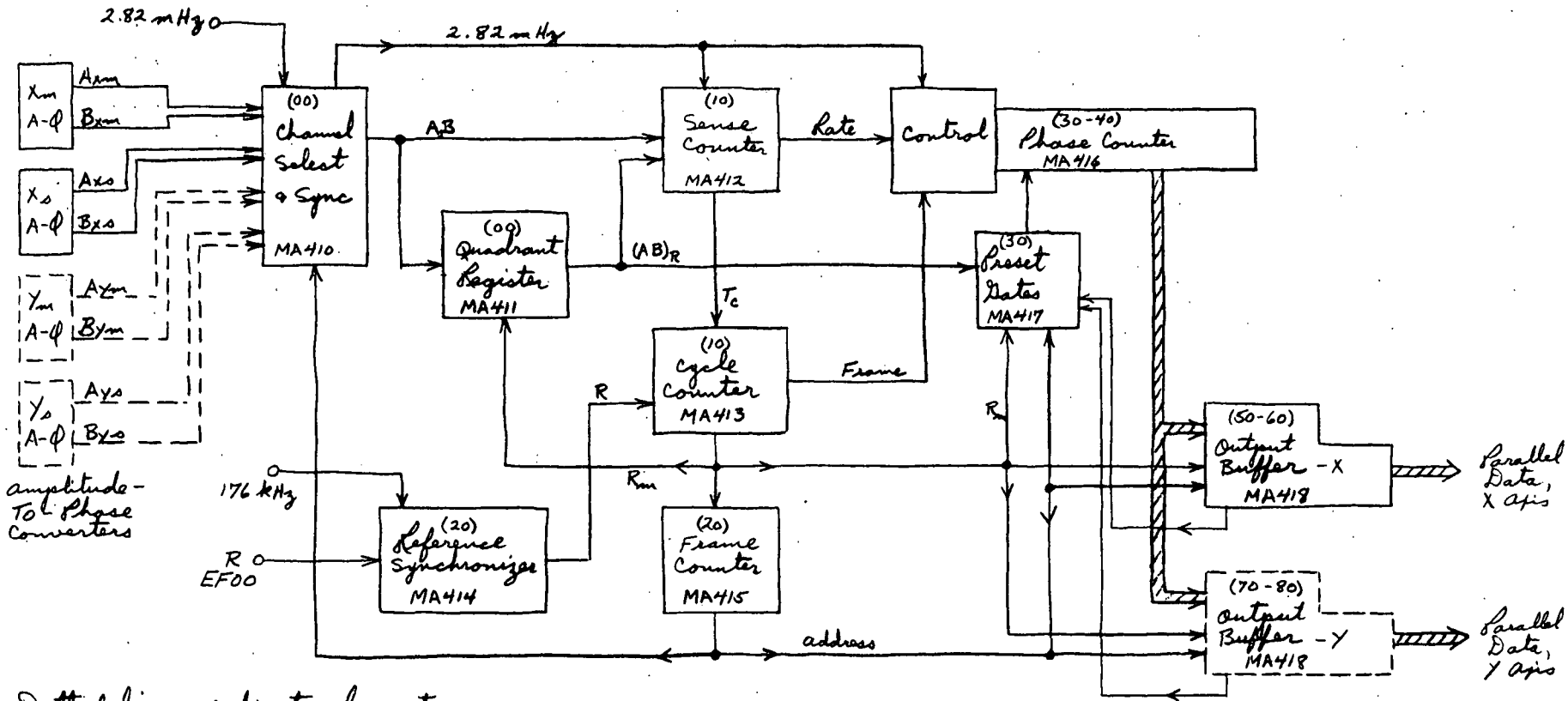

Dotted lines indicate elements for second axis. The A-ϕ converters are reference only and not part of the Encoder.

ORIGINATOR	DATE	TITLE	ENGINEERING SKETCH
Kjm	7/14/71	PADS ENCODER LOGIC (SENSOR ELECTRONICS ASSEMBLY)	TRW SYSTEMS GROUP, ONE SPACE PARK · REDONDO BEACH · CALIFORNIA
MJO PPCS/PADS			SK-MA400
			SHEET 1 OF

SYSTEMS 3003 REV. 9-67

SK

CHG LTR

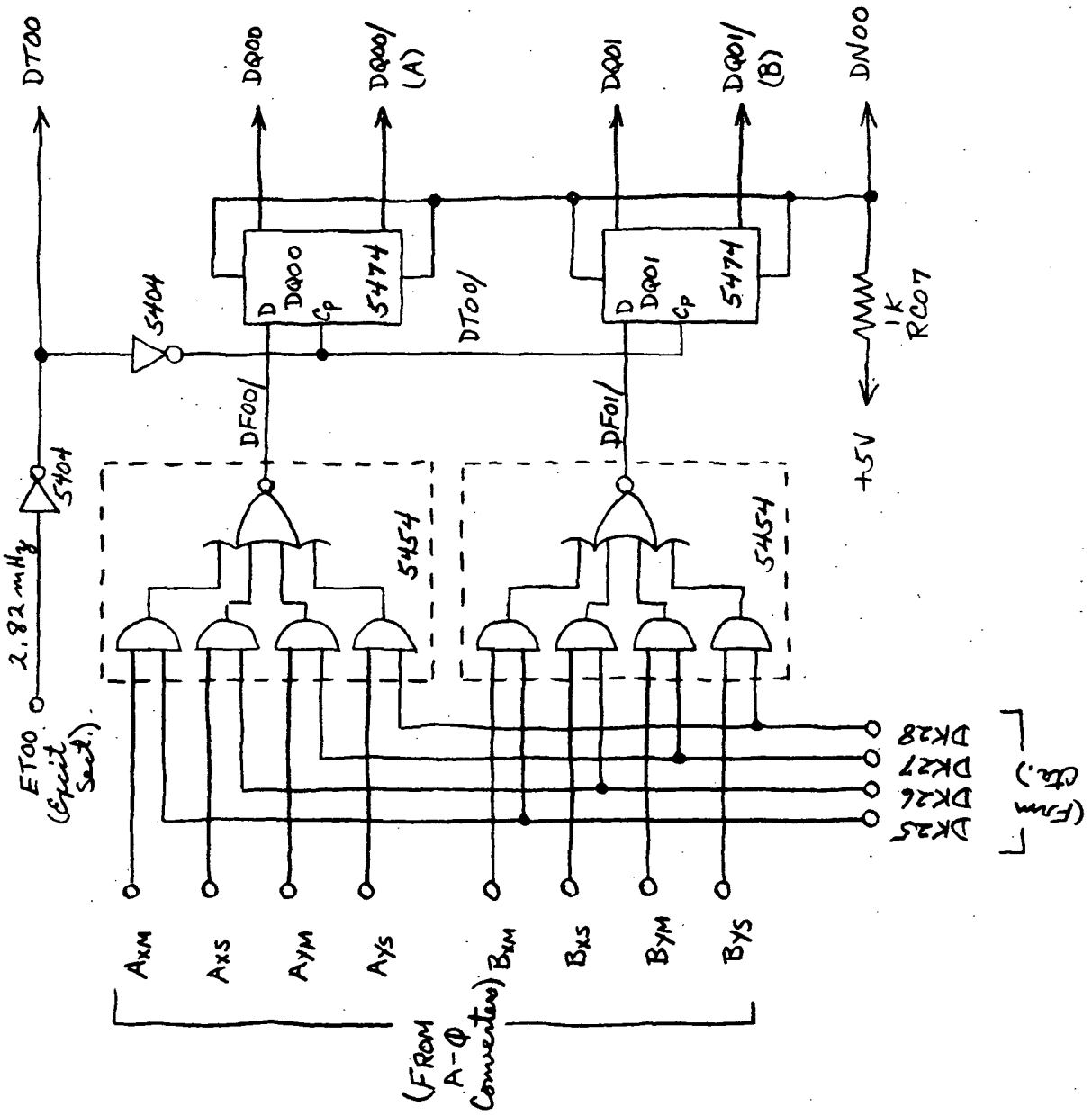

ORIGINATOR	DATE	TITLE	ENGINEERING SKETCH
KJM	7/2/71	Channel Select & Sync.	TRW SYSTEMS GROUP, ONE SPACE PARK • REDONDO BEACH, CALIFORNIA
			SK-MA410
MJO PPCS/PADS			SHEET 1 OF

SYSTEMS 523 REV. 5-67

SK

CHG LT

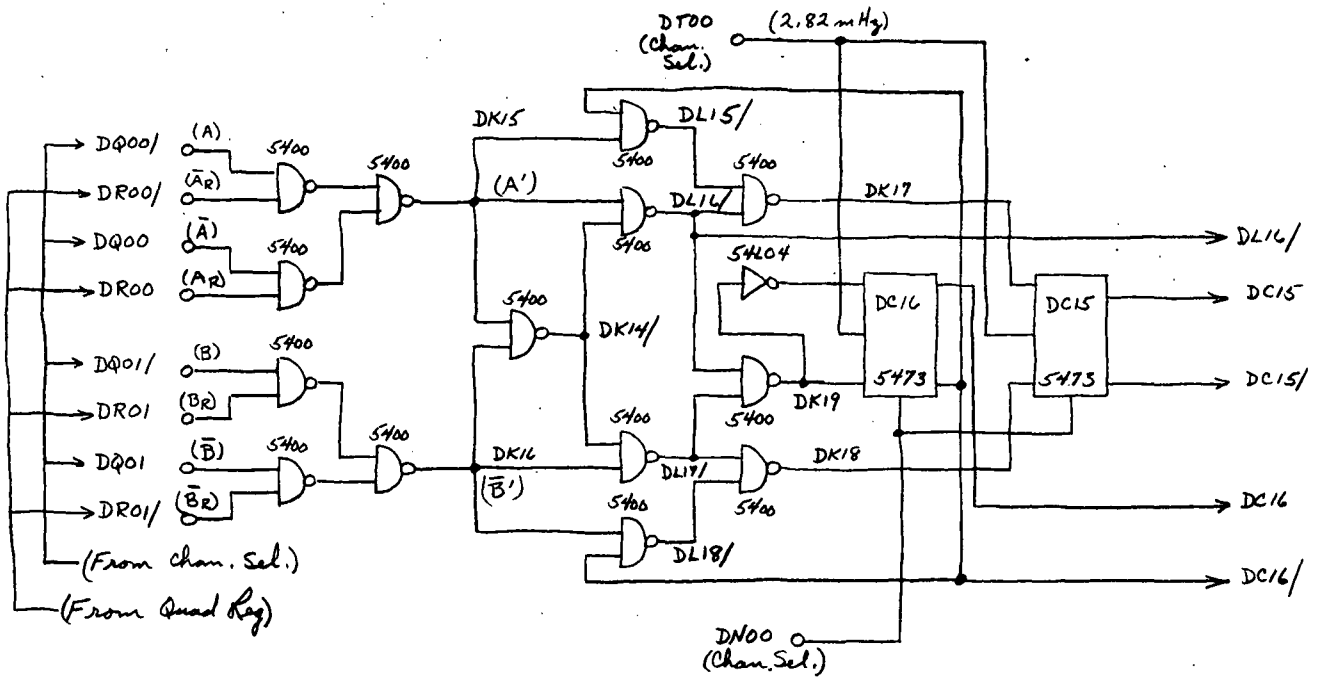

ORIGINATOR	DATE	TITLE
[signature]	7/6/71	Sense Counter
MJC PPCS/PADS		

ENGINEERING SKETCH

TRW SYSTEMS GROUP

ONE SPACE PARK • REDONDO BEACH • CALIFORNIA

SK-MA412

SHEET 1 OF

SYSTEMS 8565 REV. 6-67

SK

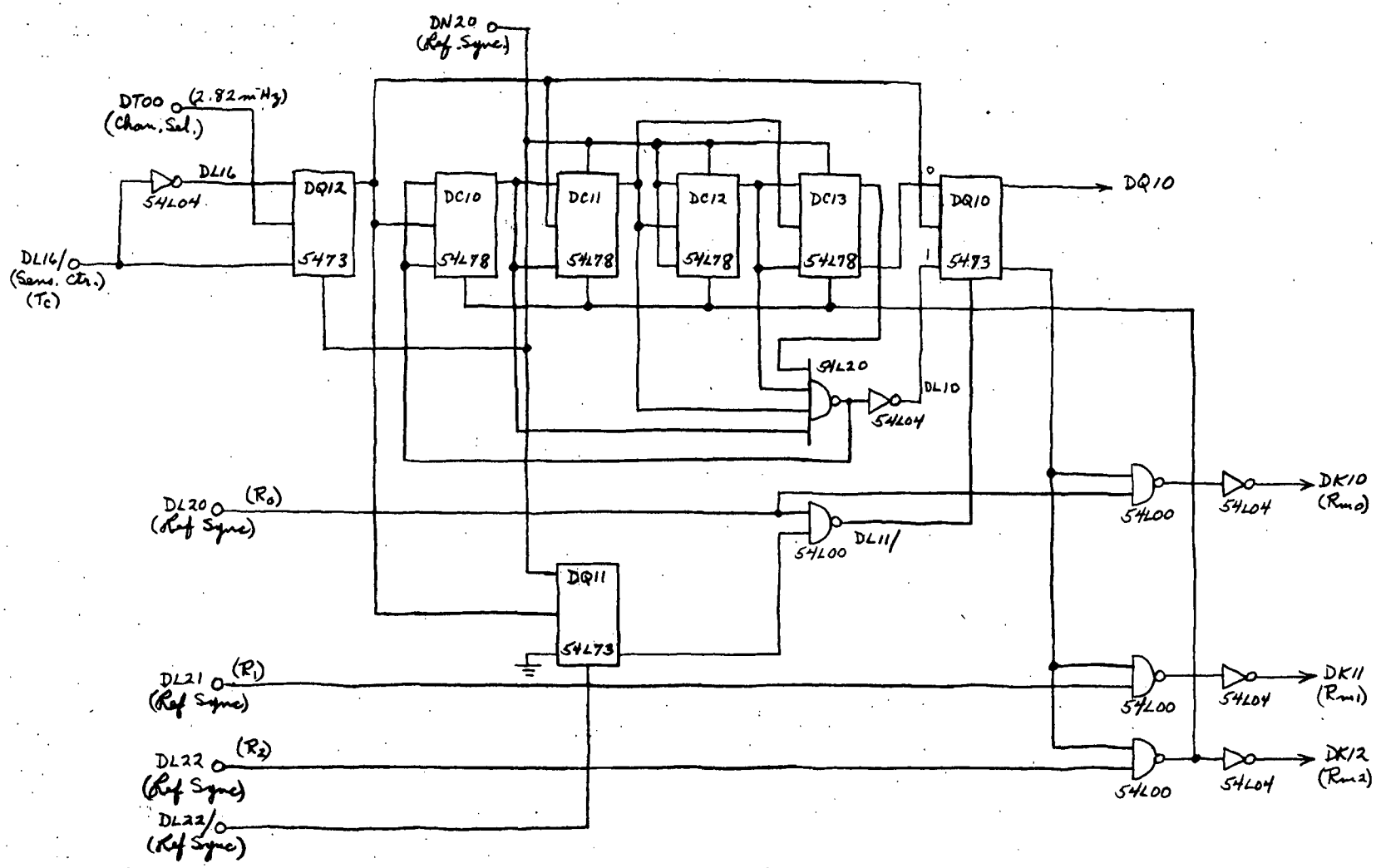

ORIGINATOR	DATE	TITLE	ENGINEERING SKETCH
[illegible]	6/23/71	Cycle Counter	TRW SYSTEMS GROUP, ONE SPACE PARK • REDONDO BEACH • CALIFORNIA
			SK-MA413
MJO PPCS/PADS			SHEET 1 OF

SK

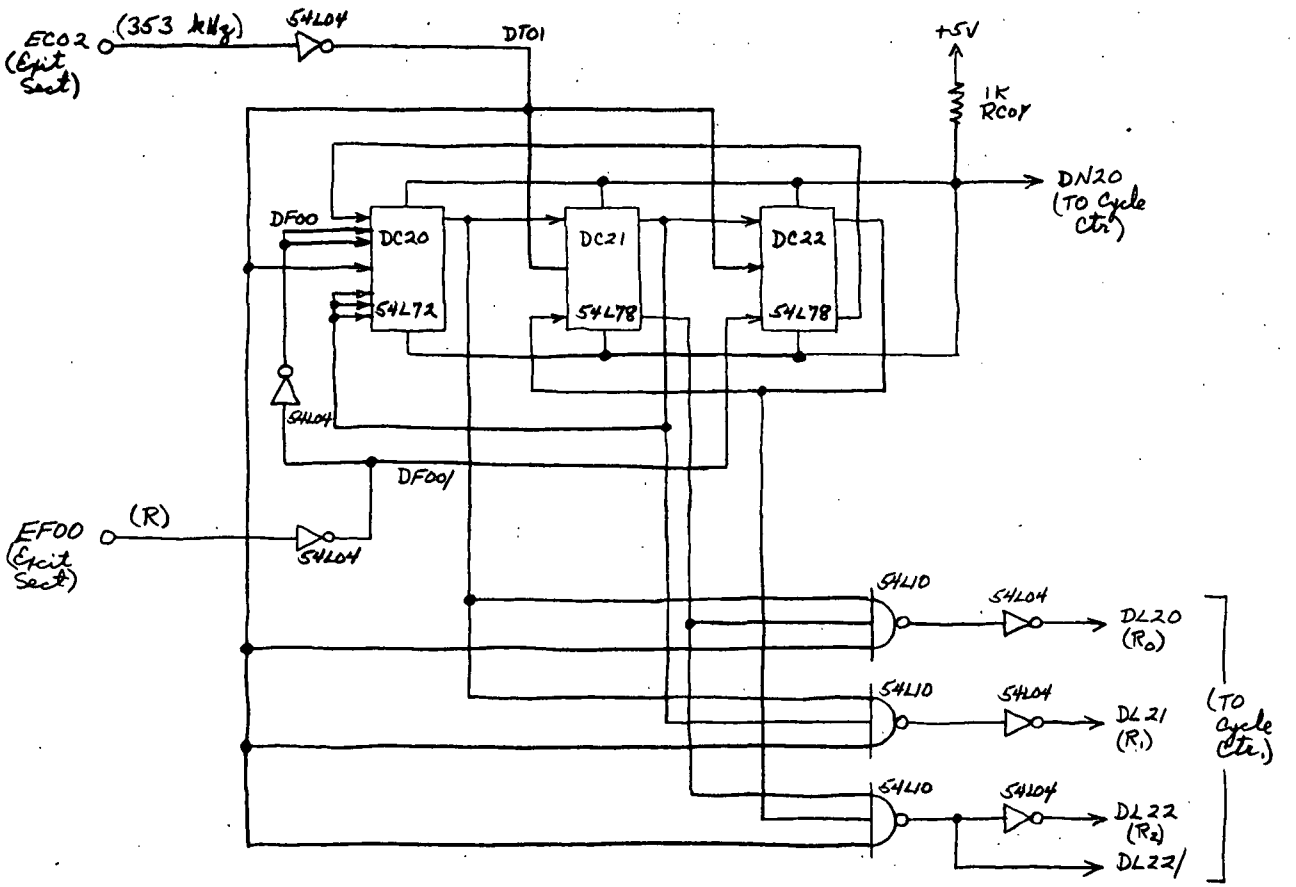

ORIGINATOR	DATE	TITLE
Rfm	9/30/71	Reference Synchronizer
MJO PPCS/PADS		

ENGINEERING SKETCH
TRW SYSTEMS GROUP
ONE SPACE PARK · REDONDO BEACH · CALIFORNIA

SK-MA414

SHEET 1 OF

SK

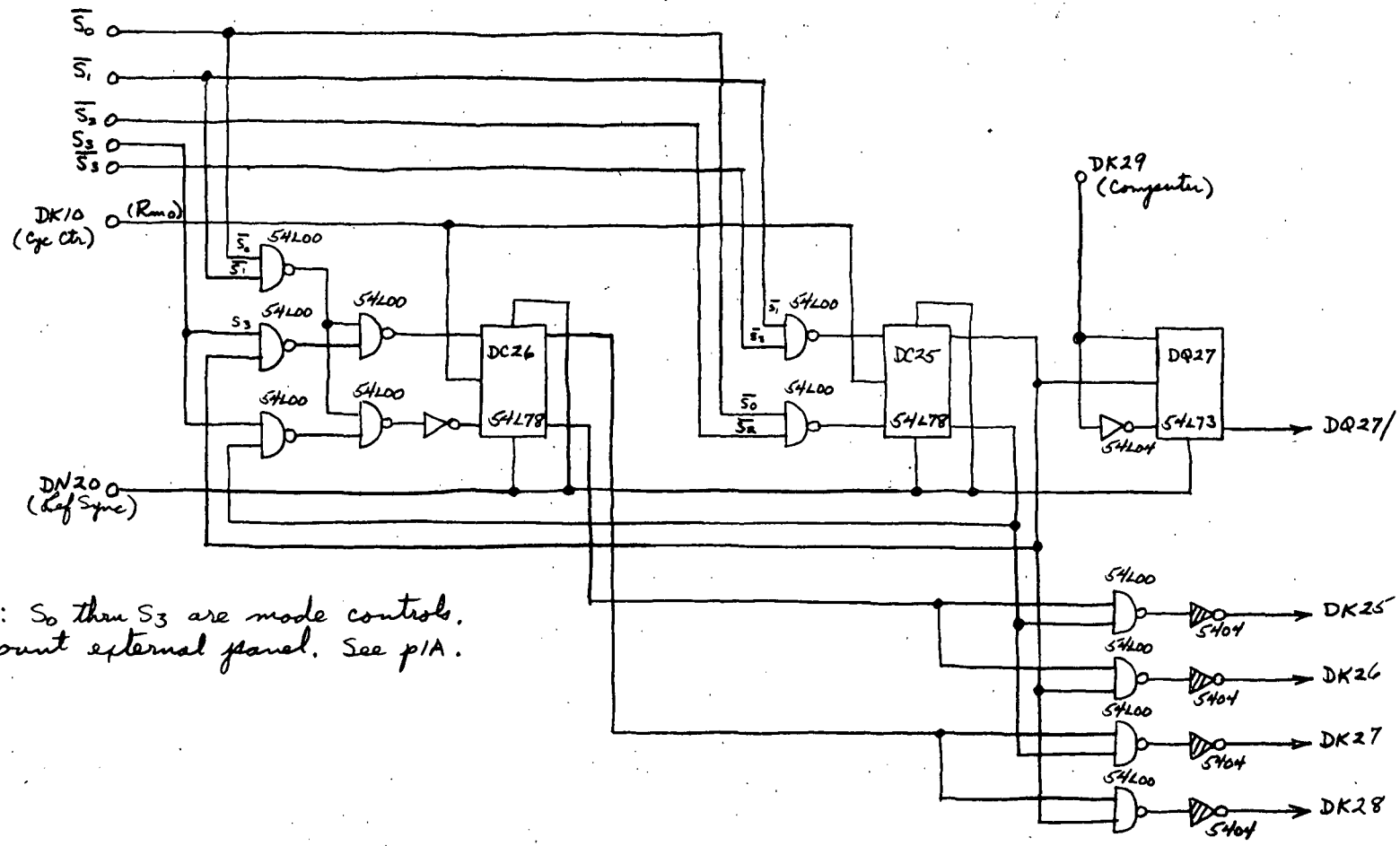

Note: S_0 thru S_3 are mode controls. Mount external panel. See p1A.

ORIGINATOR RJM	DATE 7/13/71	TITLE Frame Counter	ENGINEERING SKETCH TRW SYSTEMS GROUP ONE SPACE PARK · REDONDO BEACH · CALIFORNIA
			SK – MA 415
MJO PPCS/PADS			SHEET 1 OF

SK

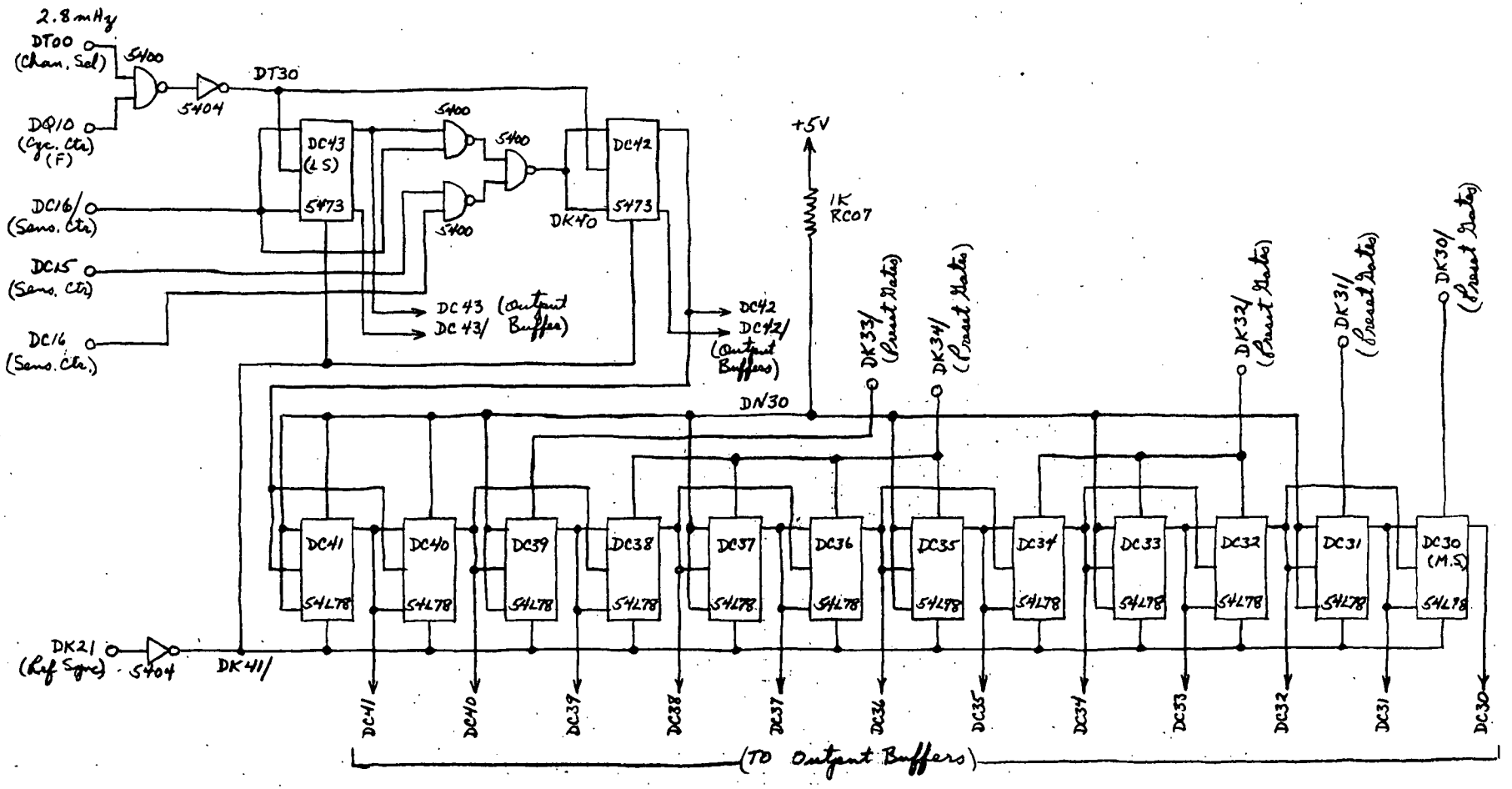

ORIGINATOR	DATE	TITLE
[illegible]	6/5/71	Phase Counter
MJO PPCS/PADS		

ENGINEERING SKETCH
TRW
ONE SPACE PARK • REDONDO BEACH • CALIFORNIA
SK - MA416
SHEET 1 OF

CHG LTR

SK

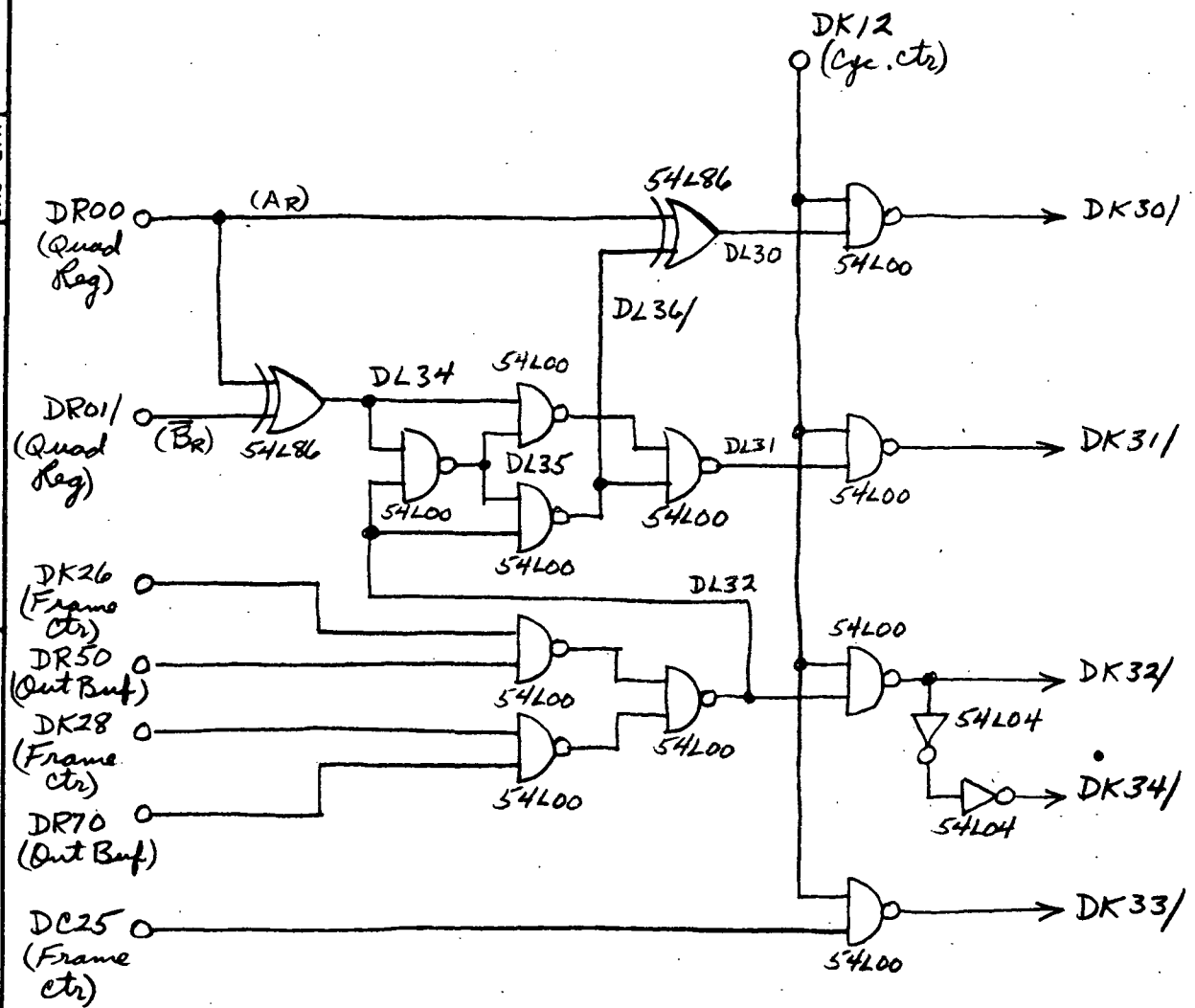

Note: DR70 doesn't exist for one apis breadboard. Leave open.

ORIGINATOR	DATE	TITLE	ENGINEERING SKETCH
KJM	7/4/71	Reset Gates	TRW SYSTEMS GROUP, ONE SPACE PARK · REDONDO BEACH, CALIFORNIA
			SK-MA417
MJO PPCS/PADS			SHEET 1 OF

SYSTEMS 528 REV. 5-67

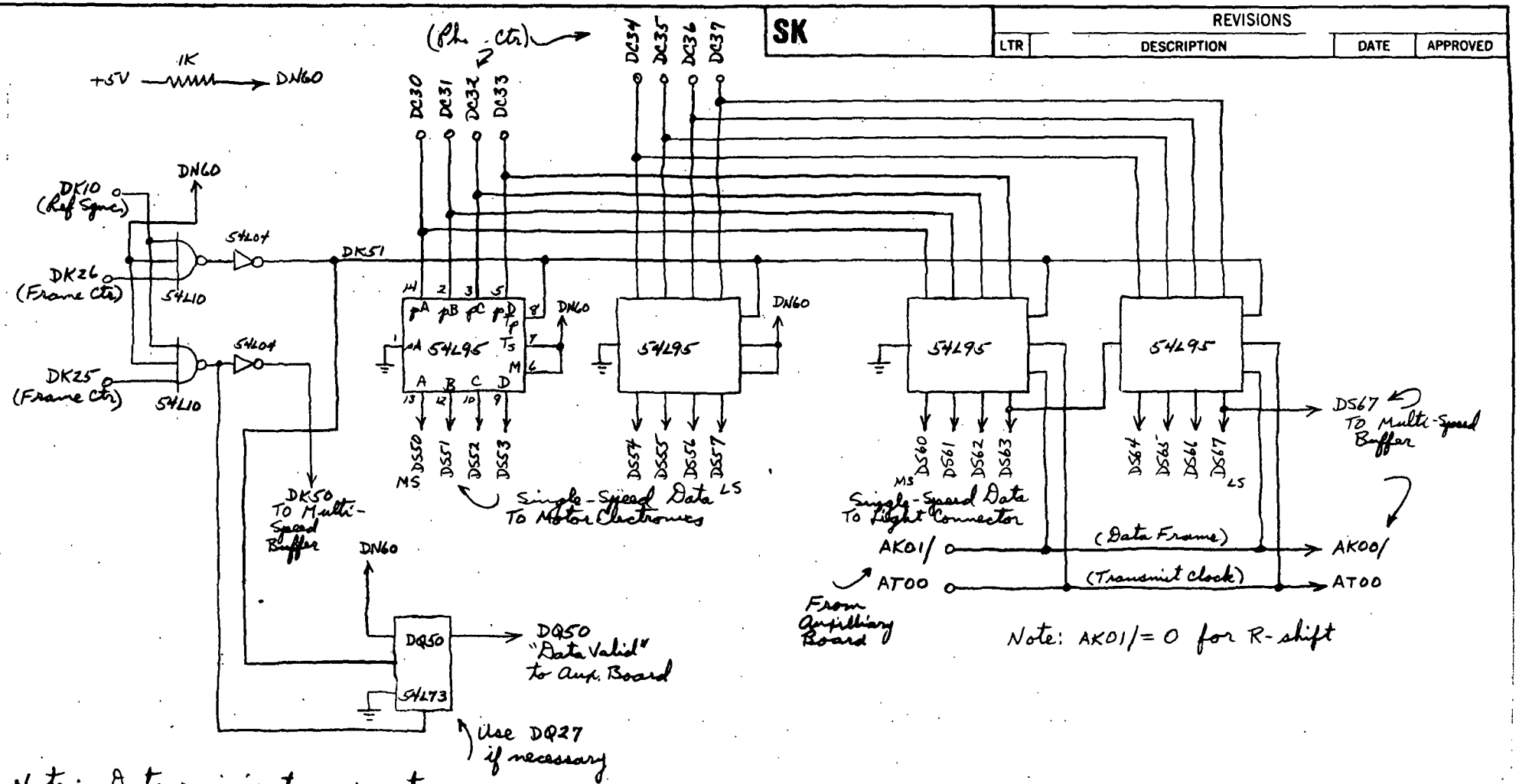
SK
REVISIONS
LTR
DESCRIPTION
DATE
APPROVED
(Phase Ctr.)
DC30
DC31
DC32
DC33
DC34
DC35
DC36
DC37
+5V
1K
DN60
DK10
(Ref Sync.)
DK26
(Frame Ctr.)
DK25
(Frame Ctr.)
54L04
54L10
DK51
54L95
DS50
DS51
DS52
DS53
DS54
DS55
DS56
DS57
DS60
DS61
DS62
DS63
DS64
DS65
DS66
DS67
MS
LS
DK50
TO Multi-Speed Buffer
Single-Speed Data
To Motor Electronics
Single-Speed Data
To Flight Connector
DS67
TO Multi-Speed Buffer
AK01/
AT00
(Data Frame)
(Transmit clock)
AK00/
AT00
From Auxiliary Board
Note: AK01/ = 0 for R-shift
DQ50
"Data Valid"
to Aux. Board
54L73
Use DQ27
if necessary
Note: Data recipient may not initiate data request, AK00/ when DQ50 is LOW.
ENGINEERING SKETCH
ORIGINATOR
A
DATE
3/31/72
MJO
PADS/SEA
TRW
SYSTEMS GROUP
ONE SPACE PARK • REDONDO BEACH, CALIFORNIA
Output Buffer
SIZE
B
CODE IDENT NO.
11982
SK-MA418A
SCALE
SHEET 1 OF
SYSTEMS 3663 REV. 12-7

SK	REVISIONS			
	LTR	DESCRIPTION	DATE	APPROVED

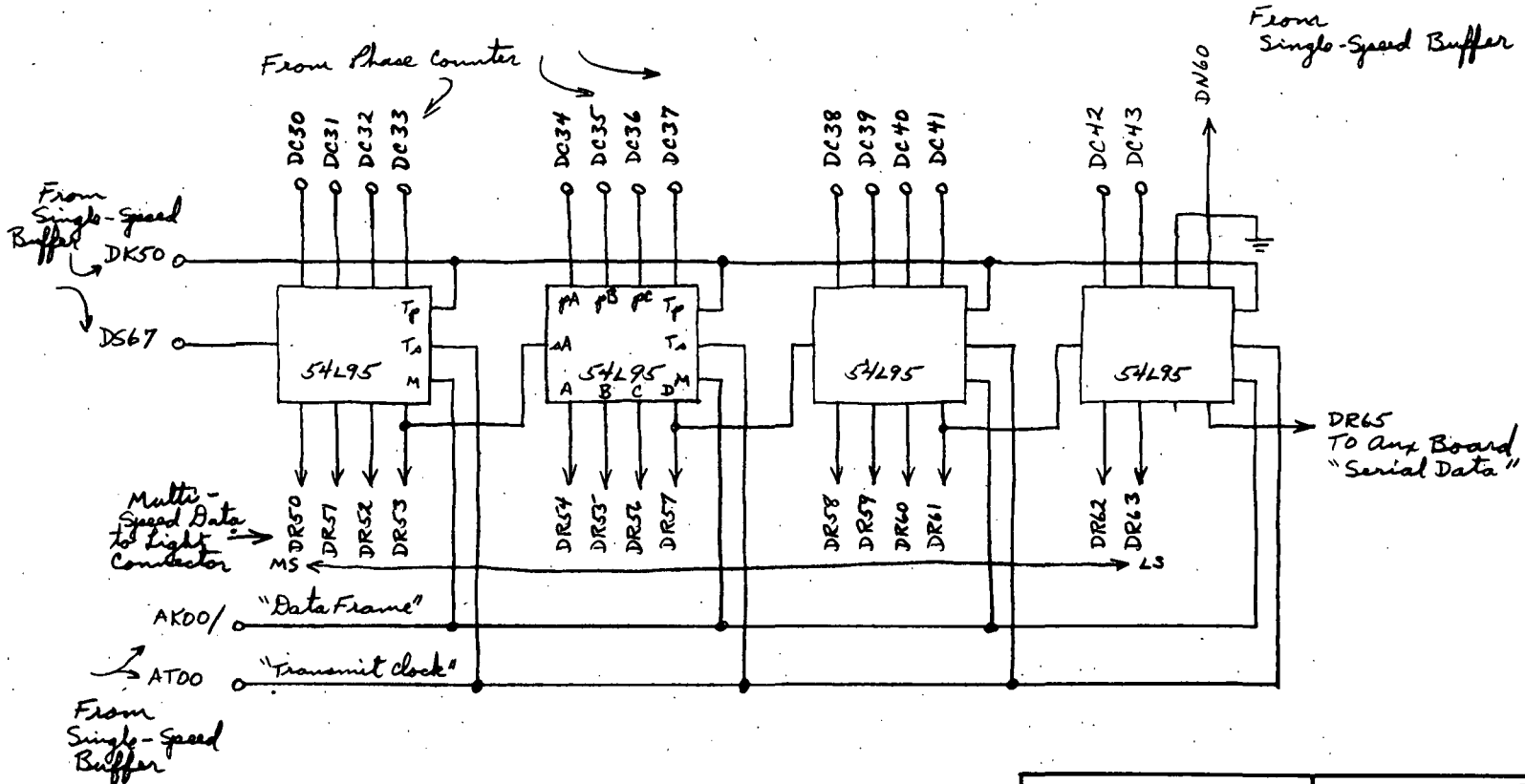

ENGINEERING SKETCH		TRW SYSTEMS GROUP ONE SPACE PARK • REDONDO BEACH, CALIFORNIA		
ORIGINATOR	DATE			
MJO		SIZE B	CODE IDENT NO. 11982	SK-MA418A
		SCALE		SHEET 2 OF

SYSTEMS 3663 REV. 12-71

SK

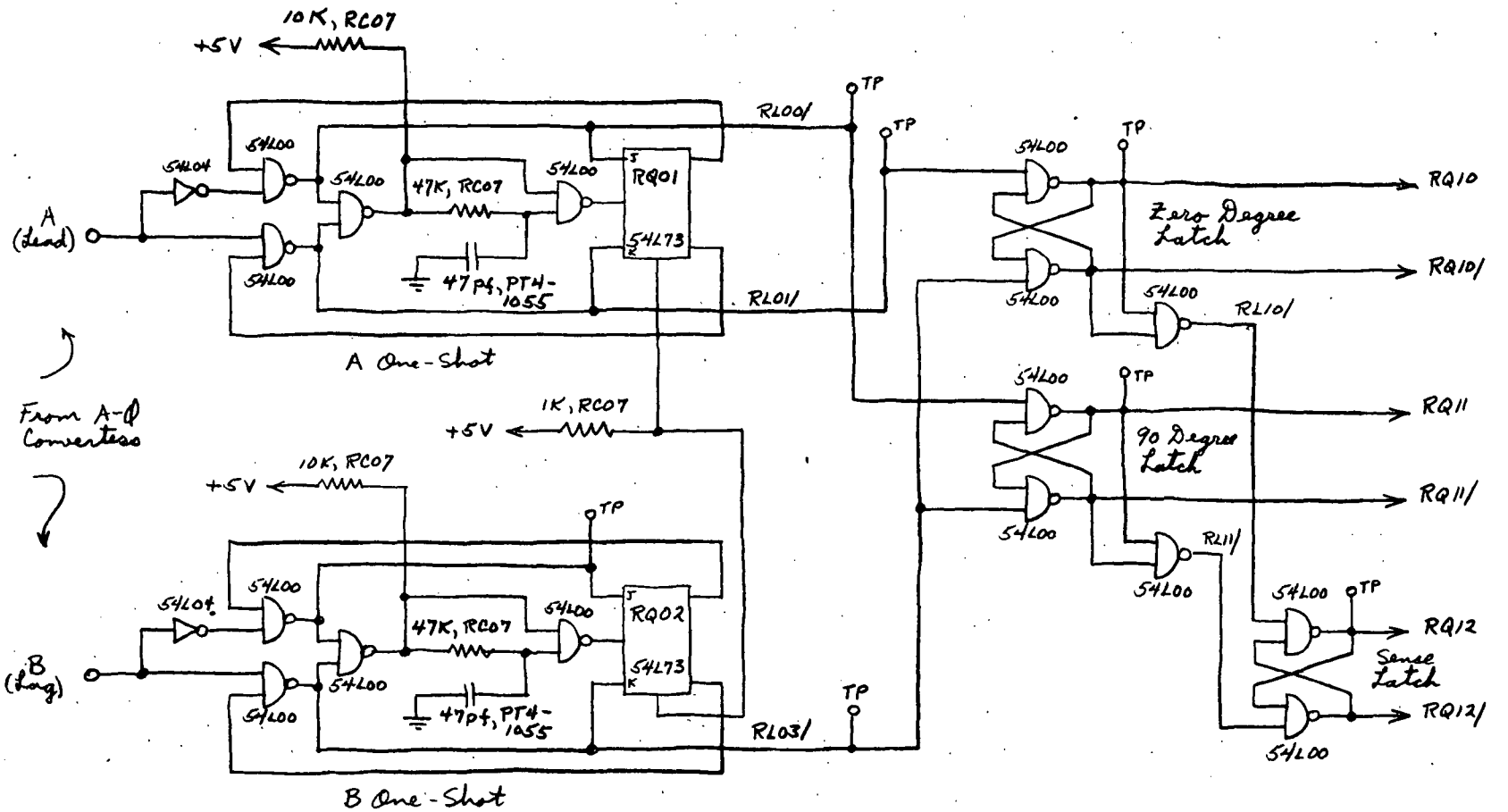

ORIGINATOR	DATE
Kym A	12/8/71
MJO PADS/SEA	

TITLE: Late Logic

ENGINEERING SKETCH
TRW SYSTEMS GROUP
ONE SPACE PARK · REDONDO BEACH · CALIFORNIA

SK-MA501A

SHEET 1 OF

SK

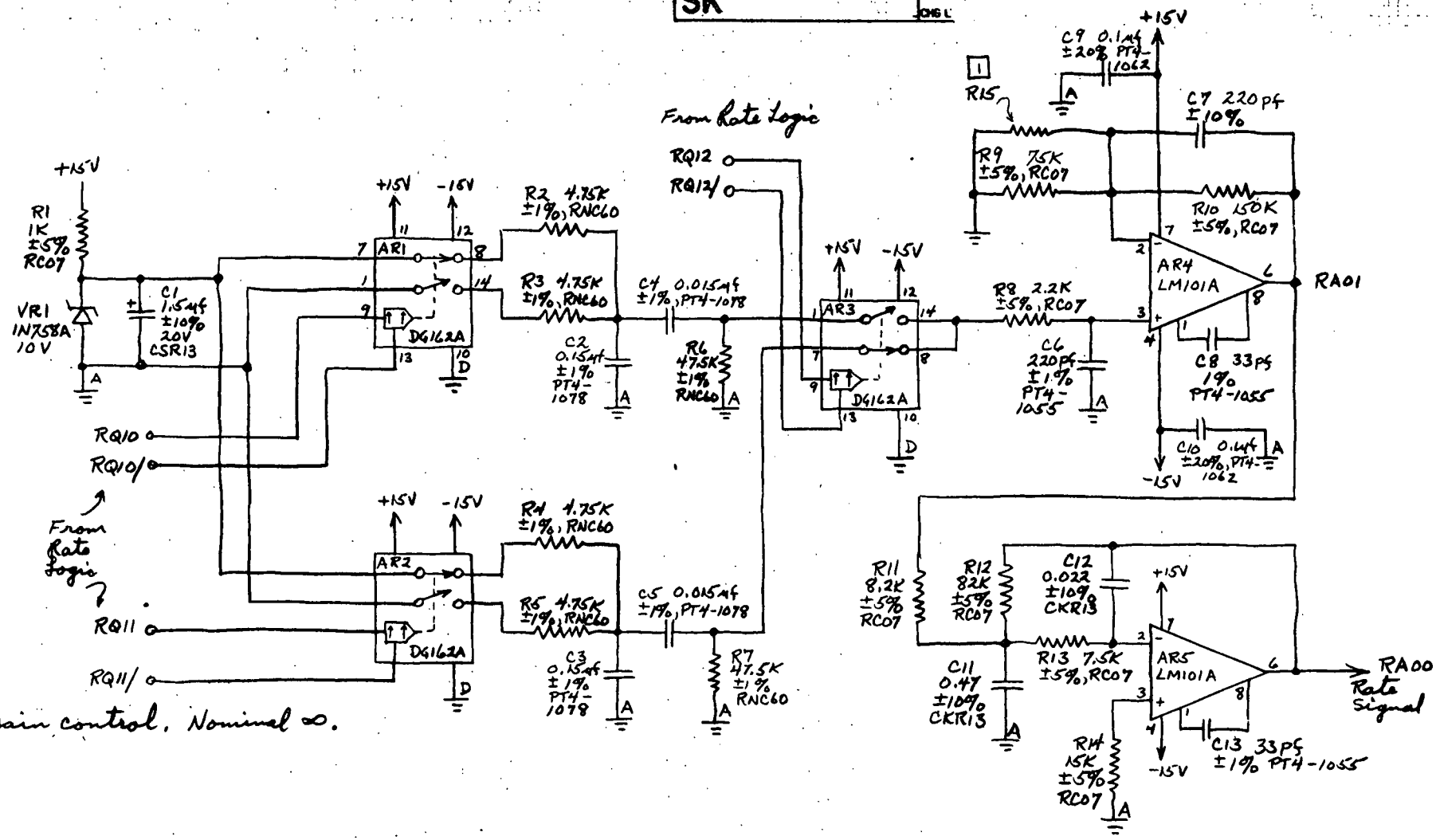

Notes:
[1] R15: Gain control. Nominal ∞.

ORIGINATOR RJM	DATE 12/10/71	TITLE Rate Analog Processing	ENGINEERING SKETCH TRW SYSTEMS GROUP ONE SPACE PARK · REDONDO BEACH · CALIFORNIA
			SK-MA502A
MJO PADS/SEA			SHEET / OF

SYSTEMS 528 REV. 5-67

SK

CHG LTR

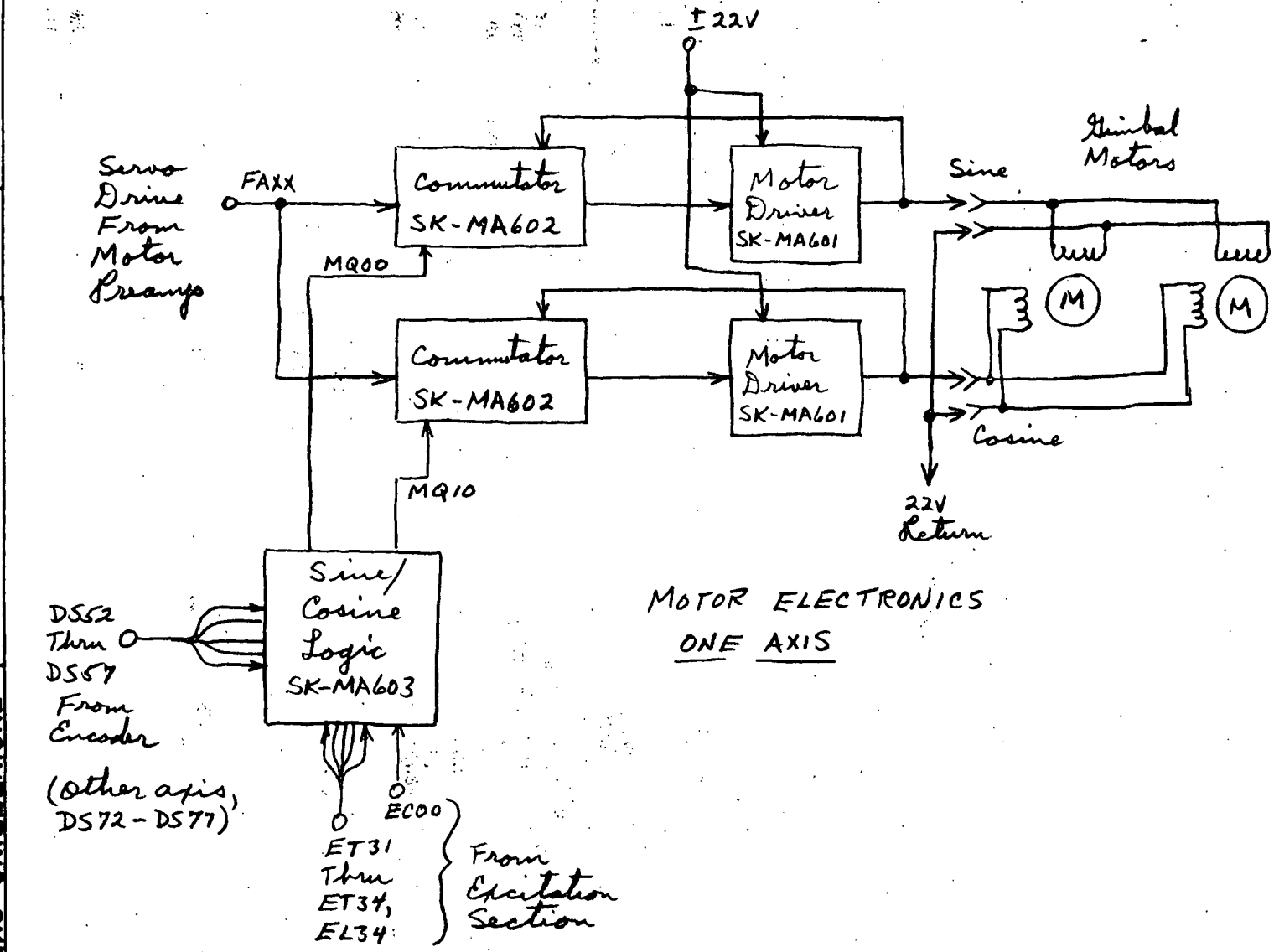

ORIGINATOR	DATE
DJM	8/9/71
A DJM	10/21/71

MJO PADS/SEA

TITLE Motor Electronics

ENGINEERING SKETCH

TRW SYSTEMS — ONE SPACE PARK · REDONDO BEACH, CALIFORNIA

SK-MA600A

SHEET / OF

CHG LTR

SK

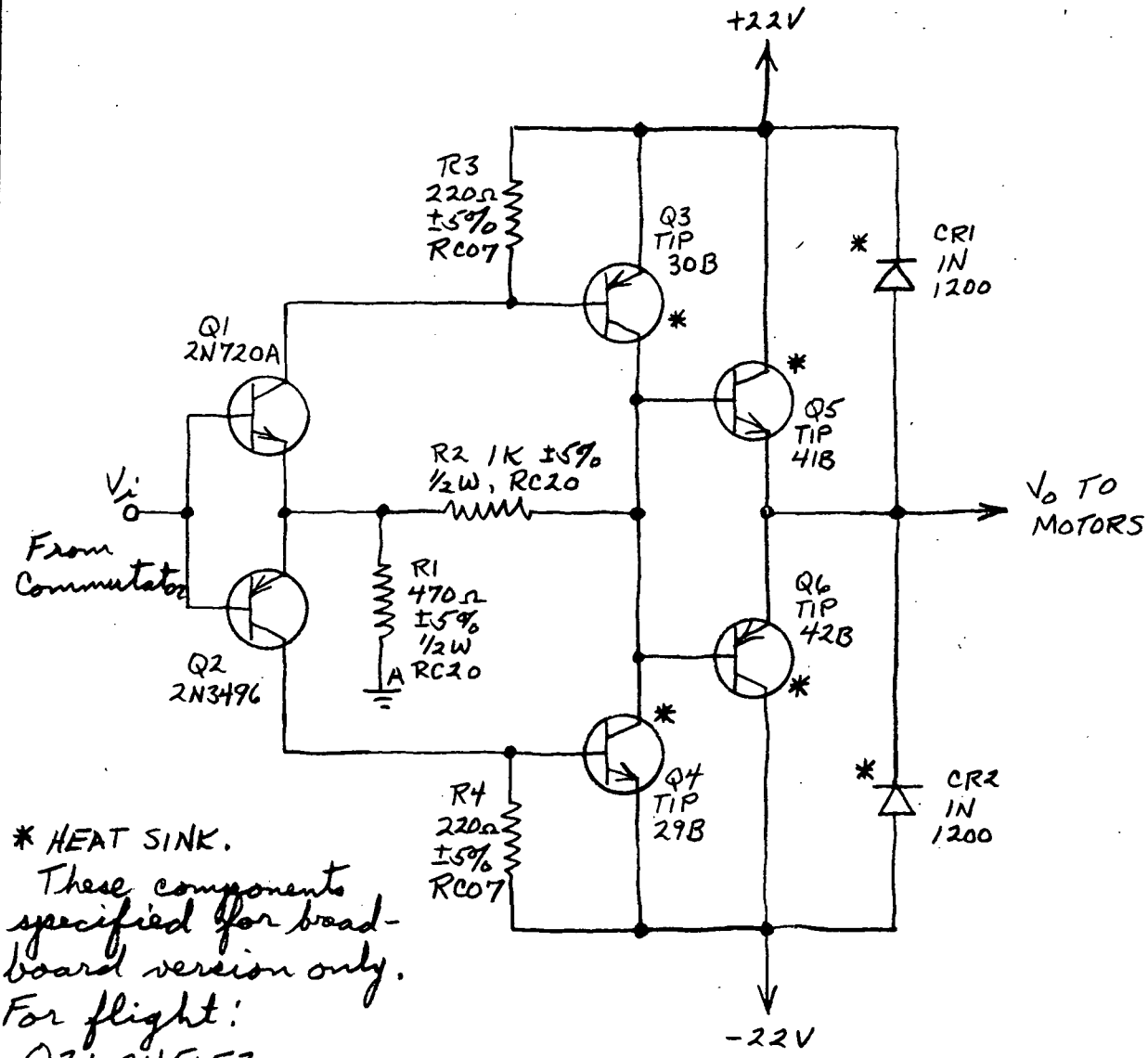

* HEAT SINK.
These components specified for bread-board version only.
For flight:
Q3: 2N5153
Q4: 2N5754
Q5: 2N5004
Q6: 2N5005
CR1, 2: 1N3893

ORIGINATOR	DATE	TITLE	ENGINEERING SKETCH
KJM	10/11/71	Motor Driver	TRW SYSTEMS GROUP, ONE SPACE PARK · REDONDO BEACH, CALIFORNIA
			SK-MA601 A
MJO PADS/SEA			SHEET 1 OF

SYSTEMS 523 REV. 5-67

SK

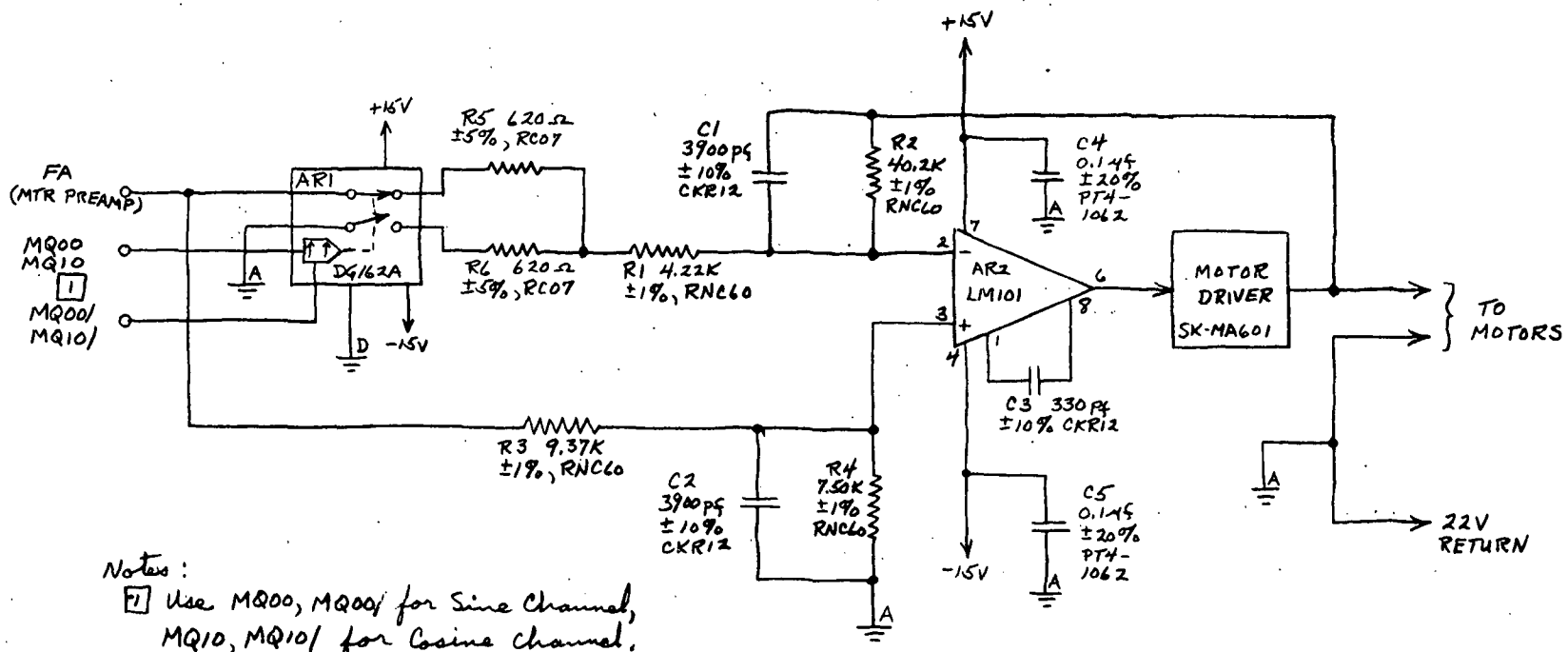

Notes:

[1] Use MQ00, MQ00/ for Sine Channel, MQ10, MQ10/ for Cosine Channel.

ORIGINATOR MJO PADS/SEA	DATE 10/20/71	TITLE Commutator	ENGINEERING SKETCH TRW SYSTEMS GROUP ONE SPACE PARK • REDONDO BEACH • CALIFORNIA
			SK-MA602A
			SHEET / OF

SYSTEMS 8503 REV. 5-67

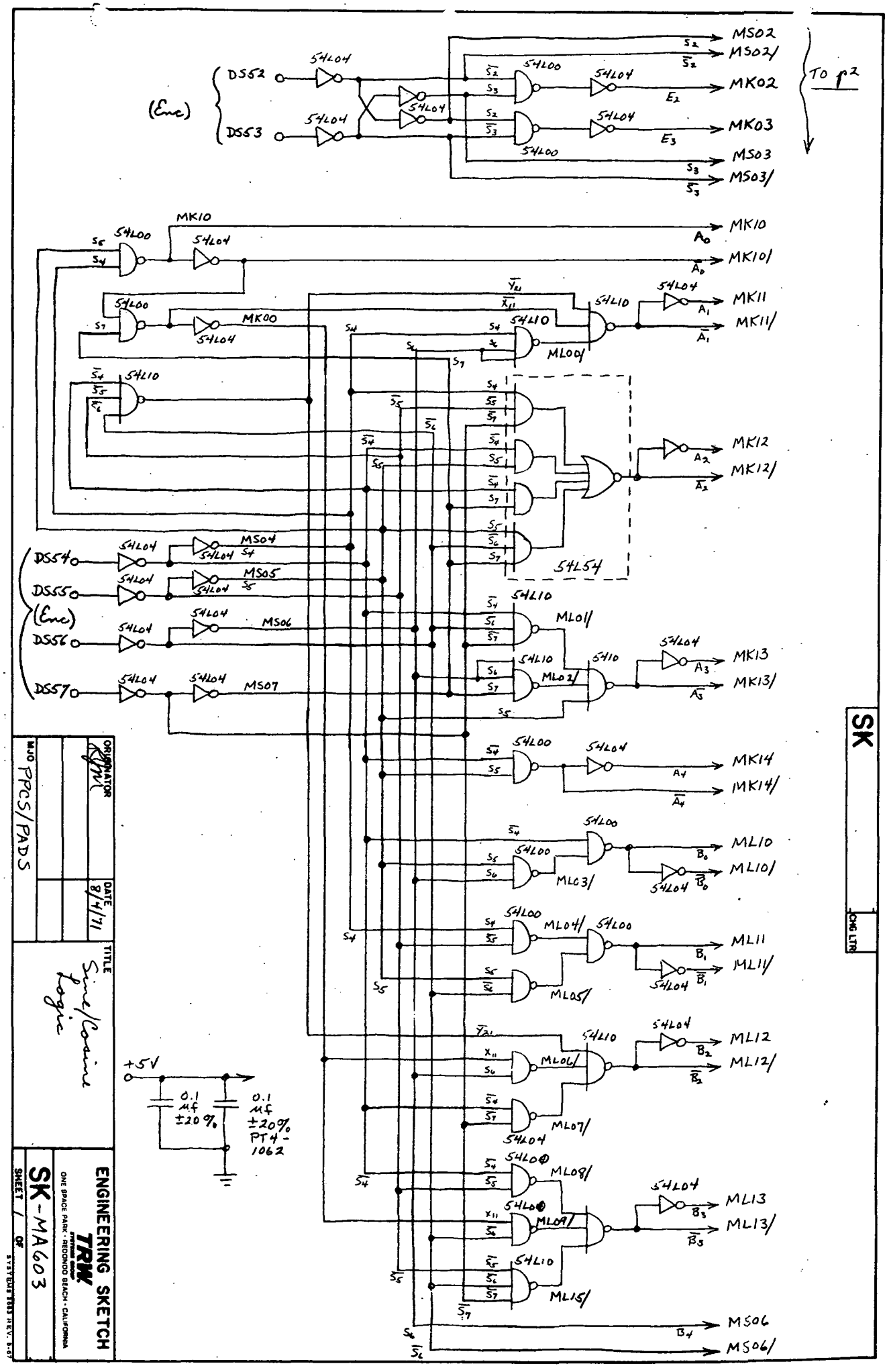
MS02
MS02/
MK02
MK03
MS03
MS03/
TO P2
(Enc)
DS52
DS53
54L04
54L00
54L10
MK10
MK10/
MK11
MK11/
MK00
MK12
MK12/
54L54
MS04
MS05
MS06
MS07
DS54
DS55
DS56
DS57
ML01/
ML02/
MK13
MK13/
MK14
MK14/
ML10
ML10/
ML03/
ML11
ML11/
ML04/
ML05/
ML12
ML12/
ML06/
ML07/
ML13
ML13/
ML08/
ML09/
ML15/
MS06
MS06/
+5V
0.1 mf ±20%
0.1 mf ±20% PT4-1062
SK
1 OF 1 LTR
ORIGINATOR
DATE 8/4/71
MJO PPCS/PADS
TITLE Sine/Cosine Logic
ENGINEERING SKETCH
TRW SYSTEMS GROUP
ONE SPACE PARK · REDONDO BEACH · CALIFORNIA
SK-MA603
SHEET 1 OF 1
SYSTEMS FORM REV. 5-67

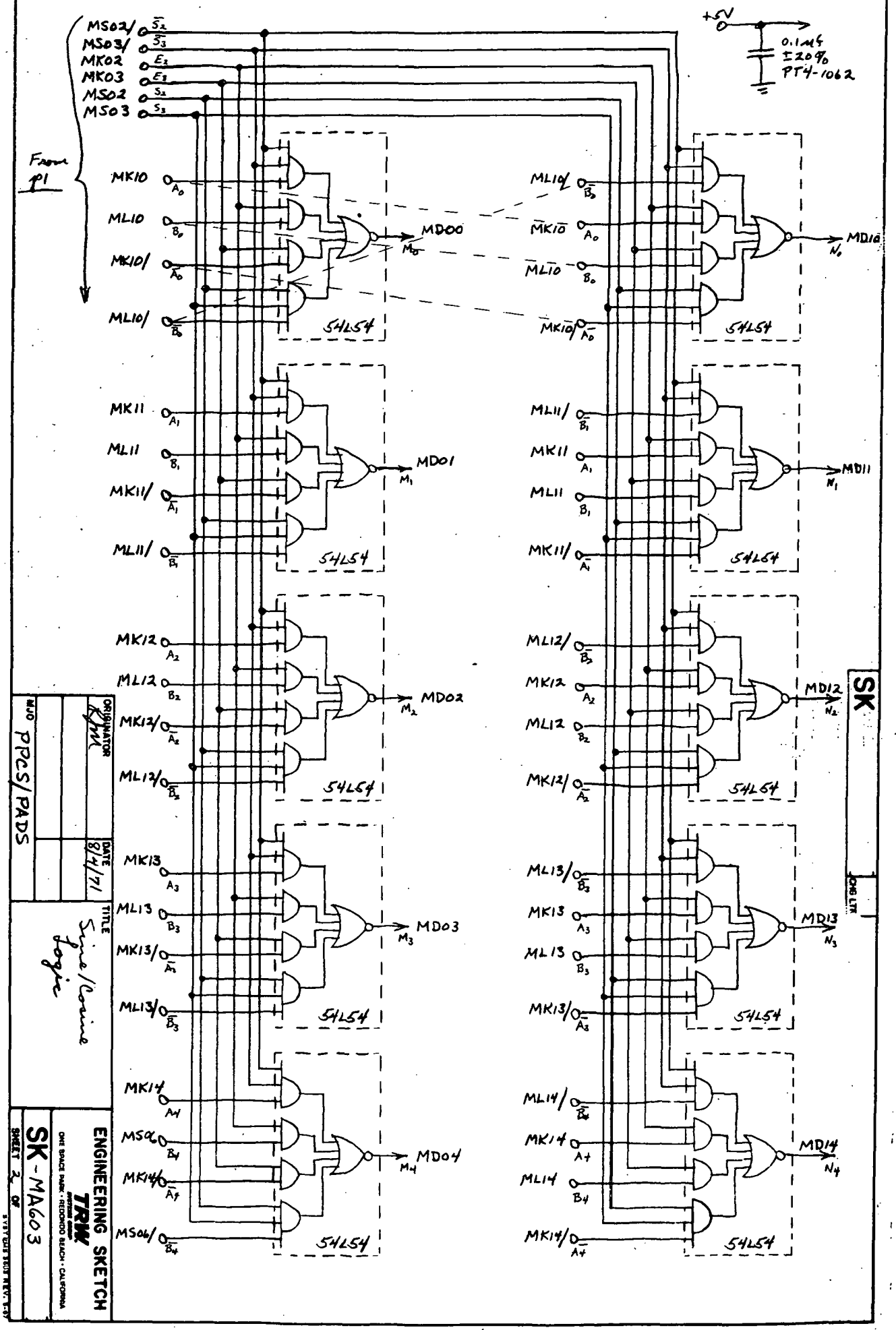
MS02/
MS03/
MK02
MK03
MS02
MS03
From P1
+5V
0.1μf ±20% PT4-1062
MK10
ML10
MK10/
ML10/
MD00
MD10
MK11
ML11
MK11/
ML11/
MD01
MD11
MK12
ML12
MK12/
ML12/
MD02
MD12
MK13
ML13
MK13/
ML13/
MD03
MD13
MK14
MS04
MK14/
MS04/
MD04
MD14
54LS54
SK
JOHNSON LTR
ORIGINATOR
DATE 8/4/71
MJO PDCS/PADS
TITLE Sine/Cosine Logic
ENGINEERING SKETCH
TRW SYSTEMS GROUP
ONE SPACE PARK • REDONDO BEACH • CALIFORNIA
SK-MA603
SHEET 2 OF

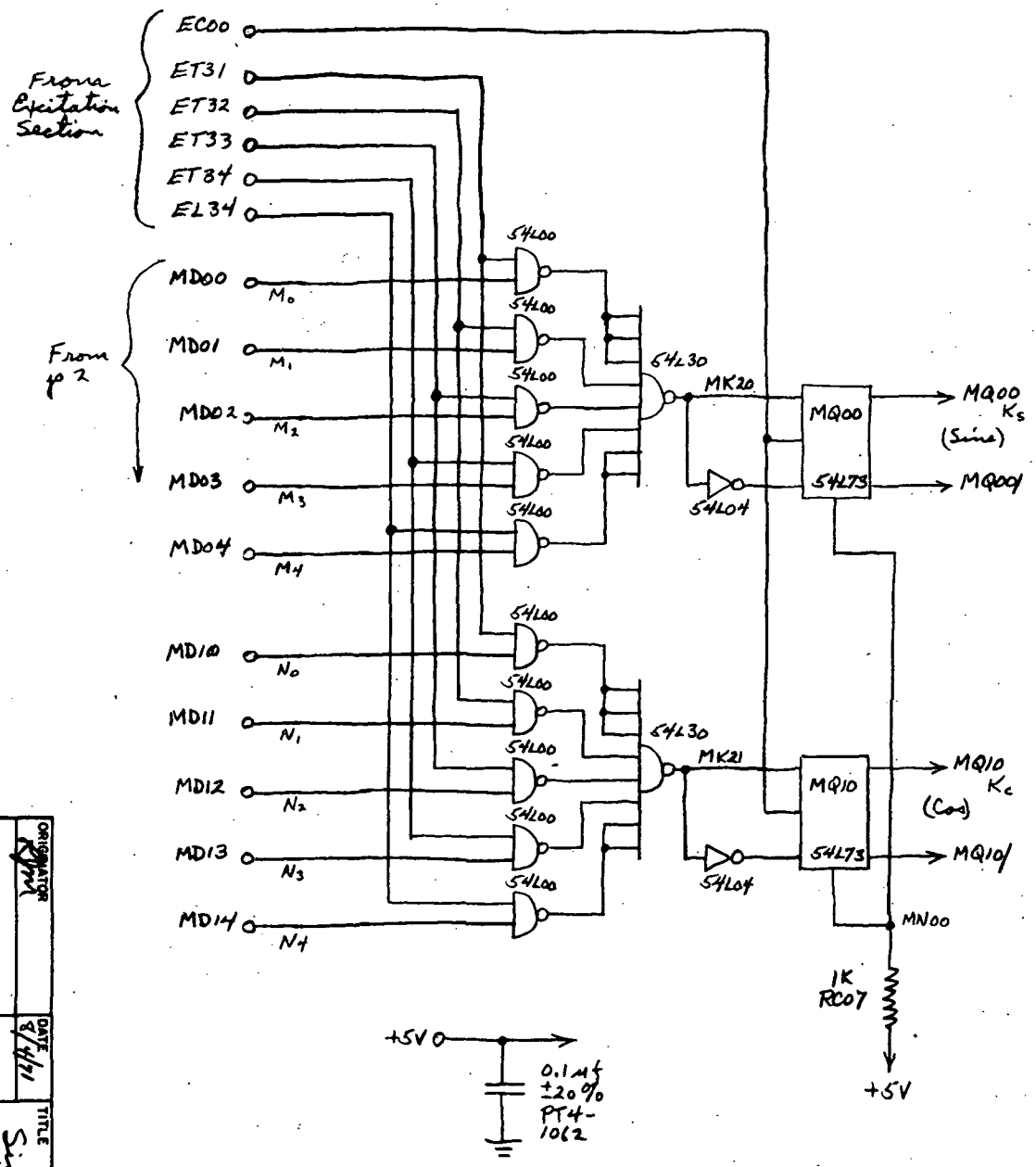

MJO PPCS/PADS	ORIGINATOR Rynn	DATE 8/4/81	
TITLE Sine/Cosine logic			
ENGINEERING SKETCH TRW ONE SPACE PARK • REDONDO BEACH • CALIFORNIA			
SK-MA603	SHEET 3 OF 17	REV. LTR	

SK

CHG LTR

SK

CHG LT

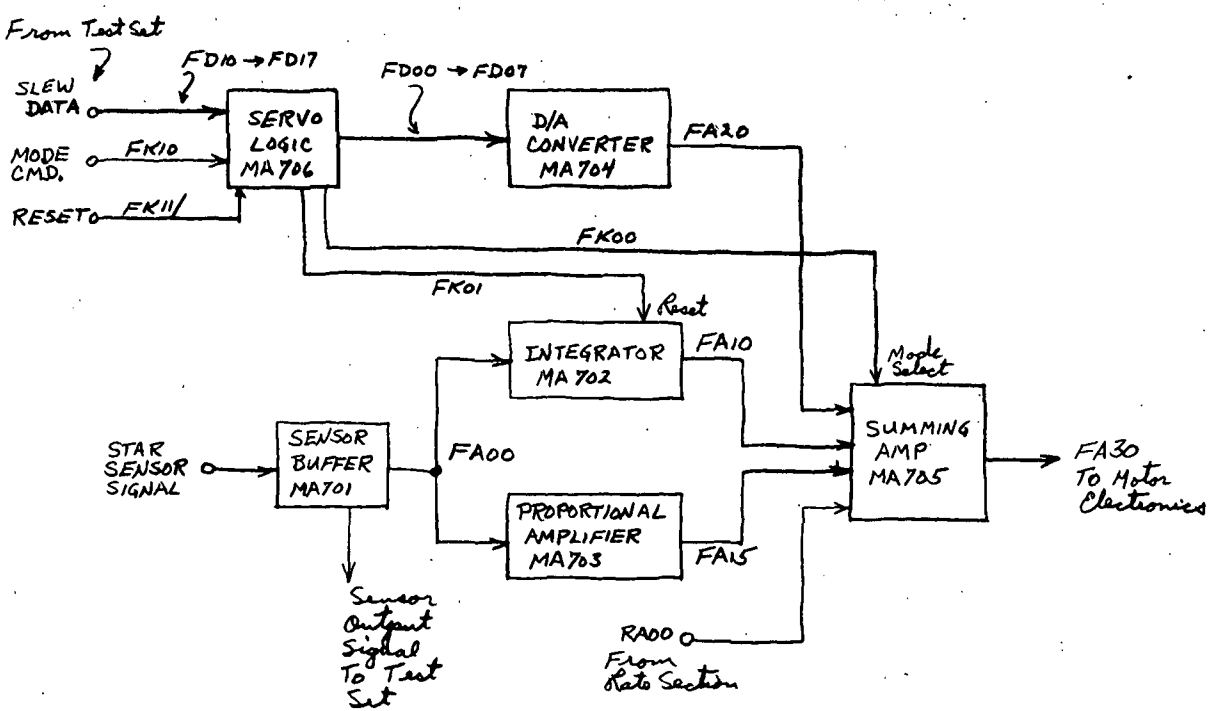

ORIGINATOR	DATE	TITLE	ENGINEERING SKETCH
RJM	12/2/71	Servo Processor Block Diagram	TRW SYSTEMS GROUP, ONE SPACE PARK • REDONDO BEACH • CALIFORNIA
			SK-MA700
MJO PADS/GEA			SHEET OF

SYSTEMS 5683 REV. 5-67

SK

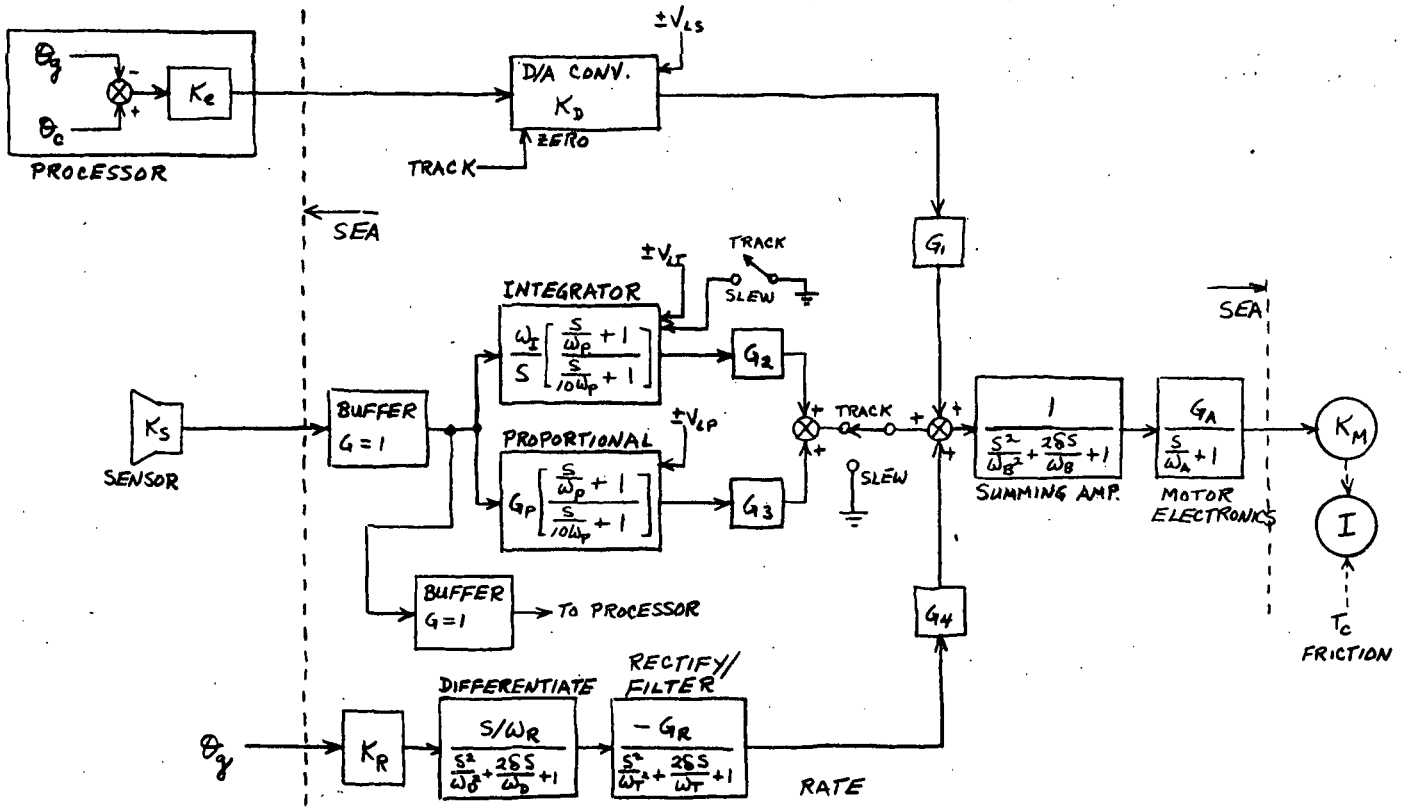

$K_S = 6.667$ mv/arc sec
$= 1.375 \times 10^3$ volt/rad

$K_M = 6$ oz in/volt
$= 3.12 \times 10^{-2}$ ft lb/volt

I(inner) $= 7.5$ oz in sec^2
$= 3.9 \times 10^{-2}$ ft lb sec^2

I(outer) $= 18.8$ oz in sec^2
$= 9.8 \times 10^{-2}$ ft lb sec^2

T_c(max) $= 38.4$ oz in
$= 0.2$ ft lb

$K_R = 1.63 \times 10^3$ volt/rad.
$\omega_R = 2.23 \times 10^2$ rad/sec.
$G_R = 5.0$ volt/volt
$\omega_D = 3.14 \times 10^3$ rad/sec
$\omega_T = 400$ rad/sec

ORIGINATOR	DATE	TITLE	ENGINEERING SKETCH
KJM	11/16/71	SEA SERVO MECHANIZATION	TRW SYSTEMS Group, ONE SPACE PARK · REDONDO BEACH · CALIFORNIA
			SK-MA700
MJO			SHEET 3 OF

TRW SYSTEMS 3455 REV. 6-67

SK

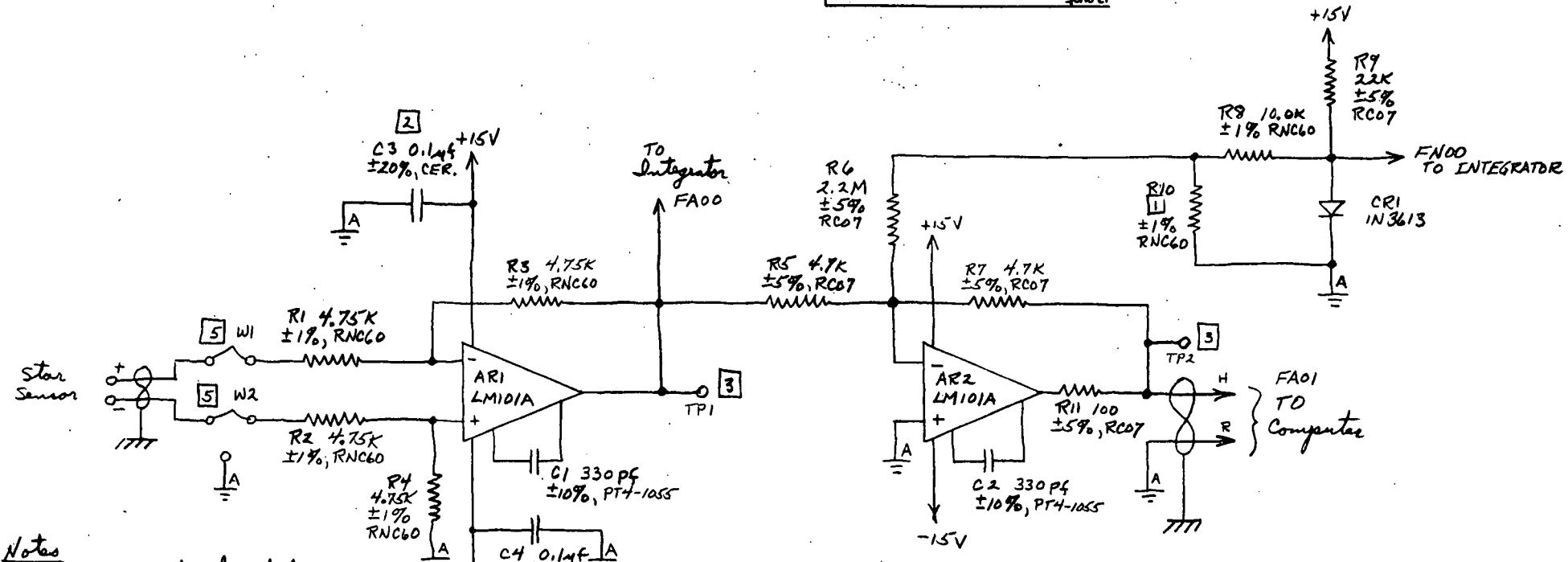

Notes

1. R10 is offset adjust for AR2. Select such that AR2 output is zero for AR1 stage input grounded. Nominal R10 is 2K, but may vary 0 → ∞.
2. These bypasses shared between AR1, AR2. Up to 6" leads for ±15V between AR1, AR2.
3. Test points
4. Any test points taken to test set panel, isolate with 47K.
5. Wire bridges. To be used for Integrator offset adjustment and AR2 buffer adjustment. Bridges normally closed.

ORIGINATOR	DATE	TITLE
KJM	11/9/71	Sensor Buffer
MJO PADS/SEA		

ENGINEERING SKETCH
TRW SYSTEMS GROUP
ONE SPACE PARK • REDONDO BEACH • CALIFORNIA

SK-MA701

SHEET 1 OF

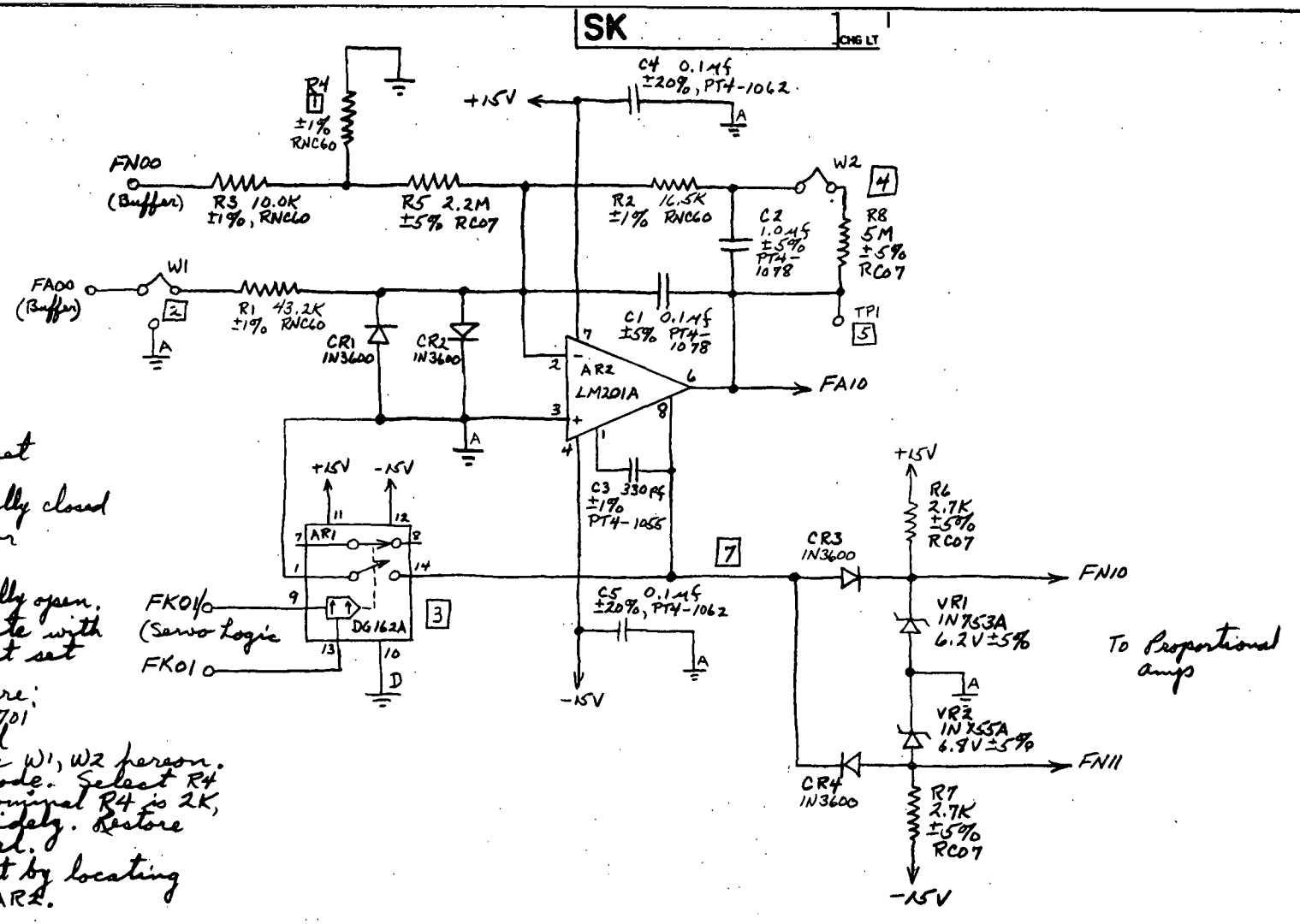

Notes

1. R4 is Integrator offset adjustment.
2. Wire bridge, normally closed
3. Contacts shown for Track mode, Pin 9 HIGH.
4. Wire bridge, normally open.
5. Test point. Isolate with 47K if taken to test set panel.
6. Adjustment Procedure: open W1, W2 of SKMA701 (Buffer), and ground Buffer inputs. Close W1, W2 for on. Place in TRACK mode. Select R4 for ZERO FA10. Nominal R4 is 2K, but may vary widely. Restore bridges to normal.
7. Keep this lead short by locating AR1, CR3, CR4 near AR2.

ORIGINATOR	DATE	TITLE	ENGINEERING SKETCH
RBM	11/30/71	Integrator	TRW SYSTEMS GROUP, ONE SPACE PARK · REDONDO BEACH · CALIFORNIA
MJO PADS/SEA			SK-MA702
			SHEET 1 OF

SYSTEMS 3885 REV. 5-67

SK

CHG LT

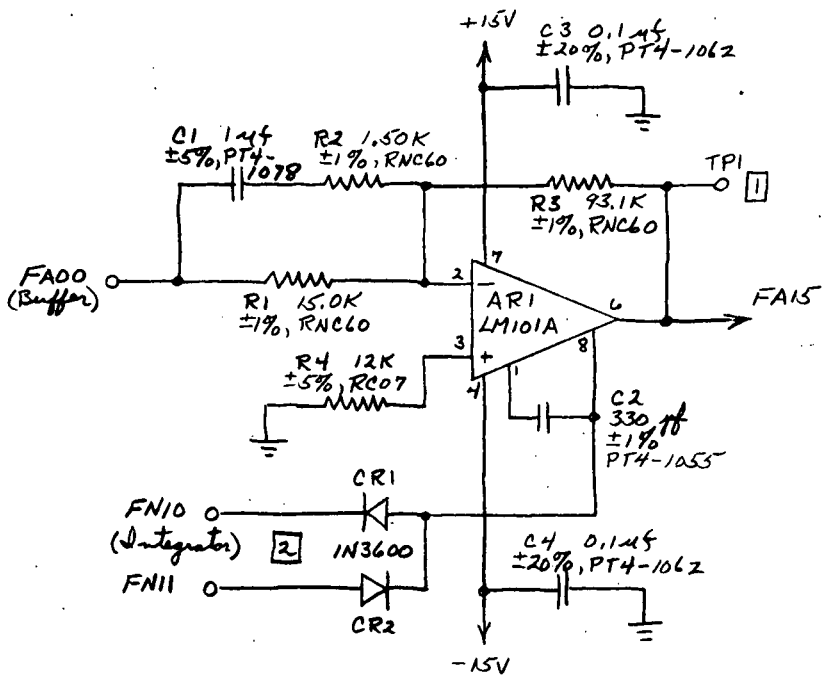

Notes

1 If test point taken to test set, isolate with 47K.

2 Locate CR1, CR2 near AR1.

ORIGINATOR	DATE	TITLE	ENGINEERING SKETCH
RJM	11/30/71	Proportional Amplifier	TRW SYSTEMS GROUP, ONE SPACE PARK · REDONDO BEACH · CALIFORNIA
			SK-MA703
MJO PADS/SEA			SHEET 1 OF

SYSTEMS 3613 REV. 5-67

CHG LTR

SK

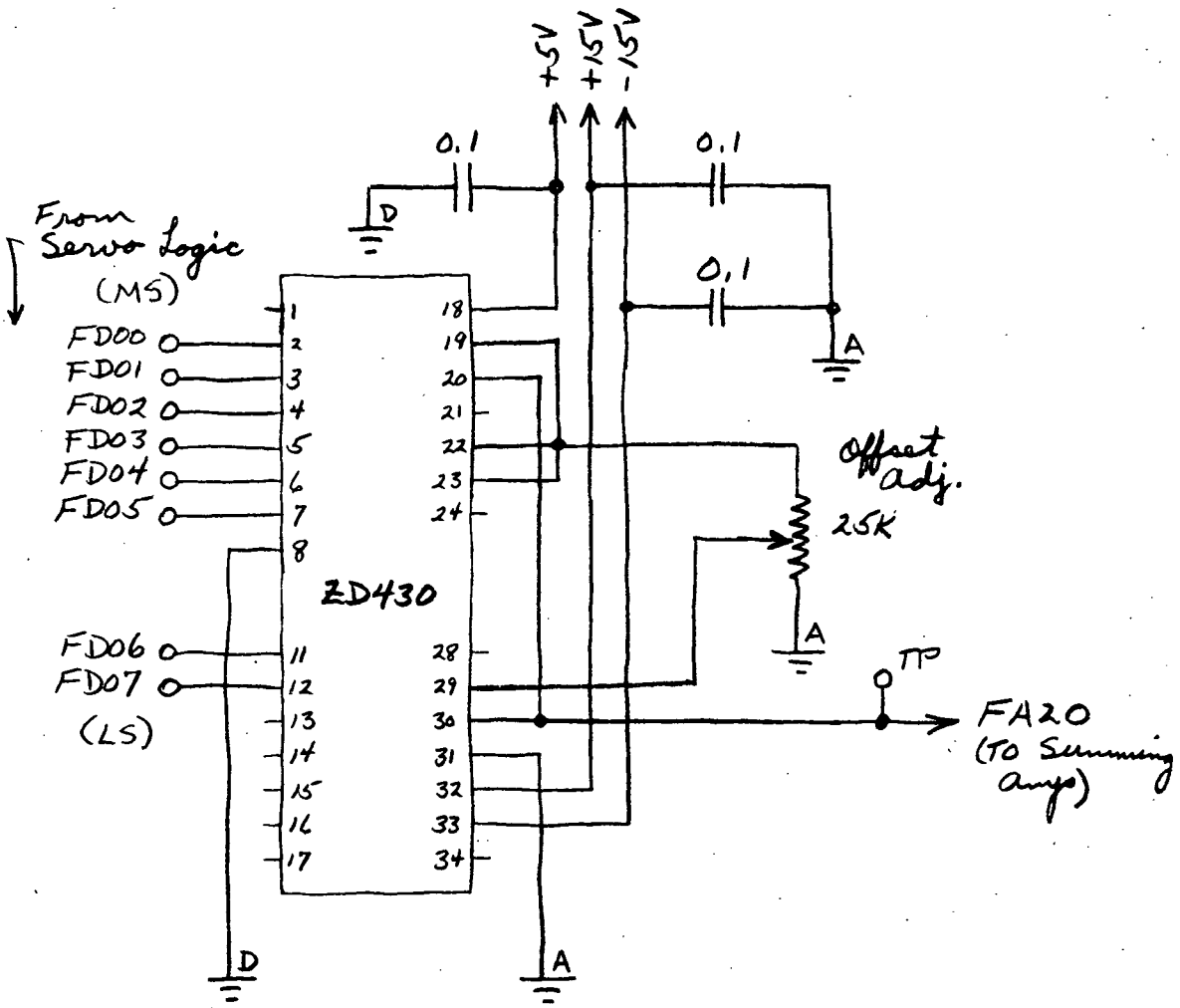

ORIGINATOR	DATE	TITLE	ENGINEERING SKETCH
KJM	12/20/71	D/A Converter	TRW SYSTEMS GROUP, ONE SPACE PARK • REDONDO BEACH, CALIFORNIA
			SK-MA704
MJO PADS/SEA		CODE IDENT NO. 11982	SHEET 1 OF

SYSTEMS 523 REV. 10-70

SK

CHG LT

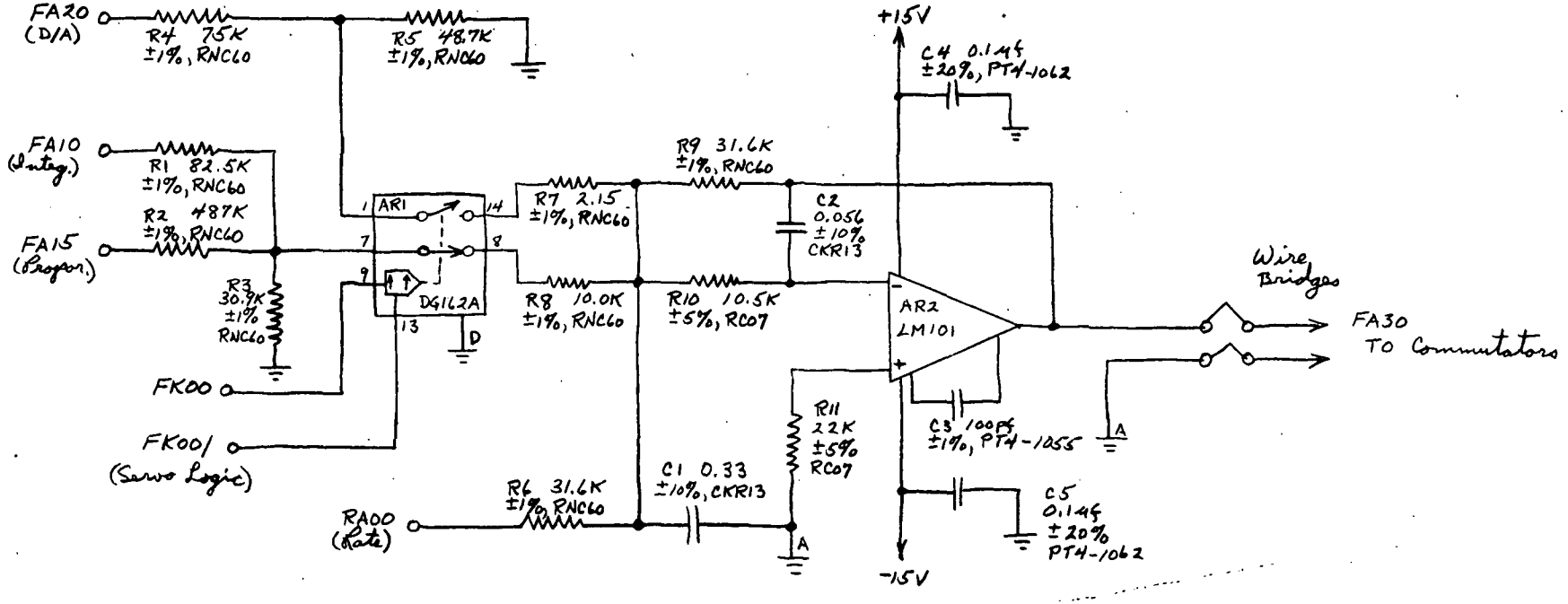

PRELIMINARY

ORIGINATOR	DATE	TITLE	ENGINEERING SKETCH
[signature]	12/2/71	Summing amplifier	TRW SYSTEMS GROUP
[signature] A	4/6/72		ONE SPACE PARK • REDONDO BEACH • CALIFORNIA
			SK-MA705A
MJO PADS/SEA			SHEET OF

SYSTEMS 3603 REV. 5-67

SK	REVISIONS			
	LTR	DESCRIPTION	DATE	APPROVED

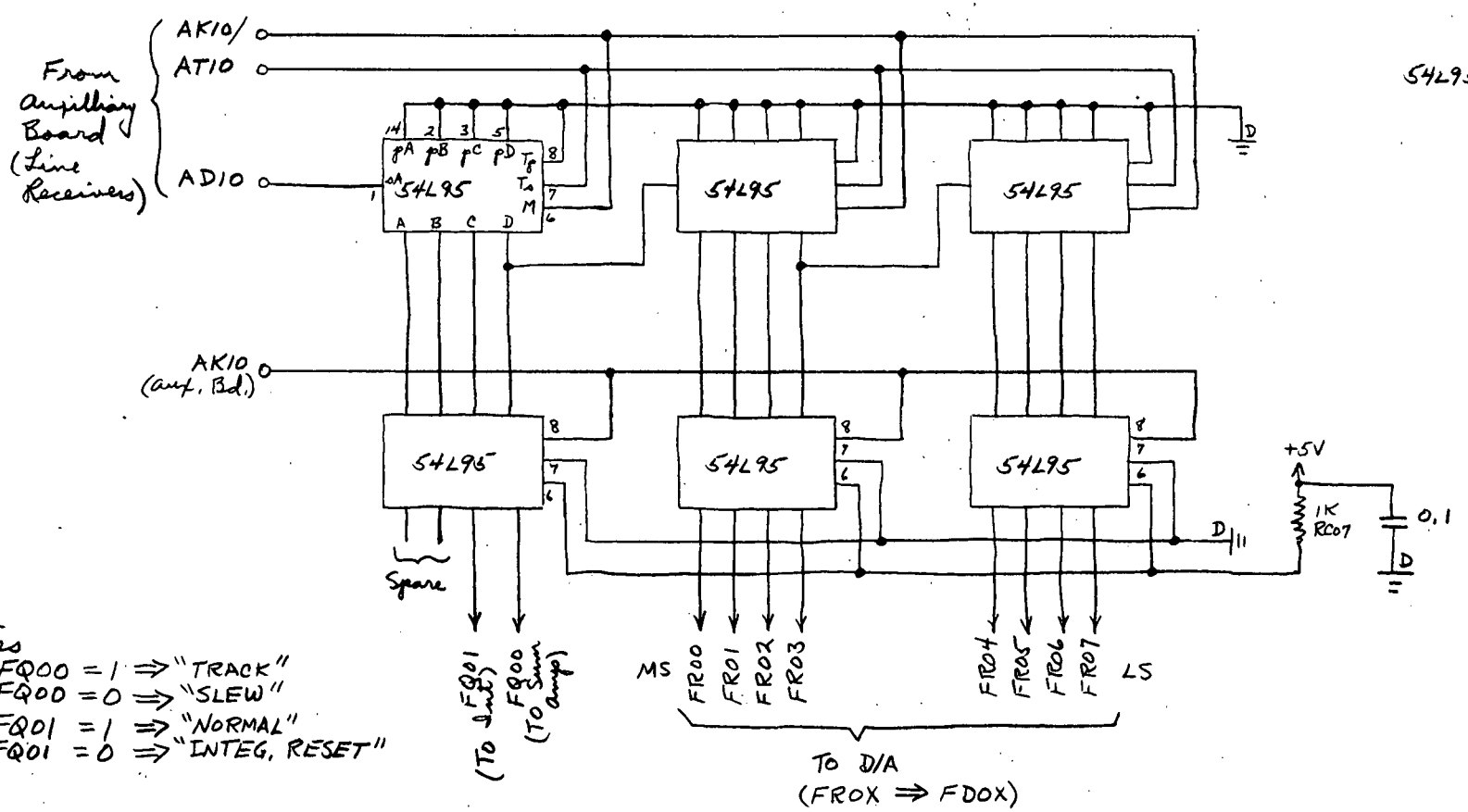

Notes
1. FQ00 = 1 ⇒ "TRACK"
   FQ00 = 0 ⇒ "SLEW"
   FQ01 = 1 ⇒ "NORMAL"
   FQ01 = 0 ⇒ "INTEG. RESET"

ENGINEERING SKETCH		TRW SYSTEMS GROUP — ONE SPACE PARK • REDONDO BEACH, CALIFORNIA	
ORIGINATOR	DATE	Servo Logic	
JM A	4/6/72		
MJO PADS/SEA		SIZE B	CODE IDENT NO. 11982 — SK-MA706A
		SCALE	SHEET 1 OF

SYSTEMS 3663 REV. 12-71